# 2-D Coherent Power Scaling of Mid-Infrared

# Quantum Cascade Lasers

By

Christopher A. Sigler

A dissertation submitted in partial fulfillment of

the requirements for the degree of

Doctor of Philosophy

(Electrical Engineering)

at the

UNIVERSITY OF WISCONSIN-MADISON

2018

Date of final oral examination:        7/9/2018

The dissertation is approved by the following members of the Final Oral Committee:
  Luke J. Mawst, Professor, Electrical and Computer Engineering
  Dan Botez, Philip Dunham Reed Professor, Electrical and Computer Engineering
  Zongfu Yu, Dugald C. Jackson Assistant Professor, Electrical and Computer Engineering
  Robert G. Bedford, Senior Electronics Engineer, Air Force Research Laboratory

# 2-D Coherent Power Scaling of Mid-Infrared Quantum Cascade Lasers

**Christopher A. Sigler**

**Under the supervision of Professor Luke Mawst and Professor Dan Botez**

**At the University of Wisconsin-Madison**

## Abstract

Scaling the continuous-wave (CW) power of quantum cascade lasers (QCLs) beyond ~5 W has proven difficult, and beam-quality degradation is common when scaling the device volume for high power. The primary objective of this work was to develop methods for spatially-coherent power scaling of mid-infrared-emitting QCLs to high CW powers. Two approaches were investigated: 1) resonant leaky-wave-coupled antiguided phase-locked laser arrays; and 2) grating-coupled surface-emitting lasers (GCSELs). These two approaches can be combined to realize high surface-emitted powers in a spatially and temporally coherent beam pattern.

Optical and thermal models of planarized leaky-wave-coupled phase-locked QCL arrays were coupled together to investigate the influence of thermal lensing on modal behavior. Self-focusing under thermally-induced index variations across the array were found to impact the field profile and promote multi-moding due to gain spatial hole burning. Two techniques were found to mitigate this effect: 1) employing anti-resonant reflective-optical waveguide terminations outside the array; and 2) chirping the element width across the array to obtain

identical optically-equivalent widths under CW operation, eliminating thermal lensing at a particular operating condition.

Five-element phase-locked arrays of 4.7 μm-emitting QCLs were demonstrated which operate in a near-diffraction-limited beam (primarily in the in-phase array mode) to 5.1 W peak pulsed power, in agreement with simulations. Spectrally resolved near- and far-field measurements indicate that the wide spectral bandwidth of the QCL core promotes multi-mode operation at high drive levels. An optimized array design was identified to allow sole in-phase mode operation to high drive levels above threshold, indicating that full spatial coherence to high output powers does not require full temporal coherence for phase-locked laser arrays.

Lastly, a novel method for obtaining a single-lobed beam pattern from transverse magnetic (TM)-polarized GCSELs is proposed: resonant coupling of the optical mode of a QCL to the antisymmetric surface plasmon mode of a $2^{nd}$-order distributed feedback metal/semiconductor grating results in strong antisymmetric-mode absorption. Lasing in the symmetric mode, resulting in a single-lobed far-field beam pattern from the substrate emission, is strongly favored around resonance. For infinite-length devices, the symmetric mode has negligible absorption loss while still being efficiently outcoupled by the grating.

# Acknowledgements

I would like to express my sincere appreciation to everyone that has given me encouragement, inspiration, and guidance to get to this point. First, I would like to thank my advisors, Prof. Luke Mawst and Prof. Dan Botez, for introducing me to this field and giving me the opportunity and guidance to complete this work. I would also like to thank my other committee members, Zongfu Yu and Robert Bedford, for their time spent on evaluating my work and providing comments and suggestions.

I would like to acknowledge the support of my colleagues: Dr. Chun-Chieh Chang, for passing on his cleanroom experience to me and teaching me about the QCL active region k·p modeling; Colin Boyle, also for training me in device fabrication and many discussions on the subject; Dr. Jeremy Kirch, for performing the MOVCD growths in this work and introducing me to COMSOL modeling; Dr. Toby Garrod, Kevin Oresick, Honghyuk Kim, Ayushi Rajeev, Ben Knipfer, and Jae Ha Ryu for the various discussions we've had and the assistance they've provided in innumerable ways. I'd also like to thank Tom Earles, for sharing his experience; Don Lindberg III, for his assistance with both performing and instructing me in device characterization; Ricky Gibson, for near-field measurements of arrays; Prof. Maryam Farzaneh and her students at UW-Stevens Point, for thermoreflectance measurements of our devices; Xiaodong Wang, for discussions on DFB analysis; and Phillip Buelow and Aaron Tan, for their assistance with polishing of devices.

None of this would have been possible without my family. To my parents and my brother, you have served as my inspiration and role models throughout my life. Finally, I would like to dedicate this work to my wife, Gina, for her patience and encouragement throughout this process.

# **Table of Contents**

# List of Figures

# List of Tables

# Chapter 1 – Introduction

## 1.1    Motivation

The mid-infrared (mid-IR) is sometimes called the molecular fingerprint region of the electromagnetic spectrum [1] because many molecules have resonant absorption peaks in this regime. Thus, the major applications for devices emitting electromagnetic waves in the mid-IR revolve around spectroscopy, including trace-gas sensing [2]–[4], standoff detection [5]–[7], process control [8], medical diagnostics [9], breath analysis [10], etc. High-power lasers in this regime could also find use as laser scalpels in surgical treatments [11], and there are windows of little atmospheric absorption due to water vapor in the mid-IR, at ~3–5 µm and ~8–10 µm, allowing for the possibility of using these wavelengths for free-space optical communication [12]. Yet another possible application is infrared countermeasures against infrared-guided (heat-seeking) missiles [13].

These applications have driven the development of optical sources emitting in this regime, including quantum cascade lasers (QCLs), the focus of this work. Each application that requires an optical source has its own requirements, such as wavelength, temperature sensitivity, continuous-wave or pulsed operation, output power, tunability, linewidth, or wallplug efficiency. Many potential applications require high output power with good beam quality (e.g., nearly diffraction-limited), which, as we will see, is difficult to obtain.

### 1.1.1   Mid-IR Sources

Sources for the mid-wave infrared (MWIR or mid-IR), long-wave infrared (LWIR), and terahertz (THz) regimes, comprised of wavelengths from ~3 to 200 µm or beyond, have suffered from various issues. Conventional semiconductor diode lasers, such as GaAs- and InP-based semiconductor lasers which have been successfully commercialized, operate by having electrons

and holes recombine across the bandgap of the material. Due to increasing nonradiative (Auger) recombination with decreasing bandgap energy, this limits the minimum energy or maximum wavelength of these devices to the short-wave infrared (SWIR or near-IR), or < 3 μm. $CO_2$ lasers are bulky but can operate at high power at various specific wavelengths in the MWIR or LWIR [14]. Lead-salt lasers must be operated at low temperatures or in pulsed operation and emit low powers because they have poor thermal conductivity and are highly temperature sensitive [15], [16]. High-performance interband-transition lasers with a low threshold current density have been reported in the mid-IR by using either GaSb-based type-I quantum wells (QWs) [17]–[19] or interband cascade lasers [20]. However, due to Auger recombination, such devices are also highly temperature sensitive and have limited wavelength ranges due to their interband-transition nature. Quantum cascade lasers, since their demonstration in 1994 [21], have become popular and promising mid-IR laser sources, fulfilling many of the requirements for the applications in this wavelength regime.

### 1.1.2   Coherent Power Scaling of Quantum Cascade Lasers

Conventional single-element QCLs have been demonstrated to emit up to ~5 W of power at a wavelength of ~5 μm [22]–[25]. Scaling beyond this limit has proven difficult, and it is even more so if a diffraction-limited beam is desired. Multi-spatial mode behavior is common when trying to scale up the device volume for high power, which degrades beam quality. Thus, a variety of techniques for scaling the device volume and power while maintaining good beam quality have been attempted. None, however, have succeeded at surpassing a simple single-element device in continuous-wave (CW) output power and beam quality. This work continues that effort.

## 1.2    Scope and Objectives

The primary objective of this work is to develop methods for spatially-coherent power scaling of mid-IR (~5 μm) emitting quantum cascade lasers to high CW powers by optimization of the optical cavity. Two approaches are investigated: 1) scaling the core volume laterally using resonant leaky-wave-coupled antiguided phase-locked laser arrays [26]–[30], which are high-index-contrast photonic crystals [31] that are relatively stable against thermally- and carrier-induced index variations experienced during CW operation [32]; and 2) grating-coupled surface-emitting lasers (GCSELs), which are distributed feedback lasers emitting in an extremely narrow beam out of the surface of the chip due to the large radiating area. These surface-emitters have a low optical power density at the emitting aperture and can operate without heating an emitting facet as in an edge-emitter, which is a source of degradation for QCLs. A novel method for obtaining a single-lobed beam pattern from transverse magnetic (TM)-polarized GCSELs which efficiently scales with length to high powers was developed as part of this work [33], [34]. These two approaches can be combined as described in [35] to realize high surface-emitted powers in a spatially and temporally coherent beam pattern. The optimization of the QCL core region is not a focus of this work. This is a complementary approach, in that a more optimized core region could be used with any of the methods developed here to continue to scale the output power.

## 1.3    Organization

In Chapter 2, the operating principles of a quantum cascade laser are introduced, with a particular focus on those topics which are important in this work. Several models for QCLs are introduced in Chapter 3, including optical models, a thermal model, and a method of optimizing QCLs for high CW power which is benchmarked against our buried heterostructures emitting ~2.5 W in CW operation [23]. In Chapter 4, methods for coherently scaling the output power of

QCLs are described along with the advantages and disadvantages of each. Here, the concept of the leaky-wave-coupled antiguided phase-locked array, the first major focus of this work, is introduced. In Chapter 5, the modeling performed to design these phase-locked arrays is presented. Experimental results obtained from another version of these arrays are presented in Chapter 6, in which five-element arrays operating predominately in an in-phase array mode emitted up to at least 5.1 W. In Chapter 7, an overview on distributed feedback and grating-coupled surface-emitting lasers is given, and in Chapter 8 a novel method of obtaining longitudinally-symmetric mode operation from TM-polarized GCSELs by resonant absorption of the antisymmetric mode is presented. Finally, in Chapter 9 a summary of the dissertation as well as paths forward for possible future work are given.

# Chapter 2 – Overview of Quantum Cascade Lasers

## 2.1    Lasers

A laser, which is an acronym for "Light Amplification by the Stimulated Emission of Radiation," requires both amplification of light (via stimulated emission) within some gain medium and oscillation of the light within some resonant optical cavity. That is, there must be some feedback mechanism such that the light travels through the amplifying region multiple times and constructively interferences with itself. A schematic example of a laser cavity is shown in Fig. 2.1, where left-propagating and right-propagating electromagnetic waves oscillate between two mirrors and are amplified as they travel between them (represented by the growing colored regions around each arrow). The right mirror is partially reflective so that some of the light can be emitted into an output beam.
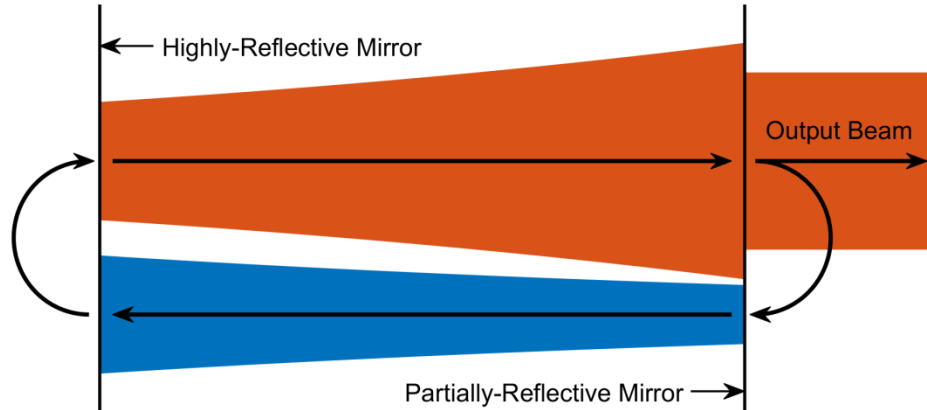


Fig. 2.1. Schematic of a laser cavity. The blue and orange colors represent the intensity of the left and right-propagating electromagnetic waves, respectively. The two are vertically offset in the schematic for visibility.

There is also a separate class of 'amplifiers' in which light passes only once through the amplifying region (for example, Erbium-doped fiber amplifiers, or EDFAs) [36]. There are

various types of lasers that use different gain media [37]: gas lasers, such as $CO_2$ lasers; liquid dye lasers, solid-state lasers, and semiconductor lasers - all of which behave differently.

Lasers are 'pumped' either optically or electrically. An optically pumped laser requires an input wave with a photon energy larger than that of the output photon energy, while an electrically pumped laser requires a voltage to be applied that is larger than the output photon energy multiplied by the charge of an electron and the number of photons emitted by each electron. When unpumped or lightly pumped, the gain medium absorbs light at the output wavelength. As the pumping level is increased, the gain medium absorbs light less and spontaneously emits some light, which is then quickly re-absorbed or emitted out of the cavity. Eventually, the gain medium begins to amplify the light as it propagates through the medium, the transition point being called 'transparency.' Once the pumping reaches some 'threshold,' the gain medium amplifies the light enough that the 'gain' provided by it can overcome the 'loss' caused by absorption elsewhere in the laser and emission out of the laser, and the light is able to oscillate within the cavity indefinitely. This is the onset of lasing. As the pumping is increased from this point, the intensity of light within the cavity increases, as does the intensity of the light which is emitted from the cavity.

## 2.2    Semiconductor Lasers

Semiconductor lasers are a particular class of laser in which the gain medium (or 'active region') is made of semiconductors. A conventional 'diode' semiconductor laser is bipolar, meaning it consists of p-type doped and n-type doped layers forming a junction, grown vertically on top of each other through a method such as metal-organic chemical vapor deposition (MOCVD) [38]. When a forward bias is applied to this p-n junction, current flows vertically through the junction and electrons and holes are able to recombine to produce photons.

Frequently, this recombination takes place in quantum wells, thin layers of a semiconductor with a bandgap lower than that of the surrounding material. This improves electron and hole confinement and hence efficiency. The cavity is typically formed by cleaving the semiconductor wafer along a crystal plane to form perfectly planar mirrors (called 'facets') on either end of the waveguide (or 'stripe'), discussed below. Sometimes, dielectric or metal layers are deposited on these cleaved facets to form highly-reflective (HR) or anti-reflective (AR) coatings. The light is emitted out one of the facets if the other is HR-coated, or both of them if neither is. This type is cavity with two mirrors providing feedback is called a Fabry-Perot cavity. Other methods for providing feedback can be used, such as something known as 'distributed feedback,' in which feedback occurs throughout the length of the cavity instead of just the ends, will be discussed more in Ch. 7.

### 2.2.1  Waveguides

The active region of a semiconductor laser is typically surrounded by additional layers (vertically, or the 'transverse' direction) which form a positive-index-step waveguide. That is, the refractive index of the material in the center of the waveguide is higher than that for the outer materials. The light within the cavity then forms an optical mode to confine the light vertically, as shown in Fig. 2.2, as it propagates along the waveguide ('longitudinally') between the mirrors at either end of the stripe. The effective index, $n_{eff}$, of the mode is related to the phase velocity, $v_p$, of the mode by $v_p = c/n_{eff}$ [36]. In regions in which the effective index is larger than the material's (refractive) index, the electric field is 'evanescent' and decays exponentially in the transverse direction. In regions in which the effective index is smaller than the material's index, the field can propagate in the transverse direction. There can be multiple modes of a given polarization supported by a waveguide, each with an increasing number of nulls and peaks in its

transverse profile. The 'order' of a mode is the number of field nulls in the mode, while the 'fundamental' mode has zero nulls, and is the mode depicted in Fig. 2.2.
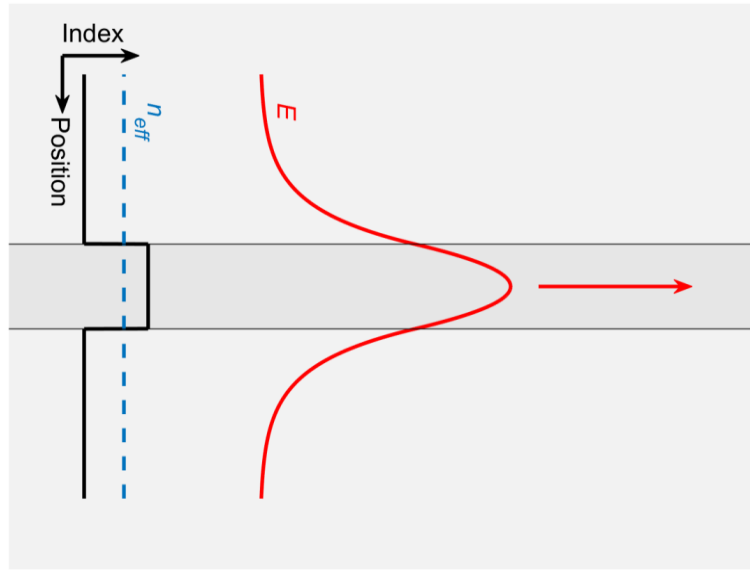


Fig. 2.2. Schematic of a three-layer positive-index-step waveguide, showing the electric field amplitude, $E$, of a fundamental mode propagating to the right. The effective index, $n_{eff}$, of the mode is between the refractive indices of the component materials.

A two-dimensional waveguide like that shown in Fig. 2.2 can support modes of two polarizations: transverse-electric (TE), in which the electric field ($E$-field) is out-of-plane; and transverse-magnetic (TM), in which the magnetic field ($H$-field) is out-of-plane. In each case, the opposite field is in-plane. For a 3-dimensional waveguide, both fields have non-zero components in all directions, though they still tend to have a dominant component in either the transverse (vertical) or lateral (sideways) direction, with the other field dominant in the other direction. While not strictly a TM (TE) mode, a mode where the dominant field in the lateral direction is the magnetic (electric) field is frequently referred to as a TM (TE) mode. There are frequently subscripts placed after the polarization to indicate the order of the mode in both the transverse and lateral directions. So, the $TM_{00}$ mode is the most fundamental mode with a dominant lateral $H$-field component and dominant transverse $E$-field component.

There are a variety of methods for laterally confining the mode, such as: gain-guiding, in which only the gain and any accompanying change in the refractive index is used to confine the light; buried heterostructures, in which a positive-index-step-waveguide is formed laterally using other electrically semi-insulating semiconductors; or etching through the active region and forming a ridge waveguide, which is also a lateral positive-index-step waveguide but uses a dielectric material on either side of the active region. Such waveguides are discussed more in detail in [39].

For InP-based quantum cascade lasers (QCLs), buried heterostructures (BHs) are the most common form of waveguide for devices emitting high continuous-wave (CW) powers (i.e., continuously driven by a DC current with no pulsing or modulation). BH QCLs are formed by etching through the active region (or 'core') to form a ridge, and regrowing Fe-doped InP on the sides of it. This InP:Fe is semi-insulating, so the current is confined to the core, it has a high thermal conductivity compared to alternative materials (such as the dielectrics $Si_3N_4$ and $SiO_2$), it has low absorption loss in these wavelengths, and it produces a small lateral index step for low scattering losses. The transverse waveguide structure has InP above and below the core as well. Sometimes, there are InGaAs confinement layers directly outside the core, to improve the optical confinement to the core, particularly for longer wavelengths.

## 2.3    Quantum Cascade Lasers

This chapter will focus on background information on QCLs that is necessary to understand the important factors in designing a high-power coherent QCL, and to introduce terms that will be used later. First, we will discuss how the two components of gain are produced in a QCL: stimulated emission via intersubband transitions and population inversion. Then, we

will describe the spectral properties of QCLs and electron backfilling. Finally, rollover and temperature effects in QCLs will be discussed.

## 2.4    Intersubband Transitions

The key component that makes a QCL differ from a conventional diode laser is that QCLs depend on intersubband transitions. That is, instead of relying on a high-energy transition when an electron and hole recombine across the bandgap, a QCL relies on a low-energy transition when an electron or hole transitions between states within a single band. Fig. 2.3 shows the band structure of 'stage' of the superlattice core of the first demonstrated QCL [21]. The moduli squared of the relevant wavefunctions for the operation of this laser are superimposed on the band diagram at their corresponding energy levels. Since the electrons remain in the conduction band after passing through one of these stages, the stages can be repeated so that each electron can produce more than one photon. Additional stages will increase the total output power, at the expense of a higher required voltage. The states within the conduction band exist due to alternating $In_{0.53}Ga_{0.47}As$ quantum wells and $In_{0.52}Al_{0.48}As$ quantum barriers, both of which are lattice-matched to InP. The wavefunctions in these band diagrams are typically found by self-consistently solving Schrödinger's and (sometimes) Poisson's equations [40], [41]. Some electric field is assumed to be applied, which results in the tilted band edges. The 'active region' is the section of a stage in which the lasing transition occurs.
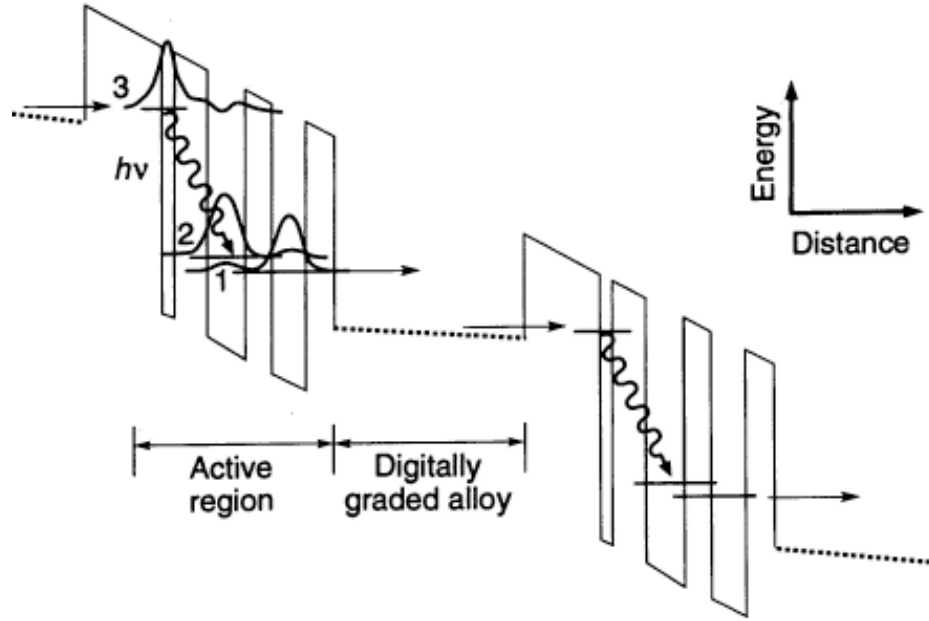
Fig. 2.3. Conduction band energy diagram of the first demonstrated QCL. From [21]. Reprinted with permission from AAAS.

The intersubband transition means that the bandgap of the semiconductor is not used, and thus an indirect bandgap semiconductor, such as silicon, could potentially be used to form the QCL. Although electroluminescence has been observed from a Si-Ge device operating in the valence band [42], most work has focused on InP- and GaAs-based structures using electrons in the conduction band. There has also been work on producing QCLs on metamorphic buffer layers, which would allow an arbitrary substrate lattice constant for more flexibility in choosing materials [43]–[45].

The use of intersubband transitions in the conduction band leads to QCLs being TM-polarized devices, while most conventional devices are TE-polarized. To understand why, consider the matrix element, or overlap integral, for an intersubband transition in a quantum well. The transition rate between two electronic states is directly proportional to this matrix element. So, if it is zero, there can be no transitions, and hence no stimulated emission. From eq. (4.18) in [39], for an interband transition, the overlap integral $H'_{21}$ is:

$$H_{21}' = \langle \psi_2 | H'(r) | \psi_1 \rangle = \frac{q}{2m_0} \int_v F_2^* u_2^* (A(r)\hat{e} \cdot p) F_1 u_1 d^3 r$$

$$= \frac{q}{2m_0} \left[ \int_v u_2^* u_1 F_2^* (A(r)\hat{e} \cdot p) F_1 d^3 r + \int_v [F_2^* A(r) F_1] u_2^* \hat{e} \cdot p u_1 d^3 r \right] \tag{2.1}$$

where $u_1 = u_c$ and $u_2 = u_v$, the Bloch functions in the conduction and valence bands, respectively, $F_1$, $F_2$ are the envelope functions for the states involved in the transition and are functions of position, $r$, $A$ is the magnitude of the magnetic vector potential of the electromagnetic wave, $\hat{e}$ is the unit polarization vector in the direction of the vector potential, $p$ is the momentum operator, and the integrals are performed over the entire volume covered by the wavefunctions. As $u_c$ and $u_v$ are orthogonal and rapidly vary within a unit cell, while the other terms are roughly constant within a unit cell, the first term in the bracket vanishes for interband transitions. For transitions entirely within the conduction band, as in a typical QCL, $u_v$ is replaced with $u_c$, and the first integral no longer automatically goes to zero, since $\int_v u_c^* u_c d^3 r = 1$. However, making the assumption that the envelope functions within the conduction band are orthogonal, as they typically are, the second integral must vanish. This is unlike the interband case, where $\langle F_{2z} | F_{1z} \rangle = \int_v F_2^* F_1 d^3 r \approx \delta_{N,M}$, as one cannot have $N = M$ when the transition occurs within a single band. Thus,

$$H_{21}' \approx \frac{q}{2m_0} \left[ \int_v F_2^* (A(r)\hat{e} \cdot p) F_1 d^3 r + 0 \right] \tag{2.2}$$

If the growth direction (i.e., normal to the layer surfaces) is $\hat{y}$, then

$$F_{1,2}(r) = F_{1y,2y}(y) \cdot e^{-ik_{1,2} \cdot r_{//}} \tag{2.3}$$

where $r_{//}$ is the in-plane components of $r$ and $i$ is the unit imaginary number. Letting the polarization of the electromagnetic field be $\hat{e} = e_x \hat{x} + e_y \hat{y} + e_z \hat{z}$, then since $p = -i\hbar \nabla$,

$$H_{21}' = \frac{q}{2m_0} \int_v F_2^* (A(r)\hat{e} \cdot p) F_1 d^3 r \tag{2.4}$$

$$= \frac{q}{2m_0} \int_v A(r) F_{2y}^*(y) e^{+ik_2 \cdot r_{//}} (-i\hbar)(e_x \frac{\partial}{\partial x} + e_y \frac{\partial}{\partial y} + e_z \frac{\partial}{\partial z}) F_{1y}(y) e^{-ik_1 \cdot r_{//}} d^3 r$$

$$= \frac{-i\hbar q}{2m_0} \int_v A(r) F_{2y}^*(y) e^{+ik_2 \cdot r_{//}} \left[ (-ik_{1x}e_x - ik_{1z}e_z)F_{1y}(y) + e_y \frac{\partial}{\partial y}F_{1y}(y) \right] e^{-ik_1 \cdot r_{//}} d^3r$$

The $e^{ik \cdot r_{//}}$ terms form the familiar phase-matching condition $\delta((k_2 - k_1) \cdot r_{//})$ when integrated:

$$H_{21}' = \frac{-\hbar q}{2m_0} \delta((k_2 - k_1) \cdot r_{//}) \left[ \int_v A(r)(k_{1x}e_x + k_{1z}e_z)F_{2y}^*(y)F_{1y}(y)d^3r + \int_v A(r)F_{2y}^*(y)e_y \frac{\partial}{\partial y}F_{1y}(y)d^3r \right] \quad (2.5)$$

As spatial variations of $A(r)$ are much slower than the envelope functions of the wavefunctions, the first integral is approximately proportional to $\langle F_{2y}|F_{1y}\rangle$, which is equal to zero since the overlap functions are orthogonal, as discussed above. If take $A(r) = A_0$ over the region of interest where the wavefunctions are significantly nonzero, then

$$H_{21}' \approx \frac{-\hbar q}{2m_0} \delta\left((k_2 - k_1) \cdot r_{//}\right) A_0 e_y \int_v F_{2y}^*(y) \frac{\partial}{\partial y}F_{1y}(y)d^3r$$

$$\approx \frac{-iqA_0e_y}{2m_0} \delta((k_2 - k_1) \cdot r_{//})\langle F_{2y}|p_y|F_{1y}\rangle \quad (2.6)$$

which is, in general, nonzero if $e_y$ is nonzero. A similar derivation is given in [46]. As the electric field in a time-harmonic source-free electromagnetic wave is co-directional with the vector potential, the matrix element can only be nonzero when there is a transverse component to the electric field (i.e., perpendicular to the layers), which corresponds to a lateral component to the magnetic field, or a TM mode. This is called the intersubband polarization selection rule [47]. Thus, conventional QCLs utilizing electrons within the conduction band are TM-polarized. This selection rule also shows why a quantum cascade vertical-cavity surface-emitting laser (QC-VCSEL) is generally not thought to be possible: a wave propagating in the $y$-direction would typically not have a strong $y$-component of the electric field, so that gain would not be provided (although, there has been one recently proposed QC-VCSEL device where a $y$-component to the electric field is generated [48]). Instead of the $H_{21}'$ parameter used above, frequently a 'dipole matrix element' $z_{ij}$ is used [40]:

$$z_{ij} = \langle F_i|z|F_j\rangle = \frac{\hbar}{2(E_j - E_i)}\langle F_i|p_z \frac{1}{m_j^*} + \frac{1}{m_i^*}p_z|F_j\rangle \quad (2.7)$$

where *i* and *j* are the two states involved in the transition. These can be shown to be proportional to each other.

Aside from prohibiting a QC-VCSEL, having a TM-polarized device can also cause interesting surface plasmon-based effects when the structure incorporates metal, which will be explored later. Or, at the very least, it can require that any metals are positioned far from the waveguide to ensure they do not cause extra absorption. Alternatively, they could be placed closer in order to confine the mode and enhance the confinement factor to the active region. The additional absorption loss of metals, however, suggests that this technique is not likely to work for high-power devices, at least in the mid-IR. Terahertz-emitting QCLs frequently use this type of metal-clad waveguide to provide strong confinement since the wavelength is quite larger than the core region thickness [49].

## 2.5    Quantum Cascade Laser Core Structure

Having established that it is possible for an incoming electromagnetic field with an electric field perpendicular to the layers to cause stimulated emission via a transition between subbands, we must consider how population inversion, where the higher energy state is more populated with electrons than the lower energy state, can be achieved. After all, if the lower-energy state has a higher population, the electromagnetic field will merely be absorbed by the lower-energy electrons as they transition to the upper state. The subbands in Fig. 2.3 form a three-level system, where the lasing transition occurs between states 3 and 2. The wavefunctions are peaked in separate wells, leading to this type of design to be called a 'diagonal-transition' design [50]. The low overlap between states 2 and 3 leads to a relatively long lifetime for state 3. Also, because the electron must tunnel through a barrier, interface roughness can lead to

broadening of the gain spectrum, raising the threshold current density [50]. The steady-state

electron sheet density of state 3 is given by [46]:

$$n_3 = \frac{\eta_i J}{q} \tau_3 \tag{2.8}$$

where $J$ is the injected current, $\eta_i$ is the injection efficiency, $q$ is the electron charge, and $\tau_3$ is the

lifetime of state 3. If we assume that state 2 is populated only by scattering of electrons from

state 3 (this is not actually the case, as will be discussed in Section 2.6 on thermal backfilling),

the electron sheet density of state 2 is given by:

$$\frac{n_2}{\tau_2} = \frac{n_3}{\tau_{32}} \quad \Rightarrow \quad n_2 = \frac{\tau_2}{\tau_{32}} n_3 \tag{2.9}$$

where $\tau_{32}$ is the mean scattering time from state 3 to state 2, and $\tau_2$ is the lifetime of state 2. Then

the population inversion is:

$$n_3 - n_2 = \frac{\eta_i J}{q} \tau_3 \left(1 - \frac{\tau_2}{\tau_{32}}\right) \tag{2.10}$$

Thus, to achieve population inversion the lifetime $\tau_{32}$ must be longer than the lifetime of level 2,

$\tau_2$. In order to achieve short state 2 lifetimes, QCLs are typically designed so that the energy

difference between states 2 and 1 is resonant with a longitudinal-optical (LO) phonon energy.

Other designs include three lower states each separated by one phonon energy, so-called 'two-

phonon resonance' or 'double phonon resonance' designs [51], to even further enhance electron

extraction from the active region. Assuming a Lorentzian lineshape, the gain cross-section is

[40]:

$$g_c = \frac{4\pi q^2 z_{32}^2}{2\gamma_{32}\varepsilon_0\lambda_0 n_{eff}L_p} \tag{2.11}$$

where $q$ is the electron charge, $z_{32}$ is the dipole matrix element between states 3 and 2, $\gamma_{32}$ is the

full-width and half-maximum (FWHM) of the transition's luminescence spectrum, $\varepsilon_0$ is the

vacuum permittivity, $\lambda_0$ is the peak emission wavelength, $n_{eff}$ is the mode's effective index, and

$L_p$ is the thickness of one period of the superlattice. Combining these, the peak material gain is then:

$$G_p = g_c(n_3 - n_2) = \frac{4\pi q z_{32}^2}{2\gamma_{32}\varepsilon_0\lambda_0 n_{eff}L_p}\eta_i J \tau_3 \left(1 - \frac{\tau_2}{\tau_{32}}\right) \tag{2.12}$$

which is proportional to the current density. The modal gain (that is, the gain experienced by an optical mode in the waveguide) is $G_m = G_p\Gamma$, where $\Gamma$ is the optical confinement factor, defined as:

$$\Gamma = \frac{\int_{core} |E_z|^2}{\int_{all} |E|^2} \tag{2.13}$$

where $E_z$ must be used in the numerator as it is the only component that will provide gain. We can see that lowering the linewidth $\gamma_{32}$ and increasing the overlap between states (dipole matrix element $z_{32}$) can improve the peak gain, and hence lower the threshold current density of the device. Additionally, the peak gain is inversely proportional to the stage thickness. Thus, thinner stages could potentially improve the device, all else being equal (there are other benefits and issues with this that will be discussed later). This is intuitive if the portion of the stage removed is within the injector, described below, which does not provide gain.

The digitally graded alloy portion of Fig. 2.3 is somewhat misleading. In reality, this region is composed of the same two materials (in a conventional design) alternating with a varying duty cycle, which averages to the conduction band edge shown above. This region is typically called the 'injector,' and is doped in order to act as an electron reservoir for state 3 [40]. The injector must also be doped to prevent space-charge formation, which can cause the bandstructure to break into separate electric field domains. In later designs, the alternating layers of the injector region were designed to form an electron Bragg reflector [50]. The reflector is designed to have a mini-gap near the energy level of state 3 in the previous active region, to prevent electron escape from this state, and to have a mini-band aligned with the lower energy

states 1 and 2, in order to facilitate electron removal from them. This aids in achieving population inversion, and hence lowers the threshold gain. The voltage drop, or 'defect,' across the injector serves to reduce the effect of electron backfilling, described below (that is, the larger the voltage defect, the lesser the backfilling).

## 2.6 Electron Thermal Backfilling

Electrons from the injector state in one stage can 'backfill' back to the lower laser state in the previous stage due to thermal energy. The conventional approximation for the population of electrons in the lower lasing state due to this effect is [52]:

$$n_{therm} \cong n_s e^{-\Delta_{inj}/kT} \tag{2.14}$$

where $\Delta_{inj}$ is the energy difference between the lower laser state and the following injector ground state, $n_s$ is the doping sheet density in the injector, and $kT$ is the thermal energy of the electrons. Note that $T$ is the electron temperature in the injector ground state, which, in general, is higher than the lattice temperature [53], [54]. A larger $\Delta_{inj}$ thus results in less backfilling. Thus, if the injector is shortened to improve the gain coefficient but the operating electric field remains the same, $\Delta_{inj}$ is lowered, resulting in more backfilling. The optimal value for $\Delta_{inj}$ is still under debate.

It has been shown that this formula overestimates the effect of backfilling, and a more accurate formula has been arrived at by considering backfilling from multiple equally-spaced states from within the injector [55]. That formula, adjusted to consider the electrons' temperature in the injector miniband, is [55], [56]:

$$n_{therm} = n_s e^{-\Delta_{inj}/2kT} \frac{\sinh\left[\frac{\Delta_{inj}}{2N_{inj}kT}\right]}{\sinh\left[\frac{(N_{inj}+1)\Delta_{inj}}{2N_{inj}kT}\right]} \tag{2.15}$$

where $n_{inj}$ is the number of states in the injector. In the rate equations, this thermal population results in a $J_{bf}$ term, which is the extra current density required to reach threshold to overcome backfilling [54], or is included in a total waveguide loss term, $\alpha_{w,tot}$ [56]. Note that this effect occurs entirely within the core, so changes to the optical confinement factor should not affect the current density required to overcome it (i.e., this is not actually an optical loss term).

## 2.7 Gain Spectrum

Fig. 2.4 shows a schematic representation of the dispersion of the three most relevant states in a QCL. The wavy arrows represent the radiative transitions, and the straight arrows represent non-radiative transitions. Since the curvatures of the subbands are nearly the same, all of the radiative transitions should produce photons of nearly the same wavelength. Thus, we should expect the gain spectrum of these lasers to be fairly small in comparison to conventional diode lasers, where the bands involved with the transition curve away from each other as a function of the wavevector $k$. However, the spectrum of Fabry-Perot QCLs typically exhibit very broad bandwidths [57].
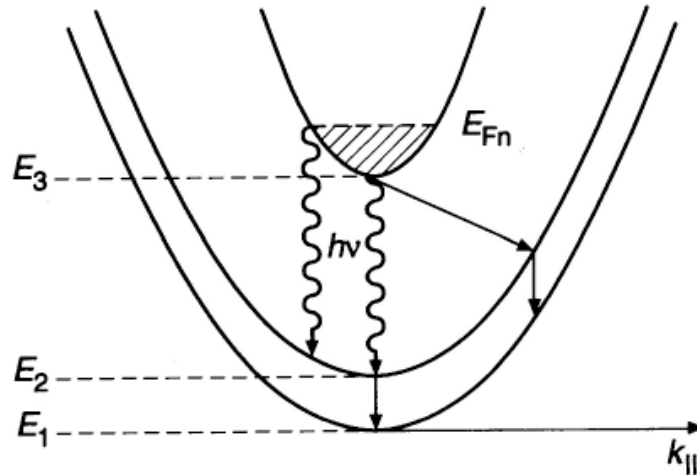


Fig. 2.4. Schematic representation of the dispersion of relevant states parallel to the layers. From [21]. Reprinted with permission from AAAS.

In reality, the subbands which form the optical transition are not perfectly parabolic, and even in the parabolic approximation they do not have the same effective mass. From the Kane $k{\cdot}p$ model, it has been shown that [58], [59]:

$$m_n^* \approx m_e^* \left(1 + \frac{2E_n(k=0)}{E_g}\right) \tag{2.16}$$

where $m_n^*$ is the effective mass and $E_n$ is the minimum energy of state $n$. This means that higher energy subbands have a higher effective mass and hence smaller curvature. More recent work has considered interface roughness within the core as the primary driver of the broad linewidth of QCLs [60].

It has been suggested that QCLs should have a linewidth enhancement factor ($\alpha = \Delta n_r/\Delta n_i$) near zero [21]. This comes from the Kramers-Kronig relationships, and a value of exactly zero would occur if the gain spectrum is perfectly symmetric [41]. Experiments have given $|\alpha|$ in the range of 0.02 to 1 [41], [61], [62], much lower than in interband devices, where $\alpha$ is in the range of 2 to 8 [61]. This not only lowers the linewidth of QCLs, but also lowers frequency chirping or modulation when a modulating drive current is applied, and results in less filamentation (see [63], [64] for discussions) in high-power operation, as variations in the real part of the refractive index are reduced. Also, since many stages are used in a QCL, each operating independently, slight changes in layer thicknesses or composition during the growth can also result in broadening of the linewidth.

## 2.8   Rollover

A 'rollover' in the output power vs. current (light-current or L-I) curves, as can be seen in Fig. 2.5, is typically observed in QCLs. As the injected current into the QCL is increased, the voltage applied must be increased, 'tilting' the band diagram even further. This results in the so-called quantum-confined Stark effect, in which energy differences and overlaps change between

the subbands. As an example to understand this, consider a band-to-band transition in a single quantum well, shown in Fig. 2.6. When the well is unbiased (no applied electric field), the lowest-order states of each band will be symmetric, and have very good overlap. When an electric field is applied, each wavefunction will shift in opposite directions. This reduces the transition energy and decreases the overlap between the two states.
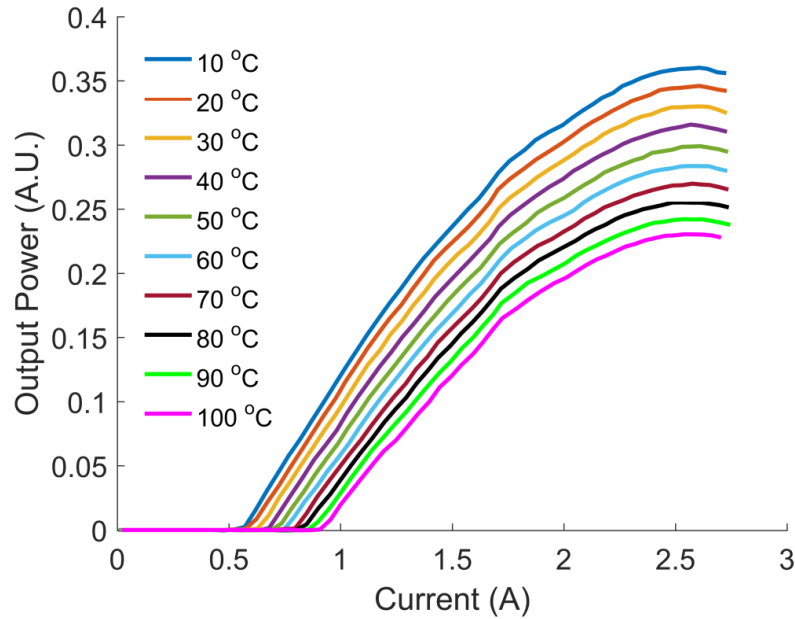


Fig. 2.5. Measured light output power vs. current (L-I) curves for a buried heterostructure QCL at different heatsink temperatures, showing typical rollover characteristics.
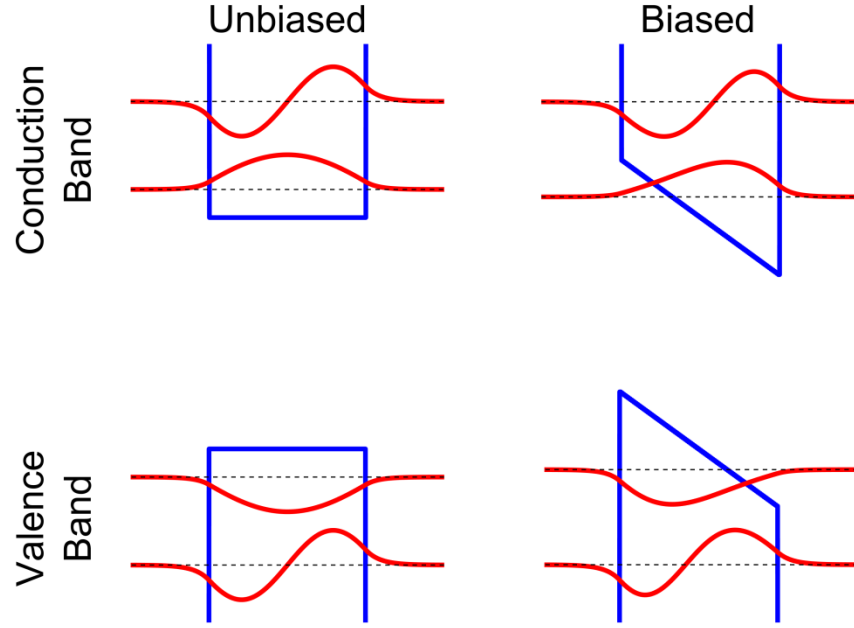
Fig. 2.6. Wavefunctions in a quantum well, without an applied electric field ('unbiased,' left) and with an applied electric field ('biased', right), showing the quantum-confined Stark Effect. The red lines are the wavefunction amplitudes and the blue lines are the conduction and valence band edges. The wavefunctions are offset according to their energy levels (thin dotted black lines).

In an intersubband transition in a QCL, the wavefunctions will shift, but the effect will not be exactly the same. While the laser is designed for some applied electric field, changes from this point will cause some misalignment in the energy levels, which can still decrease the overlap and hence matrix element, and also decrease injection from the injector into the upper laser state of the active region. These will result in a loss of gain and hence output power [65].

## 2.9    Carrier Leakage

Injected carriers in the upper laser level can be thermally excited to energy levels above it and thus lost as far as gain is concerned. This LO-phonon-assisted carrier leakage causes in turn a reduction in the injection efficiency. That is, the (total) injection efficiency, $\eta_{inj}^{tot}$, the percentage of electrons (per stage) used for the laser transition, has to be expressed as follows [56]:

$$\eta_{inj}^{tot} = \eta_{inj}^{tun}\eta_p \qquad (2.17)$$

where $\eta_{inj}^{tun}$ is the tunneling-injection efficiency into the upper laser level, and $\eta_p$ is the pumping efficiency which reflects the degree of carrier-leakage supression. That is, $\eta_p = 1 - J_{leak}/J_{th}$, where $J_{leak}$ is the leakage-current density and $J_{th}$ is the threshold current density [53]. For the simple 3-level structure in Fig. 2.3 the barriers are relatively shallow such that the upper laser level, $ul$, is the highest energy level in the active region. Then, carrier leakage from it occurs to the next injector upper miniband and unbound states above the active region; that is, to the continuum [56]. However, state-of-the-art QCLs have relatively tall barriers, such that there is at least one active-region energy state above the upper laser level. Then, leakage consists of electrons being thermally excited to states above the upper laser level followed by relaxation to the lower energy levels in the active region [56]. Thus, for state-of-the-art QCLs carrier leakage is not leakage to the continuum, but mostly a shunt-type leakage current. For an energy difference between the $ul$ state and the next higher energy state above $ul$, state $ul+1$, $E_{ul+1,ul}$, larger or equal to 50 meV $J_{leak}$ has the following dependence [56]:

$$J_{leak} \propto \frac{1}{\tau_{ul+1,ul}} exp\left(-\frac{E_{ul+1,ul}}{kT_{eul}}\right) \qquad (2.18)$$

where $1/\tau_{ul+1,ul}$ is the scattering rate from state $ul+1$ to state $ul$, and $T_{eul}$ is the electronic temperature in state $ul$. That is, in order to effectively suppress carrier leakage, the $E_{ul+1,ul}$ and $\tau_{ul+1,ul}$ values should be maximized, while the $T_{eul}$ value should be minimized.

By employing conduction-band engineering, the $E_{ul+1,ul}$ and $\tau_{ul+1,ul}$ values have been progressively increased [66] by using deep wells in the active region [67], linearly tapering the active-region barrier heights from the injection to the exit barrier [68]–[70], and stepwise tapering the active-region barrier heights [23], [66]. The last approach, called step-taper active-region (STA), is the most effective since strong asymmetry and Stark-shift reduction ensure both maximum $E_{ul+1,ul}$ and $\tau_{ul+1,ul}$ values.

From (2.12), we see that increasing the injection efficiency, by suppressing the carrier leakage, will increase the peak material gain. This also improves the internal differential efficiency of the device [56]. The variations in material composition can also be used to reduce the overall strain in the core.

## 2.10 Thermal Effects

The temperature-dependent characteristics of electrically-pumped lasers are typically summarized by two parameters: the characteristic temperature of the threshold current ($I_{th}$), $T_0$, and the characteristic temperature of the slope efficiency ($\eta_s$, the derivative of output power with respect to current just above threshold), $T_1$ [56]. The threshold current and slope efficiencies can be approximately modeled by:

$$I_{th}(\Delta T) = I_{th,0} e^{\Delta T/T_0} \tag{2.19}$$

$$\eta_s(\Delta T) = \eta_{s,0} e^{-\Delta T/T_1} \tag{2.20}$$

where $I_{th,0}$ and $\eta_{s,0}$ are the threshold current and slope efficiency at some reference temperature, and $\Delta T$ is the deviation from that temperature within the device. These parameters are typically found by measuring the L-I curves of a device in short-pulse operation (so there is little internal heating) at multiple heatsink temperatures, as shown in Fig. 2.5, and then fitting the resulting threshold current and slope efficiencies to (2.19) and (2.20). The higher these characteristic temperatures are, the less temperature-sensitive the device is. Thermal effects also play a role in the rollover, as higher temperatures enhance carrier leakage. Operating a device in low-temperature CW or pulsed mode can allow one to suppress the thermal rollover [65], though this is not practical for many applications.

The first demonstrated QCL was found to have a $T_0$ of about 110 K [71]. This was significantly higher than interband lasers operating in the mid-IR, where $T_0$ could range from 17

to 50 K [71]. Thus, the threshold current density of QCLs is far less temperature dependent. This was attributed to the following reasons [71]: 1) since the subbands of the optical transition are nearly parallel, thermal broadening of the electron distribution in the upper subband has a small effect on the gain; 2) Auger recombination is negligible in intersubband transitions; 3) The excited state lifetime has little variation with temperature. More recently, QCLs have been developed with a $T_0$ in the range of 200 K to 400 K [23], [54], [69], although some of the devices with extremely high $T_0$ values have high thresholds regardless of temperature [69], while for interband cascade lasers they have not changed much [20].

The core of a QCL has a low thermal conductivity due to its component materials' low thermal conductivity, as well as due to its superlattice structure [72], [73]. The transverse component of the thermal conductivity is ~2 W/mK and the lateral component is ~5 W/mK. The surrounding InP has a thermal conductivity of around 70 W/mK, and lattice-matched $In_{0.53}Ga_{0.47}As$ has a thermal conductivity of ~ 5 W/mK. Thus, InP is preferred as a material to surround the core to help dissipate the thermal energy generated in the core, and InGaAs confinement layers are not typically helpful for CW operation in the mid-IR if the core region is sufficiently thick to provide reasonable confinement on its own. This tradeoff is something that requires modeling, though. As the core has a low transverse conductivity, a thin core region, whether by using fewer stages or thinner stages, would be preferable to help the heat flow out of the center of it. An alternative is to use more stages with an InP spacer in the middle of them to help the heat flow laterally out of the center of the core [74].

## 2.11 Conclusions

Long-wavelength emission is obtained in quantum cascade lasers by the unique method of utilizing low-energy intersubband transitions in complex superlattice structures. Stimulated

emission can only be achieved by an electromagnetic wave with an electric field component perpendicular to the layers of the active region, rendering QCLs as TM-polarized devices. The other necessary component for achieving gain, population inversion, is achieved by ensuring the scattering time of the upper lasing state is longer than that of the lower state, which has a shortened scattering time due to LO-phonon interaction. Doped injector regions between the active region of each stage act as an electron reservoir, and are designed to act as Bragg reflectors to ensure confinement of the upper state and easy escape from the lower states, improving population inversion, and hence gain. The approximately parallel dispersion curves for the relevant states lead to a nearly delta-function density of states, but differing effective masses and nonparabolicities broaden the gain spectrum. Still, this results in a low linewidth enhancement factor, so that QCLs exhibit little frequency chirp and are expected to be relatively impervious to filamentation compared to conventional diode lasers. Thermal effects are smaller for QCLs than other semiconductor lasers in the mid-IR, but are still significant. The waveguide must be designed with this and the relative thermal conductivities of the component materials in mind.

# Chapter 3 – Optical and Thermal Modeling of Quantum Cascade Lasers

## 3.1    Introduction

This chapter introduces some of the modeling which will be used in later chapters, along with projections found for simple buried heterostructures (BHs). This modeling is focused on optical modeling of the quantum cascade laser's (QCL's) optical cavity, thermal modeling of the QCL and its packaging, and a device-level semi-empirical model of a QCL.

## 3.2    Optical Modeling

Optical modeling is required for complicated optical cavity designs of QCLs, such as phase-locked arrays or grating-coupled surface-emitters. For such modeling, the details of the physics within the superlattice core region of the QCL are not necessary. The superlattice can be considered to be a single bulk layer with certain properties: an averaged refractive index, as the layers of the superlattice are much smaller than a wavelength; the core produces gain for light with an electric field polarized in the transverse direction (perpendicular to the layers) when an electric field is applied and current passes through it; and the core has optical absorption loss due to intersubband absorption or free-carrier absorption. For transverse magnetic (TM) polarization, the averaged refractive index is found by the following:

$$n_{avg,TM}^2 = \frac{1}{\Sigma_i f_i / n_i^2} \tag{3.1}$$

where $f_i$ is the filling ratio, or normalized thickness, of each layer $i$, and $n_i$ is the refractive index of layer $i$. The gain produced by the core is linearized over a range of current density near typical thresholds, with some constant of proportionality $g$, known as the differential gain coefficient, which has units of cm/kA.

In this work, COMSOL Multiphysics, a Finite Element Method (FEM) commercial software package, was used for the optical simulations. It can be used to solve for the optical modes supported by a given structure. The 3-dimensional structure of a device can frequently be simplified to a 2-dimensional model, as shown in Fig. 3.1. For a longitudinally uniform device, a cross-section of the waveguide in the xy-plane can be used. If longitudinal variations exist, for example from a diffraction grating, the lateral geometry can frequently be ignored or modeled separately (see, for example, [35]), in which case the cross-section in the yz-plane can be used. This more complicated modeling will be covered in Chapter 7.
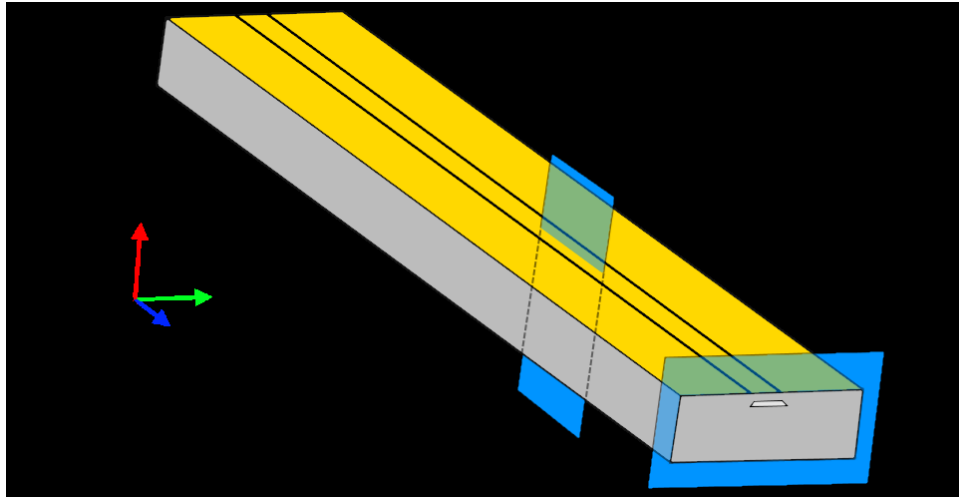


Fig. 3.1. A schematic of a general QCL chip showing the cross-sections used for optical modeling.

For longitudinally uniform devices, the waveguide cross-section is modeled in COMSOL to find the complex effective indices ($n_{eff}$) and electric field profiles for the modes of the structure by solving the 2-D vector wave equation

$$\nabla^2 \boldsymbol{E} + k^2 n^2 \boldsymbol{E} = 0 \qquad (3.2)$$

for all components of the electric field $\boldsymbol{E}$, with an assumed z-dependence of $e^{-ikn_{eff}z}$. $k = 2\pi/\lambda$ is the wavevector in free space, where $\lambda$ is wavelength in free space. The waveguide is assumed to be passive with no gain in the core, so that losses are found for all modes, and then the gain is

treated as a perturbation which does not affect the field profile in post-processing. In this work, material refractive indices were calculated by the Drude model for semiconductors, and taken from [75]–[77] for the metals, Au, Ag, Ti, and Pt. Perfectly matched layers (PMLs) were used at the outer boundaries of the models if necessary (e.g. for structures with leaky modes) to prevent reflections back towards the waveguide. The modal loss, including absorption and edge radiation losses, for a given mode $L$ is found by

$$\alpha_{Comsol,L} = \frac{4\pi}{\lambda} \text{Im}(n_{eff,L}) \qquad (3.3)$$

for the simulated wavelength $\lambda$. The TM optical confinement factor is found by

$$\Gamma_{TM,L} = \int_{core} |E_{y,L}|^2 / \int_{all} |\boldsymbol{E}|^2 \qquad (3.4)$$

when the structure has a nearly-constant current density throughout the core (e.g., similar widths for the core from top to bottom). $E_{y,L}$ is the component of the electric field which is normal to the layer surfaces (transverse direction) for mode $L$. The mirror loss

$$\alpha_m = \frac{1}{2L_c} \ln\left(\frac{1}{R_1 R_2}\right) \qquad (3.5)$$

is calculated assuming a cavity length $L_c$ and facet reflectivities $R_1$ and $R_2$, which depend on any applied coatings. The threshold current density ($J_{th,L}$) for each mode $L$ is then calculated using:

$$J_{th,L} = \frac{\alpha_{Comsol} + \alpha_m}{\Gamma_{TM} g} + J_{bf} \qquad (3.6)$$

where $g$ is the differential gain coefficient taking into account carrier leakage [56], and $J_{bf}$ is the current density due to backfilling divided by $\eta_p$ and assuming unity tunneling-injection efficiency [56]. TE-like modes, which have a small $E_y$ component, have a $\Gamma_{TM}$ of nearly 0%. Then, their calculated $J_{th}$ is large and thus these modes will never reach threshold and can be ignored. Sometimes $J_{bf}$ is included in a total waveguide loss coefficient, $\alpha_{w,tot}$ [56]. Then the equation for the threshold current density is:

$$J_{th} = \frac{\alpha_{Comsol} + \alpha_m + \alpha_{w.tot}}{\Gamma_{TM} g}. \qquad (3.7)$$

$\alpha_{w,tot}$ typically also includes intersubband-absorption loss and an internal cavity loss due to free-carrier absorption, $\alpha_i$, but since the material indices used in the COMSOL already include such losses, $\alpha_i$ is removed. It should be noted that some of the terms comprising $\alpha_{w,tot}$ are local to the core region. Since the numerator of this expression requires modal losses, $\Gamma_{TM}$ is effectively being used to convert these components into a modal loss. Thus, using a single constant for $\alpha_{w,tot}$ is not strictly accurate as $\Gamma_{TM}$ can change for different modes or waveguide structures, though it is a reasonable approximation over a limited range of $\Gamma_{TM}$.

### 3.2.1  Facet Reflectivity Modeling

COMSOL was also used for calculating the facet reflectivity of devices with coated or uncoated facets, in order to design the coating (if necessary) to achieve the desired reflectivity. To accomplish this, a 3-D model of the region around the facet is created (including the chip, coating, and air), with PML boundary conditions surrounding the model. A schematic cross-section of such a model is shown in Fig. 3.2. A boundary mode analysis is run along the cross-section of the chip at the edge of the model (at the 'Input Port'), and then the resulting TM mode(s) are input into the waveguide.

The resulting reflectivity, $R$, is found by finding the overlap of the reflected wave with the mode which was input. That is:

$$R = \left| \frac{\int E_{In} E_{Out}^*}{\int |E_{In}|^2} \right|^2 \tag{3.8}$$

where $E_{In}$ is the electric field of the input mode, $E_{Out}$ is the resulting electric field at the boundary minus $E_{In}$, and the integral is performed at the input port. COMSOL accomplishes this calculation using a built-in 'S-parameter.' The transmittance, $T$, is found by integrating the Poynting vector over the outer boundaries of air (inside the PMLs), and normalizing this power to the total input power. If there is no internal scattering, we would expect $R + T = 1$. However,

it is found for a range of waveguide geometries and coatings that typically R + T ~ 0.97. That is, typically 3% of the incident power to the facet is lost to scattering.
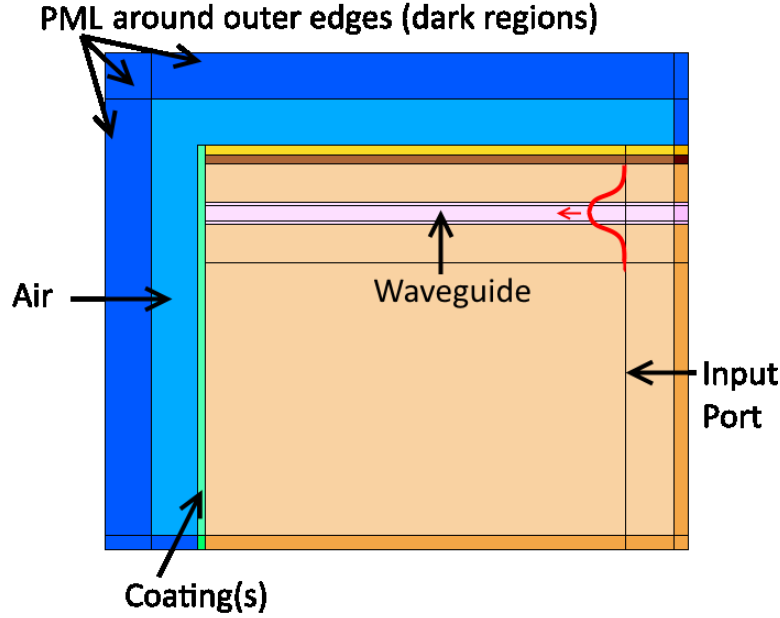


Fig. 3.2. Schematic cross-section of a COMSOL model, set up to find the reflectance and transmittance of a given QCL structure.

When calculating the output power from a device, the fraction of power delivered from the front facet relative to the total power coupled out of the cavity, $F_1$, is needed, and is calculated as follows ((3.31) in [39]):

$$F_1 = \frac{\frac{1}{\sqrt{R_1}} T_{front}}{\frac{1}{\sqrt{R_1}}(1-R_1)+\frac{1}{\sqrt{R_2}}(1-R_2)} \tag{3.9}$$

where $T_{front}$ is the transmittance through the front facet of the device. Using this method for calculating facet reflectivity, the reflectivity of a fundamental mode off of a highly reflective (HR) coating using a stack of 300 nm $Al_2O_3$ / 10 nm Ti / Au has a reflectivity of ~ 94%, and off of an uncoated facet has a reflectivity of 24% (though this varies somewhat: higher-order lateral modes [78] or narrower devices have higher reflectivities, which results in broad-area devices lasing in high order modes [64]). This uncoated facet reflectivity is slightly lower than the

typically assumed 27% calculated from a simple effective index approximation using a plane wave normally incident on the facet. This is due to the non-normal transverse components of the TM mode having lower reflectivity than the normally-incident component. Assuming 3% is scattered, this results in a front facet extraction efficiency of 92.4% for a device with an HR-coated back facet and uncoated front facet. This can be raised slightly using lower reflectivity coatings on the front facet (of course, the total mirror loss should be optimized as well). For example, with a 10% reflectivity coating on the front facet, $F_1 = 94.6\%$. The HR-coating reflectivity can be improved with thinner $Al_2O_3$ or Ti layers, to reduce scattering and absorption. Other materials could potentially be used as well to improve the coating. If this extraction efficiency is not considered, this inefficiency could be misattributed to the core region's internal differential efficiency being lower than it actually is.

## 3.3    Thermal Modeling

Thermal modeling was conducted using COMSOL as well. Typically continuous-wave (CW) operation is assumed, so that the steady-state heat-transfer equation is

$$Q = -\nabla \cdot (k\nabla T) \tag{3.10}$$

where $k$ is the material's thermal conductivity, $T$ is the temperature, and $Q$ is the input thermal power density. Table 3.1 lists the material thermal conductivities used in the COMSOL models.

TABLE 3.1. TEMPERATURE DEPENDENT THERMAL CONDUCTIVITY
VALUES USED IN THE SIMULATIONS. FROM [28]. © 2015 IEEE

| Material | Thermal Conductivity (W/m·K) |
|---|---|
| InP [73] | $2.82 \times 10^5 T^{-1.45}$ |
| Gold [73] | $337 - 660 \times 10^{-4} T$ |
| InGaAs/InAlAs Core [73] | $k_{//} = 5.3 - 3.9 \times 10^{-3} T + 5.3 \times 10^{-7} T^2$ |
| | $k_{\perp} = 2.3$ |
| Ti [73] | $31.46 - 4.338 \times 10^{-2} T + 4 \times 10^{-5} T^2$ |
| InGaAs [73] | $23 - 9.3 \times 10^{-2} T + 1.06 \times 10^{-8} T^2$ |
| Cu [73] | $349 + 14710/T$ |
| Diamond [79] | 1800 |
| In Solder [73] | $93.9 - 6.96 \times 10^{-2} T + 9.86 \times 10^{-5} T^2$ |

Some of the materials' thermal conductivities include a temperature dependence, with $T$ in units of Kelvin in these equations. The core is taken to have an anisotropic conductivity to account for the superlattice, whereas all other materials have isotropic thermal conductivities. While interface thermal resistances may exist, there is currently no good data on them and thus are not included, aside from at the gold/indium bond line as discussed later. The solder and heatsink for the chip (submount) is considered in the model. The temperature is fixed at 20°C at the bottom of the heatsink, with all other external boundaries set adiabatic. These two optical and thermal models can be coupled together in order to analyze the effects of thermally-induced index elevation across the device on the modal properties. Typically, we have found that this modeling underestimates the thermal resistance of the device, possibly due to interface thermal resistances at semiconductor/dielectric interfaces or the solder bond line (due to voids at the interface, potentially), or due to additional resistance from the testing stage.

This thermally modeling can be used for quasi-CW operation as well. For infinitely short pulse widths, $Q$ can simply be reduced proportionally by the quasi-CW duty cycle. For realistically long pulses, however, the core is warmer on average during the pulse than when there is no current flow, so a transient analysis is used to calculate the temperature rise throughout a pulse. For a 1 µs-long pulse, the average temperature rise during the pulse at duty

cycles near 0% (essentially a single-shot pulse) is still ~31% as high as the temperature rise in CW operation at the same current. Fig. 3.3 shows the simulated average core temperature for a 1 μs-long pulse with a 25% duty cycle, relative to the temperature rise under CW operation at the same current. The time-averaged temperature rise during the pulse is 43.5% as high as in CW operation, despite the 25% duty cycle. For a 100 μs-long pulse, such as that provided by a Thorlabs ITC4005QCL current controller, the temperature rise for pulse duty cycles near 0% is ~77% as high as during CW operation, according to the COMSOL model. Meanwhile, the output power will still be reduced almost proportionally to the duty cycle, aside from the slightly lower temperature. Thus, while quasi-CW operation has been used [80] to improve the average output power of a device compared to CW operation, it is not universally better if the temperature is not actually reduced proportionally because of the pulse conditions.
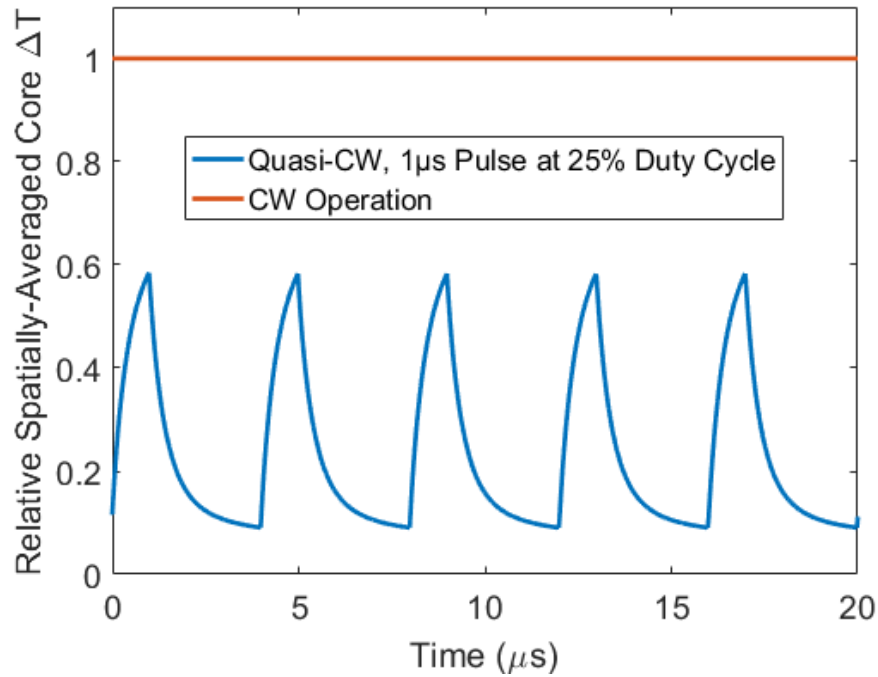


Fig. 3.3. Simulated average core temperature rise in quasi-CW operation and CW operation, showing that the core heats quickly during a pulse.

This thermal modeling is typically performed on a 2-D xy-cross-section of a device if there is no longitudinal variation that needs to be specifically considered. Comparisons were made between 2-D and 3-D models of the same device, and a small effect from heat being able to spread out in the heatsink behind the chip was found, which slightly lowers the temperature of the back of the chip (for a < 5% change in average core temperature rise, which decreases with increasing length). If further longitudinal variations exist, such as a pullback, in which a section of the core near the facet is unpumped to reduce the temperature at the facet (which has been found to be source of degradation for QCLs [81]), the 3-D model would be required.

## 3.4    Device Optimization Model

A high-level semi-empirical model of a QCL was developed to predict the CW performance of devices in order to optimize various device parameters (eg. AR coating reflectivity, length, width, etc.) for high CW power and wallplug efficiency for a given core region design, similar to that in [82]. The model is populated with parameters extracted from experimental results of devices with a particular core region design, for example by mirror loss studies. A 2-dimensional COMSOL Multiphysics model of a BH (in the xy-plane), shown in Fig. 3.4, is used to calculate the optical confinement factor, $\Gamma$, and average core region temperature rise as a function of the device's geometry and dissipated power. Operation in the fundamental $TM_{00}$ mode is assumed in this model. Once fitted to experimental data, the complete model can be used to predict device performance for other geometries and can also be used for optimizing devices for high pulsed power and wallplug efficiency, or low power consumption, etc., if desired. Results presented here are based on core region properties extracted from experimental results from ~5.1$\mu$m-emitting step-tapered active (STA) QCLs [23].
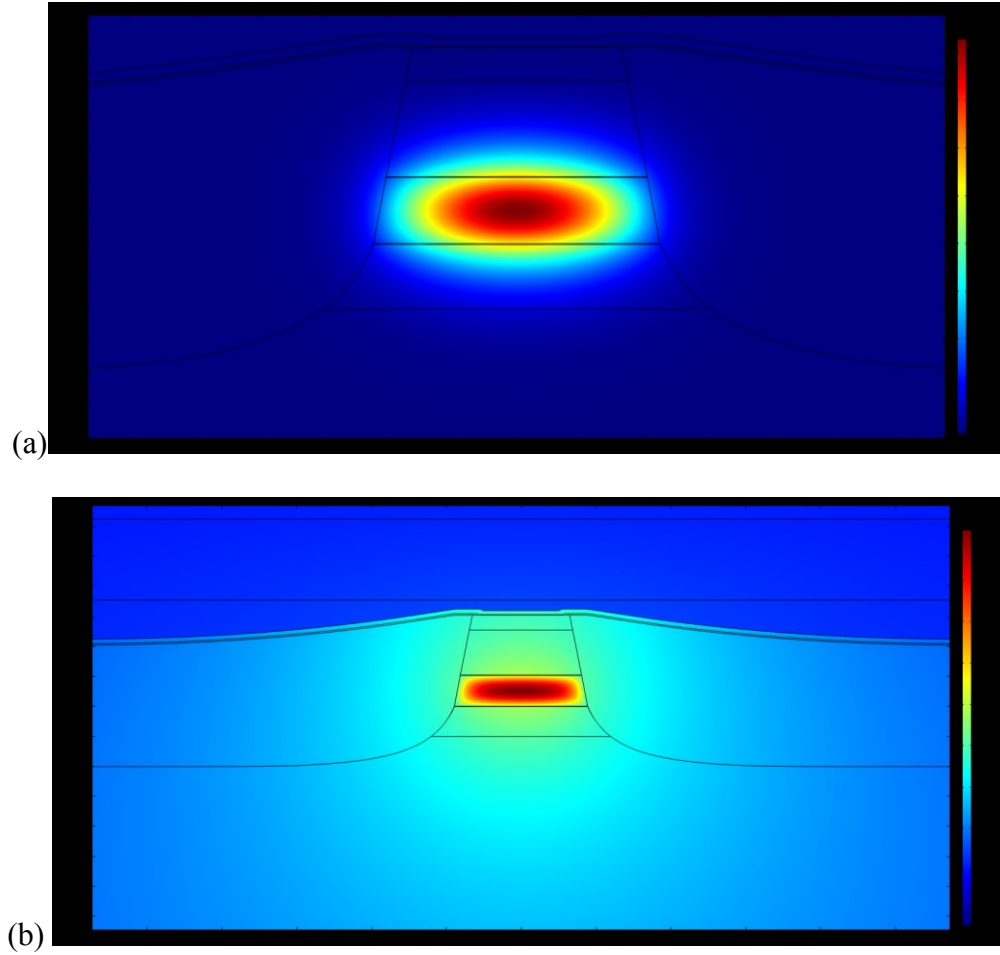
Fig. 3.4. COMSOL Model results of an 8.5 μm-wide, 3 mm-long BH, showing the (a) electric field amplitude profile of the fundamental $TM_{00}$ mode, and (b) the temperature profile with a dissipated power of 20 W.

The following equation slope efficiency is used in the model:

$$\eta_s = F_1 \frac{\hbar\omega}{q} \eta_i^d \frac{\alpha_m}{\alpha_m+\alpha_i} N_P \tag{3.11}$$

where $\alpha_m$ is the mirror loss, $\alpha_i$ is the internal loss, $F_1$ is the fraction of mirror loss that is power emitted from front facet, $\hbar\omega/q$ is the photon energy, $\eta_i^d$ is the internal differential efficiency, and $N_p$ is the number of stages in the core. The threshold current density is calculated according to (3.6). A length study (or equivalently, a facet reflectivity study) allows one to determine values for the internal loss, backfilling current density, differential gain coefficient, and internal differential efficiency.

To model the rollover of the device, the experimentally measured pulsed light-current (L-I) curve was fit to the following functional form:

$$P_{out}(J) = \eta_s A(J - J_{th}) \frac{[1 - (J/J_0)^\zeta]}{[1 - (J_{th}/J_0)^\zeta]} \tag{3.12}$$

where $J_{th}$, $\eta_s$, $J_0$, and $\zeta$ are used as fitting parameters and $A$ is the device area. $J_{th}$ and $\eta_s$ correspond to the threshold current density and slope efficiency. The last term in brackets produces the rollover in the L-I curve, and the parameter $J_0$, which is the current density the output power would drop to zero if the L-I curved continued to roll over, keeps the rollover current density constant. There is no physical basis for the last term, but it is a simple expression that can be fit to experimental data to reproduce a range of shapes for the rollover of the L-I curve. Other core region designs may produce L-I curves that are not necessarily fit well by this functional form, and may require this be changed. The denominator in the last term ensures that the rollover term does not affect the slope efficiency at threshold (i.e., when $J = J_{th}$, the last term produces unity). The measured current-voltage (I-V) curve of this device was similarly fit to an expression and is used in the model.

With a varying core region temperature, the output power, $P_{out}$, is calculated by the equation for power given above, with $\alpha_i$, $J_{bf}$, $g$, and $\eta_i^d$ having temperature dependencies that allow the measured $T_0$ and $T_1$ values to be reproduced if a heatsink temperature sweep is run on the model. From 8 μm-emitting devices, it was estimated that approximately half of the drop in slope efficiency with temperature rise is due to a rise in internal loss, and the other half to a decrease in internal differential efficiency [56]. Thus, the temperature dependence of the slope efficiency was split roughly in half between these two parameters. The temperature dependence of threshold was similarly split between the gain coefficient and backfilling current density, with most of the dependence on backfilling. Unlike the model in [82], the setup here allows the $T_0$ and

$T_1$ values to change with the device's design. For example, a device with lower mirror loss is expected to have stronger temperature dependencies due to the temperature-dependent internal loss dominating over a smaller temperature-independent mirror loss. A mirror loss study at various temperatures could allow the temperature dependencies of the individual parameters to be determined, though there has typically been such significant scatter in the data for these devices that this would require a prohibitively large sample size to perform this accurately.

To model the CW performance of a device, the confinement factor and core region temperature rise, $\Delta T$, are simulated in COMSOL Multiphysics as a function of the dissipated power in the core for a given structure. At a given current, the dissipated power is given by

$$P_{diss} = IV_{core} - P_{out} \tag{3.13}$$

where $V_{core}$ is the voltage only across the core. The remaining voltage drop, which occurs across the cladding, contacts, and substrate, has a much smaller effect on the core temperature and is ignored. Then, as the output power is a function of itself due to the dependence of $\Delta T$ on dissipated power, these equations must be solved simultaneously.

When the device structure is changed in the model, $J_{bf}$, $g$, and $\eta_i^d$ are held constant, as they are properties of the core region, while others are allowed to vary (e.g., $\alpha_m$, $F_1$, $N_p$, $\Gamma$, etc.). The internal loss is constructed to be a weighted average of the local loss within the core and within the claddings (weighted by $\Gamma$), so it varies with the device structure. This is a reasonable approximation if all of the loss outside the core is due to a consistent material (i.e., low-doped InP around the core), and no significant portion is due to absorption to higher doped layers or metals, which means the cladding may need to be thicker for designs with worse confinement. A voltage drop across the contacts, cladding, and substrate is included and subtracted out before scaling the active region voltage $V_{act}$ with the number of stages. This voltage drop was measured by fabricating circular mesa devices of a waveguide with no core region and measuring the I-V

characteristics. Variation of the injector doping is included in the model: $J_0$ (which is directly related to the rollover current density), the local loss within the core, and the backfilling current density are proportional to the injector doping, and the differential resistance of the core is inversely proportional to the injector doping (the voltage drop across the rest of the device is unchanged). Since an absolute value for the injector doping of the measured devices are not known, this scaling is merely based on a relative change in doping. This model can also be used to estimate the effects of different packaging configurations, by modifying the COMSOL model being used. For example, the performance improvement from mounting on a diamond submount instead of directly on Cu can be predicted.

Quasi-CW operation can be modeled by scaling the dissipated power and output power by the pulse duty cycle. If the pulses are short enough, these are directly proportional to the duty cycle (in addition to the normal effect of temperature on the output power). Otherwise, the transient analysis discussed in Section 3.3 can be used to determine the relationship between average temperature rise and duty cycle for a given pulse length, which can be used in the model.

The thermal resistance of a device can be extracted from this model by fitting CW L-I measurements to the model using an additional thermal resistance term. As mentioned in Section 3.3, we have found that the COMSOL thermal modeling underestimates the thermal resistance of the device. To account for this, two additional thermal resistances are included: one to account for the resistance of the stage and water cooling system, and one at the solder bond line within the COMSOL model (which might be due to voids at the interface, in theory). The thermal resistance of the stage/cooling system was determined to be ~ 0.35 K/W, based on measurements from a temperature probe on the submount next to the chip compared to the expected temperature rise at that location from the COMSOL model. The bond line thermal resistance is a

tunable parameter in the model, so it was varied until the CW model results replicate the measured results. Then, this value is used in further calculations from the model (e.g., for different device geometries). The two additional thermal resistances were necessary because of the differing scaling properties of the two sources: the stage/cooling system is a flat thermal resistance in units of K/W that does not change with the device's geometry, while any bond line resistance would be inversely proportional to device length and also decrease somewhat as the device is widened. We have found from testing chips packaged by an external service that the additional thermal resistance was not needed to fit the experimental data to the model, suggesting that it is indeed our packaging that is causing the problem.

Fig. 3.5 shows an example of fitting the model to pulsed and CW experimental data. The particular device that the model is compared against here is a buried heterostructure which is 8.5 µm wide, 5 mm long, has a 40-stage core, an HR-coated back facet, and a front facet coating with a nominally 14% reflectivity (with 400 nm of $Y_2O_3$). Its threshold current in pulsed operation was 550 mA, which corresponds to a threshold current density, $J_{th}$, of 1.3 kA/cm$^2$. The slope efficiency, $\eta_s$, at threshold was about 3.7 W/A. The characteristic temperatures were determined to be $T_0 = 183$ K and $T_1 = 383$ K. The peak pulsed power was 4.7 W at a current of 2.4 A and the maximum wallplug efficiency was about 12.6% at an output power of 3.1 W. In CW operation, it reached an output power of 2.47 W at a current of 1.78A and voltage of 17.5 V, for a wallplug efficiency of 7.9%. Its maximum CW wallplug efficiency was 10.1% at an output power of 1.8 W. It was mounted epi-side down on a Cu submount using In solder. This CW measurement was performed below room temperature, with a submount temperature of -11 °C at rollover, while the pulsed measurement was performed at 20 °C, resulting in the apparent lower threshold in CW operation in the figure (this change in heatsink temperature is included in the

model as well). The extracted thermal resistance of the device is 4.5 K/W, compared to a value

of 3.7 K/W from the COMSOL model if there is no additional thermal resistance included at the

bond line, in which case the simulated maximum CW power is 2.95 W. The additional thermal

resistance may actually occur somewhere else, but this suggests that the packaging of these

devices could potentially be improved. If a 250 µm-thick diamond submount is included in the

model between the chip and copper submount, the thermal resistance is found to be 4.2 K/W, and

the maximum CW power is 2.65 W. Thus, it appears that if the cause for additional thermal

resistance is indeed voids in the solder, this effect is much larger than could be overcome by

using a diamond submount. The confinement factor to the core $\Gamma$ was calculated to be 73.1%,

and $F_1$ was calculated to be 0.94 for this device (the remaining power is absorbed or scattered at

the HR coating or scattered internally at the front facet).
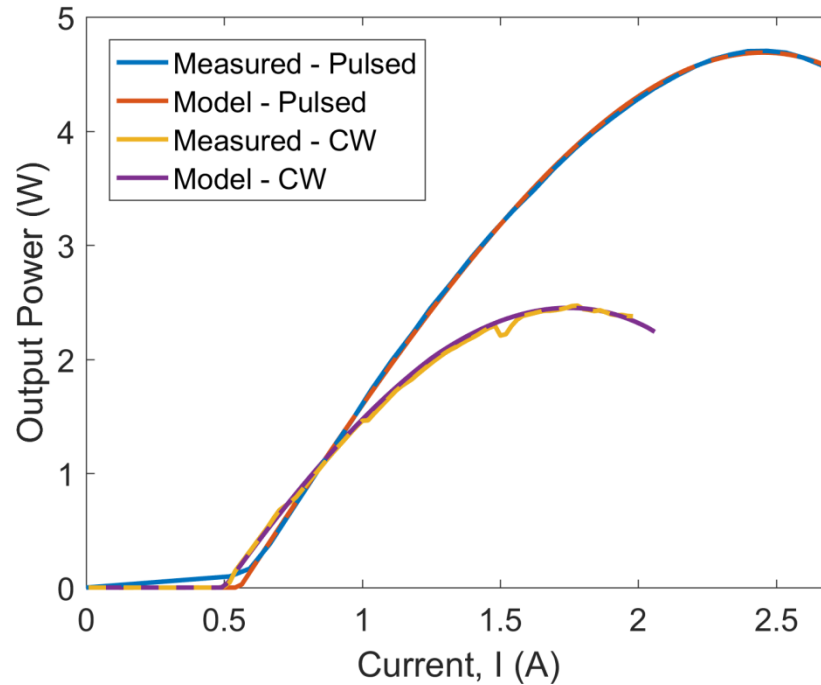


Fig. 3.5. Measured and modeled pulsed and CW L-I results for an 8.5 µm-wide, 40-stage, 5 mm-long, 5.1 µm-emitting BH QCL with a 14% front facet reflectivity.

While the slope efficiency, and hence output power in pulsed operation, is expected to increase with the number of stages in the core, the temperature rise and voltage also increase, so that the maximum CW power may not necessarily improve with increasing number of stages. Similarly, widening the device should increase the output power in pulsed operation but increase the temperature of the core in CW operation. This model allows us to see what effects these tradeoffs have on the device performance. Fig. 3.6 shows the resulting maximum CW power from a 3-dimensional sweep of $N_p$, width, and current density. This assumes the same length, facet coating, and injector doping as the device from Fig. 3.5, which is likely not optimal for all geometries. It also assumes the same packaging as the above device. This simulation suggests that the optimal device in this configuration, which emits up to $\sim$ 3.1 W in CW operation, is 22 μm wide and has 20 stages. This design would significantly reduce the growth time required for the core. Varying the assumed internal parameters of the core (e.g., $J_{bf}$, temperature dependence of backfilling, etc.) while still maintaining the fit to the original device does not significantly impact the projected performance of the optimal device or what design is optimal, so this model is fairly insensitive to errors in the assumed or extracted parameters. Such wide BHs will not operate spatially coherently, so if that is desired a more complicated structure, such as an antiguided array, is require to maintain spatial coherence, as will be discussed later.
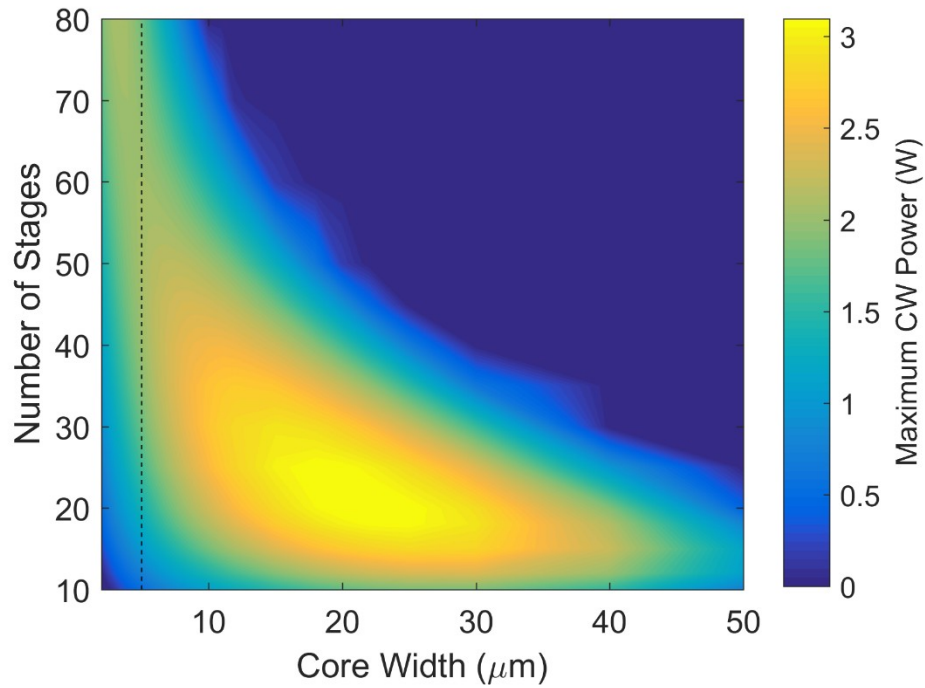
Fig. 3.6. Maximum CW power from a 3-D parameter sweep of current density, width, and number of stages for an epi-side down BH on Cu using In solder. The dotted black line at a width of 5 μm represents the approximate maximum width to ensure single-lateral-mode operation.

If the front facet reflectivity is allowed to vary as well, the optimal device is 25 μm wide, has 20 stages in the core, has a front facet reflectivity of 20%, and emits up to ~ 3.2 W, not significantly higher than fixing the reflectivity. According to the facet reflectivity model, this reflectivity could be obtained with a 240 nm-thick $Y_2O_3$ coating. The calculated thermal resistance of this device is lower than the original device, at 2.9 K/W, due to it being wider and having a thinner core. A comparison of the simulated CW L-I curves is shown in Fig. 3.7 for the original device which the model was fitted to, and for the optimized device. The threshold current of the optimized device is ~ 4× higher at 2.0 A compared to 0.5 A for the original device, and the operating voltage at maximum power is 48% lower, at 9.2 V compared to 17.65 V. Thus, while the larger volume enables it to reach higher power, its maximum CW wallplug efficiency is lower, at 7.9%, compared to 10.3% for the original device. This model could be used to

optimize for high CW wallplug efficiency instead, if desired (or even some combination of high power and high wallplug efficiency).
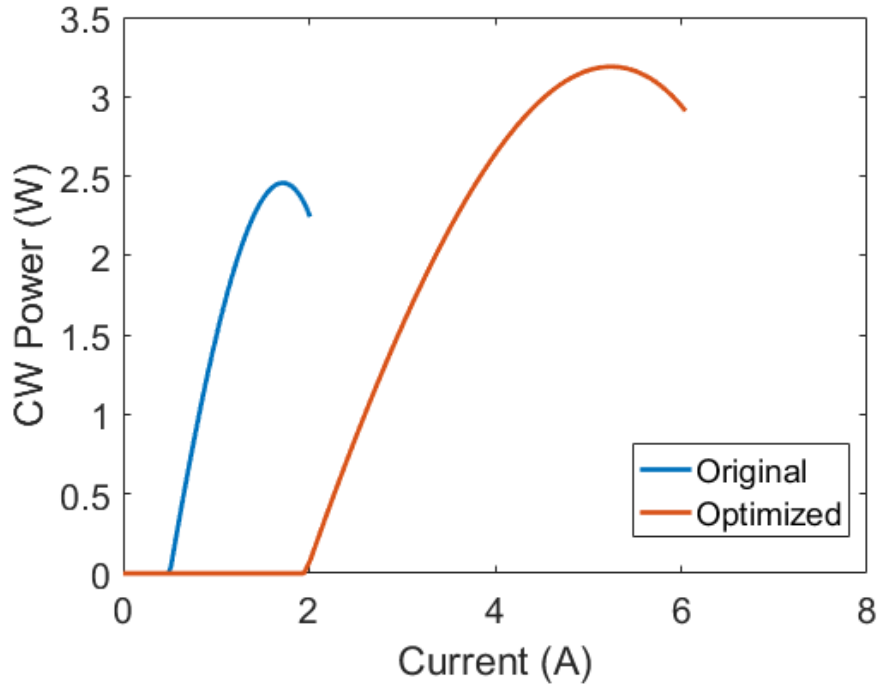


Fig. 3.7. Simulated L-I curves for two BHs. The blue curve is the device shown in Fig. 3.5, and the orange curve is the optimized, 25 μm-wide, 20-stage, BH with a 20% front facet reflectivity.

Similar optimizations can be performed with other parameters, such as injector doping, length, InGaAs confinement layer thickness, and core spacer thickness (if one is included). While InGaAs confinement layers can improve $\Gamma$ in some circumstances, it is a thermal barrier, and for 40-stage geometries the model suggests that they should not be used. Structures with fewer stages, which produce less dissipated power, may have need for such a layers to improve the confinement factor without too significant heating from their presence, as found in [82]. The model in its current form always favors longer devices, so long as an appropriately low facet reflectivity is obtainable on the front facet (to maintain a high mirror loss for high slope efficiency). In reality, highly asymmetric mirror reflectivities produce longitudinally non-uniform field profiles, which degrades performance due to gain saturation [80]. For low-loss

devices like BHs, it was found by Maulini et al. that this non-uniform gain saturation is only a significant effect for very long cavities (e.g., over 6 mm). Thus, this model that does not include this effect should be accurate for the devices modeled here. This effect could be incorporated into the model using the method in [83]. Fig. 3.8 shows an example of this, where a 6 mm-long cavity with an HR-coated back facet ($R = 94\%$), and an AR-coated front facet ($R = 5\%$) with an internal loss of 1.5 cm$^{-1}$ and small-signal gain of 15 cm$^{-1}$ is modeled (a) with and (b) without considering non-uniform gain saturation. There is a clear distortion in the intensity profile when this effect is considered, and a 3.4% drop in output power when the non-uniform gain saturation is included. The parameters in this example were chosen to exaggerate the effect; in reality, if parameters from the BH measured above are used the difference is ~1%.
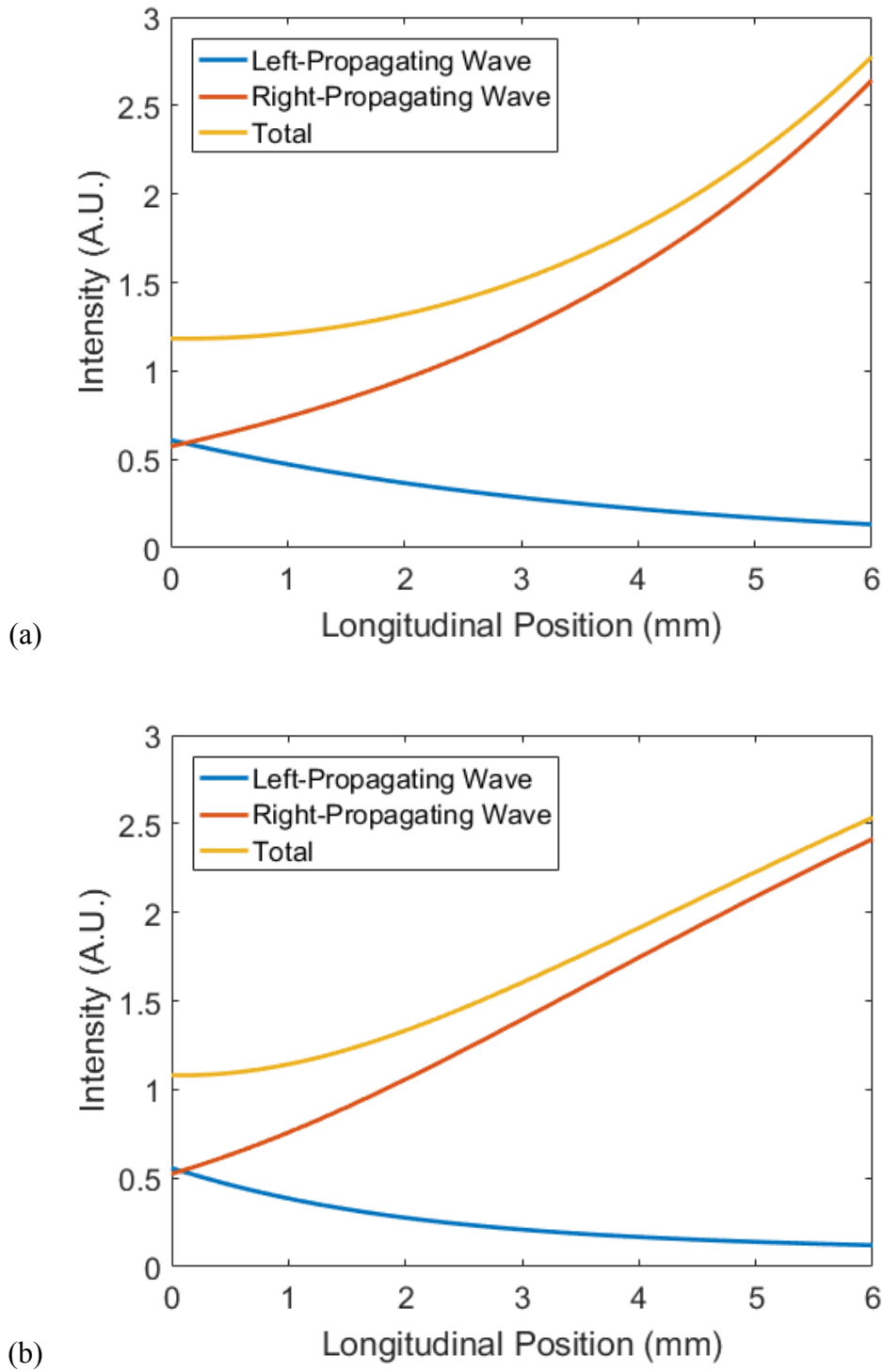
Fig. 3.8. Simulated longitudinal intensity profiles for a 6mm-long HR/AR-coated device (94%/5%) with a small-signal gain of 15 cm$^{-1}$ and internal loss of 1.5 cm$^{-1}$, (a) without considering non-uniform gain saturation and (b) considering non-uniform gain saturation.

Future work on this model also includes adding the effects of doping in the cladding, in order to optimize the tradeoff between internal loss and cladding voltage drop. A method such as that in [84] could be potentially be used for optimizing the cladding doping. However, the assumption that the only effect of doping on the refractive index of the cladding layers is that the extinction coefficient scales linearly with doping is not accurate for InP in the mid- or long-wave IR. At high doping levels, the real part of the index drops significantly due to the shifting plasma frequency of the material [85]. An iterative method which corrects the index profile as the doping profile changes could be used. However, this is problematic as it does not necessarily converge to the optimal solution. Because of the TM polarization, a surface plasmon-like behavior at the semiconductor/metal interface can occur, producing high field intensity near the metal. This optimization method would determine that a low doping is required in that region due to the high optical field intensity, when in reality high doping is required to screen out the mode before it penetrates to the metal. Thus, some changes to this optimization method would be necessary.

As mentioned previously, accurate length studies with varying heatsink temperature would allow the temperature dependence of the core region properties to be extracted. Changes to the core region design can also be modeled if the relevant parameters can be estimated. If the voltage defect, $\Delta_{inj}$, changes for the design, the backfilling current density could be altered according to (2.15) [55]. This is complicated by the fact that $\Delta_{inj}$ changes throughout the operating range of the device. A thinner stage, which would improve the thermal resistance of the device, improves the differential gain coefficient, which is inversely proportional to the stage thickness [86]. Changes to the lifetimes of the various states could be incorporated into the

various parameters (such as the internal differential efficiency) if they can be accurately modeled.

## 3.5    Conclusions

Several models were introduced in this chapter for optical and thermal modeling of QCLs. These models will be used in later chapters for designing spatially-coherent and high-power devices. From studying single-element BHs, a semi-empirical model predicts that wider devices with thinner core regions are projected to emit to higher CW powers. Such devices are not spatially coherent, so further modifications to the waveguide are necessary to obtain single-spatial-mode operation to high continuous wave powers.

# Chapter 4 – Coherent Power Scaling of Quantum Cascade Lasers

## 4.1    Introduction

Scaling the single-spatial-mode output power of quantum cascade lasers (QCLs) into the multi-watt average power range or beyond remains an important challenge. Many applications, such as remote sensing of pollutants and explosives, require multi-watt output powers in the mid-infrared (mid-IR) spectral region with high beam quality. One of the limiting factors for the maximum power of QCLs is the volume of the core region. QCLs exhibit a maximum operating current density ($J_{max}$) beyond which the output power drops, which is the 'rollover' in the light-current (L-I) characteristics. This is dependent on the injector doping level, but is typically in the range of 4-5 × the threshold current density, $J_{th}$. For a typical single element device, such as a buried heterostructure (BH), increasing the volume of the active region in any dimension, whether the number of stages, width, or length (with appropriate facet coatings to account for the changing mirror loss), will generally increase the maximum pulsed output power of the device by either increasing the slope efficiency or rollover current.

While high-power devices are typically relatively long, devices with long cavities can experience a significant reduction in efficiency [80]. This occurs due to non-uniform gain saturation, and is exacerbated with higher internal loss and a larger difference in reflectivity between the two facets. Thus, this effect is worse for devices emitting in the long-wave regime (i.e., 8-10 μm) than the mid-wave regime (i.e., 4-5 μm) due to higher absorption losses at longer wavelengths, and for devices with a high-reflection (HR)-coated back facet and low-reflectivity-coated front facet. As the cavity length is increased, the front facet's reflectivity is generally decreased to maintain an optimal mirror loss, which produces a more non-uniform longitudinal intensity profile in the waveguide, causing the reduction in efficiency. Additionally, the device

density and yield decrease as the length increases, due to the larger area of the wafer required for each chip. Thus, most devices in the literature are not longer than ~ 7 mm long, though some out to 10 mm have been reported [87].

Increasing either of the other two dimensions reduces heat transfer out of the core of the device, degrading continuous-wave (CW) performance. Adding additional stages also can potentially cause strain relaxation (depending on the core region design), increases the operating voltage, and adds growth time. Widening the core region without introducing any other changes allows additional lateral modes to lase, which degrades beam quality. In fact, broad area QCLs have been shown to emit a double-lobed far field [64] due to high-order lateral mode being favored to lase [78]. Additionally, due to the poor transverse thermal conductivity of the superlattice core [72], [73], the thermal conductance of broad area devices is quite poor. Recently, there has been work investigating the benefits of QCLs with fewer stages than typical (e.g., 10-20 stages compared to ~40) [25], [82], [88]–[90], as this will improve the thermal conductance of broad area devices. This technique could be combined with some of the methods detailed in this chapter for coherent power scaling to obtain high CW power and single-spatial-mode operation from devices with large core volumes.

Thus, in order to obtain high powers in a narrow beam, a variety of methods for (spatially) coherent power scaling have been developed. Many of these involve *arrays* of QCLs, in which separate QCL core regions are optically coupled together. This chapter reviews the literature on coherent power scaling of mid-infrared and long-wavelength-infrared (LWIR) quantum cascade lasers, with a focus on leaky-wave-coupled antiguided phase-locked arrays.

## 4.2 Single-Element Devices

While widening a ridge waveguide or BH QCL typically allows multiple lateral modes to lase, there are techniques that allow such single-element devices to maintain good beam quality. One method for scaling the output power of a single-element device while maintaining a good beam quality is to 'taper' (sometimes called 'flare') the waveguide, as shown schematically in Fig. 4.1. A review of such devices can be found in [91]. This method has been implemented in two ways for QCLs: as a flared master-oscillator power amplifier (MOPA) or a merely as a tapered laser [92]. Another method is to angle the cavity, so that the cleaved facets are no longer normal to the stripe, as shown schematically in Fig. 4.2. Other methods include suppressing high-lateral-order modes by forming trenches near the sidewalls along a broad area stripe [93], or introducing loss using metal absorption at the sidewalls of the stripe to discriminate against the higher-order modes that will have a larger overlap with this loss [94]. All of these methods will still have the problem of poor thermal conductivity, regardless of lateral-mode selectivity, due to their broad-area nature, though this could be mitigated by using fewer stages in the core.
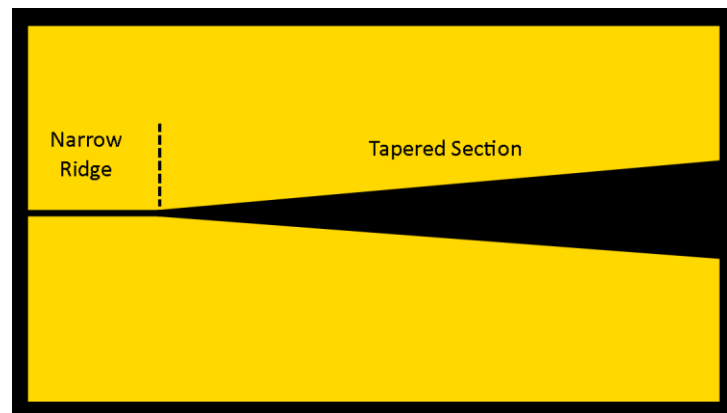
Fig. 4.1. Schematic top-view of a tapered waveguide, which could be used as either a MOPA or as a tapered laser.

Fig. 4.2. Schematic top-view of a laser chip with an angled cavity.

### 4.2.1 Master Oscillator Power Amplifiers

The idea behind a monolithic MOPA is to form a cavity for a low-power laser (oscillator), and then add an additional gain section at an output of the cavity that amplifies the light without providing feedback. If the amplifier section is tapered, with the oscillator section narrow enough to only allow a single lateral mode, this could allow a single mode to spread out to fill the flared amplifier, which increases the output power and narrows the output beam. This taper must be gradual enough to maintain single-mode operation, which is known as an adiabatic taper [92]. There are also other geometries possible for forming a MOPA, such as pumping an amplifier from an external laser source.

In [95], the authors fabricated an incoherent array of flared MOPAs using QCLs emitting between 9.2 and 9.8 µm. They obtained up to 3.9 W of near-diffraction-limited peak pulsed power from a single 100 µm-wide aperture, with distributed feedback (DFB) providing the cavity in the seed section. Up to 1.5 W of peak pulsed power in a diffraction-limited beam was reported in [96], where the authors found that tapering the amplifier section successfully narrowed the far field beam pattern by a factor of 3 compared to an untapered device.

The primary issue with MOPAs in the near-IR was the lack of an index structure laterally [97]. Thus, any perturbations in the index, such as due to filamentation [91], greatly affect the mode profile. Additionally, during CW operation the center of the amplifier will be hotter than the edges, causing a lensing effect in the index. This thermal lensing can cause phasefront aberrations in CW operation. Additionally, since the amplifier section is not meant to provide feedback to the cavity, the facet reflectivity must be very low, < 1%, which can pose a challenge, and may require an isolator. The seed and amplifier sections typically have separate contacts for tuning them individually, which makes epi-side down mounting for CW operation difficult, as a special mount with isolated sections is required.

Another method for high coherent power using MOPAs is to utilize a single master oscillator to power multiple separate amplifiers [98]. The current to each amplifier can be tuned to adjust the phase of output in order to ensure phase matching between all the amplifiers. This is called active coherent beam combining, as opposed to the passive coherent beam combining that will be described later, in which merely the geometry of the device maintains the phase relationship without requiring tuning (in theory). One drawback to this active combining is that, similar to a single MOPA, every amplifier must have a separate contact, which makes packaging difficult. An individually addressable epi-side down bar is possible [99], however, so epi-side down mounting of a MOPA may be feasible.

### 4.2.2  Tapered Lasers

A tapered laser has essentially the same geometry as a flared MOPA, but the cavity of the laser encompasses the entire chip. Thus, there is no AR coating required (though a low-reflectivity coating may still be used, if desired), a single electrical contact can be used for the

chip, and no feedback is required to form the cavity specifically in the seed section (either by reflection or grating feedback).

An incoherent array of tapered QCLs operating between 9.2 and 9.7 μm were fabricated in [100]. Devices emitted up to 1.6 W of peak pulsed power at room temperature with a distributed Bragg reflector (DBR) at the back facet. The $M^2$ beam quality figure of merit (a measure of how close to being diffraction-limited the beam is, defined in [101]) ranged from 1.4 to 2.0, making them nearly diffracted-limited. In [101], the authors fabricated 1° and 2° tapered QCL emitting at 9.5 μm with peak pulsed powers of 2.5 W and 3.8 W, respectively, at room temperature with a nearly diffraction-limited beam pattern ($M^2 \sim$ 2.08 and 2.25). A 1° tapered QCL emitting at 8.1 μm with a peak pulsed power of 4.0 W at room temperature and a nearly diffraction-limited beam pattern ($M^2 \sim$ 1.8) has been reported as well [102]. A smaller taper, for better thermal conductance in CW operation, was used to obtain 4.5 W of CW power in a single-lobed beam in [24].

### 4.2.3 Angled Cavity Lasers

It has been shown that tilting the facets of a semiconductor laser suppresses higher order lateral modes [103]. This can allow a broad-area device to operate in nearly a single lateral mode, producing a single-lobed beam pattern, as opposed to the double-lobed beam pattern typically seen for broad area QCLs without an angled cavity [64].

In [104], the authors fabricated a broad area ridge waveguide 60 μm wide with an angled cavity tilted by 17°, emitting up to 1.2 W of peak pulsed power with an $M^2$ value of 2.0. A broad area (300 μm wide) ridge waveguide with a cavity tilted by 12°, emitting up to 203 W of peak pulsed power at a current of 130 A and with an $M^2$ value of 5.0 at high drives was reported in

[105]. So, while this does not produce quite a single-mode device for such broad areas, it is still significantly better than without the angled cavity.

## 4.3    Spectral Beam-Combining

Spectral (or wavelength) beam-combining, in which uncoupled single-element devices emit distinct wavelengths and are combined externally, is one approach for combining multiple low-power lasers into a spatially coherent and high-power beam [106]. This can be accomplished using a dispersive element, such as a diffraction grating, to combine multiple beams of different wavelengths. Wavelength-selective feedback can force each single-element device to operate at a specific wavelength defined by its position. Depending on the implementation, the external cavity can be designed to only allow feedback for a given device at the wavelength that would produce a beam that overlaps with the other beams, thus forcing a nearly-diffraction-limited beam, if the individual devices operate in a single spatial mode. There have been several spectrally-combined QCL arrays reported in the literature.  A 20 W output power with $M^2 = 1.5$ from this type of system was reported in [107]. In another system, each laser has its wavelength defined internally using distributed feedback, and the external grating serves to only combine the beams [108]. Since the dispersion of the external grating does not necessarily match the wavelengths of the individual lasers, pointing errors can result in the far field beam pattern. In [109], the authors found that an eight-element array only had a 4-5 $\times$ increase in output power compared to a single element due to the devices being forced to operate off the peak of their gain bandwidth, though with a near-diffraction limited beam ($M^2$ value of 1.5). This could be mitigated by placing the devices closer together, to obtain more closely-spaced wavelengths, though this increases the thermal crosstalk between devices in CW operation. One potential

drawback of this approach is that spectral brightness cannot be improved in this fashion, if that is a concern.

## 4.4    Phase-Locked Arrays

As opposed to single-element devices, phase-locked arrays of QCLs are formed by monolithically combining the output from multiple, separate, core regions in a coherent fashion. Arrays are an attractive approach to scale the CW output power due to the improved thermal conductance compared to a broad area single-element device of the same volume, provided high beam quality can be adequately maintained. It has been theoretically shown that strong overall coupling occurs only when each element equally couples to all others (known as "parallel" or "global" coupling) [110]. Global coupling provides maximization of intermodal discrimination and uniform near-field intensity profiles, which suppresses the onset of high-order-mode oscillation at high drive levels above threshold. Furthermore, global coupling leads to arrays that are fundamentally more stable against coupling-induced instabilities than serially-coupled arrays [111], which have been found to readily exhibit multi-mode operation at high drive current above threshold. That said, the analysis in [111] found that the critical coupling constant for stability is directly proportional to the linewidth enhancement factor α, which is much smaller for QCLs than conventional interband lasers [61], so that the difference in improved stability of globally-coupled arrays compared to serially-coupled arrays is likely lessened. Nevertheless, the best possible stability would be preferred (i.e., a globally-coupled array).

### 4.4.1  Evanescently-Coupled Arrays

The simplest method to create an array is to position BHs close to each other laterally, so that the optical modes overlap and they couple together to form what is known as an evanescently-coupled array, as shown in Fig. 4.3 for a one-dimensional array. A great deal of

work was performed with this type of array in the near-IR, with the conclusion that this type of array has multiple problems [97].
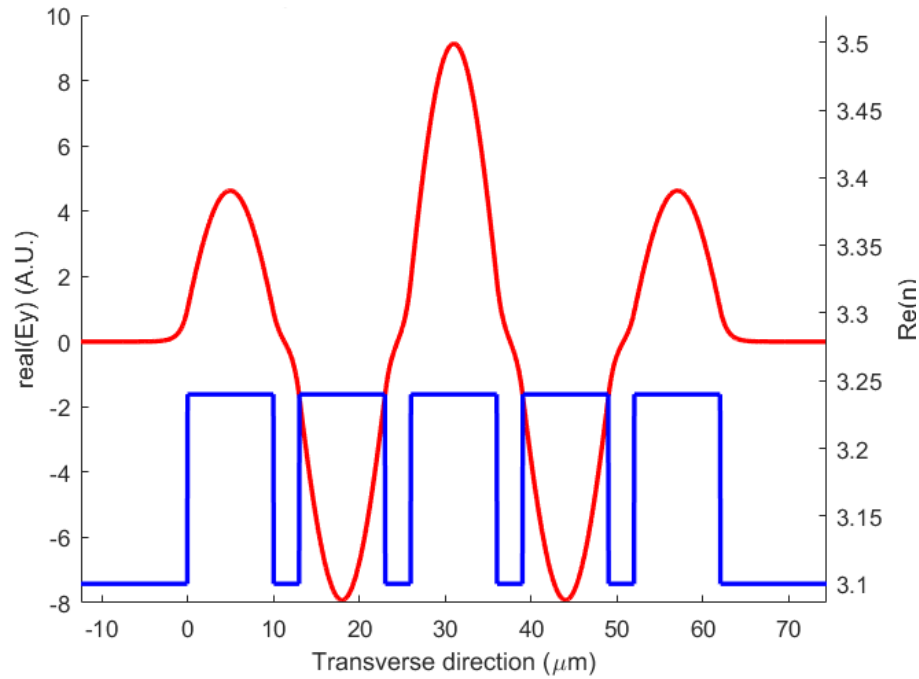


Fig. 4.3. Schematic of a 1-D evanescently-coupled array, showing its lateral index profile (blue) and the amplitude profile (red) of the favored out-of-phase array mode.

First, since the gain is provided in the core regions in the 'elements' (the high-index regions), the mode with the largest overlap (or confinement factor) to the elements is favored to lase. This mode is actually the 'out-of-phase' mode, shown above in Fig. 4.3, in which the electric field amplitude is 180° out of phase between adjacent elements. This creates a null in the 'interelements' (the high index regions), which results in this mode having the largest confinement factor. This out-of-phase mode has a primarily double-lobed far field, which is typically not ideal. This can be corrected, however, using phase-shifting films for every other element at the output facet of the device (while ensuring the reflectivity is not changed for each element) [112].

Secondly, there is only nearest neighbor coupling between elements, which results in a cosine-shaped envelope to the in-phase mode profile. This can cause gain spatial hole burning (GSHB) at the array level. This essentially means that the gain will be more efficiently 'used' by the in-phase mode in the center elements, and unused gain in the outer elements will be available to other array modes. Thus, the intermodal discrimination is not very good above threshold, and the onset of additional modes lasing causes broadening of the output beam.

In the mid-IR, an evanescently-coupled BH QCL array was fabricated emitting at 8.4 μm [113]. The authors obtained out-of-phase mode operation with near-diffraction-limited lobes to 0.23 W of peak pulsed power. In another case, shallow-etched evanescently-coupled ridges with interelement gain (e.g., the core was unetched) and a small positive index step ($\Delta n = 0.005$), operating at $\lambda = 4.6$ μm, produced a relatively wide in-phase-like beam pattern (4.2 × the diffraction limit) just above threshold, that further widened with increasing drive, from a 700 μm-wide array composed of 100 elements [114].

## 4.4.2  Y-Junction Arrays

Another technique to produce arrays of semiconductor lasers is to use a tree-like structure with Y-junctions, as shown schematically in Fig. 4.4. These have been fabricated at a wavelength of 10.8 μm using six ridgeguides coupled by these Y-junctions [115], and produced in-phase mode operation in pulsed operation. There was, however, no increase in brightness compared to a single ridge, due to modal competition. A four-element Y-junction array using coupled buried heterostructures at 4.6 μm has also been fabricated which operated in multiple modes up to 1.5 W of CW power [116]. As discussed in [117], the coupling efficiency for a simple Y-junction is higher for out-of-phase modes, so trees with more Y-junctions are more likely to favor an out-of-phase mode.
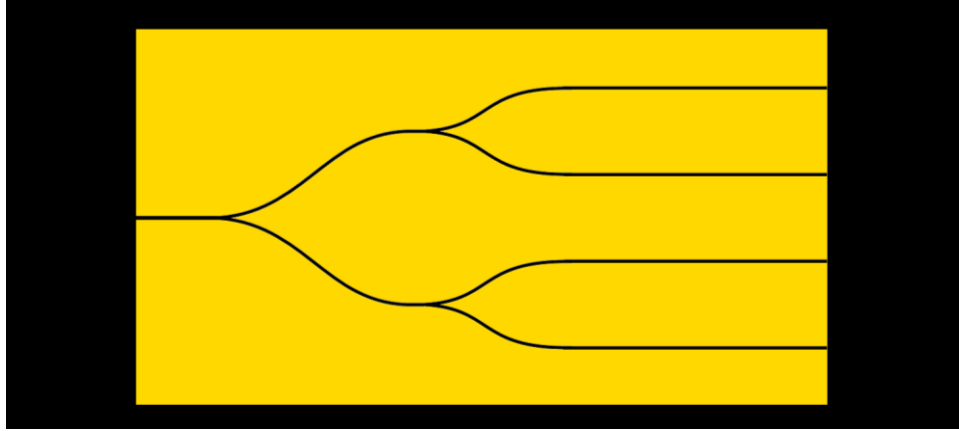
Fig. 4.4. Schematic top-view of a 4-element Y-junction tree array.

Another method of forming the Y-junction uses a $1 \times 2$ multi-mode interferometer (MMI). This has been used to obtain 15 W of pulsed power from an uncoated eight-element QCL array of ridge waveguides emitting at a wavelength of 4.8 μm, with a nearly diffraction-limited far field beam pattern from the array-side of the device [118]. The array-side far field beam pattern had ~30 lobes due to the large 100 μm spacing between branches at the facet (the wider the spacing between elements, the more dense the lobes are in the far field, though it does reduce thermal cross-talk in CW operation). The beam was not measured at the single-element side of the device. The transmission efficiency of the MMI was estimated to be 94% for the in-phase mode based on experimental results, and the simulated transmission efficiency of the out-phase-mode was nearly 0%. Thus, MMIs appear to perform far better than simple Y-junctions for high coupling of the in-phase mode and low coupling of the out-of-phase mode. The MMI was 139 μm long and 20 μm wide, so the thermal conductance in these regions would be somewhat worse for CW operation than the 5 μm-wide branches. Because the eight branches all originated from a single stem, this device operates with global coupling, so this is a quite promising approach to scaling the CW power of QCLs.

One issue that could make CW operation difficult for Y-junction arrays is that the InP regrowth required for BHs, which is typically used for CW operation, could be challenging for the complex geometry involved. Indeed, even for a single BH, mounds on the sides of the ridges often form, such as that shown in Fig. 4.5(a). These or other artifacts would be even more likely to occur in the sharp angles of the junctions/MMIs, and result in poor thermal contact when mounting epi-side down. These mounds can be polished down by chemical-mechanical polishing (CMP), as shown in Fig. 4.5(b), which we have found to be a suitable process for producing > 1 W of CW power from BHs.



(a)

| 2 μm | EHT = 3.00 kV | Signal A = InLens | Date :27 Jul 2016 | ZEISS |
| Pixel Size = 27.96 nm | WD = 3.4 mm | Photo No. = 22553 | Time :10:16:28 | |

(b)
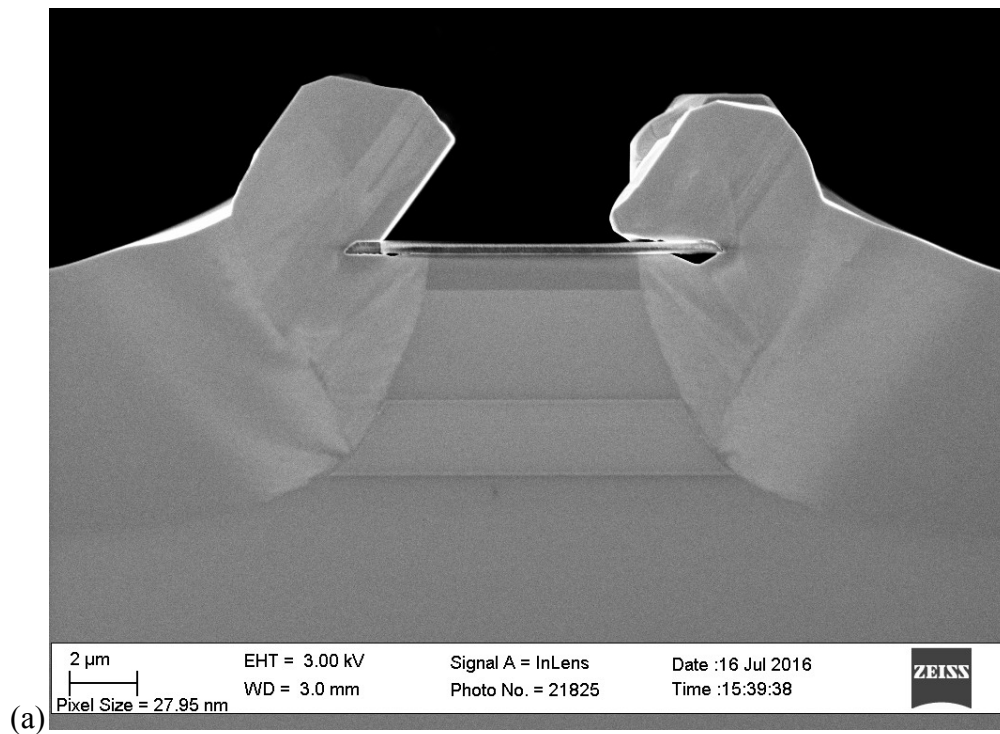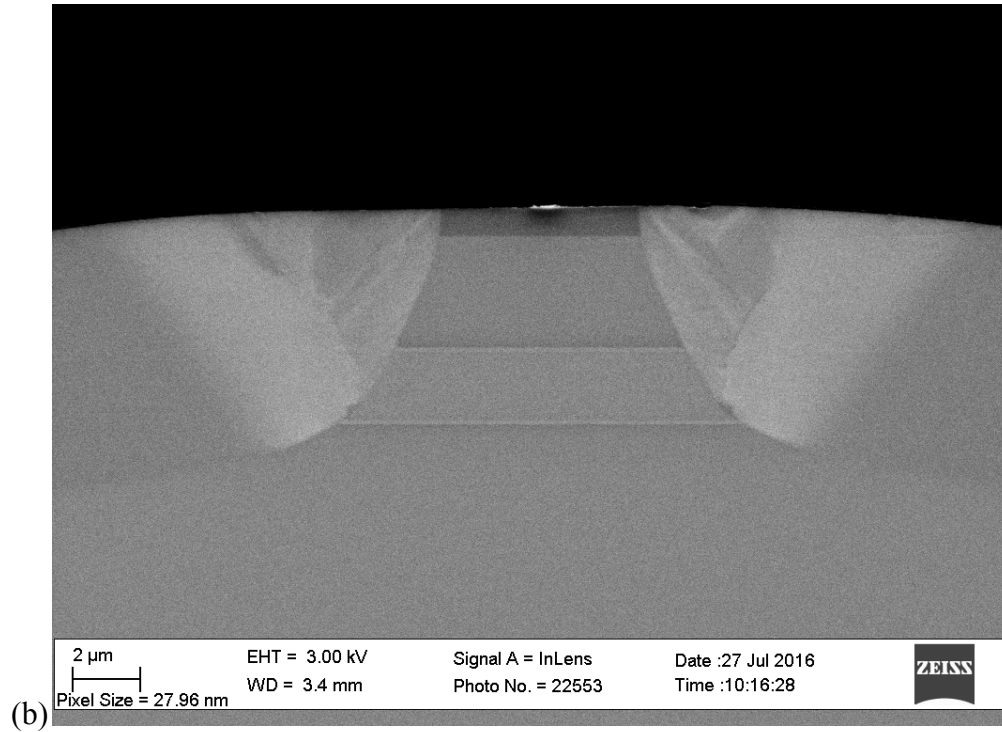
Fig. 4.5. (a) An SEM image of a QCL BH after InP:Fe regrowth, showing mounds on either side of the dielectric mask on top of the ridge; (b) An SEM image of a QCL BH after CMP to polish down the mounds.

### 4.4.3  Talbot Filters

Integrated Talbot cavities have been employed at the back end of three-element [119] and six-element [120] ridge waveguide QCL arrays for intermodal discrimination. For the three-element array, up to 375 mW of peak pulsed power were obtained in a nearly diffraction-limited in-phase beam pattern [119], but at a serious penalty in efficiency (i.e., halving of the slope efficiency), most likely due to strong edge diffraction losses in the Talbot cavity of such a low-element-number array. For the six-element array, 4 W of peak pulsed power was obtained in both the in-phase and out-of-phase array modes [120], as expected from theory [121] when the Talbot-cavity length is equal the half the Talbot length $Z_t$. The Talbot filter method does not in general employ global coupling for phase-locking, but rather a type of nearest-neighbor coupling (diffraction coupling), thus multi-mode performance is expected for large-element-number arrays

[122]. Fig. 4.6 shows a schematic of a general Talbot filter, showing the region in which an input mode to the cavity diffracts to (i.e., the two nearest-neighbor waveguides on the other side of the filter).
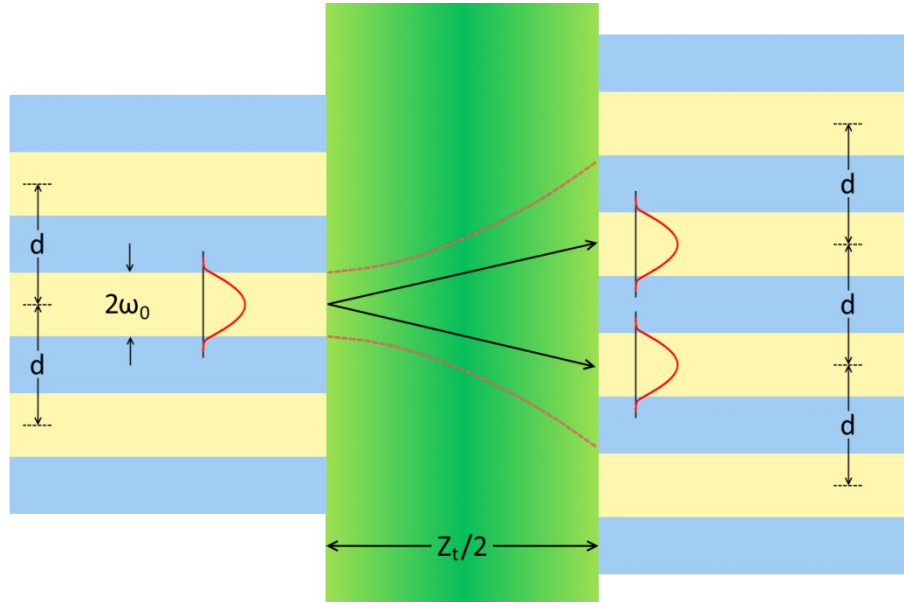


Fig. 4.6. Schematic of a Talbot filter, showing that each element couples to the nearest neighbors on the opposite side of the filter. Yellow regions are the ridge waveguides (elements), blue regions are the interelements, and the green region is the Talbot filter.

### 4.4.4  Two-Dimensional Photonic Crystals

Another method for scaling the core region volume while attempting to maintain a narrow beam pattern is to form a two-dimensional photonic crystal. Some implementations using diffraction gratings, called photonic crystal distributed feedback (PCDFB) lasers, typically have a low index contrast (on the order of $\Delta n \sim 0.008$) as the grating does not penetrate the core [123]–[125]. This type of device can produce a nearly diffraction-limited beam in pulsed operation to at low drives, but heating in CW operation or even pulsed operation at high drive can overwhelm the low index contrast. The temperature rise is non-uniform throughout the structure (the core will heat more than the claddings, and the lateral edges will typically be cooler than the center), and since the semiconductors' refractive indices elevate with increasing

temperature, the periodicity in index isn't maintained for the photonic bandstructure. Additionally, these have a broad area core, which has a poor thermal conductivity. Thus, these devices work well only in low duty cycle pulsed operation, and the beam is likely to broaden significantly in CW operation.

In [124], the authors fabricated a PCDFB QCL operating at 4.7 μm, which emitted 0.5 W per facet of diffraction limited peak pulsed power from a 100 μm-wide aperture. The device emitted up to 12 W of peak pulsed power (combined from both facets), but the far field beam profile was not reported at higher drive levels. This work was followed up in [125], where up to 34 W of total peak pulsed power was obtained in a narrow beam: $M^2 \sim 2.5$ near threshold, broadening up to $M^2 \sim 9$ at high drive. They attribute this to thermal effects at high drive for this broad area device, as is expected for this small-index-step device.

Two-dimensional high-index-contrast photonic crystals have been reported [126] in which the core was etched through and regrown via hydride vapor phase epitaxy (HVPE) with InP:Fe (the Fe-doping is used to make it electrical insulating to block current flow) to provide the large index step and better thermal conductance. The device lased in a 4°-wide, double-lobed far field beam pattern from a 550 μm-wide aperture, up to a peak pulsed power of 0.88 W. Thus, while the high index contrast and improved thermal conductance can be expected to improve device performance in CW operation, great care must be taken in ensuring the photonic crystal structure actually produces a desirable beam pattern.

### 4.4.5 Leaky-Wave-Coupled Phase-Locked Antiguided Arrays

To obtain high spatially coherent CW output powers, a high index contrast device without a broad-area core is needed which is favored to lase in a mode producing a single-lobed beam, in order to maintain coherence despite index elevations from self-heating. Phase-locked

arrays of antiguides, which have also been called resonant optical waveguide (ROW) arrays, offer these properties. An antiguide is simply a negative-index step waveguide. That is, for a three layer structure, the center has a lower refractive index than the layers in either side, as shown in Fig. 4.7 along with the electric-field amplitude profile ('near-field') of the fundamental mode of this antiguide. The effective index of such a structure is lower than all three layers' indices, so the mode propagates laterally in all layers. Thus, a lateral antiguide emits light out of the sides of the stripe as the mode propagates down the stripe, seen by the wave propagating away from either side of the antiguide in Fig. 4.7. This is sometimes termed a 'leaky mode.'
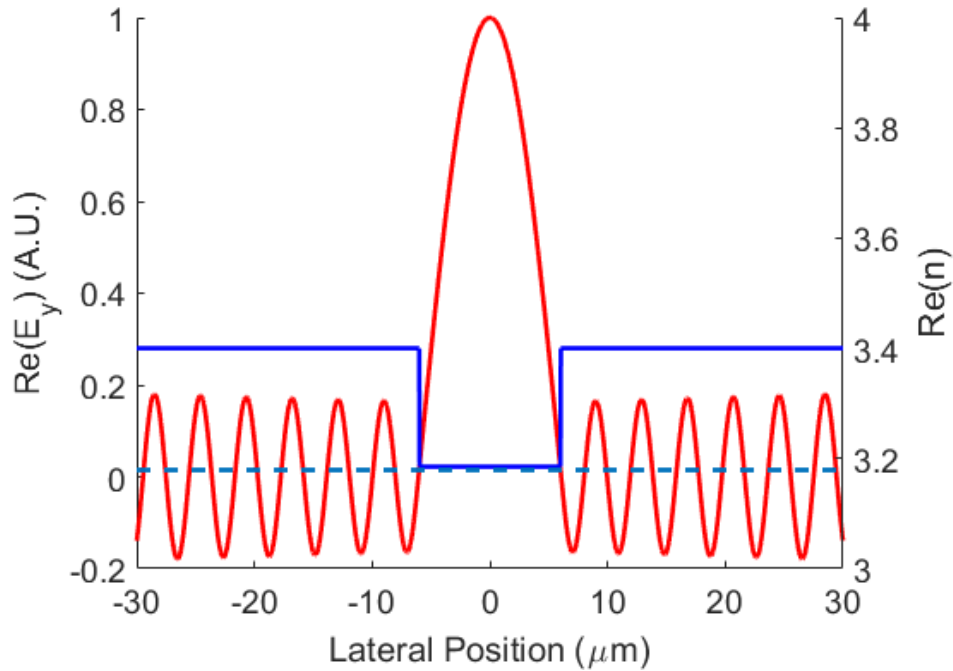
Fig. 4.7. Schematic of a single antiguide, showing its index profile (blue), the electric field amplitude profile of the favored fundamental mode (red), and the effective index of this mode (dotted blue).

Normally, this edge radiation loss is a poor design for a waveguide, but in an array where multiple antiguides are placed side-by-side, this lateral propagation allows the antiguides to couple to each other and produce an in-phase mode, shown in Fig. 4.8 (hence called 'leaky-

wave-coupling'). The core region, and hence gain, is placed in the low-index regions, called the "elements." The high-index regions, called 'interelements,' are designed to have high loss. This interelement loss can be introduced with little effect on the resonant in-phase mode, due to it having little intensity in the interelement regions [127]. In contrast, when the interelement width of an array approaches the width required to produce resonance, the non-resonant array modes experience enhanced field overlap with the lossy interelement regions [97], [127]. Thus, they are strongly suppressed in structures with high interelement loss [26], [27], [127], [128]. The indices shown in the schematic in Fig. 4.8 and described here are typically actually effective indices of the transverse mode in each region (that is, there is a vertical positive-index-step waveguide in each region with a fundamental mode with an effective index which is used to model the device laterally). The index step is typically about 0.05-0.12, an order of magnitude higher than the index elevation caused by thermal lensing. Thus, these devices should be less affected by heating in CW operation. The edge radiation loss is inversely proportional to the number of elements, so it is reduced significantly compared to a single antiguide [127].
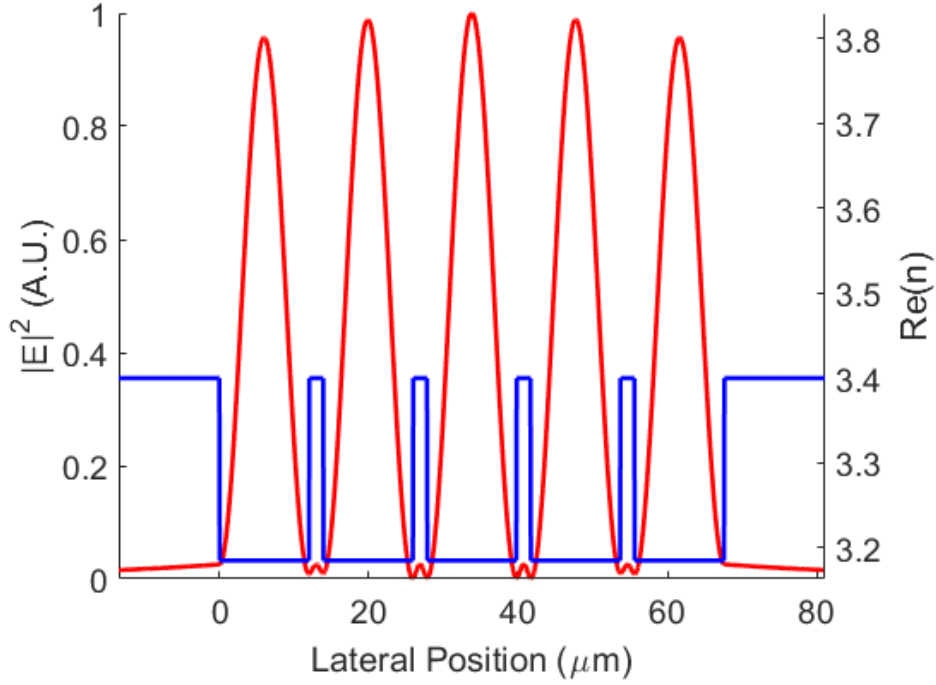
Fig. 4.8. Schematic of a 1-D phase-locked antiguided array, showing its index profile (blue) and the intensity profile of the favored in-phase array mode (red).

Such devices are designed so that the in-phase mode is at resonance laterally, which leads to full transmission between the elements and thus global coupling. Resonant leaky-wave coupling occurs when the interelement regions' widths, $S$, are equal to an integer multiple of half the projected wavelength $\lambda_1 = \lambda / \sqrt{n_1^2 - n_{eff}^2}$ in the lateral direction within the interelement regions [26], [127], where $n_{eff}$ is the array mode effective index and $n_1$ is the transverse effective refractive index within the interelement region (i.e., $S_{res} = m\lambda_1/2$, where $m$ is an integer). As $n_{eff}$ is approximately equal to $n_2$, the transverse effective refractive index in the element regions, this means that the interelement width at resonance, $S_{res}$, is approximately inversely proportional to the index step $\Delta n = n_1 - n_2$ (i.e., $S_{res} \propto 1/\Delta n$). To achieve in-phase mode resonance for linear arrays, $m$ must be an odd integer. Operating at resonance produces a uniform intensity profile for the in-phase mode, which prevents gain spatial hole burning at the array level. Within the

elements, the intensity is still peaked at the center of the element, so for example the unused gain at the edges of the elements can still be used by array modes of coupled first-order element modes (i.e., array modes with two intensity peaks in each element). At and near resonance the structures are analogous to $2^{nd}$-order *lateral* distributed-feedback (DFB) structures [31], [129]. Thus, they can be considered to be high-index-contrast photonic crystal structures (HC-PCs) that allow long-range coupling in a stable, in-phase array mode of uniform intensity profile [26]. A grating could be included longitudinally to make a 2-D photonic crystal with a narrow linewidth. Fig. 4.9 shows an example of the photonic crystal bandstructure for the HC-PC shown in Fig. 4.8. The circled intersection shows the location of the in-phase mode in Fig. 4.8.
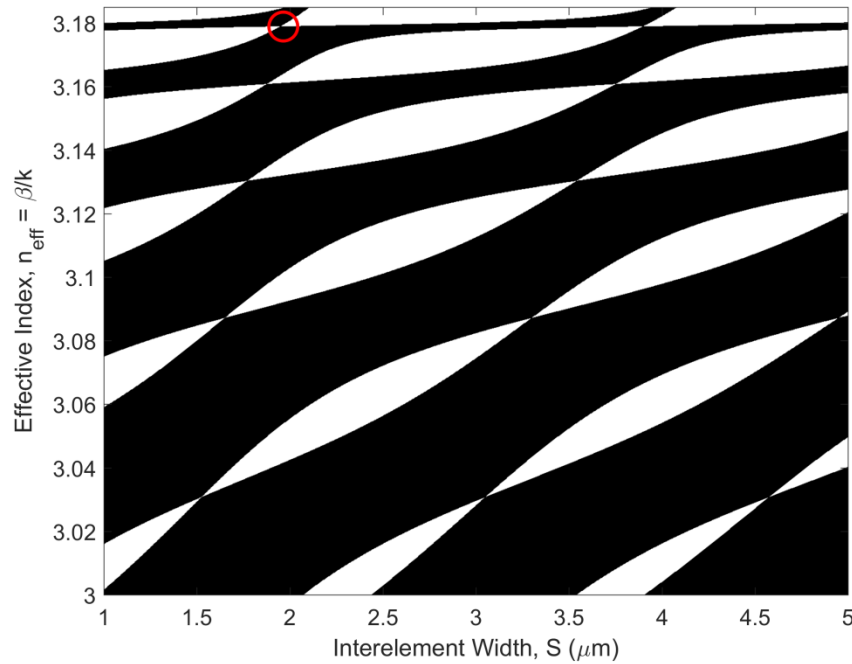


Fig. 4.9. Photonic bandstructure of the HC-PC shown in Fig. 4.8. Black regions are allowed bands, white regions are forbidden regions, and the red circle shows the location of the in-phase mode shown in Fig. 4.8.

These devices were initially termed resonant optical waveguide (ROW) arrays [27], [130]. In the near-IR, a 40-element HC-PC/ROW array with a 200 µm-wide aperture was

fabricated [131] which produced 10W of peak pulsed power in a near diffraction limited beam. Later, 1.6 W of CW power was obtained in a near diffraction limited beam, with 1 W in the main lobe [32].

In the mid-IR, an 8.36 µm-emitting HC-PC QCL was fabricated by selective regrowth of interelement layers within curved trenches which had a threshold current of 10.4 A and emitted up to 5.5 W of peak pulsed power in a beam with a full-width at half-maximum (FWHM) which was 1.65 × the diffraction limit at 1.8 × threshold [132]. 82% of the light was emitted in the main lobe of the far field, so that it emitted about 4.5W of near diffraction limited power in the main lobe. The following chapters will discuss further work on HC-PCs emitting around 4.7 µm, which have more difficult tolerances and geometries to fabricate due to the shorter wavelength.

This type of device does have problems as well. First, the tolerance to obtain resonance is tight, making fabrication difficult. The tolerance in interelement width scales with wavelength, however, so fabricating these devices in the mid-IR should be easier than in the near-IR, where tolerances are about 0.1 µm. The interelement width at resonance scales with the wavelength as well. Thus, a HC-PC in the mid-IR is more difficult to fabricate than in the LWIR due to both tighter fabrication tolerances and narrower trenches to etch and regrowth within for the interelement region, as will be seen later. Secondly, the far field beam pattern from the in-phase mode is primarily tri-lobed, as shown in Fig. 4.10, which is the simulated far field beam pattern from the in-phase mode shown in Fig. 4.8. This is calculated by taking the square of the Fourier transform of the electric-field amplitude profile and applying a $\cos^2(\theta)$ obliquity factor [133]. Depending on the exact design, 60-80% of the emitted intensity is contained in the main lobe. The side-lobes are due to the periodic nature of the emitted light.
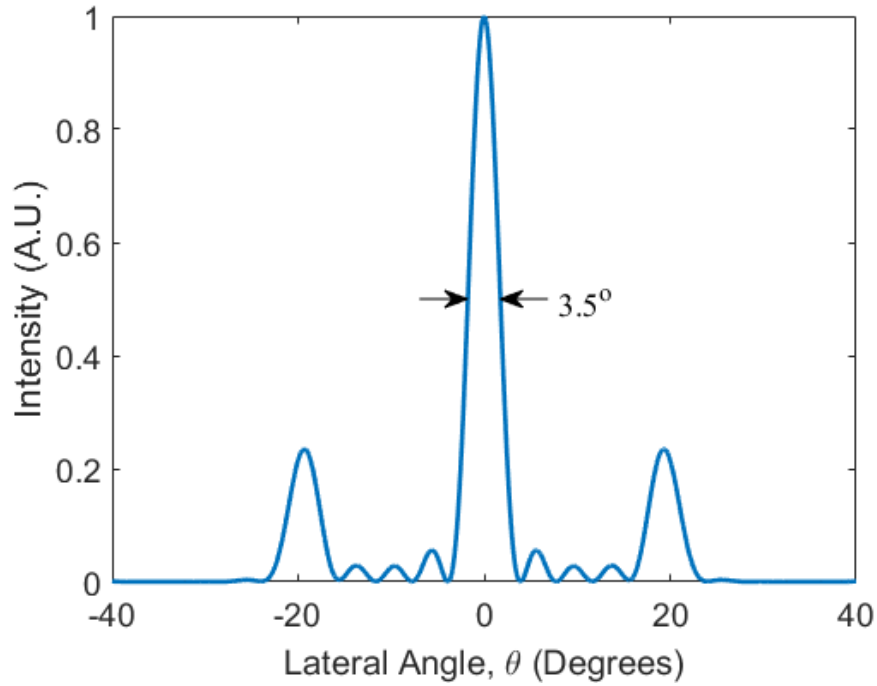
Fig. 4.10. Simulated far field beam profile of the in-phase mode shown in Fig. 4.8, found by taking the square of the Fourier transform of the electric-field amplitude profile and applying a $\cos^2(\theta)$ obliquity factor.

### 4.4.6 Anti-Resonant Reflective-Optical Waveguides

An anti-resonant reflective-optical waveguide (ARROW) device uses multiple-quarter lateral-wave reflectors on either side of a leaky stripe to selectively reflect back fundamental element modes which meet the anti-resonance condition, and allow higher-order modes to propagate through and radiate laterally from the waveguide [134]. These reflectors can be placed outside a single antiguide or a ROW array. Thus, the ARROW terminations can be used to reduce edge-radiation losses for the desired in-phase mode of a ROW array. Fig. 4.11 schematically shows the lateral index profile for a single-element ARROW device, along with the intensity profile of the favored fundamental mode. The inner, high-index region has width $S_{ref} = 3\lambda_1/4$ and the outer, low-index region has width $d_{ref} = \lambda_0/4$, where $\lambda_0$ ($\lambda_1$) is the laterally projected wavelength in the low-index (high-index) region. Despite having an antiguided

structure, very little light is radiated away laterally from the fundamental mode, allowing strong intermodal discrimination with a low threshold for single-spatial-mode operation to high power. Such a structure increases the maximum width for single-spatial-mode operation compared to conventional single-element devices, which could increase the maximum coherent output power if the additional loss to the fundamental mode from the ARROW structure can be minimized.
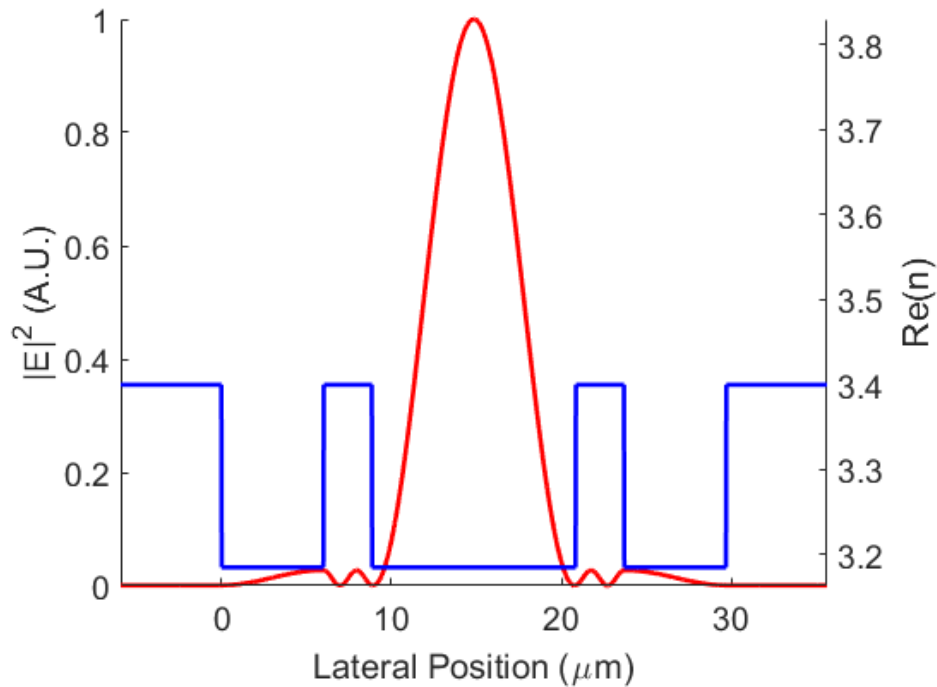


Fig. 4.11. Schematic of a 1-D single-element ARROW device, showing its index profile and the intensity profile of the favored fundamental mode.

## 4.5    Conclusions

Scaling the spatially-coherent CW output power of mid-IR quantum cascade lasers is a difficult but important task. A variety of methods have been developed for accomplishing this, using either larger-volume single-element devices or arrays. Due to the low thermal conductivity of the QCL core, broad area devices experience excessive heating in CW operation that degrades performance. Breaking the core up into multiple regions, as in an array, improves the thermal

conductance of a large-volume core. The antiguided array device concept (or HC-PC) offers a path to increase the device core's volume while providing strong selectivity for a single spatial mode, is capable of maintaining coherence in CW operation, and improves the thermal conductance compared to a single-element broad-area device.

# Chapter 5 – Design of Planar Leaky-Wave Coupled Phase-Locked Arrays of Quantum Cascade Lasers

## 5.1    Introduction

A demonstration of resonant leaky-wave coupling of long-wavelength-infrared (LWIR) quantum cascade lasers (QCLs) by selective regrowth of interelement layers in curved trenches has already been reported, in which in-phase mode operation to 5.5 W of pulsed power in a near-diffraction-limited (D.L.) far-field beam pattern was obtained [132]. To ensure better control over the array geometry and the element/interelement dimensions, a process for fabricating arrays with planar geometry, involving nonselective regrowth of interelement layers on a surface planarized by chemical polishing (CP), was developed [135].

Here, we present theoretical investigations of the optical and thermal properties of such planarized phase-locked high-index-contrast photonic crystal (HC-PC) QCL arrays. Most of this work has been published previously in [28]. Designs are established for achieving single in-phase mode operation from arrays with 3-7 elements, and with large fabrication tolerances. Self-focusing due to thermally-induced index variations across the array is shown to ultimately limit the single-mode operational range under continuous-wave (CW) operation. Methods to mitigate the focusing effects of the index variations and to improve the intermodal discrimination of these arrays are studied. We project that 7-element devices would provide multi-watt range coherent (in-phase mode) output powers under CW operation.

## 5.2    Planarized Phase-Locked HC-PC QCL Array Structure

A schematic cross-sectional view of the high-index-contrast photonic crystal (HC-PC) structure under evaluation is shown in Fig. 5.1(a).
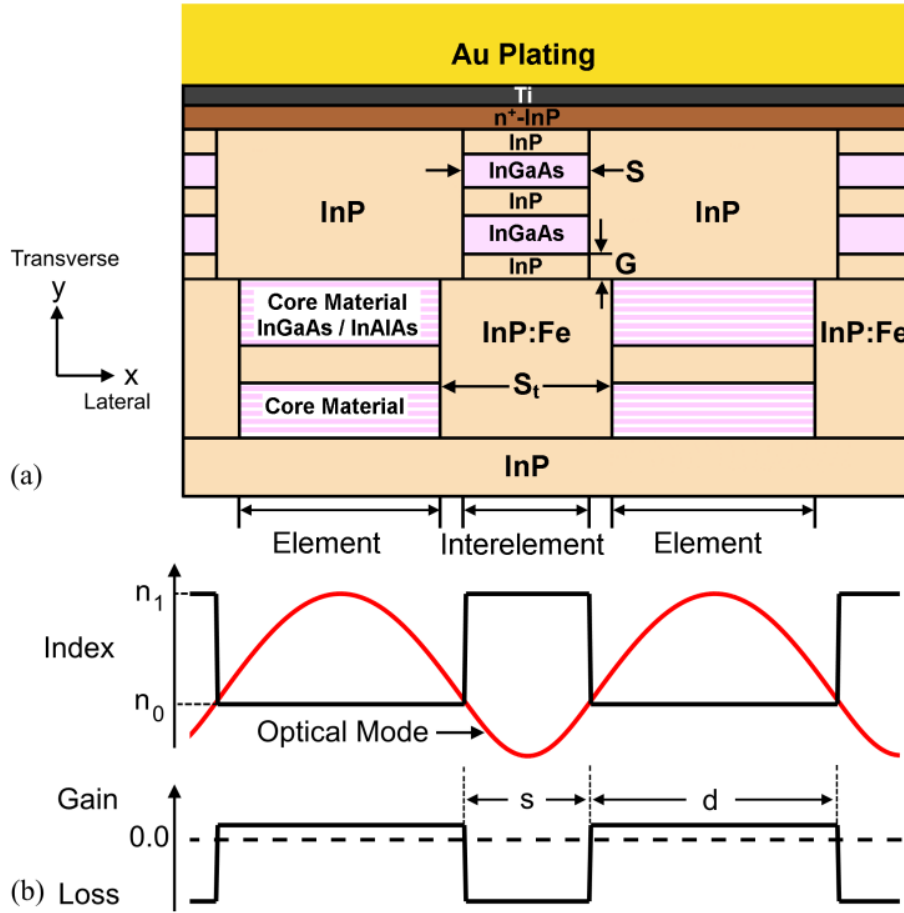
Fig. 5.1. Schematic representation of: (a) cross-sectional view of the HC-PC QCL structure under study; (b) resulting built-in index and gain variation laterally across the array. © 2015 IEEE

As discussed in Ch. 4, resonant leaky-wave coupling, schematically shown in Fig. 5.1(b), occurs when the interelement regions' width $S$ (the high-index region) is equal to an integer multiple of half the laterally projected wavelength $\lambda_1$, in the lateral direction within the interelements [26], [127]. This leads to parallel coupling among the low-effective-index array elements, which contain the core material, and subsequently a uniform near-field intensity profile for the resonant mode composed of in-phase coupled fundamental element modes [27]. Interelement loss is used to create intermodal discrimination when the interelement width is near

the in-phase mode resonance, as the non-resonant modes have roughly an order of magnitude higher intensity in the interelement regions [27], [127].

In Fig. 5.1(a) above, the high-index interelement regions are formed by incorporating one or more InGaAs layers, which has a higher index than either InP or core material. Multiple layers can be used to produce the appropriate interelement effective index and loss, while ensuring that the InP upper cladding layer, above the core material in the element regions, is thick enough to ensure negligible loss. Intermodal discrimination is provided by electric field penetration to the metals in the interelement region. This requires that the upper InP layers in the interelement regions be thin, particular the highly-doped contact layer, as it has a much lower refractive index than low-doped InP and will screen out the field more quickly. A (relatively thin) 50 nm-thick InP:Si (doped to $2 \times 10^{19}$ cm$^{-3}$) contact layer is considered for this study. The thickness of the Ti layer can be used to tune the interelement loss without significantly affecting the interelement-field profile or index. The trench width $S_t$ and the interelement-region width $S$ can be controlled separately in this process by proper mask design. Thus, the difference $S_t$ - $S$, which represents the lateral gap between the core and InGaAs interelement layers, is a parameter that can be adjusted while designing the array, as will be discussed below. The parameter $G$ in Fig. 5.1(a) represents the thickness of the transverse gap between the top of the core material in the element regions and the bottom of the lower InGaAs layer in the interelement regions, and its effect on the device design will also be discussed below. The InP spacer layer in the core material brings the benefit of more efficient lateral heat removal [74] at a cost on the optical confinement factor.

This device structure can be fabricated by using a multiple-step etch-and-regrowth process, as described in [135], and shown in the scanning electron microscope (SEM) images of Fig. 5.2. Note that these SEM images show the fabrication of an alternative design for which the

bottom half of the core material is left intact. The basic process flow is as follows: (i) a 40-stage, 4.8 μm-emitting QCL core structure, based on the active region design by Evans *et al*. [136], and including the 0.5 μm-thick InP spacer layer, is grown by metalorganic chemical vapor deposition (MOCVD). (ii) Both core region halves are periodically removed laterally via Inductively Coupled Plasma (ICP) etching, producing vertical sidewalls for the remaining core material. (iii) Semi-insulating InP:Fe is regrown by MOCVD over the whole structure [Fig. 5.2(a)] after removal of the $SiN_x$ mask. (iv) Chemical polishing (CP), using a 9:1 acetic acid:HCl solution, is employed to polish down the overgrown InP:Fe, in order to ensure a planar geometry prior to the regrowth of interelement-region layers [Fig. 5.2(b)]. The resultant InP:Fe regions block current from flowing outside the core material of the array elements. They also provide lateral heat removal through the conductive InP material in the interelement regions, as discussed below. (v) The interelement-region layers consisting of a multilayer stack of InP and InGaAs are non-selectively regrown over the planarized surface. Due to their planar morphology [Fig. 5.2(c)], these layers have uniform thicknesses. In turn, the dimensions of the interelement regions can be well controlled. (vi) The element regions are defined through ICP etching, followed by nonselective regrowth of the InP upper-cladding layers [Fig. 5.2(d)]. (vii) A second CP step is used to polish the excess InP grown atop the interelement regions. (viii) A heavily doped ($2 \times 10^{19}$ $cm^{-3}$) InP:Si contact layer is grown on top for forming a low-resistance electrical contact to the Ti/Au layers deposited above [Fig. 5.2(e)]. As an alternative process, step (iii) can be replaced by regrowing planar semi-insulating InP:Fe by low-pressure hydride vapor phase epitaxy (HVPE)s [126], [137], removing the need for the chemical polishing in step (iv). As this regrowth is selective, this process requires that the $SiN_x$ mask not be removed before regrowth.
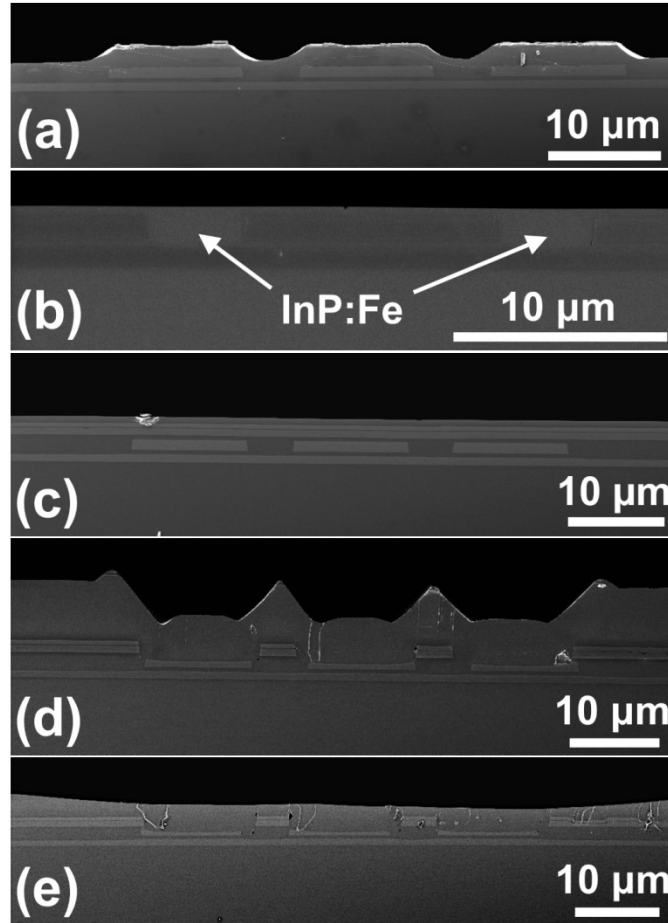
Fig. 5.2. Cross-section SEM images of planarized process steps after (a) InP:Fe regrowth; (b) first chemical-polishing step; (c) interelement layer regrowth; (d) element etching and regrowth of InP-cladding layer; and (e) completed structure. © 2015 IEEE

## 5.3 Modeling

The optical design of the HC-PC structure was carried out using COMSOL Multiphysics to identify the expected threshold current densities and the "fabrication window" for achieving sole in-phase mode operation to high drive levels. The two-dimensional structures were simulated as described in Section 3.2 to find the complex effective indices ($n_{eff}$) and field profiles for relevant modes. The mirror loss, $\alpha_m$, is calculated assuming an HR-uncoated devices of length L = 3 mm, with facet reflectivities $R_1 = 0.95$ and $R_2 = 0.27$. The threshold current density ($J_{th}$) for each array mode was then calculated by using (3.7), where the differential gain

coefficient $g$ was taken to be 6.8 cm/kA [138]. The 'waveguide' loss coefficient $\alpha_w$ includes losses due to backfilling, intersubband-absorption loss, and an internal cavity loss due to free-carrier absorption $\alpha_i$, but since the material indices used in the simulation already included such losses, $\alpha_i$ was removed. We took $\alpha_i$ to be 0.5 cm$^{-1}$, so its removal lowered $\alpha_w$ from 3.3 cm$^{-1}$ to 2.8 cm$^{-1}$ [138].

Thermal modeling was conducted using a 2-D COMSOL model as well, as described in Section 3.3. The material conductivities used are given in Table 3.1. The chip is considered to be mounted on a diamond submount (300 μm thick) with In solder (4 μm thick), which is then bonded to a Cu heatsink (1.5 mm thick by 3 cm wide). These two optical and thermal models were coupled together in order to analyze the effects of thermally-induced index elevation across the array on the modal properties. The indices of all the semiconductors in the model were made temperature dependent by adding a linear dependence on temperature, with a *dn/dT* value of $2 \times 10^{-4}$ K$^{-1}$, inferred from the temperature-dependent spectra of distributed feedback QCLs in the literature [139]–[141].

## 5.4    Results and Discussion – Three-Element Array

Fig. 5.3 shows the magnetic-field intensity profiles for the fundamental transverse modes in the element and interelement regions of the design shown in Fig. 5.1, found from 1-D transfer-matrix method models. The loss for the fundamental transverse mode in the interelement regions is 92 cm$^{-1}$. This large interelement mode loss is due to the waveguide's proximity to the metal contact and the thin highly-doped contact layer, resulting in surface-plasmon-like coupling, as seen in Fig. 5.3(b).
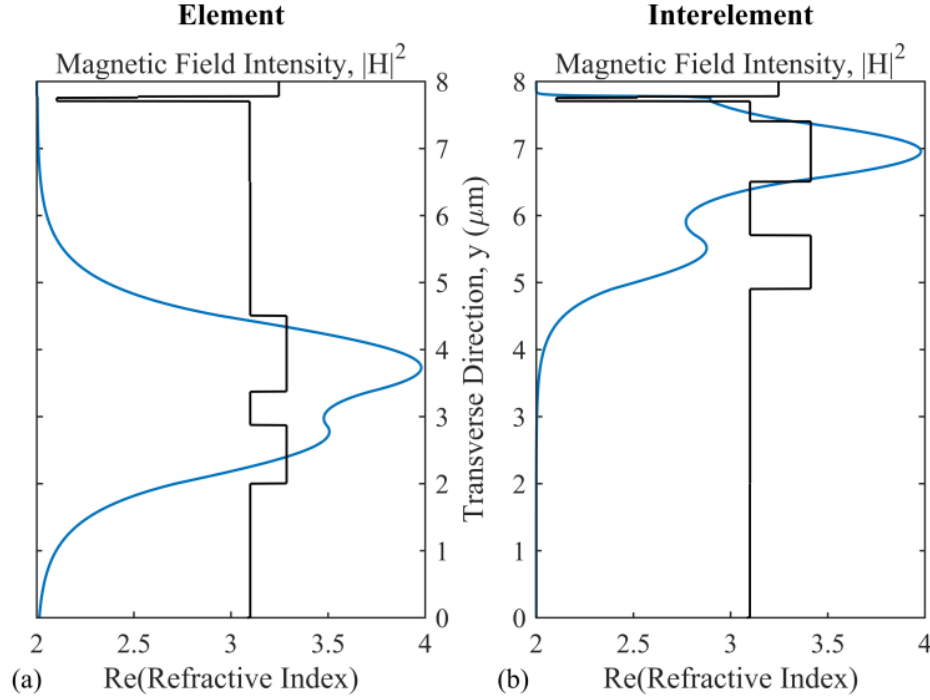
Fig. 5.3. Simulated intensity profile of the magnetic field for the fundamental transverse mode in the (a) element region and (b) interelement region of the three-element array of the design shown in Fig. 5.1. © 2015 IEEE

Fig. 5.4 shows the simulated threshold current density curves and field profiles of relevant modes for a three-element array of the design shown in Fig. 5.1, as the interelement trench width $S_t$ is varied. The element width is 12 μm, $S_t - S = 0$ μm, $G = 0.4$ μm, and the index step is $\Delta n = 0.058$. Note that this index step is an order of magnitude larger than for photonic crystal distributed feedback (PCDFB) QCLs [123], [124], thus it provides optical-mode stability against drive- and temperature-dependent index perturbations. There is a 0.8 μm-wide range in trench width (i.e., $S_t$ values in the range 5.5 μm to 6.3 μm) for which the ratio of the $J_{th}$ values for competing array modes compared to the $J_{th}$ value of the in-phase array mode is greater than 50%. This gives a large tolerance in device fabrication for ensuring single-mode operation to high drive levels. Note that this tolerance in $S_t$ is significantly larger than that ($\Delta S_t \sim 0.1$ μm) for near-IR resonant arrays [13].
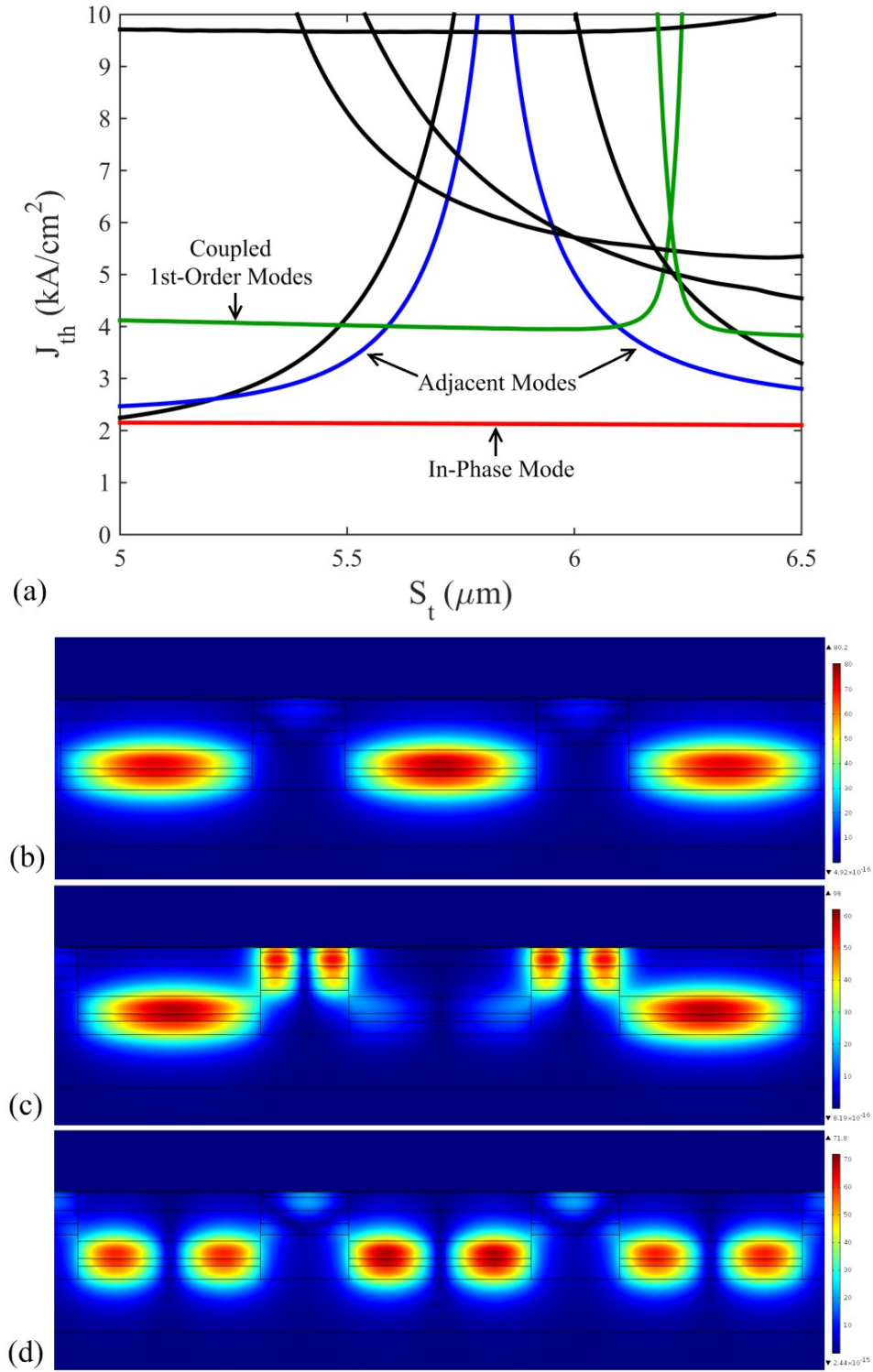
Fig. 5.4. (a) Simulated threshold current densities for modes supported by a three-element HC-PC; The simulated electric field intensity profile for the (b) in-phase array mode, (c) adjacent array mode, and (d) array mode composed of coupled first-order element modes at $S_t = 5.8$ μm in the design shown in Fig. 5.1. © 2015 IEEE

As seen in Fig. 5.4(c), the adjacent mode [27] has high intensity in the lossy interelement regions. The threshold current density and near-field intensity uniformity of the in-phase mode is nearly constant across this range as well, with $J_{th}$ = 2.13 kA/cm$^2$. A uniform near-field intensity across the array is desirable to suppress multi-mode operation resulting from gain-spatial-hole-burning (GSHB) at the array level [27]. The threshold current density for the array mode composed of resonantly-coupled first-order element modes is about two times higher than that of the in-phase array mode in this $S_t$ range, at approximately 4.0 kA/cm$^2$. An alternate design, involving a more complex fabrication process, can help discriminate even further against first-order modes by etching the top corners of the element regions, where first-order modes have high intensity [132]. The percentage of the emitted intensity contained in the main lobe of the far-field beam pattern is 60.9% for this structure, at the resonant $S_t$ value of 5.8 μm.



Fig. 5.5. Simulated threshold current densities for modes supported by three-element HC-PCs with and without a transverse gap between the core and InGaAs layers. © 2015 IEEE

Fig. 5.5 shows the effect of removing the transverse gap $G$ [in Fig. 5.1(a)] on the $J_{th}$ vs, $S_t$ curves. This has the effect of raising the so-called transverse field-overlap parameter [97] $|\kappa|^2$, calculated by $\kappa = \int_{-\infty}^{\infty} E_{y1}^*(y) E_{y2}(y) dy$, where $E_{y1}$ and $E_{y2}$ are the electric field amplitudes of the modes in the two regions for which this parameter is being calculated (in this case, the fundamental transverse modes of the element and interelement regions of the array). The electric fields are calculated by 1-D modal simulations of the transverse structure in the two regions, as in Fig. 5.3. $|\kappa|^2$ increases from 9.1% to 15.5% by decreasing G to 0 μm. A higher field-overlap value between the element and interelement improves the coupling between those regions, which causes increased field intensity in the lossy interelement for all the modes, and thus increases both the in-phase mode threshold current as well as the intermodal discrimination. As has been shown previously, a non-unity field-overlap parameter creates a phase shift [142] at the interface which causes the resonance to shift from what is predicted using the 1-D effective index method. Then, changing the field-overlap value shifts the $S_t$ value at resonance [97], which can be seen in Fig. 5.5, where the resonant $S_t$ value is lowered from 5.8 μm to 5.7 μm when the gap is removed. The field-overlap parameter can also be improved by re-shaping the transverse modes in the two regions (e.g., by lowering the InP-spacer layer in the element, adjusting interelement layer thicknesses, etc.) or by etching through only the top core region and leaving a continuous bottom core region. However, etching only through the top-core region reduces the lateral thermal conduction from the lower-core region and can result in current spreading in the lower-core region. Reducing $S_t - S$ in Fig. 5.1 improves the lateral coupling (which is not accounted for in the calculation of $|\kappa|^2$), resulting in a similar effect on $J_{th}$ as that seen in Fig. 5.5. The major difference is that reducing $S_t - S$ also decreases $S_t$ at resonance by approximately the same amount since the resonance is controlled by the interelement width $S$. This reduction in $S_t$, the

separation between elements, improves the aperture filling factor in the near field, resulting in more power in the far-field beam pattern main lobe [97], but also reduces heat transfer through the high-thermal-conductivity InP interelement trench.

## 5.5    Results and Discussion – ARROW Terminations

As discussed previously, anti-resonant reflective-optical waveguide (ARROW) terminations on near-IR HC-PC structures have been shown to selectively reduce the loss of modes composed of coupled fundamental element modes which meet the anti-resonance condition [134]. Thus, the ARROW terminations can be used to reduce edge-radiation losses for the desired in-phase mode, by adding multiple-quarter lateral-wave reflectors on either side of the array, with the inner, high-index region of width $S_{ref} = 3\lambda_1/4$ and the outer, low-index region of width $d_{ref} = \lambda_0/4$ (shown in Fig. 5.6), where $\lambda_0$ is the laterally projected wavelength in the low-index region. Fig. 5.7 shows the effect of adding these reflectors to a three-element HC-PC device. $J_{th}$ at $S_t = 5.8$ μm is lowered to 1.88 kA/cm$^2$, a reduction of 12%. The effect of changing the widths of the reflector regions at the in-phase mode resonance was studied to optimize their performance, and a 0.5 μm-wide window of nearly equal discrimination was found for both regions of the reflectors.
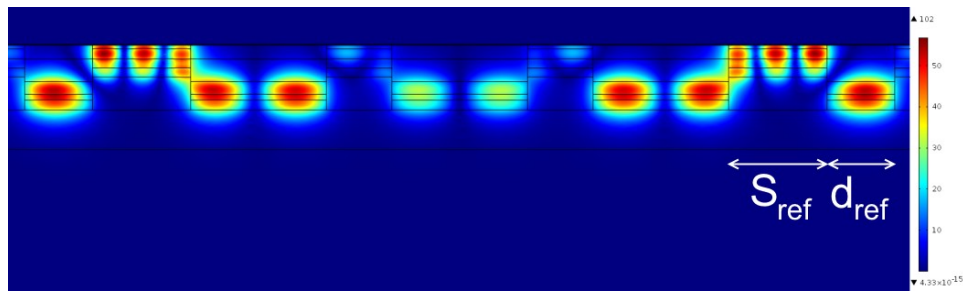


Fig. 5.6. Simulated near-field intensity of the array mode composed of coupled first-order element modes for $S_t = 5.8$ μm, in the design with ARROW terminations. © 2015 IEEE
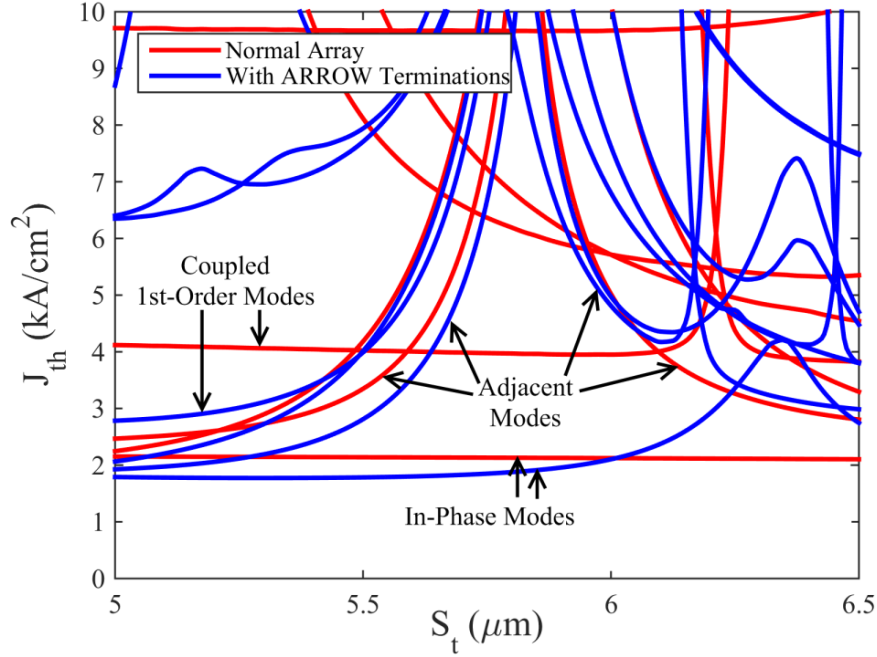
Fig. 5.7. Simulated threshold current densities for modes supported by three-element HC-PCs with and without ARROW terminations. © 2015 IEEE

As expected, the threshold of the in-phase mode decreased due to a reduction in lateral radiation losses. In addition, there is an increase in threshold observed for the array mode composed of coupled first-order element modes. To understand this, Fig. 5.6 shows the intensity profile of that array mode at $S_t = 5.8$ μm for the ARROW device. By comparison to that mode in the normal array shown in Fig. 5.4(d), the high field intensity in the interelement regions of the reflectors increases absorption loss and decreases the confinement factor to the active regions. This is a new and beneficial effect, not previously identified in near-IR antiguided-array lasers with ARROW-type terminations.

## 5.6    Results and Discussion - Scaling to Seven Elements

Fig. 5.8(a) shows the threshold current density vs. $S_t$ curves for the three-element array compared to a seven-element HC-PC array of same design. Edge-radiation loss is approximately inversely proportional to the number of elements, $N$, resulting in a decreased threshold value for

the in-phase mode, although the intermodal discrimination is also reduced [130]. Furthermore, the range of interelement widths over which sufficient intermodal discrimination is achieved is inversely proportional to $N-1$ [143], [144]. Thus, as the number of elements increases the process window for achieving single-mode operation diminishes. To improve on the poor intermodal discrimination of the seven-element array, a more optimized design was developed. The element widths were reduced from 12 µm to 8 µm, which significantly increases the edge radiation losses of the array modes as well as the in-phase mode's threshold current density. The increased edge losses also lead to improved intermodal discrimination. To reduce $J_{th}$ to a level comparable to the three-element array, the lateral separation between the element cores and interelement InGaAs layers ($S_t$ - $S$ in Fig. 5.1) was increased to 0.5 µm, which increases the $S_t$ value at resonance by the same amount. The thicknesses of the interelement layers were also adjusted, to reshape the mode in the interelement so that the field overlap $|\kappa|^2$ increases to 14.8%. In turn, this improves the discrimination while also increasing the threshold, due to higher coupling to the lossy interelement regions.
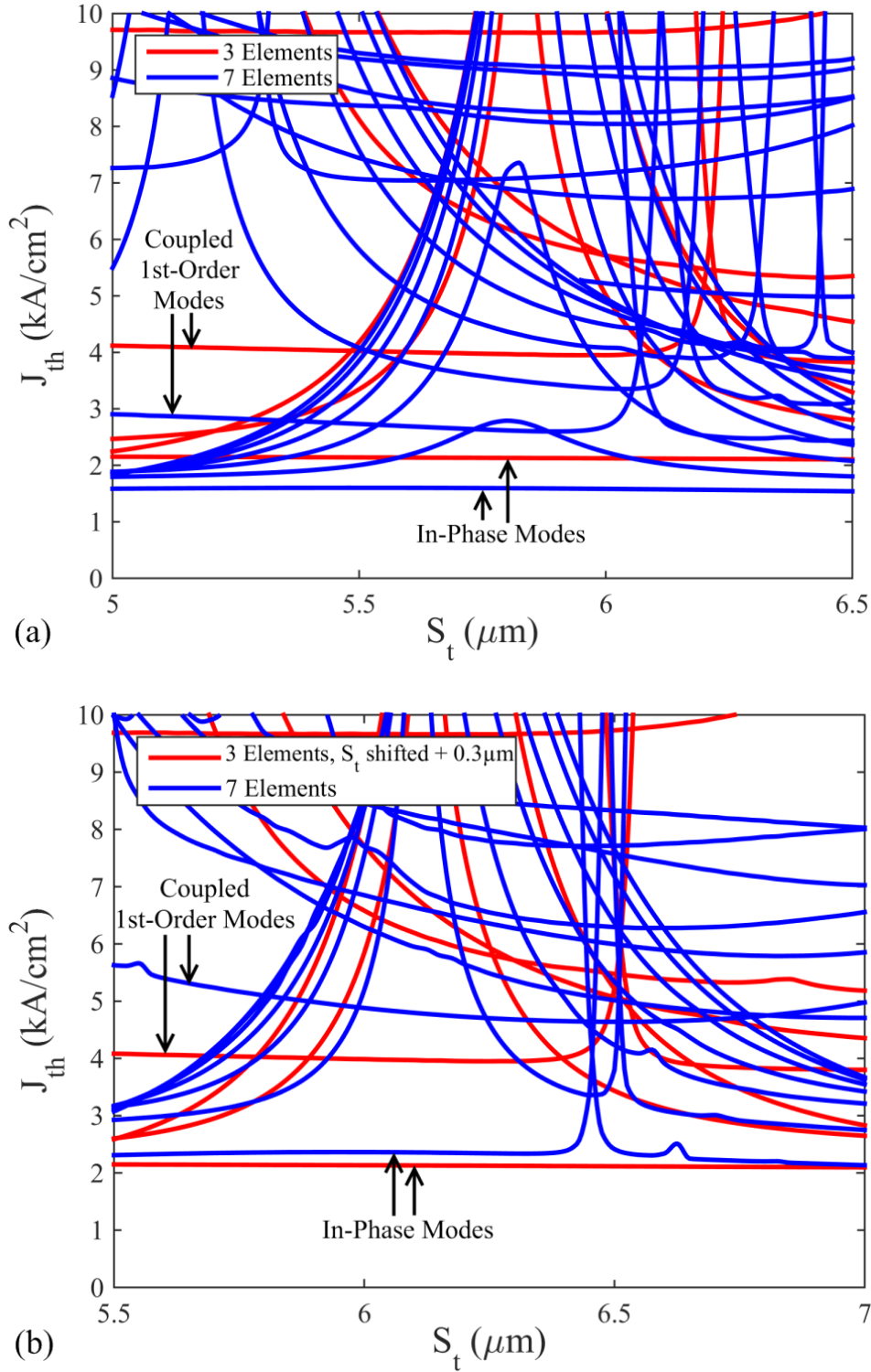
Fig. 5.8. Simulated threshold current densities for relevant modes supported by: (a) a seven-element HC-PC and three-element HC-PC of the same design; and (b) the three-element HC-PC and an optimized seven-element HC PC. The three-element curves have been shifted to higher $S_t$ values by 0.3 μm for ease of comparison. © 2015 IEEE

A comparison of $J_{th}$ vs. $S_t$ is shown in Fig. 5.8(b) between the optimized seven-element design and the three-element array design. It can be seen that the optimized design has significantly improved discrimination compared to the seven-element structure which uses the design optimized for three elements [Fig. 5.8(a)]. The new seven-element design has a 0.52 μm-wide range in trench width for 50% discrimination in $J_{th}$, a reduction of ~ 35% compared to the three-element structure. The seven-element structure has a slightly higher threshold of 2.36 kA/cm$^2$, an increase of 11% compared to the three-element structure. This is a key result, allowing us to scale from three to seven elements, and thus scale the coherent output power. Due to the narrower elements and wider interelements ($S_t$ at resonance is 6.2 μm), the seven-element array has less of the emitted intensity in the main lobe of the far-field beam pattern, at 53.5%. It was found that the same adjustments for a three-element array raised the in-phase-mode threshold without significantly improving discrimination.

ARROW terminations can be added to this seven-element design to lower the in-phase mode threshold further. For this larger array, we find that adding the standard-width reflectors actually decreases discrimination against the array mode composed of coupled first-order element modes. Fig. 5.9(a) displays the intensity profile for the lowest-loss such array mode, showing that there is little interelement field compared to that same array mode seen for the three-element ARROW structure. The widths of the interelement and element sections of the ARROW terminations can be tuned to shift the peak threshold value of the array mode composed of coupled first-order element modes, improving the peak intermodal discrimination. An example of this is shown in Fig. 5.9(b), where $S_{ref}$ was changed from 8.4 μm to 7.8 μm and $d_{ref}$ was changed from 4.0 μm to 3.3 μm at $S_t = 6.1$ μm ($S_{ref} - S_t$ was held constant in the simulation).
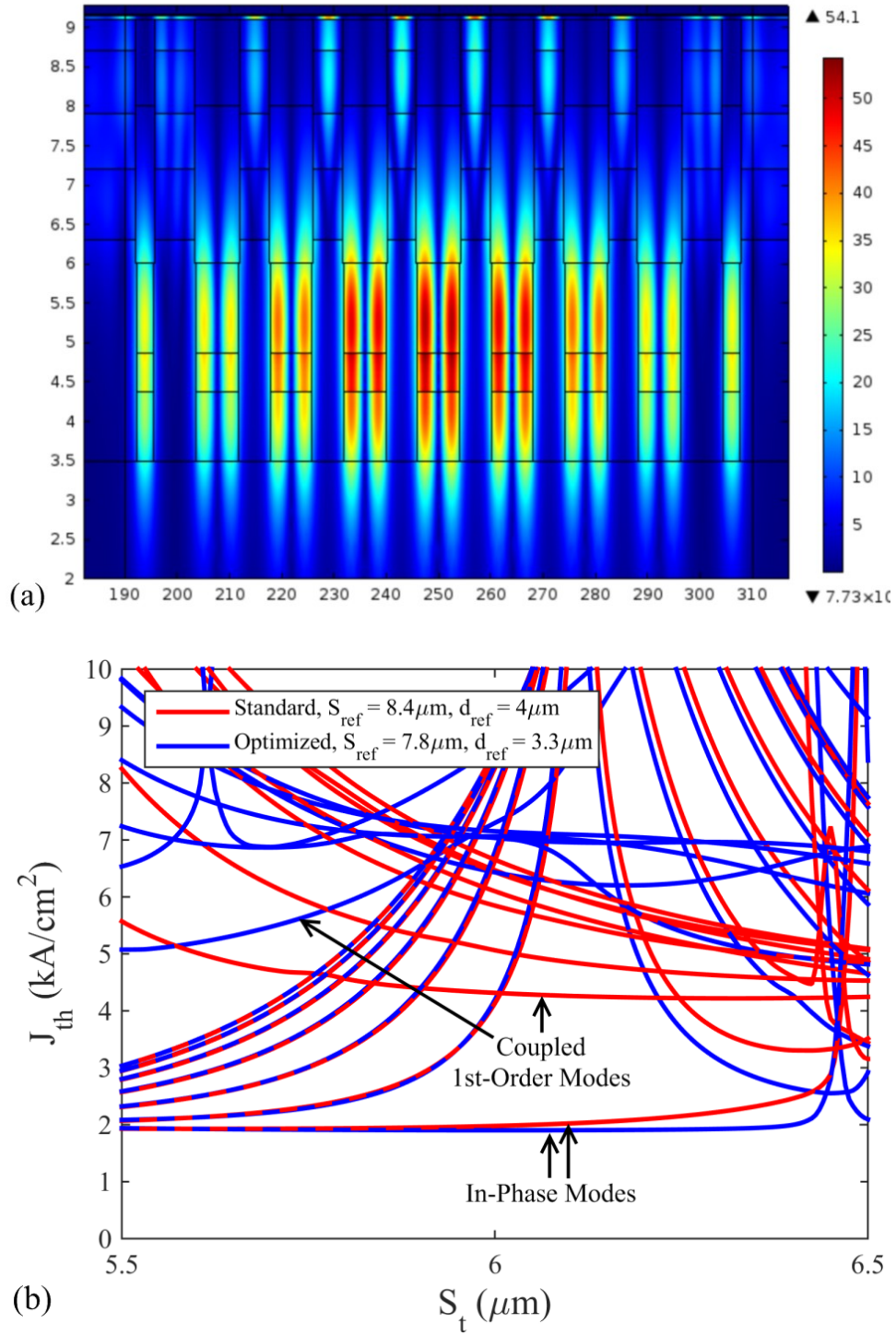
Fig. 5.9. (a) Intensity profile of the lowest-loss array mode composed of coupled first-order element modes of the seven-element ARROW array using standard width reflectors; (b) Simulated threshold current densities for modes supported by seven-element ARROW HC-PCs with standard-width reflectors and optimized-width reflectors. © 2015 IEEE

## 5.7    Results and Discussion – Thermal Lensing

The thermal and optical models in COMSOL were coupled together in order to analyze the effects of the thermally-induced index elevation across the array. Fig. 5.10 is a representative example of the effect that a thermally-induced index variation has on the $J_{th}$ vs. $S_t$ curves, as well as on the uniformity of the in-phase array mode. We characterize uniformity here by the ratio of the field intensity in the central element (integrated over the entire element) to the intensity in an element at the edge of the array. These simulations assume 10% wallplug efficiency with the other 90% being uniformly dissipated as heat in the core regions. We assume 3 W of output power, so that there is $P = 27$ W of thermal power being generated in the core regions. No additional changes were added to the threshold current density calculations to account for the temperature rise (e.g., $\alpha_w$ remained constant, etc.), in order to study only the effects of the elevated refractive indices on $J_{th}$. Projections indicate that the maximum wallplug efficiency of mid-IR QCLs is above 40% [23]. While these arrays suffer additional losses compared to a BH, increasing their wallplug efficiency similarly would dramatically reduce the dissipated power for the same output power, which would reduce the effects of thermal lensing that will be seen.
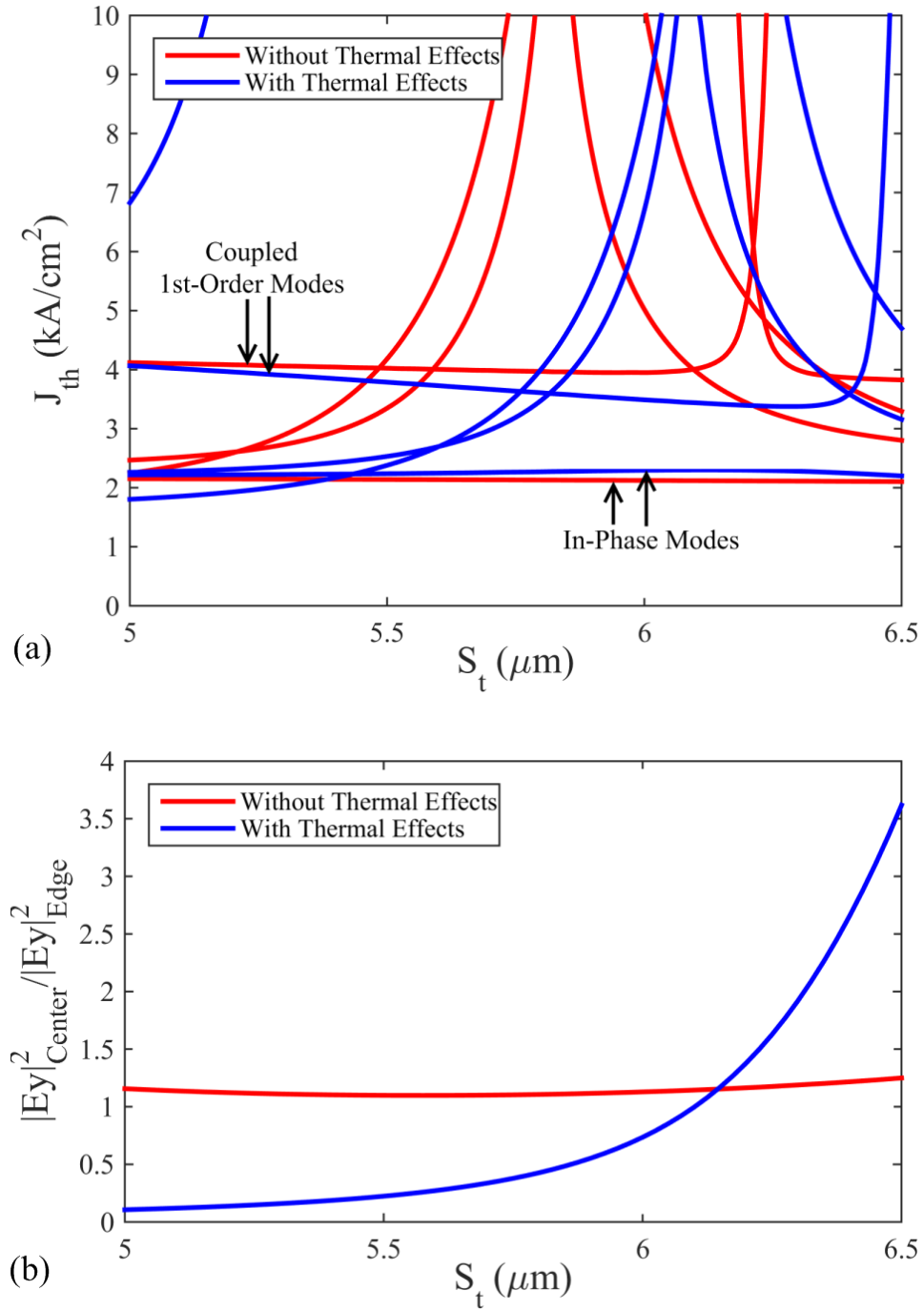
Fig. 5.10. (a) Simulated threshold current densities for modes supported by three-element HC-PCs, with and without thermal effects; (b) The in-phase mode uniformity, defined to be the ratio of the intensity in the central element to the intensity in an edge element, with and without thermal effects. © 2015 IEEE

As has been shown in the past from 1-D modeling [145], thermal lensing causes array modes to defocus at $S_t$ values below resonance and self-focus above resonance, and this is seen in Fig. 5.10(b). The major effects on $J_{th}$ in Fig. 5.10(a) are that the threshold of the array mode composed of coupled first-order element mode decreases, and the resonant value of $S_t$ shifts to wider trenches by about 0.2 μm. A possible explanation for the shift in $S_t$ is that the heating is stronger in the elements (since this is the origin of all of the thermal energy in the simulation), increasing the elements' indices more than the interelements', and hence decreasing the index step between them, which would shift the resonant interelement width to higher values (as the resonant interelement width is approximately inversely proportional to $\sqrt{\Delta n}$).

In addition to the benefits reported previously (lower in-phase mode threshold, absorption of coupled-first-order-mode array modes), adding ARROW terminations to this design improves the in-phase mode uniformity, as shown in Fig. 5.11, when thermal effects are included.
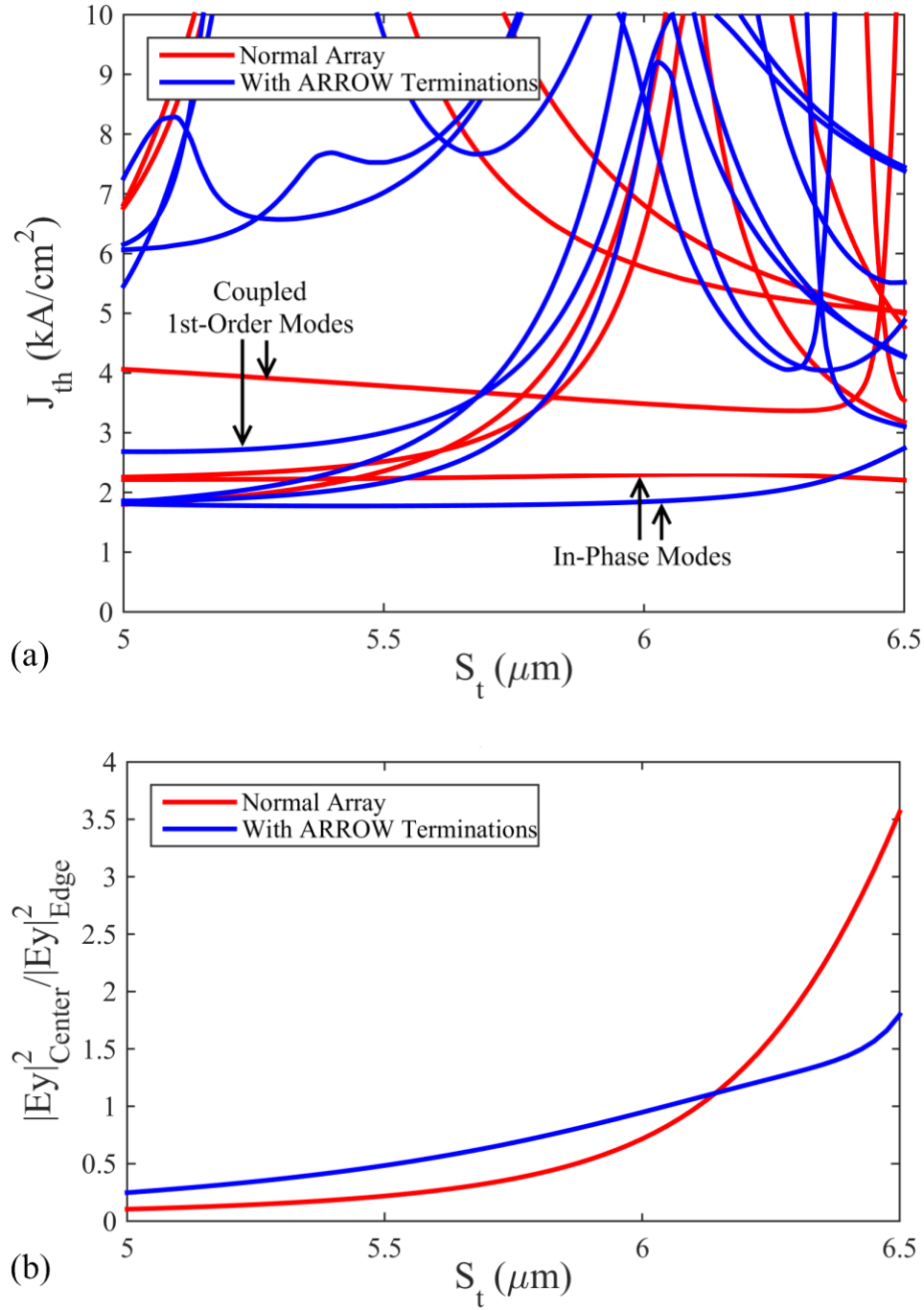
Fig. 5.11. (a) Simulated threshold current densities for modes supported by three-element HC-PCs under CW operation, with and without ARROW terminations; (b) The in-phase mode uniformity with and without ARROW terminations. © 2015 IEEE

Another method to reduce the thermal effects on in-phase mode uniformity is to increase

the field-overlap parameter between the elements and interelements. The effect of reducing the

transverse gap $G$ to 0 µm is shown in Fig. 5.12. The in-phase mode uniformity is improved, and

the discrimination is highly improved, but the in-phase mode threshold is higher as well.
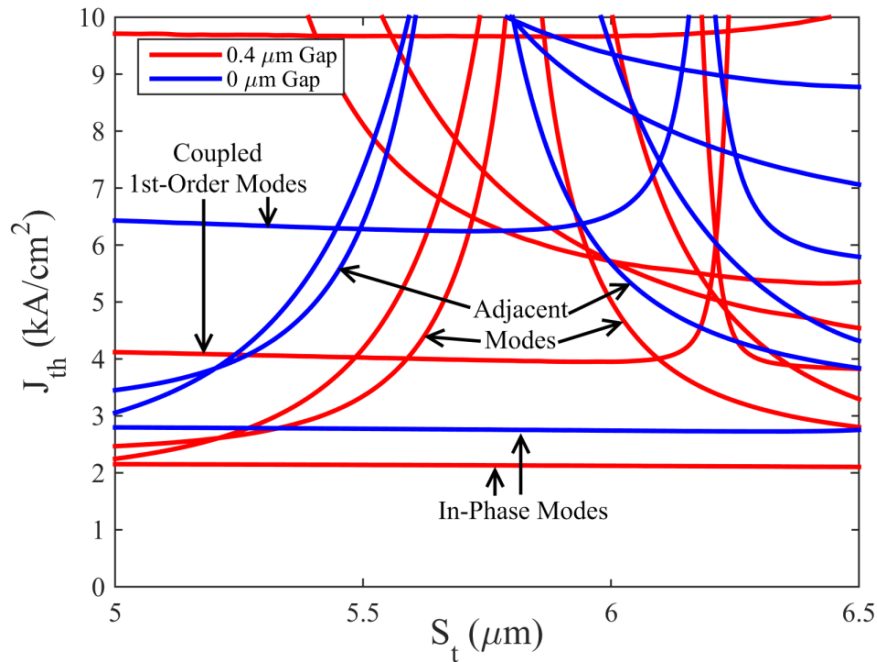


(a)



(b)
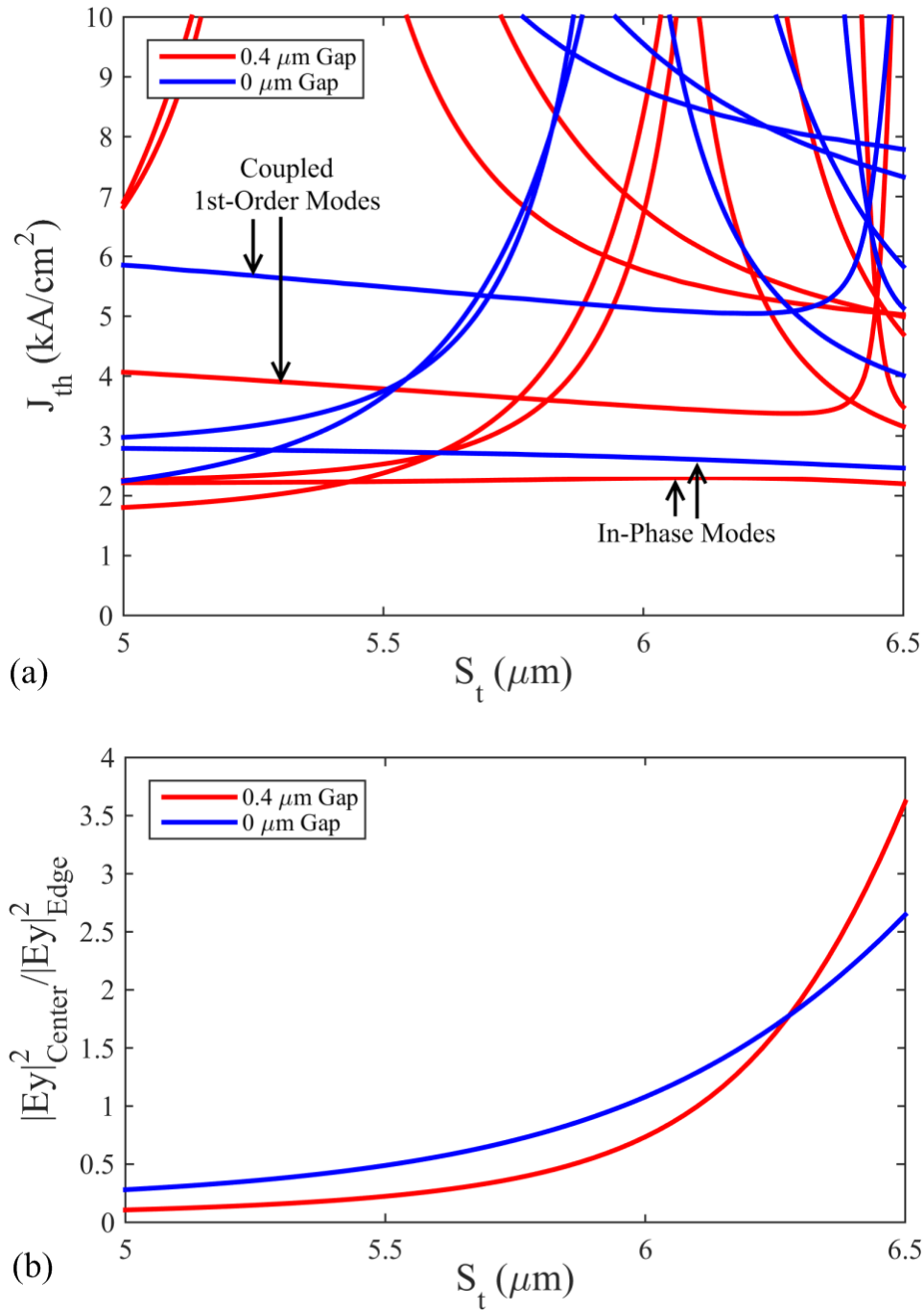
Fig. 5.12. (a) Simulated threshold current densities for modes supported by three-element HC-PCs under CW operation, with and without a transverse gap between the element and interelement; (b) The in-phase mode uniformity with and without a transverse gap between the element and interelement. © 2015 IEEE

Completely eliminating both lateral ($S_t$ - $S$) and transverse gaps also eliminates the thermally conductive InP regions between the core and InGaAs in the interelements, trapping thermal energy below the array, as shown in Fig. 5.13. However, the average (maximum, $\Delta T_{max}$) core temperature rise is 47.5 K (60.2 K) with the gaps and 48.2 K (61.4 K) without the gaps, a difference of only 0.7 K (1.2 K). These correspond to thermal conductance values $G_{th}$ = $J_{th}V_{th}/\Delta T_{max}$ = $P/(A\Delta T_{max})$ [73] of 415 W/cm$^2$·K and 407 W/cm$^2$·K, respectively, where $A$ = (3×12 µm)×(3 mm). The effect of the gaps on the temperature in the core regions is small, as most of the heat transfer from the core occurs through the InP cladding above it. When the transverse gap is reduced, the thickness of the upper cladding in the element is reduced as well in this design, improving conduction to the plated gold layer and offsetting the poorer conduction elsewhere. The design shown in Fig. 5.1, in which $S_t - S = 0$ µm, but there is a transverse gap $G$, can provide good discrimination, while allowing heat transfer between the core and interelement through conductive InP. Designs which leave the bottom core intact further trap heat beneath the array.
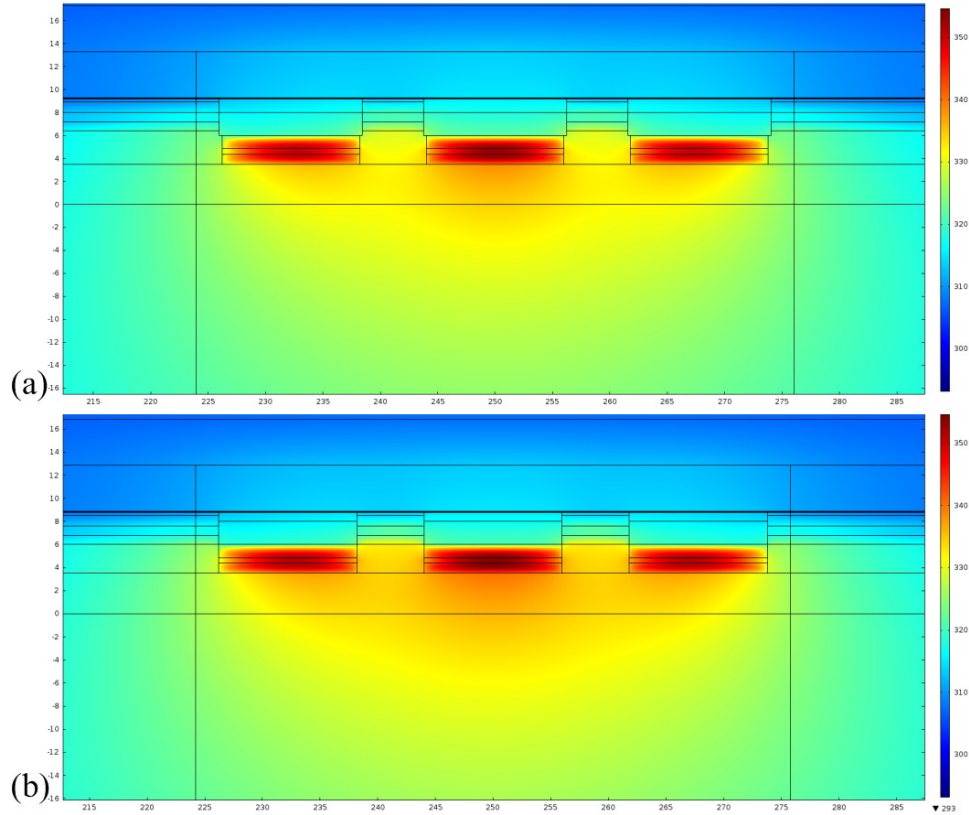
Fig. 5.13. Simulated temperature profiles for three-element HC-PCs under CW operation: (a) with and (b) without transverse and lateral gaps between elements and interelements. © 2015 IEEE

Further improvements in the transverse field-overlap parameter, beyond that possible by removing the transverse gap, are possible by re-designing the interelement regions. Fig. 5.14 shows a schematic of the new structure, which mimics that of the curved-layer HC-PC (discussed in the following chapter) while assuming a rectangular geometry in all regions for simplicity in modeling. The transverse-overlap parameter is 52.4% for this design. The lower core is not etched through in the interelements, which improves the overlap from 45.3% if both cores are etched through, though this does increase the thermal resistance of the device by ~ 0.1 K/W.
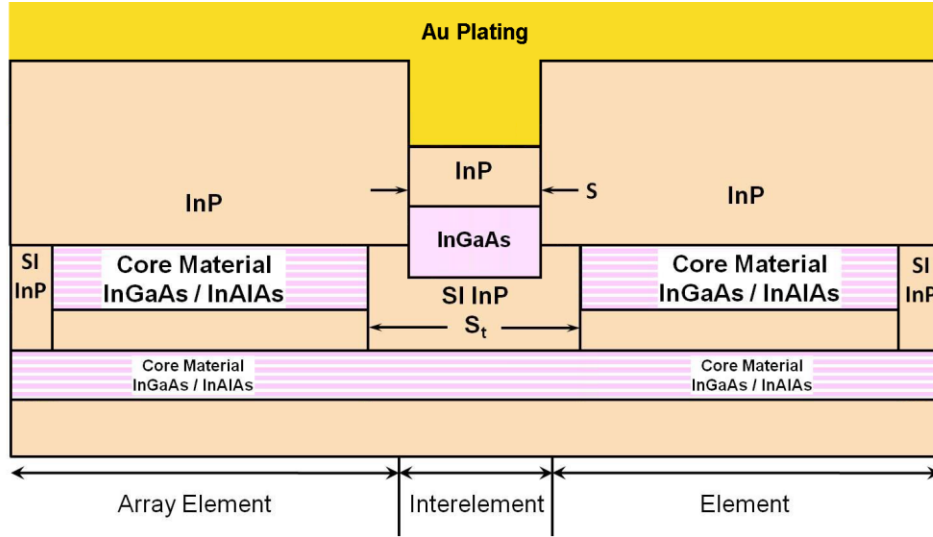
Fig. 5.14. Cross-sectional schematic of an HC-PC design with an overlap of 52.4%, found to have reduced effects from thermal lensing.

Fig. 5.15 shows the effect of thermal lensing on the in-phase mode's uniformity by improving the overlap from the 15.5% in Fig. 5.12(b) ($G = 0$ μm) to this new design's 52.4%. This higher-overlap design has its resonance at $S_t \sim 4.9$ μm in pulsed operation and has an index step of 0.073. As the resonance point is different between the two designs, the x-axis in Fig. 5.15 was shifted to center the axis at the point at which the in-phase mode is uniform for both designs, for clarity. While in both cases, there is a point near resonance where the field is uniform, the new design would allow an HC-PC with a slightly off-resonance interelement width to have a more uniform near field.
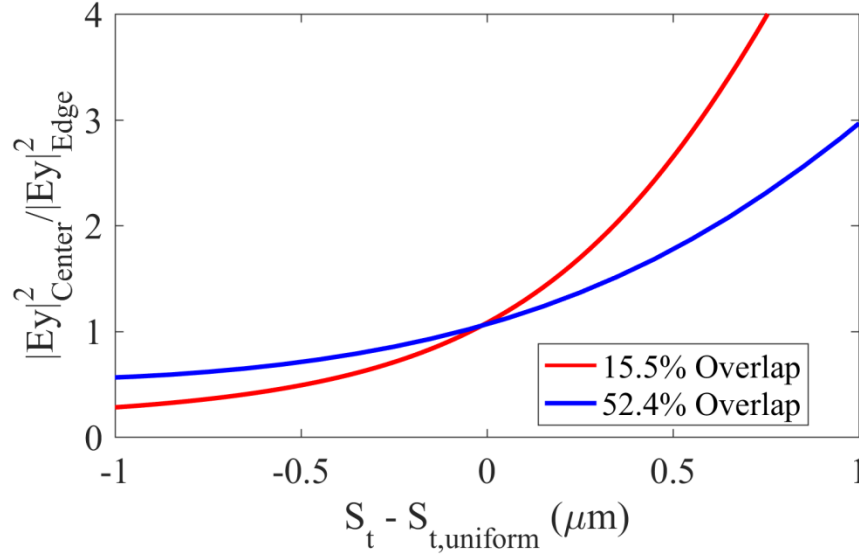
Fig. 5.15. Simulated in-phase mode uniformity, with thermal effects, for designs with a transverse overlap of 15.5% (from Fig. 5.12(b), $G = 0$ μm) and 51.4%. The x-axis was shifted for clarity. $S_{t,uniform}$ is the value of $S_t$ at which the in-phase mode is perfectly uniform for each design.

## 5.8    Element Chirping

While improving the field-overlap parameter, $|\kappa|^2$, does reduce the non-uniformity caused by thermal lensing, we have developed another approach to produce a uniform near-field during CW operation. Because the temperature profile is nonuniform, with the central element of the HC-PC having a larger temperature rise, the refractive index of this element is elevated to a higher value than the edge elements (on the order of $4 \times 10^{-4}$ for a 3 mm-long device with 27 W of dissipated power). The lateral wavelength, $\lambda_0$, of the mode within an element is:

$$\lambda_0 = \lambda / \sqrt{n_2^2 - n_{eff}^2} \qquad (5.1)$$

where $n_2$ is the transverse effective index of the element region. So, while the built-in index step, $\Delta n$, between the element and interelement regions may be large, it is the difference between the effective index of the mode and of the element region which affects the propagation within the elements. This difference is approximately $5 \times 10^{-3}$, an order of magnitude smaller than the built-

in index step for these HC-PCs (hence why the approximation $n_{eff} \approx n_2$ was made in Ch. 4). Thus, the small relative increase in the element's effective index $n_2$ due to the elevated temperature make the central element appear wider optically, compared to the lateral wavelength, than the outer elements. Thus, to keep all elements at the same optical width of $d \sim \lambda_0/2$, the width of the central element can be reduced since $\lambda_0$ is shorter for that element in CW operation. Fig. 5.16 shows a comparison of the in-phase mode uniformity for two HC-PC designs: (a) one in which all three elements have the same width of 12.0 μm, and (b) one in which the central element's width has been reduced to 11.5 μm. While the 'chirped' design in (b) has a non-uniform field profile in pulse operation (without heating), it would have a significantly more uniform mode profile in CW operation regardless of interelement width. Thus, this chirping must be designed for a specific operating condition for a given device. At resonance, the near field profile is fairly uniform regardless of chirping, but for slightly non-resonant devices this chirping could improve the uniformity in CW operation. The HC-PC design used in Fig. 5.16 is different from that in previous figures in this chapter, so the behavior is not exactly the same. The interelement trench width, $S_t$, at resonance for this design is 4.8 μm without heating and ~5.0-5.1 μm with 27 W of dissipated power, for both chirped or unchirped designs. This element chirping does not have a significant impact on the threshold current densities of the modes.
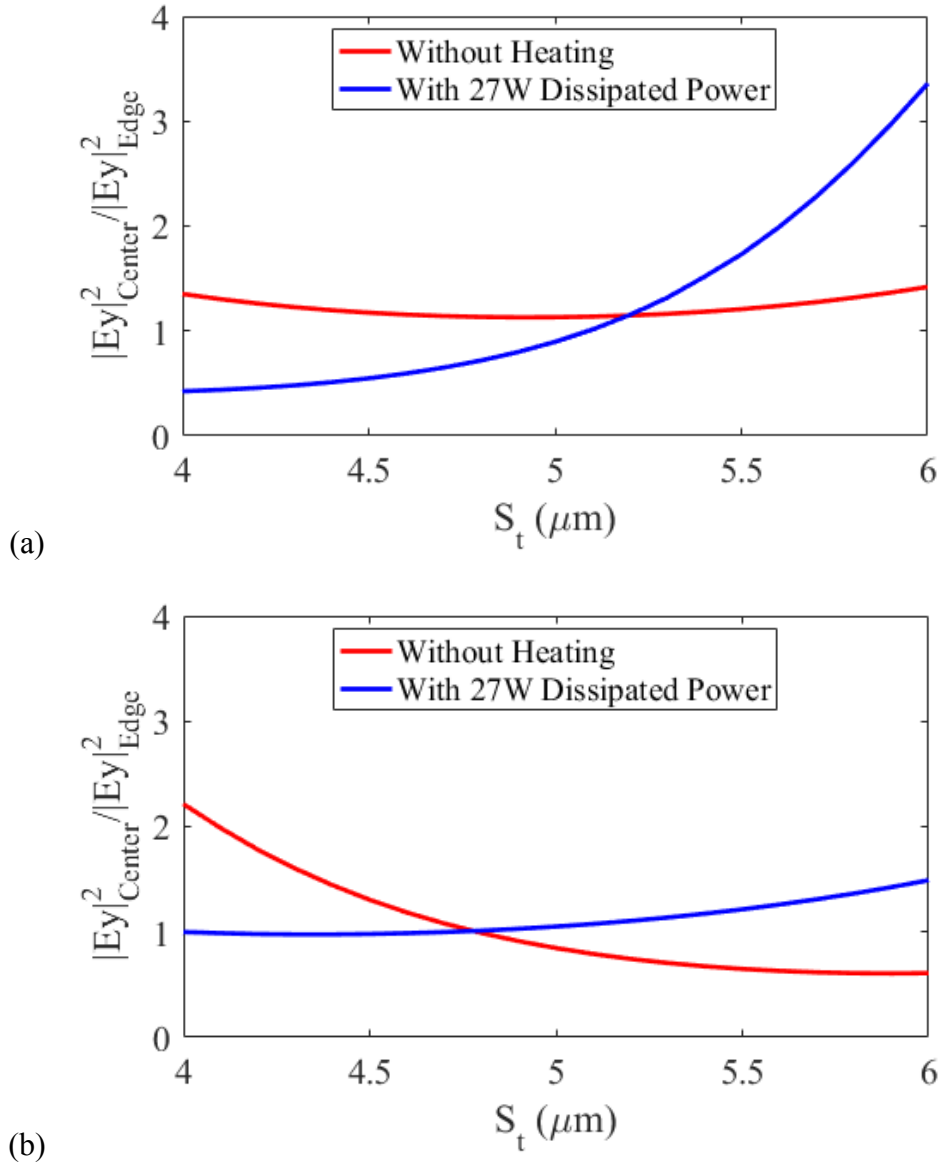
Fig. 5.16. Simulated in-phase mode uniformity as a function of interelement width, $S_t$, with and without 27 W of dissipated power, of: (a) a design with all elements of width 12.0 µm; and (b) a design with central element of width 11.5 µm and outer elements of width 12.0 µm.

We find this method is effective for 5-element arrays as well, where a width of 11.0 µm for the central element and a width of 11.15 µm for the two adjacent elements gives a more uniform profile in CW operation than even the unchirped HC-PC has in pulsed operation. For quasi-CW operation, the amount of chirping required is reduced due to the reduced heating. We

also investigated the effect of widening the central element, and found that it has the reverse effect on uniformity, resulting in highly non-uniform profiles in both pulsed and CW operation.

## 5.9    Conclusions

In conclusion, the optical and thermal characteristics of planarized phase-locked HC-PC QCL arrays were theoretically investigated. Large aperture, seven-element designs have been established with a reasonably large process window for achieving single in-phase array-mode operation. Such devices have potential to produce coherent single (in-phase) mode operation to multi-watt range CW output powers. ARROW terminations were found to decrease the in-phase array-mode threshold current density, improve discrimination against array modes composed of coupled first-order element modes, and improve near-field uniformity of three-element arrays under CW operation. In addition, the widths of the ARROW terminations can be tuned to improve the peak intermodal discrimination of seven-element arrays.

Full-wave optical HC-PC simulations have been coupled with two-dimensional heat flow analysis to investigate, for the first time, the influence of thermal lensing on modal behavior. It was found that the thermally-induced index elevation shifts the resonant interelement width to higher values, increases the in-phase-mode threshold current density, decreases the coupled first-order mode threshold, and causes focusing and defocusing of the in-phase mode around resonance. Improved coupling between the element and interelement regions can improve discrimination and reduce the focusing effects in CW operation. Improving the wallplug efficiency of the device would significantly reduce the heating, and hence thermal lensing, experienced for the same output power. Element chirping, in which the inner elements of the array are narrowed slightly, can also combat the effect of thermal lensing. In combination with single-lobe-emitting, $2^{nd}$-order metal/semiconductor gratings [33] placed in the element regions,

such arrays hold the potential to provide high coherent surface-emitted powers from 2-D high-contrast photonic crystal lasers [35].

# Chapter 6 – Demonstration of Near-Resonant Leaky-Wave-Coupled Phase-Locked Arrays of Mid-Infrared Quantum Cascade Lasers

## 6.1 Introduction

This chapter reports on the properties of *near-resonant* leaky-wave coupled quantum cascade lasers (QCLs) emitting at 4.7 μm, which operate with up to 3.6 W peak pulsed power with a near-diffraction-limited (D.L.) beam pattern with the center lobe's full-width at half-maximum (FWHM) ≤ 1.7 × the simulated FWHM of the in-phase mode (this will be the comparison used throughout the chapter for giving a reference point for the beam pattern). Design simulation studies accurately predict the array geometry required for obtaining in-phase-mode operation, which is in good agreement with the experimental results. Then, in Section 6.6, we analyze the spectrally-resolved modal properties of these devices. We show that non-resonant devices can be significantly impacted by a large spectral bandwidth, leading to multi-mode operation at increasing drive currents. Further optimized, resonantly-coupled designs can be used to minimize the impact of the large spectral emission bandwidth and allow for single lateral array-mode operation to high drive levels. This work has been published in [29] and [30]. These devices hold the potential for reaching > 10 W near-diffraction-limited output powers by scaling the number of array elements.

## 6.2 Phase-Locked HC-PC QCL Array Structure

A schematic cross-sectional view of the fabricated high-index-contrast photonic crystal (HC-PC) structure is shown in Fig. 6.1 (two elements are shown), with an interelement region width that can be adjusted to target the resonant-coupling condition. Also shown in red are the transverse electric field intensity profiles of the transverse modes at the center of the interelement and element regions.
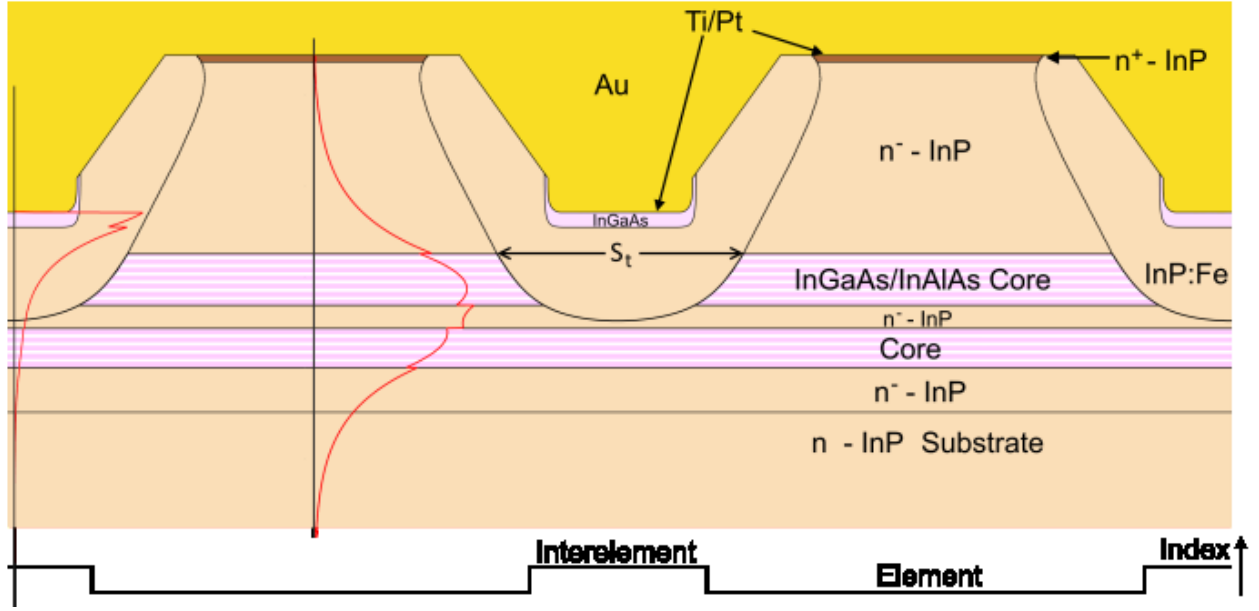
Fig. 6.1. Schematic representation of the cross-sectional view of HC-PC QCL structure under study.

We quantify the interelement width by the width of the trench at the top of the upper core region, which we call $S_t$, as shown in Fig. 6.1. In the center of the core region an InP-spacer layer is placed, which acts both as a lateral heat remover [74] as well as the base layer for the regrowth of the interelement regions. The structure design optimization approach for achieving single-mode operation has been addressed previously in Ch. 5 and [28]. The interelement regions have $In_{0.53}Ga_{0.47}As$ layers and lowered Ti/Pt/Au regions that create a higher effective refractive index than in the element regions, as well as strong interelement losses due to surface plasmon coupling to the metal (as schematically shown in Fig. 6.1). As a result, an array of antiguides of large index step ($\Delta n > 0.05$) is formed, which can be designed to strongly favor in-phase array-mode operation. In principle, resonant leaky-wave coupling occurs when the interelement regions' width is equal to an integer multiple of half the laterally projected wavelength, $\lambda_1 = \lambda/\sqrt{n_1^2 - n_{eff}^2}$, in the lateral direction [26], [27], [97], where $\lambda$ is the wavelength, $n_1$ is the

transverse effective index in the interelement region, and $n_{eff}$ is the array mode's effective index. However, this condition on the interelement width is exact only in the effective-index approximation, since for actual 2-D waveguide structures the resonance point is shifted due to significantly low overlap between the fields of the fundamental transverse modes in the element and interelement regions [97], [142], as was discussed in Ch. 5. Thus, full-wave modeling, such as using COMSOL Multiphysics, is necessary to analyze the array structure to find the actual resonance condition where the photonic bandgap is zero [31]. In practice, resonance is achieved either by fixing the interelement width and adjusting the regrown layer thicknesses in order to vary the lateral index step, or by introducing a variation in interelement width on the photomask, as was done in this work where we present results from two arrays of different interelement widths. Here, the desired resonant mode is composed of fundamental element modes coupled in-phase and with an interelement spacing $S_t \sim \lambda_1/2$ [97]. As discussed below, for the devices described here, the resonance condition was not met as a result of too large an interelement spacing. Generally, an iterative fabrication process is used to experimentally achieve resonant devices.

A 35-stage core region with a 0.5 μm-thick InP spacer layer was grown by metalorganic chemical vapor deposition (MOCVD) using a core region structure similar to that of state-of-the-art 4.6-4.7 μm-emitting QCLs [146]. Low-doped ($2 \times 10^{16}$ cm$^{-3}$) 2 μm-thick cladding layers were grown around the core region. An additional 2 μm of higher-doped InP is grown to complete the upper cladding layer. Wet and dry (ECR) chemical etching were used to make deep trenches that stopped within the InP-spacer layer, with a period of ~17 μm, with variations in the trench width on the photomask for each device. InP:Fe and $In_{0.53}Ga_{0.47}As$ layers were then preferentially regrown by MOCVD in the trenches by using the SiN$_x$ mask employed for trench etching. After

regrowth of the interelement regions, a $SiN_x$ film was placed, for current confinement, ~5 μm away from the array edges. Then, a two-step metallization process was carried out: 1) Ti (5 nm)/Pt (5 nm)/Au (200 nm) films were evaporated to provide interelement loss; and 2) a Ti(10nm)/Pt(25nm)/Au(200nm) metal contact is overlaid for wire bonding. After thinning of the wafer and backside metallization, 3 mm-long, high-reflectivity (HR)-coated chips were tested under pulsed operation in the epi-side up configuration. Note that we did not employ top-side Au plating on these devices, which will be utilized in the future to improve surface planarity for epi-side down mounting, nor did we attempt CW operation for these devices.

MOCVD-regrowth studies have indicated that the regrowth of the interelement regions at relatively high temperature (675 $^o$C) results in improved surface morphology and controllable thickness for the layers within the interelement regions. Cross-sectional scanning electron microscope images of the fabricated arrays are shown in Fig. 6.2.
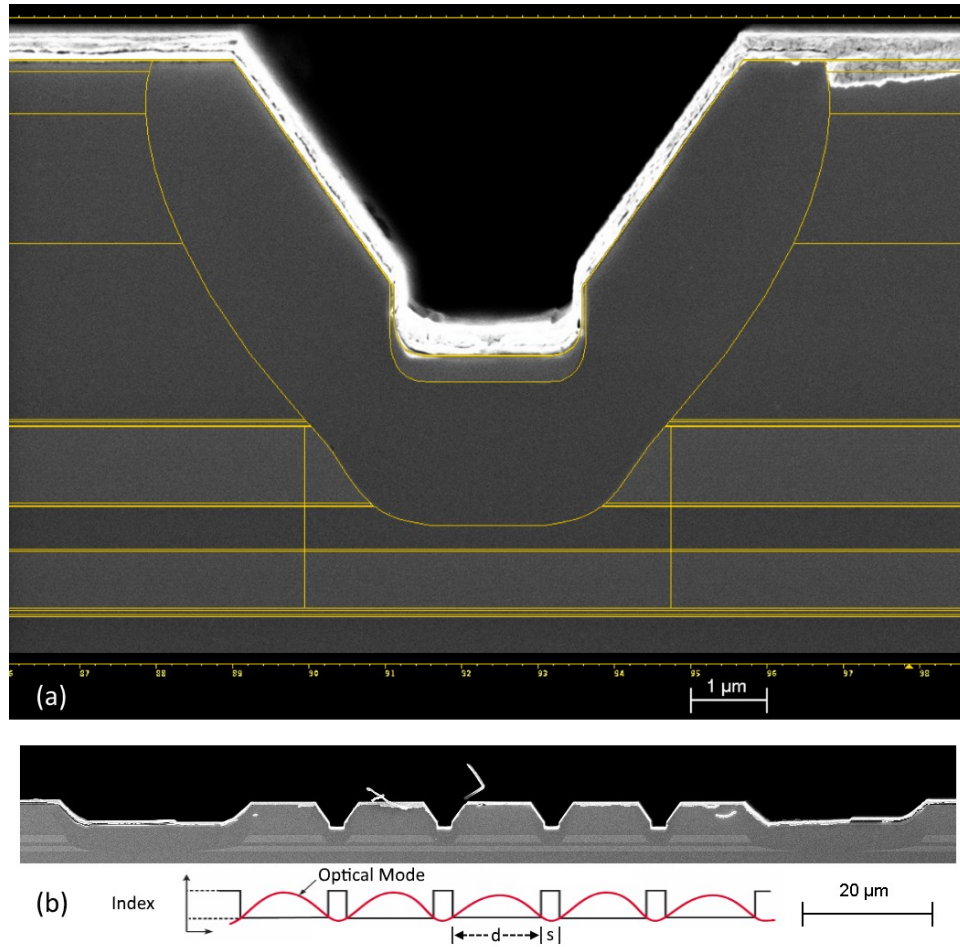
Fig. 6.2. SEM images of the fabricated 5-element array; (a) interelement region overlaid with COMSOL simulation profile, (b) complete 5-element device, with a schematic of the effective index structure and in-phase mode profile. © 2017 IEEE

## 6.3  Experimental Device Results

Fig. 6.3 shows the light-current (L-I) curves of two 5-element arrays of different interelement width, in pulsed operation (200 ns-wide pulses, 20 kHz rep. rate). The threshold currents are as low as 4.55 A, which corresponds to a threshold current density $J_{th}$ value of ~ 1.67 kA/cm$^2$ in the lower core when considering current spreading under the interelement regions and 5 μm into the lower core's corners at the array edges. For the structure lasing in a near-diffraction-limited beam pattern the threshold current is ~ 5.3 A; that is, significantly lower

than for previously published ($I_{th} \sim 10.4$ A)  8.4 µm-emitting, leaky-wave coupled arrays of near-diffraction-limited beam patterns [132].
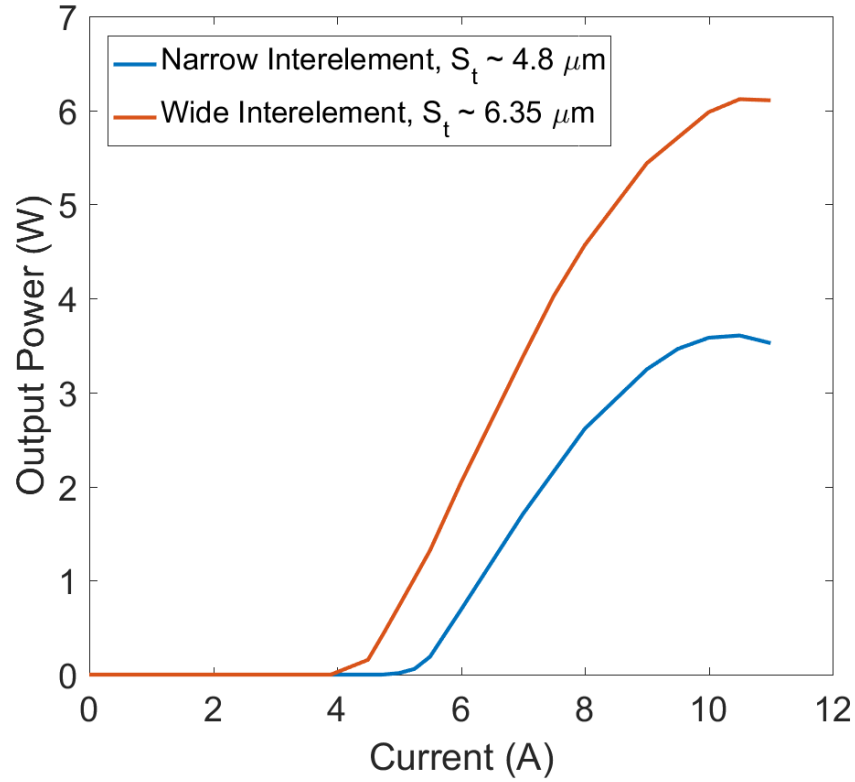


Fig. 6.3. Measured L-I characteristics under pulsed operation (200 ns-long pulses, 20 kHz repetition rate) for two arrays with different interelement spacings. © 2017 IEEE

The measured spectra for one device ($S_t \sim 4.8$ µm) are shown in Fig. 6.4 under different drive currents. The spectral characteristics were measured using a Fourier transform infrared (FTIR) spectrometer with a thermoelectric cooler (TEC)-cooled deuterated triglycine sulfate (DTGS) detector.
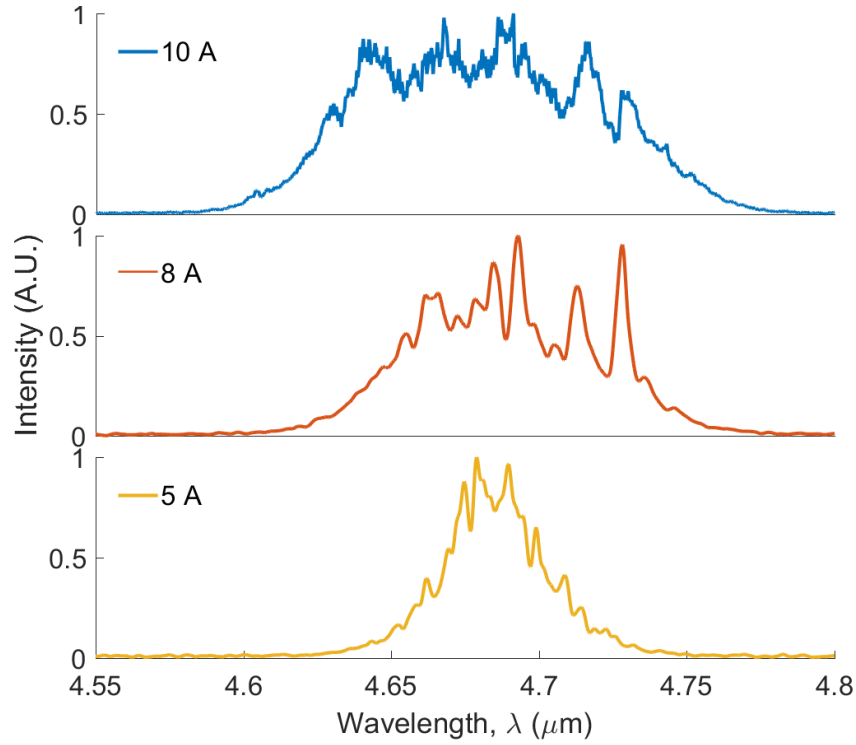
Fig. 6.4. Measured spectrum under different drive currents for the array with narrow interelement spacing (4.8 μm). © 2017 IEEE

To measure the far-field beam patterns of the devices including the full spectral band, the device is placed on a rotational stage centered at the output facet, 40 cm away from a liquid nitrogen-cooled InSb detector with a 25 μm-wide vertical slit placed in front of it, giving each individual measurement an angular resolution of 0.007°. 200 ns-long current pulses with a repetition rate of 20 kHz are used and a boxcar integrator converts the power pulse into a single data point. The rotational mount is rotated and a data point is taken approximately every 0.25°. The emitted far-field beam patterns (Fig. 6.5 and Fig. 6.6) for both devices (of Fig. 6.3) indicate operation near threshold in the in-phase array mode. The beams broaden at higher drive currents due to the onset of adjacent modes reaching threshold [97], [127]. For the device of smaller interelement width ($S_t \sim 4.8$ μm), the central lobe FWHM is 1.7 × D.L. at 3.6 W output power, for the ~80 μm-wide aperture, that is, near-diffraction-limited operation to a drive level of 1.9 ×

threshold (Fig. 6.6). For the device of larger interelement width ($S_t \sim 6.35$ µm), the beam broadens more with increasing current (Fig. 6.5), indicating that above threshold lasing occurs in a much larger mixture of additional array modes up to 6.1 W front-facet emitted power, with a lobewidth $\sim 3.5 \times$ D.L.
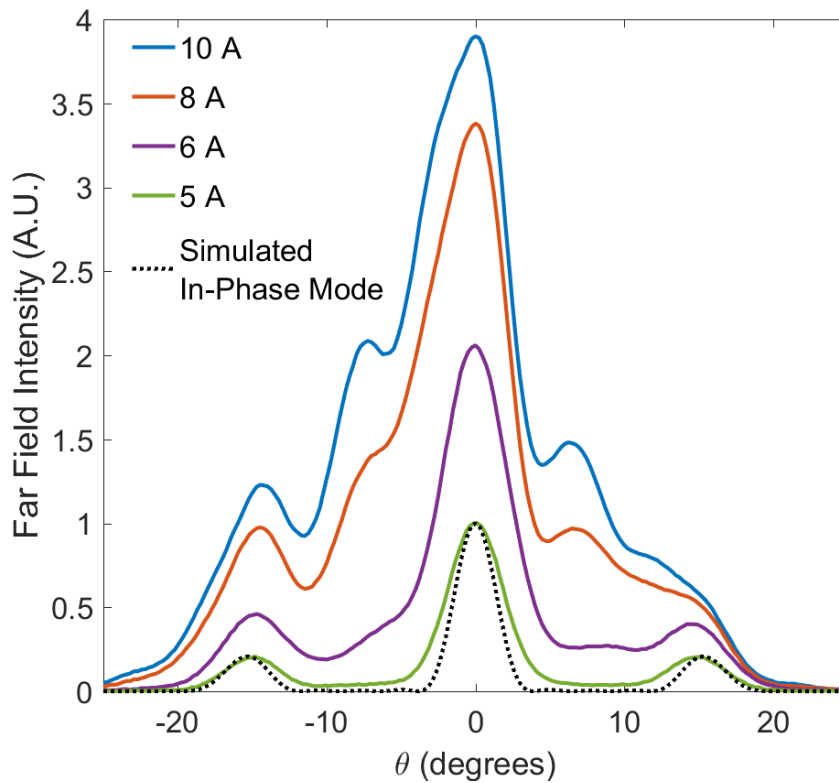


Fig. 6.5. Measured (upper) and simulated (lowest) lateral far-field patterns for the HC-PC device with an interelement width of 6.35 µm. © 2017 IEEE
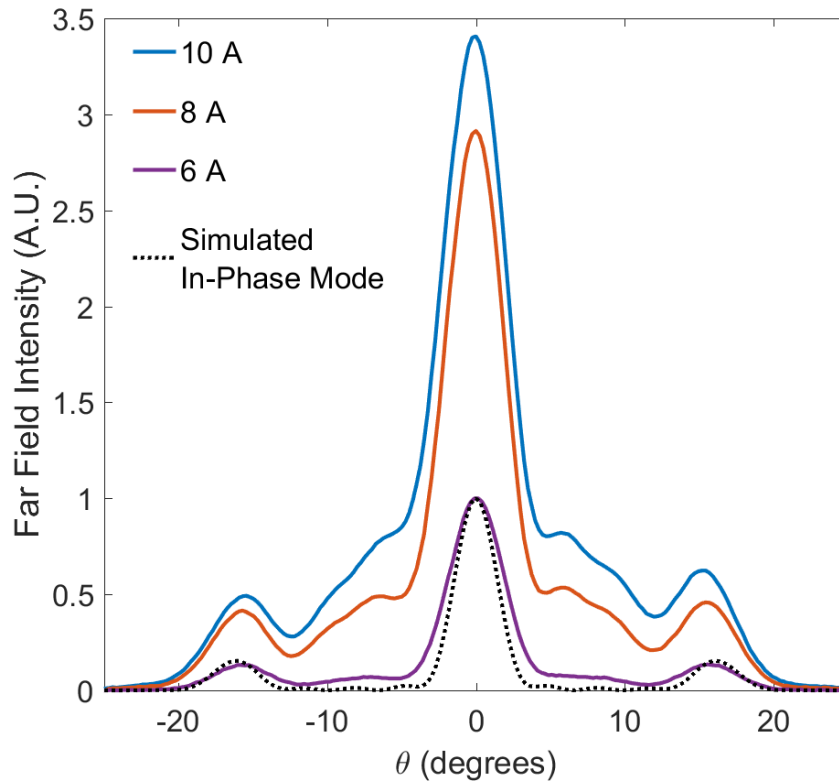
Fig. 6.6. Measured (upper) and simulated (lowest) lateral far-field patterns for the HC-PC device with an interelement width of 4.8 μm. © 2017 IEEE

It has been found that testing these devices at a repetition rate of 5 kHz with a 100 ns-long pulse improves their performance. In this case, the maximum output powers are 5.4 W and 7.6 W, as shown in Fig. 6.7, compared to 3.6 W and 6.1 W, respectively, for the original higher duty cycle testing conditions. This improvement is attributed to heating during the pulse, as measurements using a mercury cadmium telluride (MCT) detector showed significant drop in power throughout the pulse at high drive. A less temperature-sensitive core region design and improved current confinement to the elements should improve this drop in power. Far-field beam profile measurements found no significant difference in the beam pattern using different pulse operating conditions. Thus, when operating with a 100 ns-long pulse and 5 kHz repetition rate,

the device with narrower interelements ($S_t \sim 4.8$ µm) emitted a beam with FWHM of $1.7 \times$ D.L. at ~5.1 W peak pulsed output power.
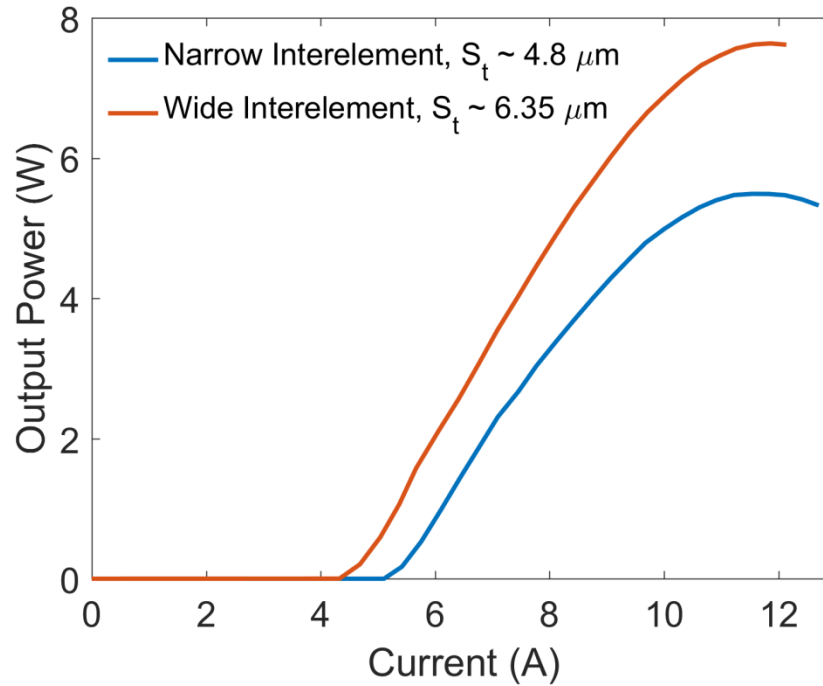


Fig. 6.7. Measured L-I characteristics under pulsed operation (100 ns-long pulses, 5 kHz repetition rate) for the two arrays shown in Fig. 6.3.

15 µm-wide, 3 mm-long ridge waveguides with HR-coated back facets and uncoated front facets were fabricated from the same base QCL material. They have a pulsed slope efficiency of 2.5 W/A, compared to 1.0-1.4 W/A for the HC-PC devices, and a peak pulsed wallplug efficiency of 6.3%, compared to 1.6-2.8% for the HC-PC devices. The reduction in power for the HC-PC lasers is attributed to additional losses from the array structure, as well as to unused gain in the lower core portions of the interelement regions.

## 6.4    Simulation Studies: Correlation to Experiment

Design studies of the 5-element array structures were carried out using COMSOL to find the expected threshold currents and fabrication tolerances for a given design. Threshold current

$I_{th}$ vs. interelement trench width $S_t$ curves for modes of a 5-element, 4.7 μm-emitting array, with regrown layers, that take into account the regrown layers' curvatures, as shown in Fig. 6.2(a), have been calculated.

In order to account for the non-uniform current distribution in the core regions of these devices, a COMSOL electrical model was employed which uniformly spreads the current in the active core regions while blocking all current flow in the regrown InP:Fe interelement regions. This assumption of current spreading is supported by thermoreflectance imaging, in which the temperature profile at the facet of a device is probed by measuring a change in reflectivity due to changes in temperature [147]. The temperature rise, $\Delta T$, which is proportional to the relative change in reflectivity, $\Delta R/R$, is shown in Fig. 6.8 for one 2 mm-long array driven at a current of 4.2 A, pulse width of 35 μs, and 3% duty cycle. This measurement was performed by collaborators. Since the temperature rise is expected to be higher in the areas in which power is dissipated, this method highlights the regions in which current is flowing. The higher reflectivity in the upper core and relatively uniform reflectivity change in the lower core indicates that the current must be spreading in the lower core. This is expected to raise the threshold current of the device as well as reduce output power by causing different stages of the core to be operating at different current densities and electric fields.
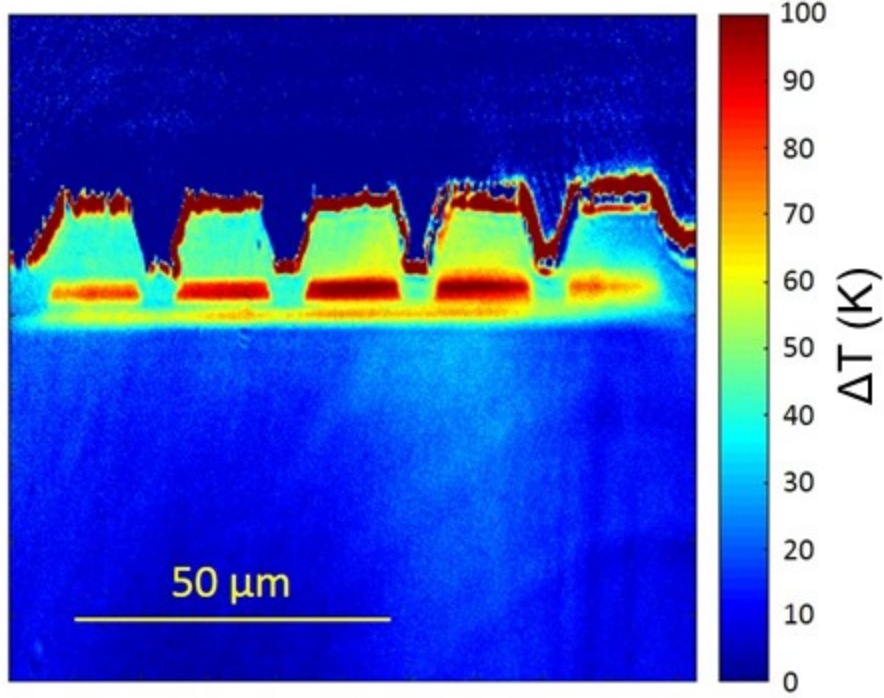
Fig. 6.8. Thermoreflectance image of a five-element HC-PC at a current of 4.2 A, with the reelative reflectivity change, $\Delta R/R$, converted to a temperature change, $\Delta T$, using a calibration coefficient of $C_{th} = 10^{-4}$ K$^{-1}$.

An example of the resulting current distribution in the COMSOL model is shown in Fig. 6.9. We do not expect that the current actually perfectly spreads and produces gain uniformly laterally across the core regions, or that the InP:Fe perfectly blocks current flow, but this model gives a first approximation of the current and gain distribution. Then, in order to calculate the modal gain for a given mode $L$, ($g_{modal,L}$), we assume the local gain, $g_{local}$, is proportional to the transverse component of the local current density, $J_y(x,y)$: $g_{local} = J_y g$, where $g$ is the differential gain coefficient, which we took to be equal to 6.8 cm/kA [138]. Thus, this model ignores the effects of any other modes already lasing (i.e., gain spatial-hole burning).
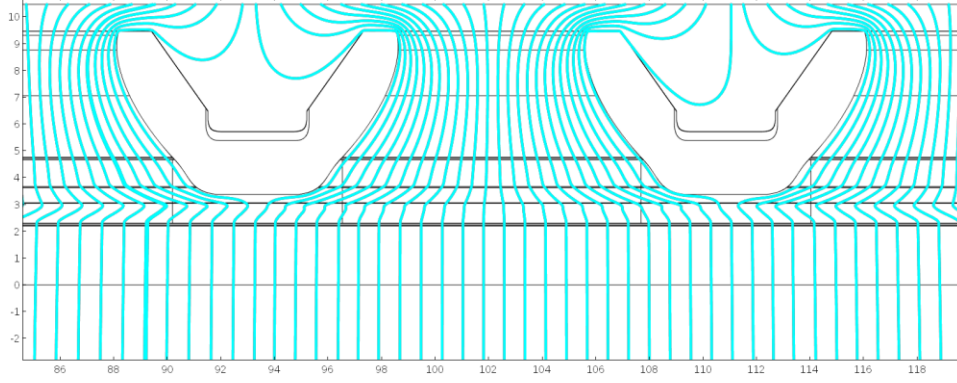
Fig. 6.9. COMSOL-simulated current distribution, showing element and interelement (blocking) regions at the center of a five-element array. © 2017 IEEE

The modal gain for array mode $L$ is then equal to the overlap of its intensity with the gain distribution:

$$g_{modal,L} = \frac{\iint_{Core} g_{local}(x,y)|E_{y,L}(x,y)|^2 dxdy}{\iint_{Array}|E_L(x,y)|^2 dxdy}$$

$$= \frac{\iint_{Core} J_y(x,y)g|E_{y,L}(x,y)|^2 dxdy}{\iint_{Array}|E_L(x,y)|^2 dxdy}. \qquad (6.1)$$

An input current, $I_0$, is assumed in the electrical model, which produces a current-density distribution $J_{0,y}(x,y)$, which is directly proportional to $I_0$. Thus, the current distribution at threshold, for a given mode $L$, is equal to

$$J_{y,th,L}(x,y) = \frac{I_{th,L}}{I_0} J_{y,0}(x,y). \qquad (6.2)$$

At threshold for a given mode $L$, the modal gain must be equal to the total losses:

$$g_{modal,th,L} = \alpha_m + \alpha_{array,L} + \alpha_{bf} \qquad (6.3)$$

where $\alpha_m = \frac{1}{2L_c}\ln\frac{1}{R_1 R_2}$ is the mirror loss, assuming an HR-uncoated device of cavity length $L_c =$ 3 mm and facet reflectivities $R_1 = 0.94$ and $R_2 = 0.24$; $\alpha_{array,L}$ is the modal array loss calculated from COMSOL and includes edge radiation loss and absorption loss; and $\alpha_{bf}$ is the effective loss due to backfilling or electron leakage [56], taken to be 2.8 cm$^{-1}$.

Combining (6.1)-(6.3) gives:

$$I_{th,L} = \frac{\alpha_m + \alpha_{array,L} + \alpha_{bf}}{g} \frac{\iint_{Array} |E_L(x,y)|^2 dxdy}{\iint_{Core} J_{y,0}(x,y)|E_{y,L}(x,y)|^2 dxdy} I_0. \tag{6.4}$$

Fig. 6.10(a) shows the resulting simulated threshold current as a function of interelement trench width, $S_t$, for the competing array modes (high threshold modes have been removed for clarity), using the geometry shown in Fig. 6.2(a).
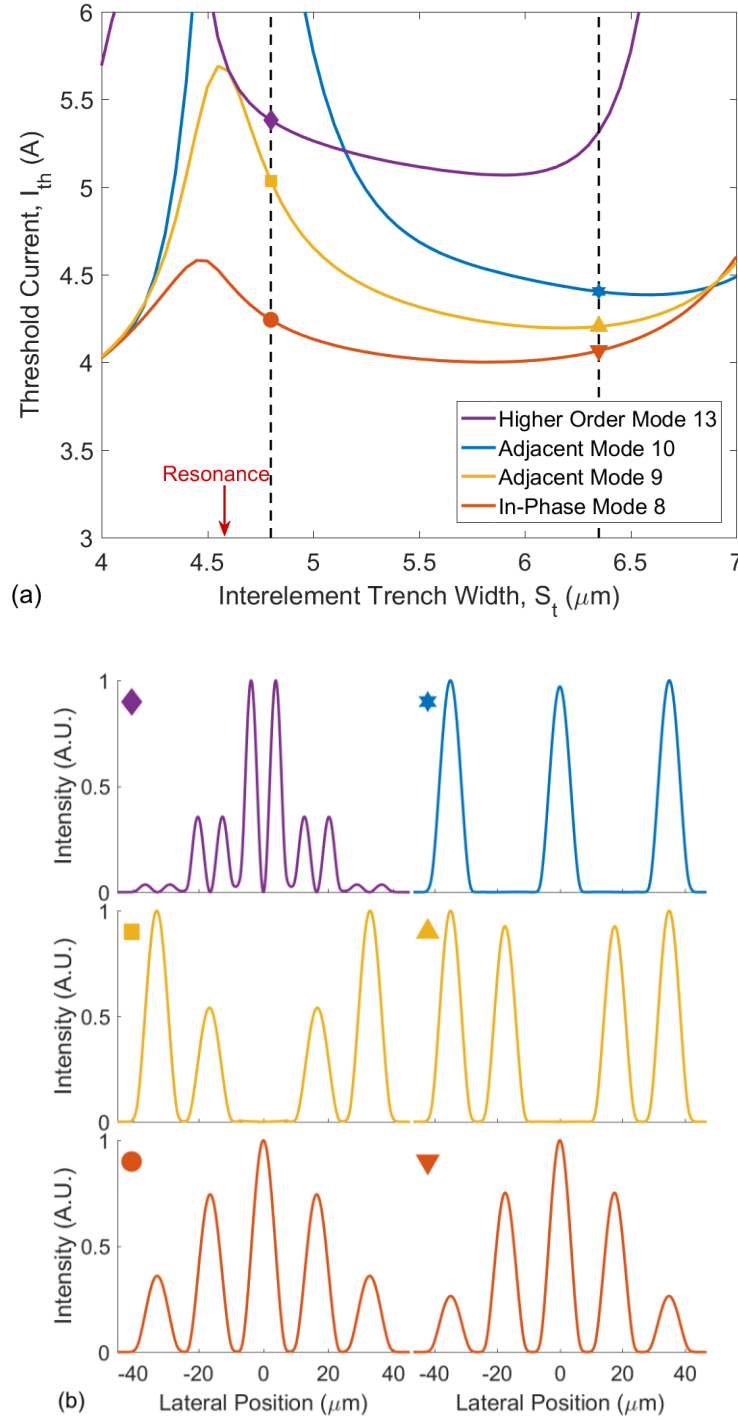
Fig. 6.10. (a) Simulated threshold currents for selected modes supported by 5-element HC-PC devices as a function of interelement trench width, $S_t$. The dashed black lines correspond to the interelement widths ($S_t = 4.8$ µm and $6.35$ µm) of the devices whose far-field patterns are shown in Fig. 6.6 and Fig. 6.5, respectively. (b) Simulated lateral electric field intensity profiles for the lowest threshold modes from (a). The colors and symbols in the upper-left of each profile correspond to colors and symbols in (a) and indicate which mode at which interelement width is being plotted. © 2017 IEEE

The mode numbers correspond to the number of field-intensity minima across the array for a given mode. For example, the in-phase mode, which has minima at either side of the four interelement regions, is called mode 8 [97]. This simulation assumes a wavelength from the center of the spectrum at low current (i.e., 4.69 µm for the narrow interelement device). The simulated threshold current is 4.24 A, compared to the actual threshold current of 5.3 A for the narrow interelement device ($S_t \sim 4.8$ µm). At this interelement width, the in-phase mode 8 has a modal array loss, $\alpha_{array,8}$, of 2.06 cm$^{-1}$; adjacent mode 9 has a modal array loss of 3.34 cm$^{-1}$; and mode 13, composed of out-of-phase coupled 1$^{st}$-order element modes [127], [128], has a modal array loss of 2.99 cm$^{-1}$. The larger losses for the competing modes are primarily a result of enhanced field overlap of those modes with the lossy Ti in the interelement regions, compared to that for the in-phase mode near its resonance [127]. Though mode 13 has lower modal loss than mode 9, it has ~10% lower intensity overlap with the current distribution, leading to a higher threshold current.

The wide interelement device ($S_t \sim 6.35$ µm) was modeled separately based on SEM images taken of it, as it had variations in its geometry not taken into account solely by the $S_t$ variation of Fig. 6.10 (for example, its elements are slightly narrower than for the narrow interelement device, which leads to a lower threshold current). This separate simulation gave a threshold current of 3.83 A (indeed lower than that shown in Fig. 6.10(a)), using this device's center wavelength (4.74 µm), compared to the actual threshold current of 4.55 A.

The disparity between the model and experiment could be due to inaccurate assumptions for the backfilling loss and differential gain, leakage current into the interelement and outer trenches due to imperfect current blocking, non-uniform current spreading, scattering losses in the interelement regions due to longitudinal non-uniformities created during the etch-and-

regrowth process, or different values for the differential gain coefficient in the element and interelement regions. The simulated intermodal discrimination is much larger for $S_t$ = 4.8 μm than for 6.35 μm, which agrees with the observed difference in behavior of the far-field beam pattern between the two devices. At $S_t$ = 6.35 μm, modes 8, 9, 10, and 13 have modal array losses of 1.66 cm$^{-1}$, 1.88 cm$^{-1}$, 2.20 cm$^{-1}$, and 2.95 cm$^{-1}$, respectively, resulting in the poor discrimination between modes 8, 9, and 10 in Fig. 6.10(a) at this interelement width. SEM images of the emitting facet showed significant variations in the interelement geometry across the wide-interelement array aperture, which could explain the asymmetric far-field profile at high powers for that device.

Note that if we were to assume perfect current confinement to the element regions (such as by using proton implantation to block current flow in the interelement regions [148]), so that the core regions with current flow would have a well-defined width and constant current density, then (6.1) and (6.3) reduce to a typically used form for devices with a well-defined area (equivalent to (3.7)):

$$J_{th,L} = \frac{\alpha_m + \alpha_{array,L} + \alpha_{bf}}{g\Gamma_{2D,L}}. \tag{6.5}$$

Thus, we can compare the threshold currents in the case of uniformly distributed current flow and perfect confinement, in order to find the benefit possible from complete current confinement to the element regions. We find that our model predicts a reduction of ~0.6 A, or ~15%, in the threshold current from confining the current flow only to the element regions.

Fig. 6.10(b) shows the simulated lateral electric field intensity profiles for the lowest threshold modes at the interelement widths of the two fabricated devices (i.e., at $S_t$ = 4.8 μm and 6.35 μm, respectively). While the in-phase mode is off resonance in both cases, as the modes have non-uniform intensity profiles, the narrower-interelement-width profile is nearly resonant.

Simulations suggest that resonance occurs at approximately $S_t \sim 4.6$ μm, at which point the in-phase mode has nearly uniform intensity across the five elements and the adjacent-mode threshold is peaked, as expected from theory [127]. The low edge radiation losses (~0.1-0.2 cm$^{-1}$ from modeling) for these devices results in a more uniform (less saddle-shaped) near-field for the in-phase mode at resonance [127]. It is also found from modeling this 2-D geometry in COMSOL as an infinite-extent array (by modeling a single period with periodic boundary conditions) that at $S_t \sim 4.6$ μm the relevant band edges cross, which is the exact condition for resonant leaky-wave coupling [31]. At $S_t = 4.6$ μm, modes 8, 9, and 13 have modal array losses of 2.42 cm$^{-1}$, 4.35 cm$^{-1}$, and 3.19 cm$^{-1}$, respectively, leading to the enhanced discrimination between the in-phase mode and the adjacent mode than in the near-resonant case at $S_t = 4.8$ μm, as shown in Fig. 6.10(a). This enhanced intermodal discrimination is a result of enhanced field overlap with the lossy Ti in the interelement regions as one approaches resonance [97], [127].

## 6.5    Design Optimization

By optimizing the design of the array, using the same 35-stage base with an InP spacer and still only etching through the upper core, array modes competing with the in-phase mode can be suppressed to higher drive levels. For such a structure, the built-in index step $\Delta n$ is 0.06 and the 1-D modal loss in the interelement is $\sim 295$ cm$^{-1}$. Then, the in-phase mode, mode 8 [97], is (laterally) resonant for $S_t \sim 5.0$ μm and exhibits the lowest $I_{th}$ value near resonance. Adjacent array modes, modes 7 and 9, being nonresonant, have significant interelement field [97]; thus, are suppressed due to strong absorption to metals (Ti and Au) in the interelement regions. The $I_{th}$ values for modes 7 and 9 are then $\geq 40$ % higher than the in-phase-mode $I_{th}$ value over a $\sim 0.7$ μm-wide region in $S_t$ variation: from 4.6 μm to 5.3 μm; thus, allowing for large fabrication tolerances.

Etching and regrowing InP:Fe in the lower core as well can bring significant benefits to the array's performance as the current flow is confined to the element regions entirely. Fig. 6.11 shows the simulated threshold current versus interelement width curves for an optimized design with only the upper core etched through and a design with both cores etched through. To reduce the total regrowth thickness required to obtain an InGaAs layer at a similar position, the InP spacer is 250 nm-thick in the design with both cores etched (compared to 500 nm in the other design). A thicker spacer is necessary when trying to stop the etch within the spacer to ensure adequate tolerance, while when etching through both core cores the thinner spacer also provides the benefit of an improved confinement factor.
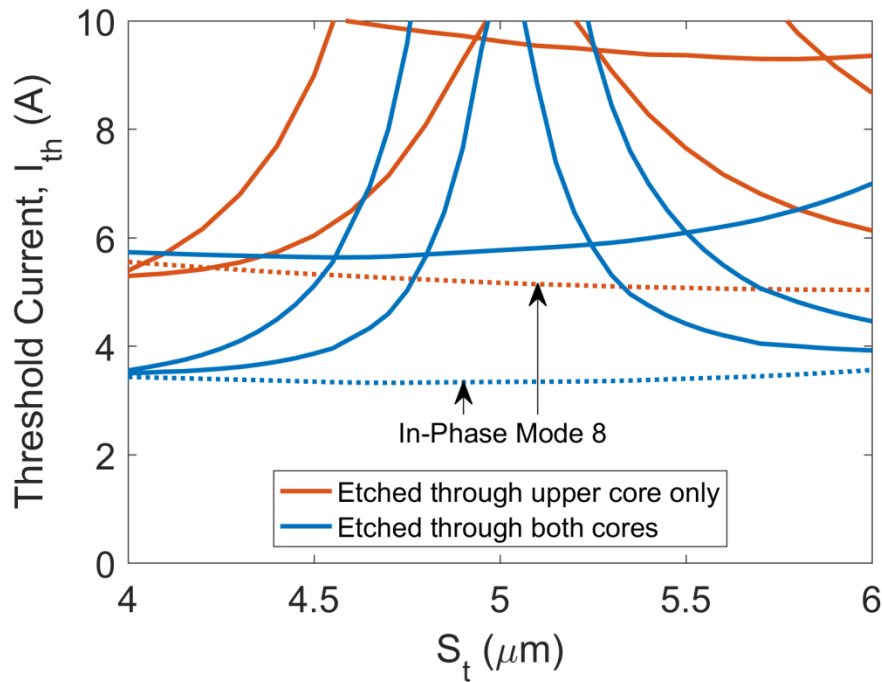


Fig. 6.11. Simulated threshold currents for selected modes supported by 5-element HC-PC devices as a function of interelement width, $S_t$, at the design wavelength of 4.7 µm, using both a design with only the upper core etched through and a design in which both cores are etched through and filled in with InP:Fe to confine current flow. The dotted black lines in the plot are the in-phase mode.

## 6.6 Spectrally-Resolved Modal Characteristics of Leaky-Wave Coupled QCL Phase-Locked Arrays

Fabry-Perot QCLs have been shown to exhibit very broad spectral bandwidths that widen with increasing output power [57]. The large spectral width of QCLs results from the instabilities arising from electron-light dynamics. Prior simulations of antiguided phase-locked arrays of QCLs performed in [29] considered only a single laser wavelength value located at the center of the core region's gain spectrum, while the geometrical array parameters were varied. Thus, the impact of the inherent wide spectral bandwidth of QCLs on the array-beam properties has not been previously studied. Furthermore, while spectrally resolved far-fields of a single-element terahertz QCL device have been measured [149], there are no prior reports regarding the spectrally resolved near- and far-field measurements for phase-locked QCL arrays. Here, we further analyze the modal behavior of two such devices employing spectrally resolved near- and far-field measurements and their correlation to simulation. These studies help elucidate the role of the QCL spectral width on array-mode properties. A key finding is that the inherently large spectral bandwidth of this QCL's active region can promote multi-spatial mode operation for array designs not optimized for achieving a large intermodal-discrimination process window around the resonance condition. New, optimized resonant-array designs are presented which exhibit enhanced intermodal discrimination for achieving sole in-phase array-mode operation and thus hold potential for maintaining a diffraction-limited beam pattern to high drive levels above threshold.

### 6.6.1 Experimental Results

Fig. 6.12 shows the light-current (L-I) curves of two 5-element arrays with interelement widths of 5.3 µm and 6.0 µm, in pulsed operation. The devices were driven by an Avtech

AVOZ-DF3-B pulsed voltage driver with 200 ns-long pulses at a 20 kHz repetition rate. The power was measured by placing a thermopile in front of the device with two AR-coated plano-convex lenses to focus the emitted light onto the thermopile, and the resulting power measurement was corrected for the lenses' transmissivity and collection efficiency. The element widths are nominally the same for the two devices, resulting in slightly different total widths for the arrays: ~80 μm and ~83 μm at the top of the upper core. The threshold currents are ~ 4.7 A, which corresponds to a threshold current density, $J_{th}$, value of ~ 1.7 kA/cm$^2$ in the lower core when considering current spreading under the interelement regions and 5 μm into each of the two lower corners of the core at the array edges. The peak powers of the devices reached 4.5 W and 5.8 W for the narrow and wide interelement devices, respectively. Higher output power is observed from the device with wider interelement width, since modal losses are reduced with designs which are further from the resonance condition [29].
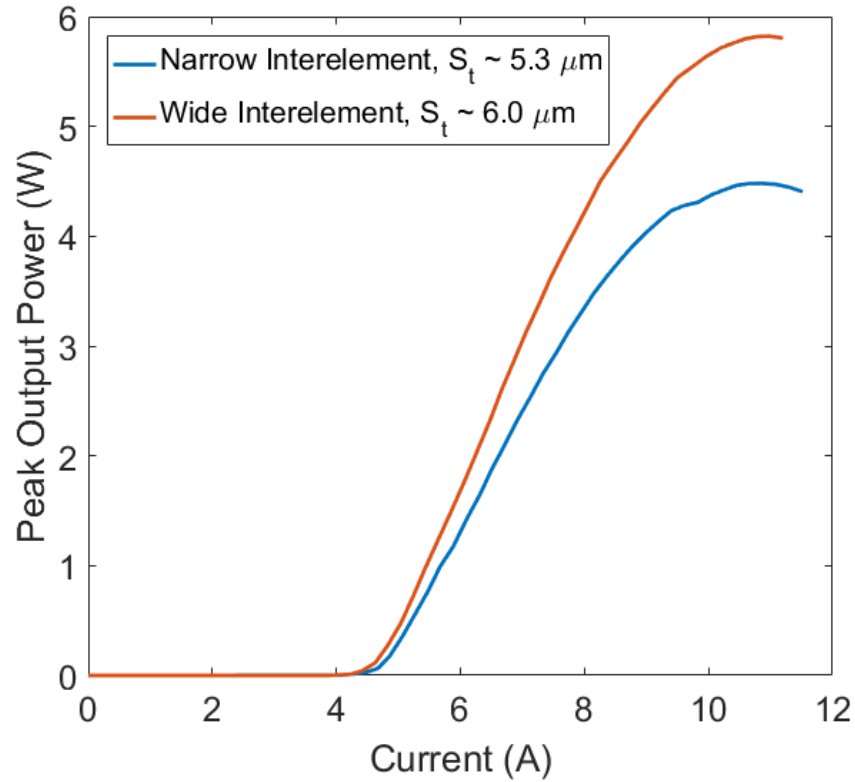
Fig. 6.12. Measured L-I characteristics under pulsed operation (200 ns-long pulses, 20 kHz repetition rate) for two arrays of different interelement widths.

The measured spectra for one device ($S_t \sim 6.0$ µm) are shown in Fig. 6.13 under different drive currents. The spectral characteristics were measured using a HORIBA 1250 mm-long spectrometer and a liquid nitrogen-cooled InSb detector, with a ~3 nm spectral resolution. The beam was focused on the entrance slit of the spectrometer using a spherical lens to collect light within a divergence half-angle of ~16°.
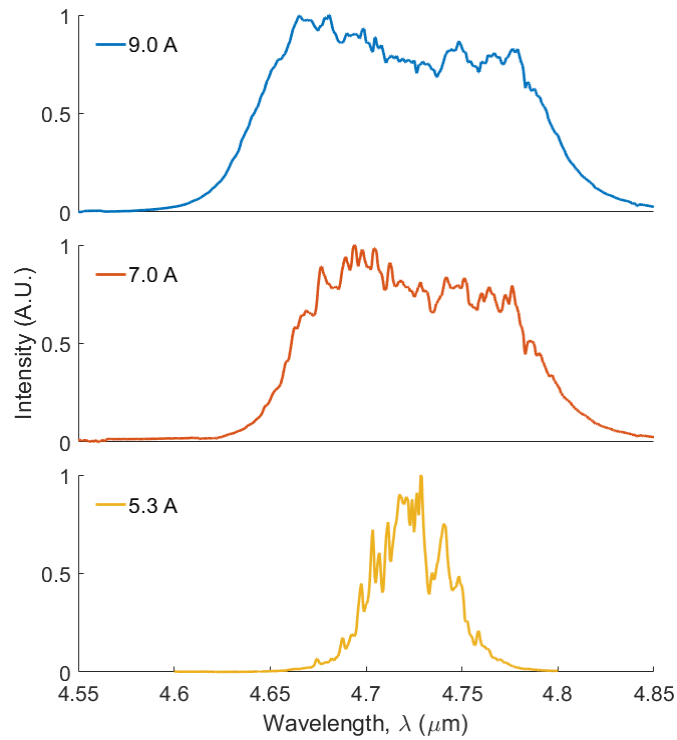
Fig. 6.13. Measured spectrum under different drive currents for the array with wide interelement spacing ($S_t \sim 6.0$ µm).

## 6.6.2 Near-field Measurements

All near-field measurements described in this chapter were measured by collaborators. Initially the full spectral band near-field is directly imaged. The output facet of the QCL is imaged using a 0.85 numerical aperture GeSbSe antireflective-coated infrared asphere (effective focal length ¼ 1.87 mm, working distance ¼ 0.72 mm) directly onto an InSb 640 × 512 pixel focal plane array (FPA) cooled to 76 K with a pixel pitch of 15 µm. The optical system results in a magnification of ~85 and a spatial sampling of just under 180 nm. Images are collected using a 0.96 µs exposure time triggered by the pulsed repetition frequency (PRF, 1kHz to prevent detector saturation) of the pulsed current source and are averaged over 2500 frames, and corrected to remove the background. This approach typically results in near-field images utilizing 10 bits of the 14-bit sampling. To spectrally resolve the near-field, we use a similar

setup as for the full-spectrum above, but instead of imaging onto an FPA, we image the near-field onto 100-μm wide entrance slits of a 300-mm long spectrometer with a 300 line∕mm grating. To attain reasonable near-field resolution, we adjust the setup to attain a magnification of ≈ 210. The exit slits of the spectrometer are set equal to the entrance slits and an amplified single-channel PbSe detector and lock-in amplifier, with a time constant of 300 ms, are used to measure the spectrally resolved signal. The spectral resolution is estimated to be < 5.2 nm. To build up a lateral near-field profile, the imaging lens is translated horizontally, thus translating the near-field image across the entrance slits. The imaging lens translation step size is chosen to correspond to a 1 μm spatial sampling on the QCL facet (object space). The devices are operated with a pulse width of 200 ns, at a submount temperature of 20°C, and a PRF of 10 to 20 kHz, depending on the device and detector saturation. We did ensure that there is no significant performance difference between 1 and 20 kHz, such that the duty cycle was appreciably small and there was little pulse-to-pulse thermal "memory."

Line scans of full spectral band near-field images are from the center height of the image and the average of three detector rows. There is a slight asymmetry in the near-field, which is likely due to fabrication non-uniformity. Fig. 6.14 shows the near-field images for operation near threshold, showing good agreement between the near-field summed over all spectral bands and the near-field profile directly imaged with the InSb FPA. The narrow interelement device [Fig. 6.14(a)] contains strongly peaked central lobes relative to the outer two lobes. The two measurements in Fig. 6.14(a) are taken at slightly different current drives, with the directly imaged measurement at 0.1 A higher drive, resulting in some difference between the directly imaged near-field and a summation of the spectrally resolved near-field. In addition, low signal data points in the outer lobes are in the noise floor for certain wavelengths, thus they do not

contribute to the spectral sum. In contrast, Fig. 6.14(b) shows the wide interelement device where there is a little more power in the outer two lobes relative to the inside three lobes, and the two curves agree well with each other as the measurements were taken at the same current.
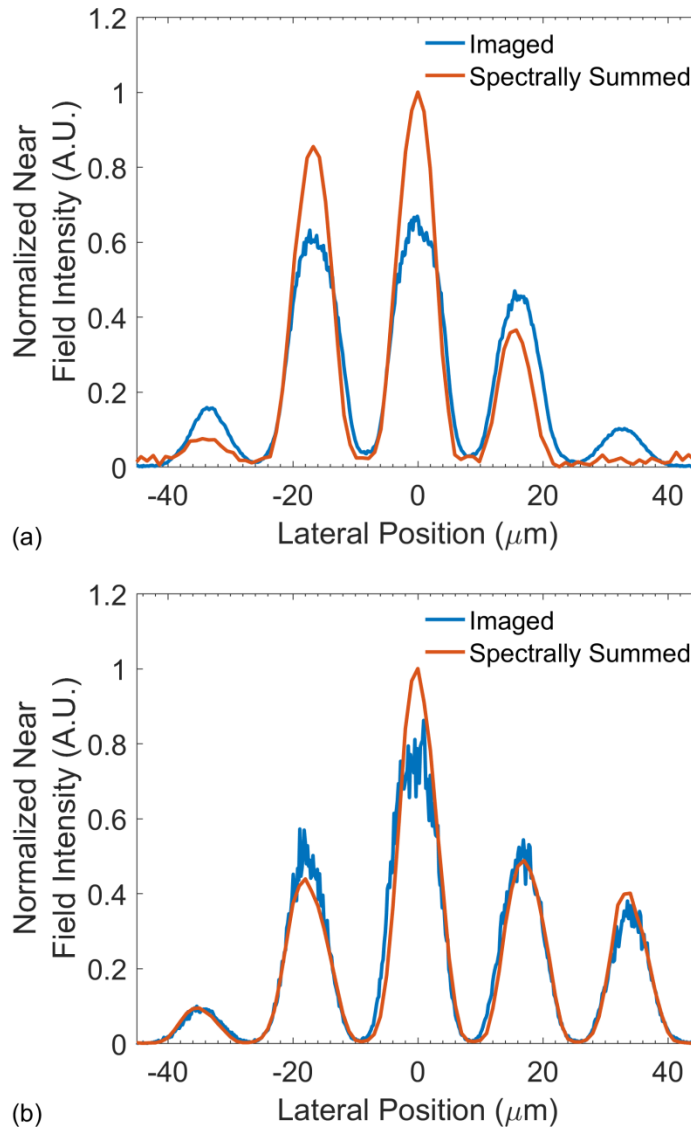


Fig. 6.14. Comparison of near-field profiles directly imaged and summed from the spectrally resolved imaging for the (a) narrow interelement device and (b) wide interelement device.

Fig. 6.15 shows the full-spectral-band near-field profile as a function of current for the wide interelement device, as well as the simulated in-phase mode profile for this device. Simulations show the in-phase mode of these devices was highly non-uniform and peaked in the

center element of the array. This suggests that the in-phase mode lases first near threshold for this device, and as the drive current increases other modes with more intensity in the outer elements begin to lase and fill in the near-field to give a nearly uniform intensity profile, in agreement with what was found from analyzing the far-field beam patterns in Section 6.3.
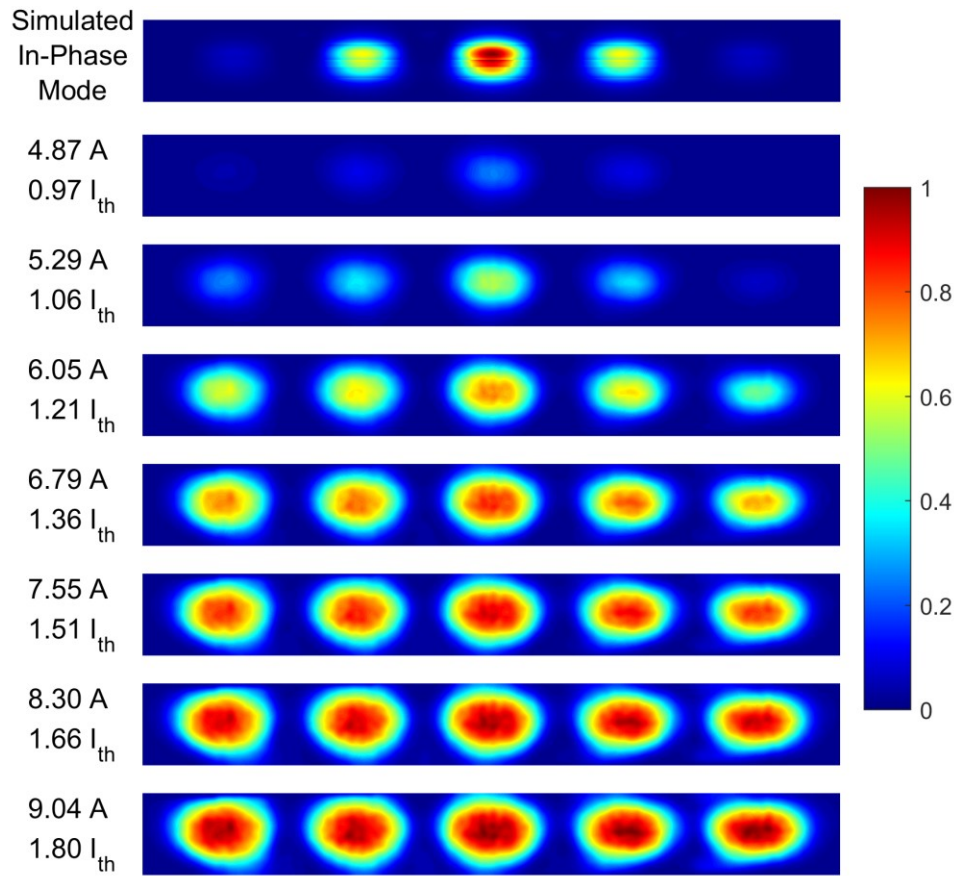


Fig. 6.15. Measured full-spectrum near-field profile of the wide interelement device as a function of current (bottom); simulated in-phase mode near-field intensity profile for this device geometry (top).

### 6.6.3  Spectrally Resolved Far-field Measurements

In contrast with [149], where a microbolometer focal plane array was used in conjunction with an FTIR spectrometer to capture the spectrally resolved far-field in parallel, we measure the spectrally resolved far-field with a single pixel detector, which in general should increase the measurement time and improve the signal-to-noise ratio of the measurement. The device is

placed 18 cm away from the 1 mm-wide entrance slit of a HORIBA 1250 mm-long spectrometer with a 300 line/mm grating. A cylindrical lens is used to focus the vertical axis of the beam onto the entrance slit of the spectrometer. A liquid nitrogen-cooled InSb detector is used with a lock-in amplifier with 300 ms time constant to record the spectrum of the device for a given angle. The device is rotated to obtain different slices of the far-field passing through the entrance slit to build the full spectrally resolved beam pattern. The estimated angular and spectral resolutions of this system are 0.32° and 3 nm, respectively.

Full-spectrum far-fields as a function of current are shown for the two devices in Fig. 6.16 (measured as described in Section 6.3), along with the simulated in-phase mode, which is the ideal diffraction-limited beam pattern. These indicate operation near threshold primarily in the in-phase array mode, with central lobe full-widths at half-maximum of 1.1 × D.L. and 1.3 × D.L., for the narrow and wide interelement devices, respectively. The sidelobe intensities near threshold are in agreement with the simulation to within the noise of the measurement for the narrow interelement device, and up to 6% lower intensity than the simulation for the wide interelement device. The beams broaden at higher drive currents due to the onset of adjacent modes reaching threshold [97], [127]. For the device of smaller interelement width ($S_t \sim 5.3$ μm) with an ~80 μm-wide aperture, the central lobe FWHM is 1.7 × D.L. at 10.0 A and 4.3 W output power. That is, it has near-D.L. operation to a drive level of 2.1 × threshold (Fig. 6.16(a)). For the device of larger interelement width ($S_t \sim 6.0$ μm), the beam broadens more with increasing current (Fig. 6.16(b)), with a lobewidth ~ 2.6 × D.L at 9.0 A and a peak power of 5.1 W, indicating that above threshold lasing occurs in a much larger mixture of additional array modes. In the direction perpendicular to the array, the measured far-field has a FWHM of 45°, compared

to a calculated FWHM of 43° for the fundamental transverse element mode, suggesting they are diffraction-limited in this direction.



(a)

(b)
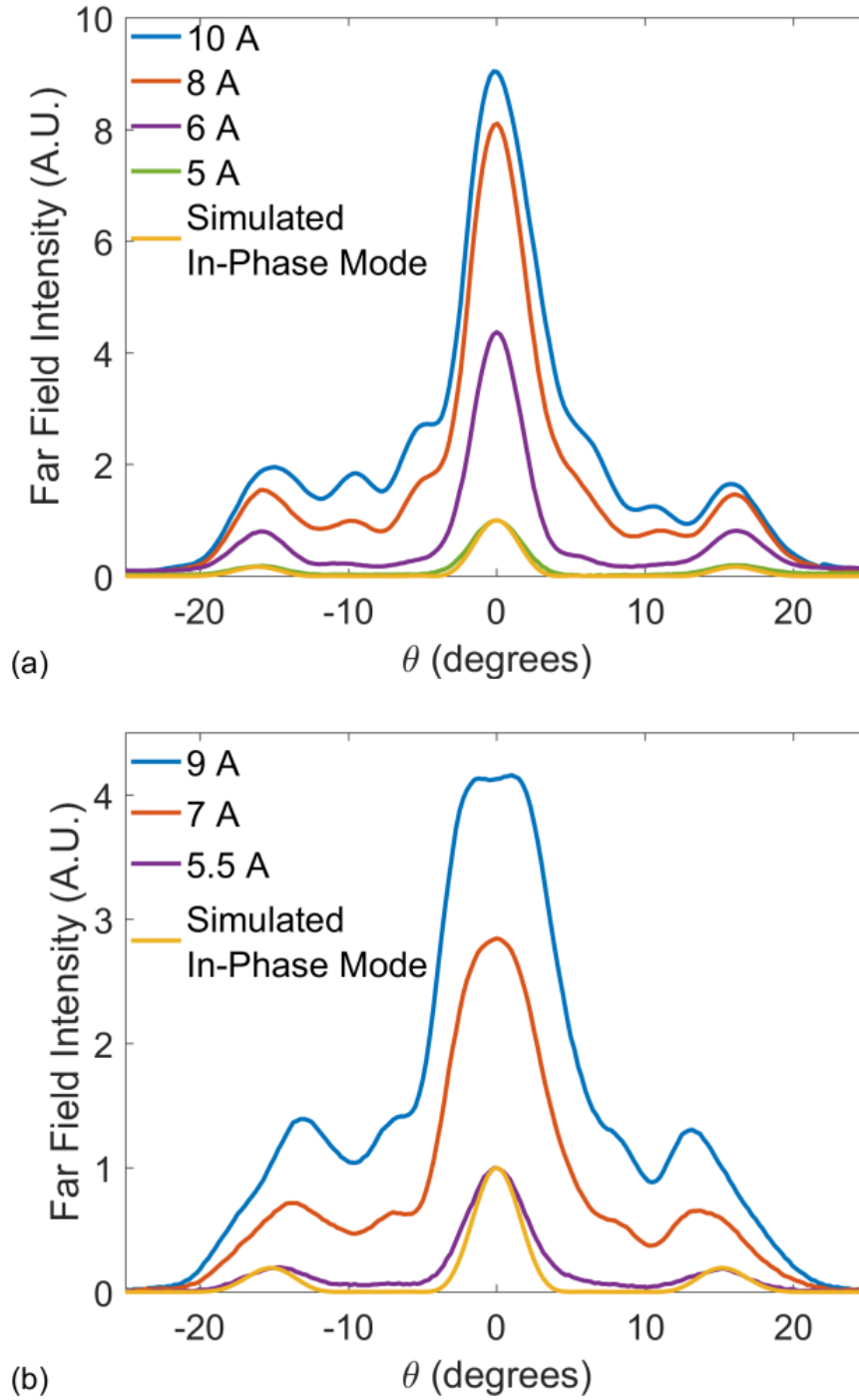
Fig. 6.16. Measured (upper) and simulated (lowest) lateral far-field patterns for HC-PC device with an interelement width $S_t$ of (a) 5.3 µm, and (b) 6.0 µm.

In these leaky-wave-coupled arrays, the near- and far-field distributions are found to be wavelength dependent. Fig. 6.17, Fig. 6.18, and Fig. 6.19 show contour plots of the measured spectrally resolved near- and far-fields for the narrow interelement device near rollover, wide interelement device near threshold, and wide interelement device near rollover, respectively. Fig. 6.20, Fig. 6.21, and Fig. 6.22 show selected line scans of the spectrally resolved near- and far-fields of the devices in the same order. Spectrally resolved far-fields of the narrow interelement device were measured near threshold, at 5.9 A, and showed little deviation from the expected in-phase mode far-field at all measured wavelengths. Due to the near- and far-field measurements being taken with different systems and variations in the measured spectra for a given device over time, the near- and far-field measurements at a specific wavelength are not necessarily comparable. Thus, we measure the spectrum for a given device and drive level between the two systems and find an offset between corresponding peaks in the spectra, which ranged up to 6 nm. We then compare the near- and far-fields at two wavelengths separated by that offset. Both the near- and far-field measurements are corrected for background noise and the detectivity of the detector, which varies with wavelength.

Fast Fourier transforms (FFTs) of the near-field imaging from image space (emission plane) to angular space are used to compare the near-field imaging to the far-field imaging. The square root of near-field intensity is zero-padded such that the 'padded' data is four times larger than the original data. This results in an angular resolution of 0.73° for the transforms of the spectrally-resolved near-field profile. In all cases the angular resolution is comparable to the experimental resolution. The square of the Fourier transform is normalized to the maximum value for comparison to the far-field imaging intensity. In this approach, we assume a uniform planar phasefront at the output facet, essentially true for a device operating in the ideal in-phase

mode. The dotted lines in Fig. 6.20, Fig. 6.21, and Fig. 6.22 show these Fourier-transformed near-fields and allow a comparison with the measured spectrally resolved far-fields. We can see in the spectrally resolved near-field images that at shorter wavelengths (e.g. 4.65 µm), more energy is found in the outer elements, and the far-field beam pattern is significantly different from that expected for a flat phase front, indicating operation in non-resonant modes. At longer wavelengths ($\approx$ 4.75 µm), the mode is primarily confined in the central lobes and the far-field is in-phase-like for the narrow interelement device, indicating operation primarily in the in-phase mode. Fig. 6.21(b) and Fig. 6.22(b) show the wide interelement device is operating with a nearly flat phase front near threshold at most wavelengths, and a more complex profile at high power. At some wavelengths, we see significantly asymmetric near-field profiles, and the corresponding far-field profiles have poor beam quality. We attribute the asymmetry to fabrication non-uniformities.
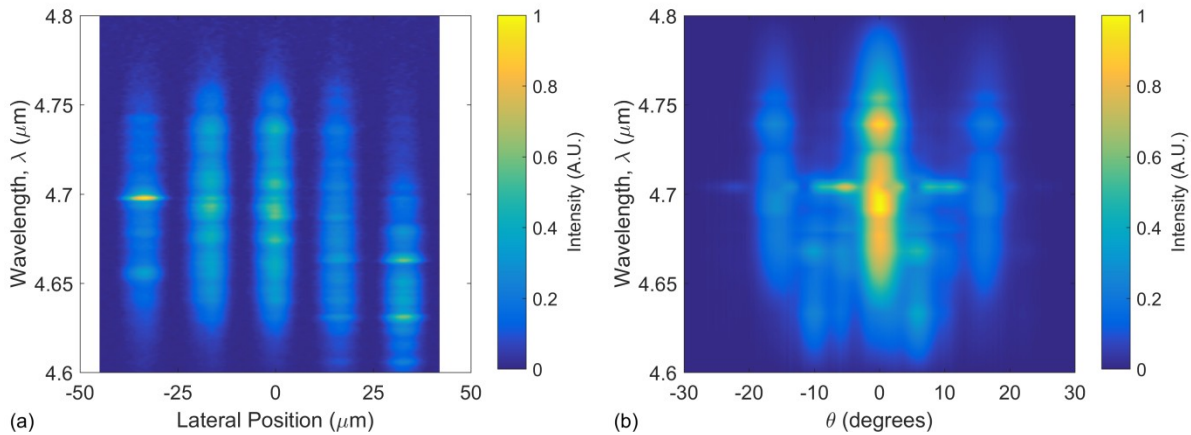


Fig. 6.17. Contour plots of the spectrally resolved (a) near-field and (b) far-field profiles for the narrow interelement device at a current drive near rollover (9.2 A).
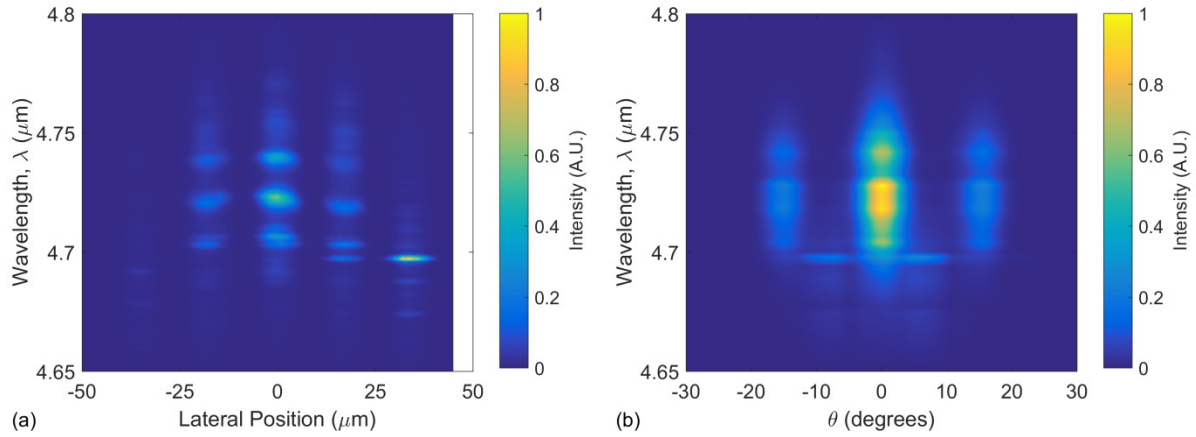
Fig. 6.18. Contour plots of the spectrally resolved (a) near-field and (b) far-field profiles for the wide interelement device at a current drive near threshold (5.3 A).
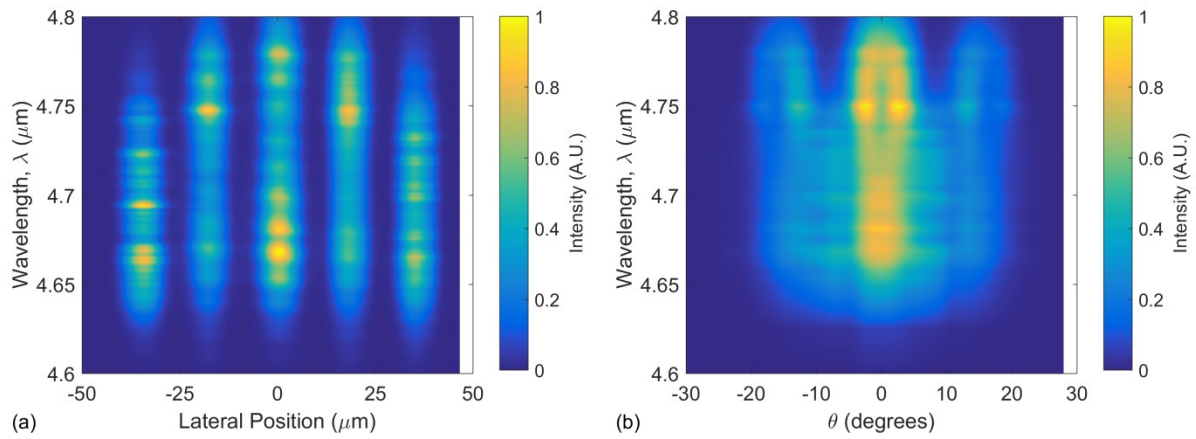


Fig. 6.19. Contour plots of the spectrally resolved (a) near-field and (b) far-field profiles for the wide interelement device at a current drive near rollover (9.0 A).
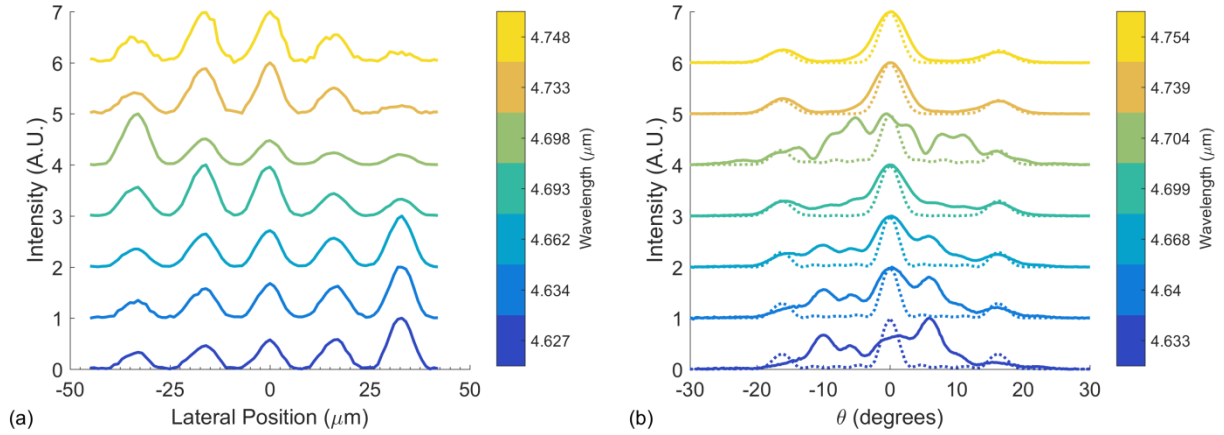
Fig. 6.20. Line scans at selected wavelengths of the measured spectrally resolved (a) near-field and (b) far-field profiles (solid lines) for the narrow interelement device at a current drive near rollover (9.2 A). The dotted lines in (b) are FFTs of the measured near-field profile.
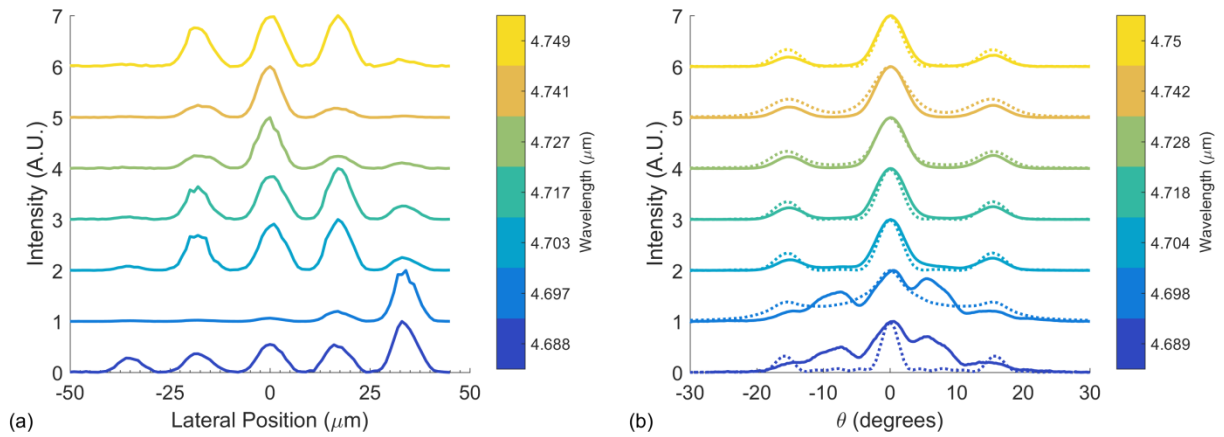


Fig. 6.21. Line scans at selected wavelengths of the measured spectrally resolved (a) near-field and (b) far-field profiles (solid lines) for the wide interelement device at a current drive near threshold (5.3 A). The dotted lines in (b) are FFTs of the measured near-field profile.
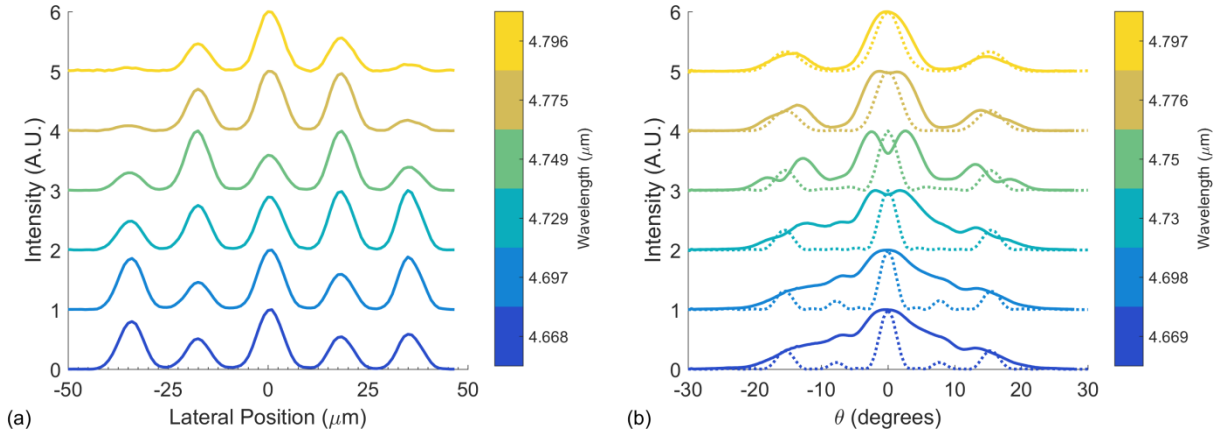
Fig. 6.22. Line scans at selected wavelengths of the measured spectrally resolved (a) near-field and (b) far-field profiles (solid lines) for the wide interelement device at a current drive near rollover (9.0 A). The dotted lines in (b) are FFTs of the measured near-field profile.

### 6.6.4 Modeling and Discussion

To understand the modal characteristics of these devices, simulations of these 5-element array structures were performed using COMSOL Multiphysics to find the expected threshold currents and electric field profiles for the modes supported by the structures. The models' geometries were created based on SEM images of the cross-section at the emitting facet of the devices, such as those shown in Fig. 6.2. Expected threshold currents are calculated based on the modal loss and field profile calculated by COMSOL, as discussed in Section 6.4. The models are set up such that each interelement is identical and symmetric, as we expect longitudinal variations to exist, making the visible cross-section at the facet not necessarily representative of the entire device. Thus, the model produces only symmetric and antisymmetric mode profiles, and so the asymmetric near-field profiles seen in the measurements are not found.

As the interelement width needed to achieve resonance is proportional to the wavelength [97], the resonance point shifts across the spectrum of the QCLs. Simulations suggest the resonance point at the design wavelength of 4.7 μm was approximately $S_t \sim 4.6$ μm. Since both of these devices had interelement widths larger than that at resonance, at longer wavelengths the

resonance point shifts closer to their interelement widths, thus improving intermodal discrimination at longer wavelengths. Fig. 6.23 shows an example of this for the narrow interelement device ($S_t \sim 5.3$ μm). This figure plots the simulated threshold currents for selected competing array modes as a function of the emitting wavelength (high threshold modes have been removed for clarity). Since the device is significantly far from resonance, this change in intermodal discrimination across wavelength is not large enough to bring the array into resonance within the core-region's spectral band. However, as seen in Fig. 6.20, the far-field beam profile is improved at longer wavelengths, in agreement with there being enhanced intermodal discrimination at these wavelengths. As the wavelength increases, absorption losses for the materials increase and the modes are less confined to the core, resulting in the increasing threshold with wavelength for all modes. This simulation assumes a constant differential gain coefficient regardless of wavelength.
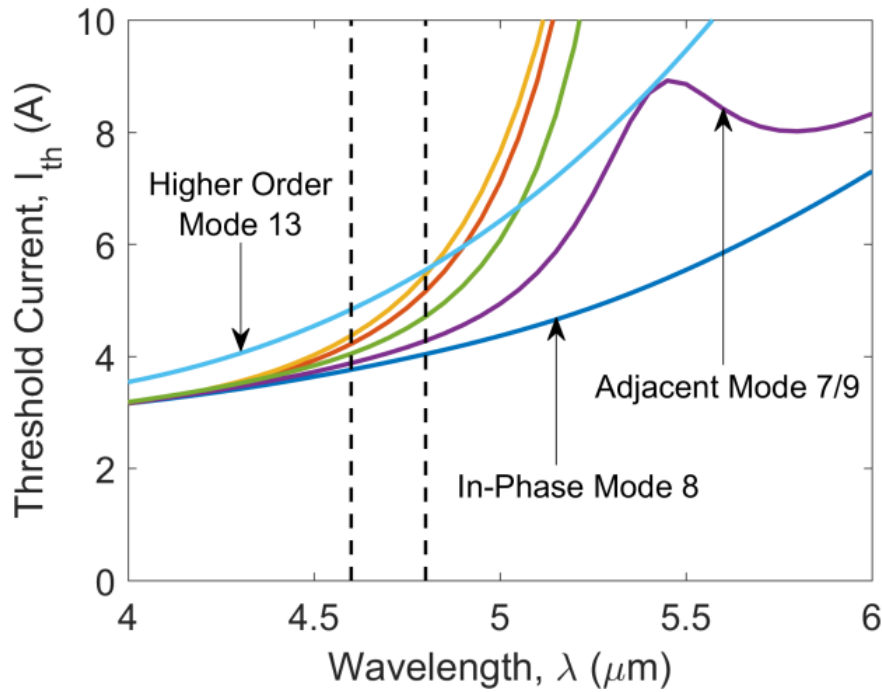
Fig. 6.23. Simulated threshold currents for selected modes supported by the narrow interelement ($S_t$ ~ 5.3 μm) 5-element HC-PC device as a function of wavelength. The dotted black lines represent the approximate wavelength bounds within which these devices lased.

The fabricated devices have suboptimal structures, leading to a narrow window for single-lateral-mode operation. A more optimized design, primarily consisting of removing the Pt layer from the front-side metallization, narrowing the elements (10 μm instead of 12 μm-wide), and widening the regrown InGaAs layer by growing thinner InP:Fe, can broaden the window for large intermodal discrimination. Fig. 6.24(a) shows an example of simulated threshold currents vs. interelement width for geometries based on that of the fabricated devices as well as for an optimized design. This simulation shows that the intermodal discrimination is larger for the narrow interelement device than for the wide interelement device, leading to the broader beam pattern for the wide interelement device. The window for single-lateral-mode operation for the optimized design is large: there is a ~ 0.85 μm-wide region in $S_t$ variation in which the

competing modes have a threshold over 40% higher than the in-phase mode, though the in-phase mode does have a higher threshold compared to the simulation based on the fabricated devices.

Fig. 6.24(b) shows, for the same two structures, the simulated in-phase mode uniformity, which we define as the ratio of the integral of the electric field intensity in the central element to that in an element at an edge of the array, as a function of interelement width. The insets show the lateral in-phase mode intensity profile at an interelement width 0.7 μm above resonance for both structures, which is the width obtained for the narrow interelement device. The more uniform profile of the optimized design will help reduce gain spatial hole burning at the array level, regardless of the obtained interelement width. Thus, the in-phase mode can more efficiently utilize gain, reducing the gain available to other modes to achieve lasing. A uniform near-field profile also reduces the beam width of the central lobe of the far-field, though it does increase the intensity of the side lobes.

Because of the lower doping of the InP substrate ($\sim 2\times10^{17}$ cm$^{-3}$) compared to the highly doped contact layer on the frontside ($\sim 2\times10^{19}$ cm$^{-3}$), the backside contact requires annealing to improve the resistance of this contact. This can allow Au to diffuse into the device on the front-side if a blocking metal layer, such as Pt, is not used. Thus, this design requires that the backside contact be annealed before the metal on the frontside has been deposited to avoid Au diffusion.
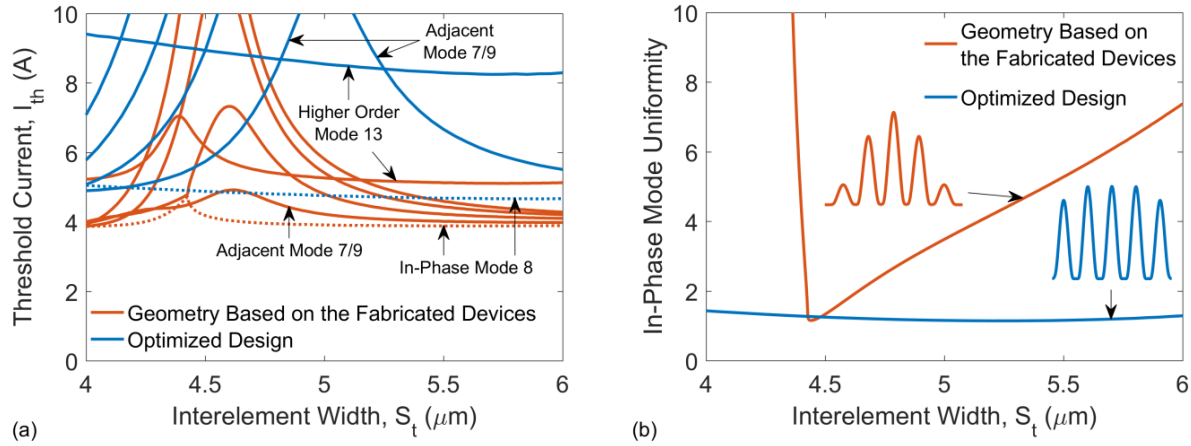
Fig. 6.24. Simulated threshold currents for selected modes supported by 5-element HC-PC devices as a function of interelement width, $S_t$, at the design wavelength of 4.7 μm, using both a geometry based on the fabricated devices and an optimized design. The dotted lines are the in-phase modes for each structure. (b) Simulated in-phase mode uniformity, for the same two structures. The insets show the lateral in-phase mode intensity profile at an interelement width 0.7 μm away from resonance for each structure.

Fig. 6.25 shows the simulated threshold current as a function of wavelength for this optimized design, (a) near resonance with $S_t = 5.7$ μm, and (b) at resonance, for $λ = 4.7$ μm, with $S_t = 5.0$ μm. Fig. 6.25(a) is at the same interelement width offset from resonance as the fabricated narrow interelement device, showing that this far from resonance there is significantly larger intermodal discrimination in comparison to the fabricated-device's case shown in Fig. 6.23, and there is significant wavelength dependence within the device's spectral band. Fig. 6.25(b) shows that an optimized device operating at resonance at its design wavelength should exhibit single in-phase mode operation across its full spectral band. That is, as expected, achieving full spatial coherence from a phase-locked laser array does not require full temporal coherence (i.e. narrow linewidth).
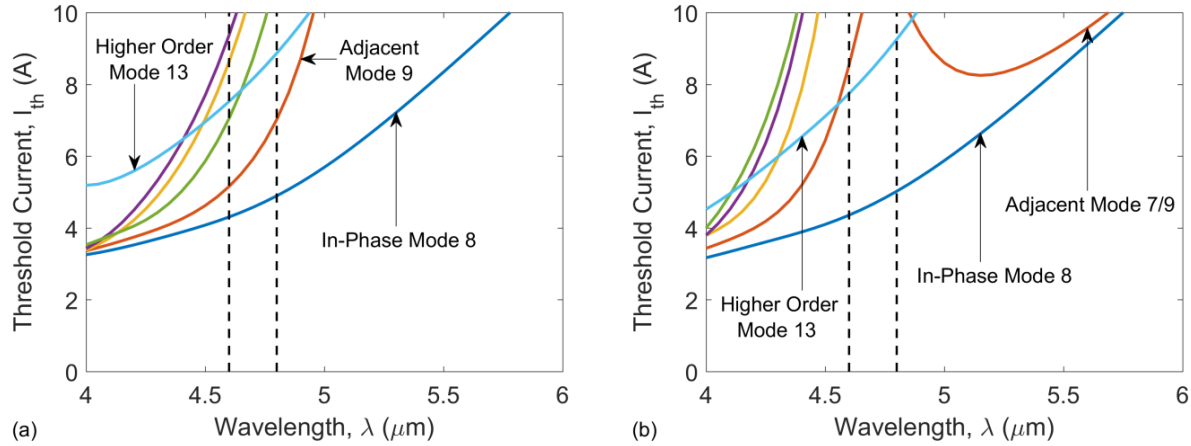
Fig. 6.25. Simulated threshold currents for selected modes supported by the optimized HC-PC design as a function of wavelength, at an $S_t$ value of: (a) 5.7 µm, and (b) 5.0 µm, the resonance condition. The dotted black lines represent the approximate wavelength bounds within which the fabricated devices lased.

The simulated near- and far-field profiles were numerically fit to the measured near- and far-field profiles to determine the modal composition of the emitted beam. This was accomplished by finding the combination of contributions from modes solved by COMSOL which minimizes the total error between the simulated and measured profiles. Fig. 6.26 and Fig. 6.27 show the result of this fitting for the overall far-field beam patterns of the narrow and wide interelement devices, respectively, near rollover. For the narrow interelement device the measurements were made at 9.2 A, and for the wide interelement device the measurements were made at 9.0 A. This fitting assumes that the mode profiles are as calculated at a wavelength of 4.7 µm, ignoring the variation across the spectrum, which is minor. This fitting shows our best estimate of the relative contribution of the in-phase mode to the overall beam patterns for the two devices, with the narrow interelement device having greater contribution from this mode, as would be expected since it is closer to resonance. For both devices, the calculated relative contributions of the in-phase mode are larger at lower current drives: 65.5% at 5.5 A for the wide interelement device, and 87.6% at 5.0 A for the narrow interelement device. Only the competing

array modes composed of coupled fundamental element modes are necessary to fit these measurements. That is, this indicates that no array modes composed of coupled 1st-order element modes are lasing in these devices.
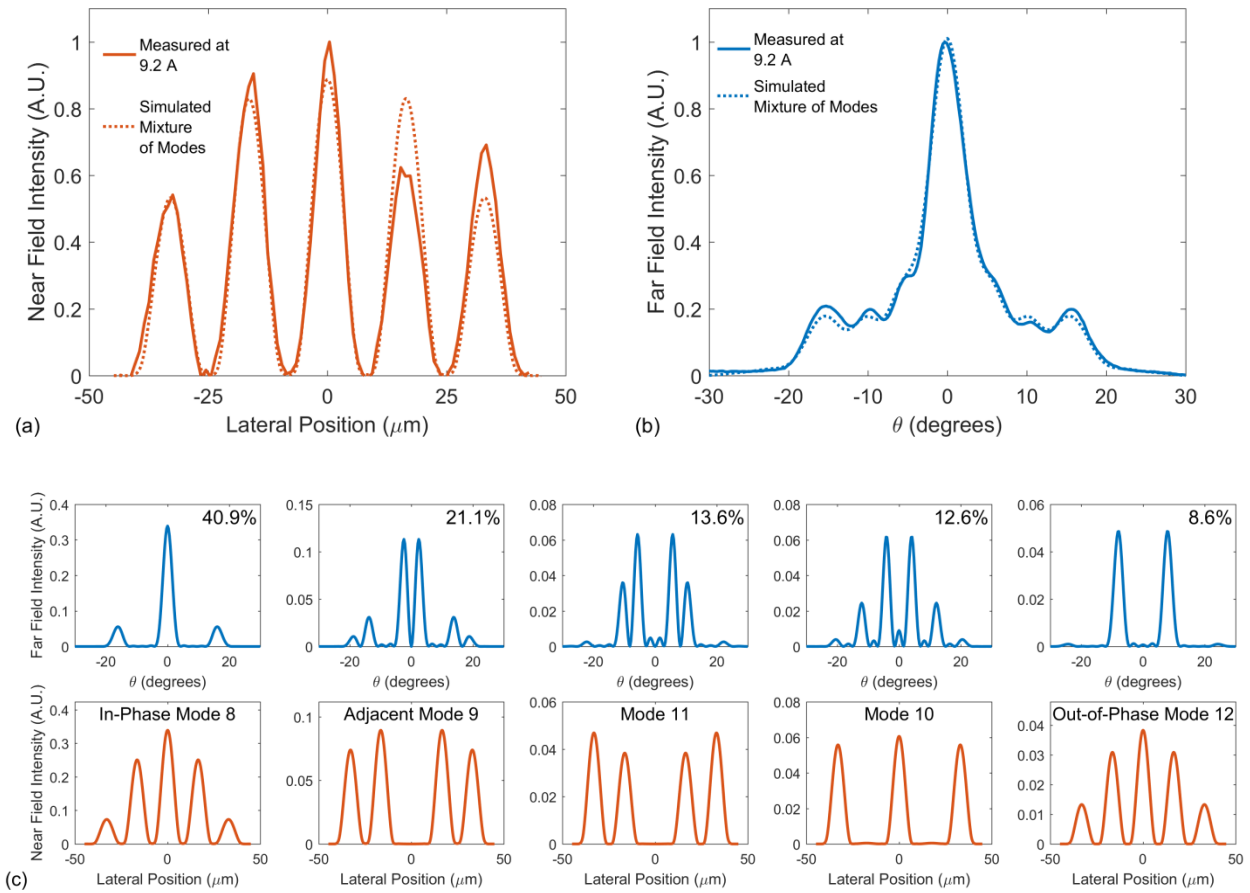


Fig. 6.26. Modal decomposition of the measured full spectral-band near and far-field patterns for the narrow interelement device near rollover (9.2 A): (a) comparison of the measured near-field profile to a simulated mixture of modes; (b) comparison of the measured far-field beam pattern to a simulated mixture of modes; (c) near- and far-field profiles of the modes contributing to the mixture in (a) and (b), and their relative contributions to the mixture in the top-right corner of the far-field plots.
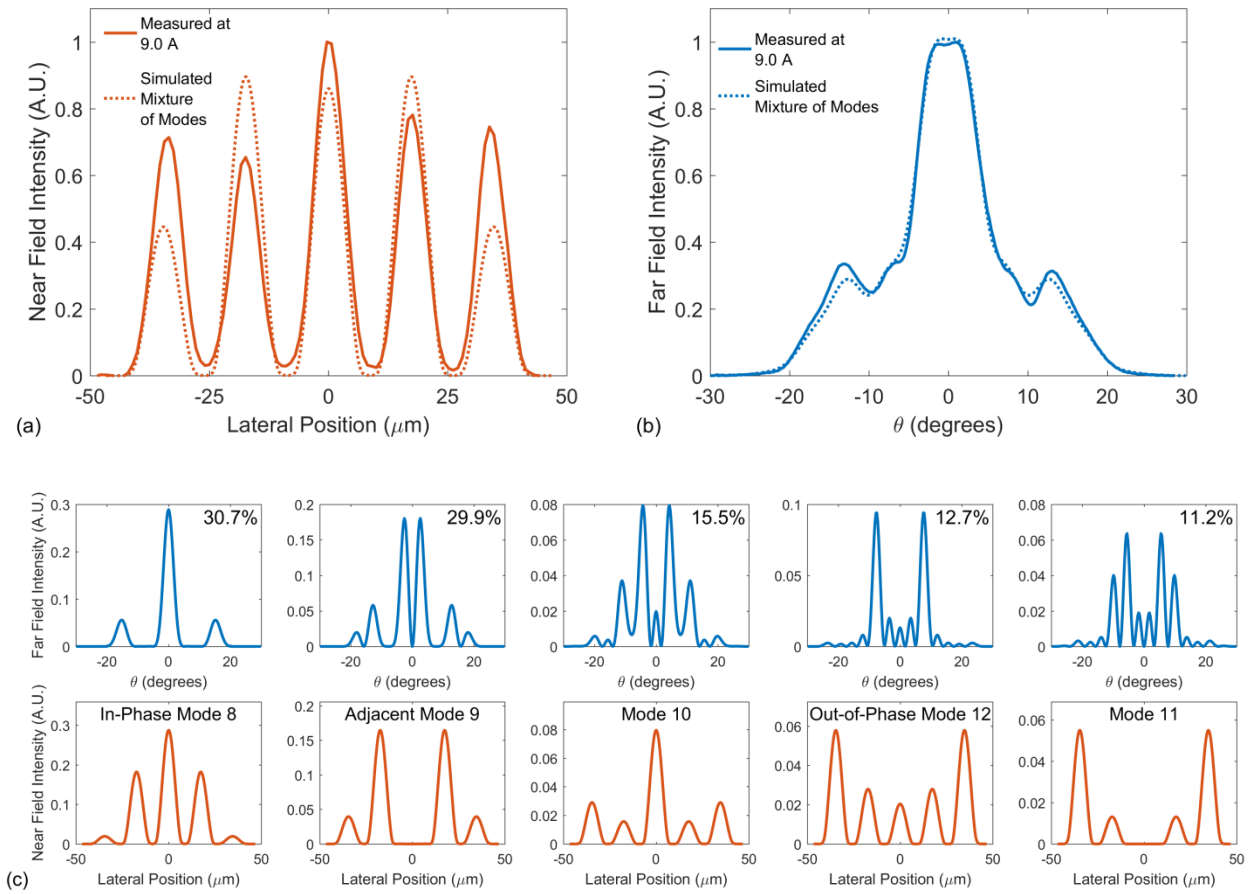
Fig. 6.27. Modal decomposition of the measured full spectral-band near- and far-field patterns for the wide interelement device near rollover (9.0 A): (a) comparison of the measured near-field profile to a simulated mixture of modes; (b) comparison of the measured far-field beam pattern to a simulated mixture of modes; (c) near- and far-field profiles of the modes contributing to the mixture in (a) and (b), and their relative contributions to the mixture in the top-right corner of the far-field plots.

Fig. 6.28 shows fitting of near- and far-field patterns for the wide interelement device at high drive current, specifically at a wavelength of 4.75 μm, showing predominantly adjacent mode 9 lasing at this wavelength, which is the primary reason for the broadening of this overall beam.
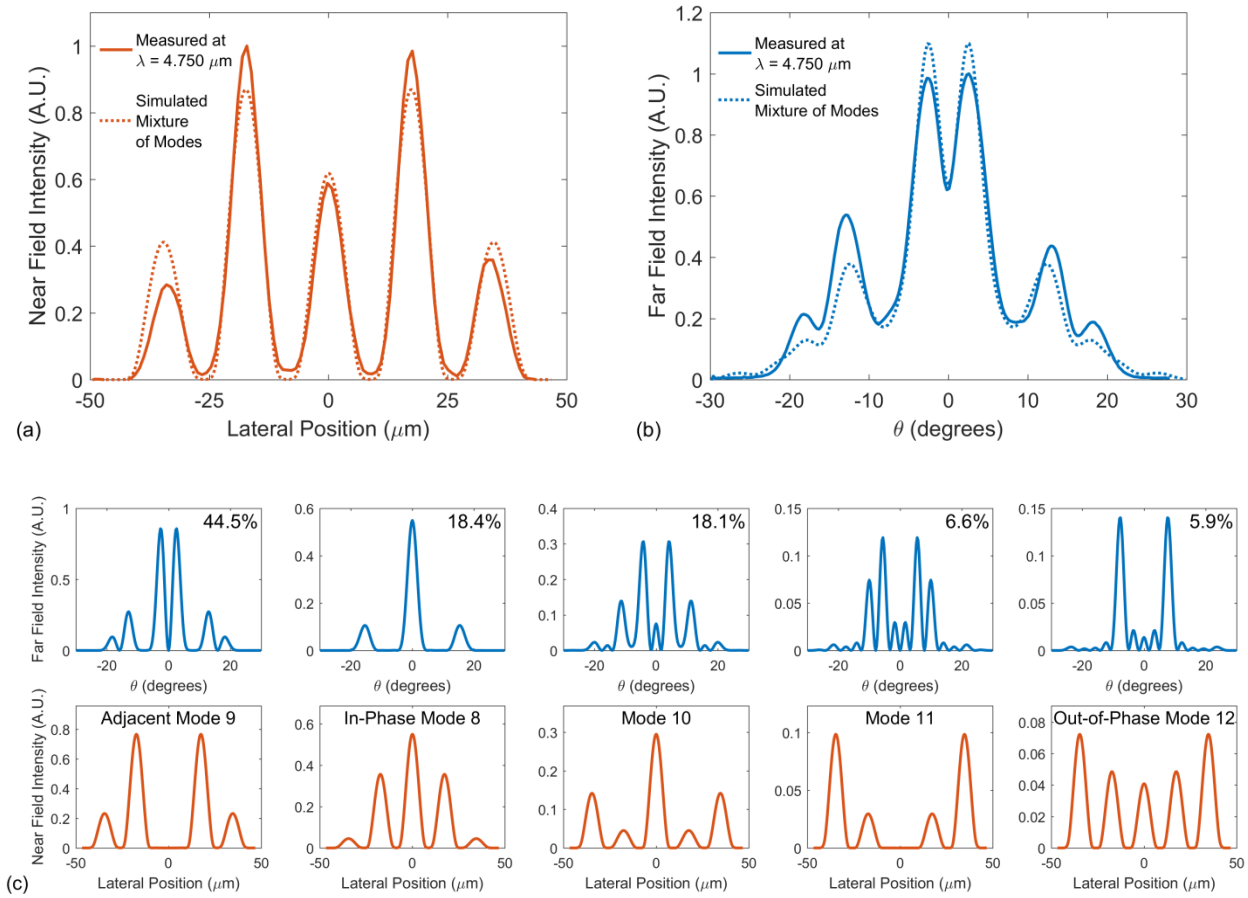
Fig. 6.28. Modal decomposition of the measured near- and far-field patterns for the wide interelement device near rollover (9.0 A), at a wavelength of 4.75 µm: (a) comparison of the measured near-field profile to a simulated mixture of modes; (b) comparison of the measured far-field beam pattern to a simulated mixture of modes; (c) near- and far-field profiles of the modes contributing to the mixture in (a) and (b), and their relative contributions to the mixture in the top-right corner of the far-field plots.

## 6.7 Three-Element Resonant Array

Three-element arrays were fabricated using the same base design of 35-stages with a 0.5 µm-thick InP spacer as the arrays described above, with the core design changed to that of a step-tapered active region with resonant extraction (STA-RE) as described in [23] for improved performance. The fabrication process was adjusted to remove Pt from the epi-side metallization, as modeling has suggested this has a deleterious impact on intermodal discrimination and in-phase mode uniformity. In order to allow annealing of the backside contact, composed of

AuGe/Ni/Au layers, without diffusing Au into the device due to the absence of Pt, the wafer thinning, backside metallization, and annealing steps were performed before the frontside metallization.

The highest power three-element array (3mm-long and HR-uncoated) emitted up to about 5.3 W of power (150 ns-long pulse, 5 kHz pulse repetition rate), as shown in the LIV curves in Fig. 6.29(a). When compared against ridge waveguides fabricated and tested from the same material, these arrays' IV characteristics suggest that there is significant leakage current through the InP:Fe in the interelement regions and outer trenches, raising their threshold. The spectra of this device near threshold and near rollover, at 6.0 A and 10.0 A, respectively, are shown in Fig. 6.29(b). The emission wavelength near threshold is around 5.36 μm, significantly longer than the 51.7 μm measured for the ridge waveguides fabricated from the same QCL material. Near rollover, there is an additional peak around 5.10 μm.
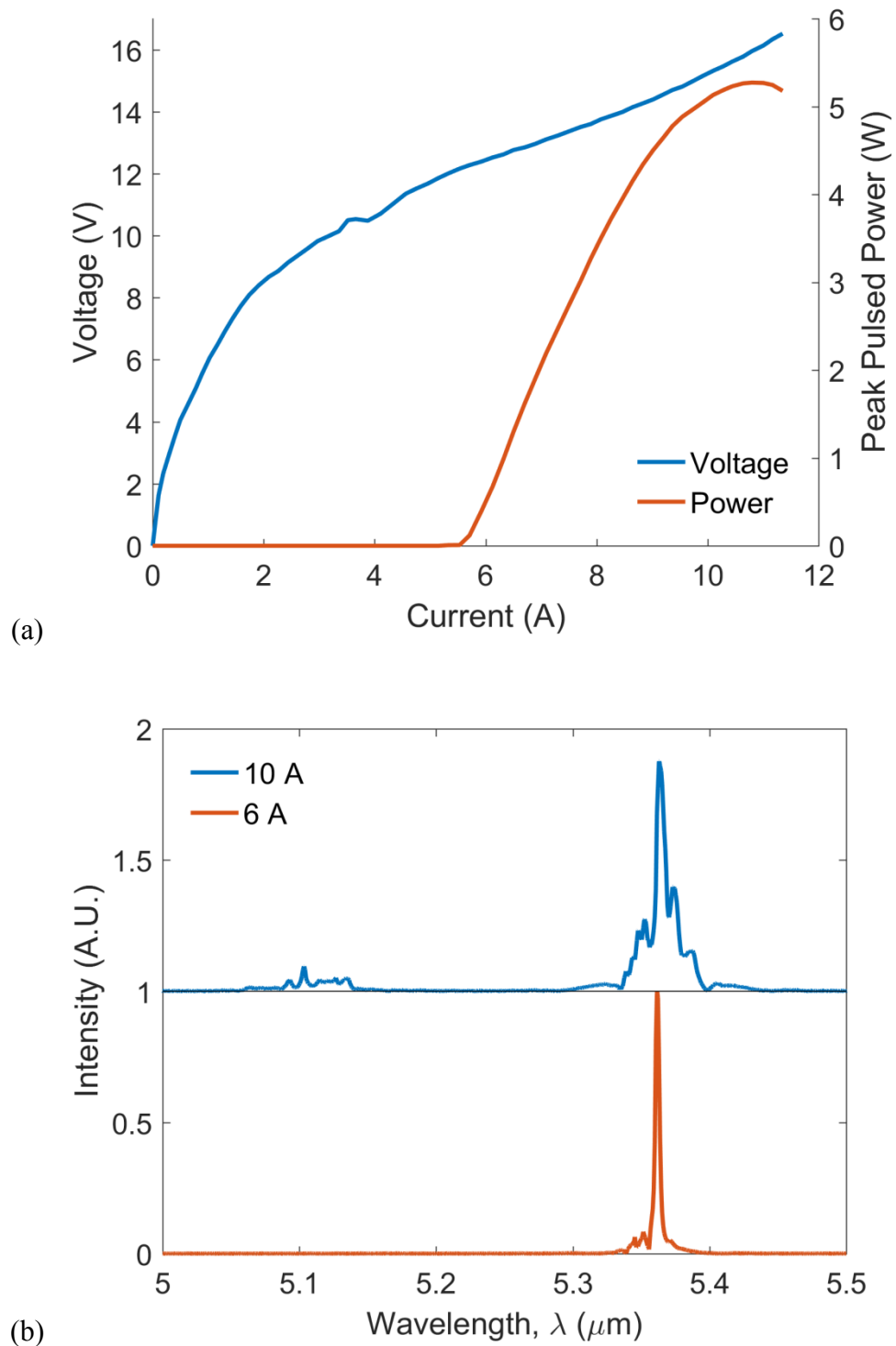
Fig. 6.29. (a) Measured pulsed LIV characteristics for a 3-element curved layer HC-PC device. (b) Measured spectra of the same device near threshold (6.0 A) and near rollover (10.0 A). The higher-current measurement is offset on the y-axis for clarity.

SEM images of previous devices showed that the outer trenches etched deeper and wider than the interelements, causing the outer elements to be slightly narrower than inner elements, by $\sim 0.2$–$0.5$ µm. The mask design for this device used $0.5$ µm wider outer elements with the intent to produce elements of equal width in the device. This device was imaged by SEM and modeled in COMSOL Multiphysics, as shown in Fig. 6.30(a) where the fitted COMSOL geometry is overlaid on the SEM image for one of the interelement regions. The simulated threshold current vs. interelement trench width ($S_t$) is shown in Fig. 6.30(b), assuming an emission wavelength of $5.36$ µm, where the dotted black line indicates the observed $S_t$ value for this device, $4.8$ µm. This device appears to be operating with an interelement width about $140$ nm narrower than that required for resonance, which is at $S_t = 4.94$ µm. As the interelement width at resonance is roughly proportional to the wavelength, the interelement region is slightly wider than that required for resonance, $4.75$ µm, for the $5.10$ µm emission near rollover.

(a)



(b)
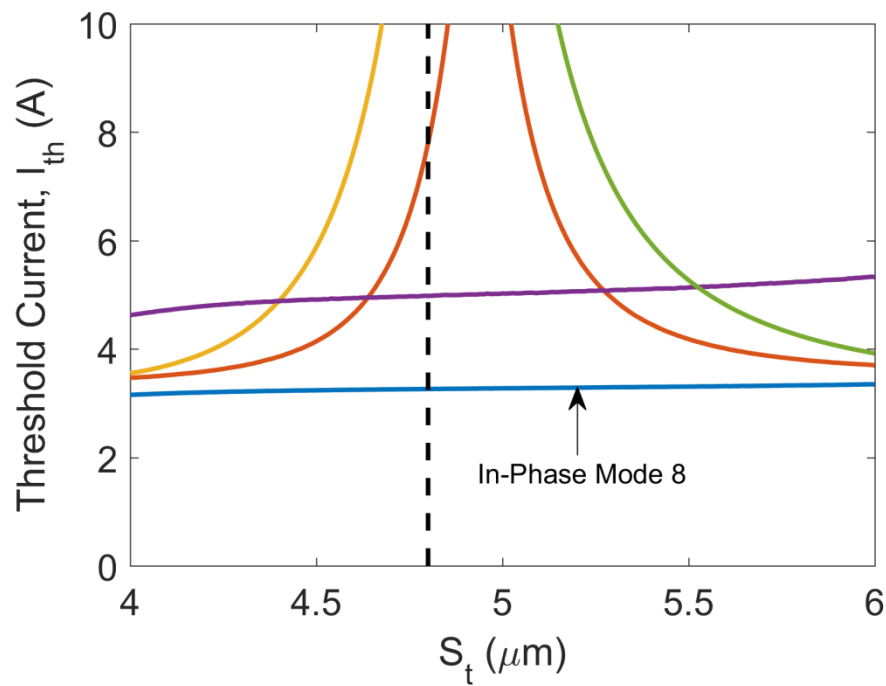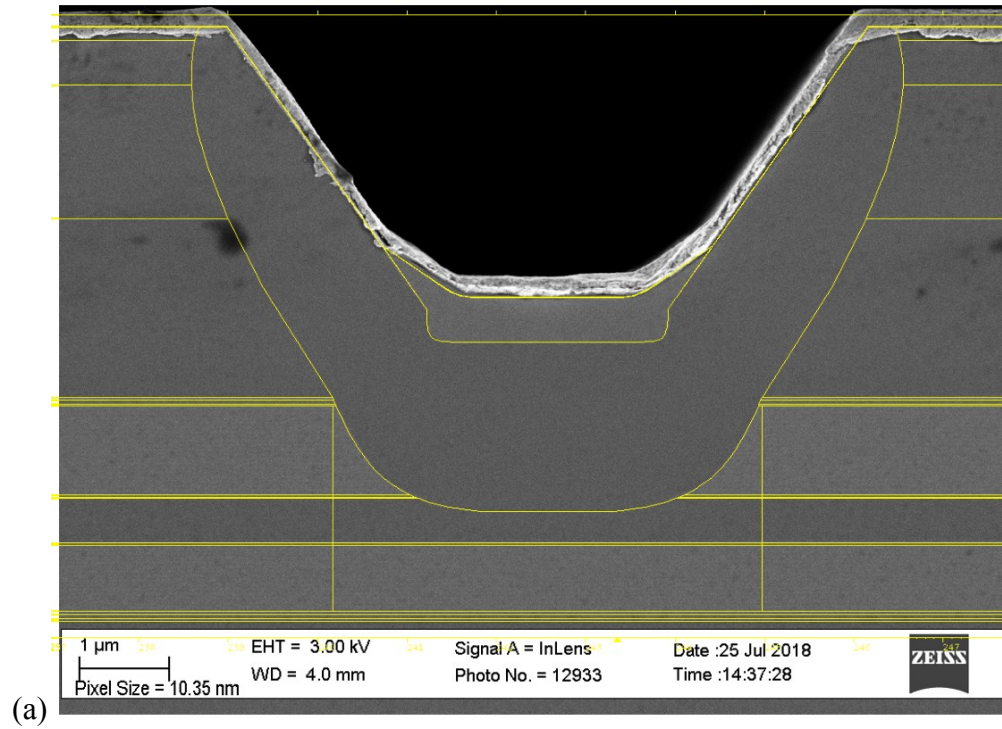
Fig. 6.30. SEM image of an interelement region of the device from Fig. 6.29 with a COMSOL model geometry overlaid on it. (b) Simulated threshold currents for modes supported by the three-element HC-PC shown in Fig. 6.29 as a function of interelement trench width, $S_t$. The dotted black line indicates the observed value of $S_t$ for this device ($S_t = 4.8$ μm).

Near-field imaging performed by collaborators, shown in Fig. 6.31(a), shows a fairly uniform near-field profile, with the outer lobes slightly more intense than the inner lobe. The resulting near-field profile of the in-phase mode modeled by COMSOL is shown in Fig. 6.31(b) for wavelengths of 5.1 μm and 5.36 μm, and is in fairly good agreement with the measured near field profile. The simulated far-field beam profile of the in-phase mode (using $\lambda = 5.36$ μm) is shown along with the measured far-field beam profile at various drive currents in Fig. 6.32. The measured far-field's central lobe is diffraction limited at 6 A, just above threshold. At 10 A and 5.1 W of output power, close to rollover, the measured far-field's FWHM is 1.12× the diffraction limit, with relatively small sidelobes.



(a)

(b)
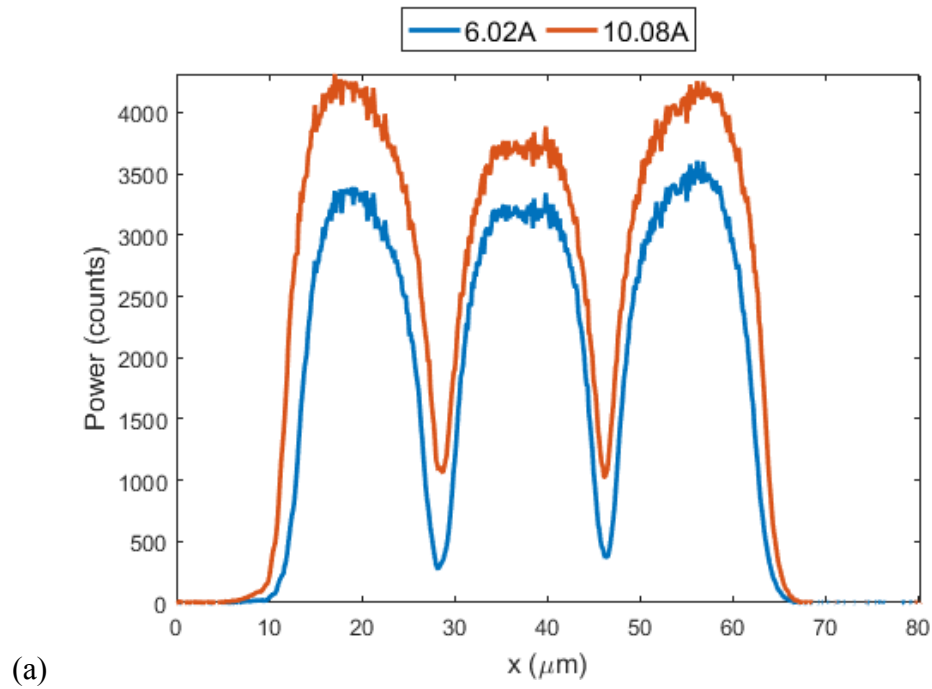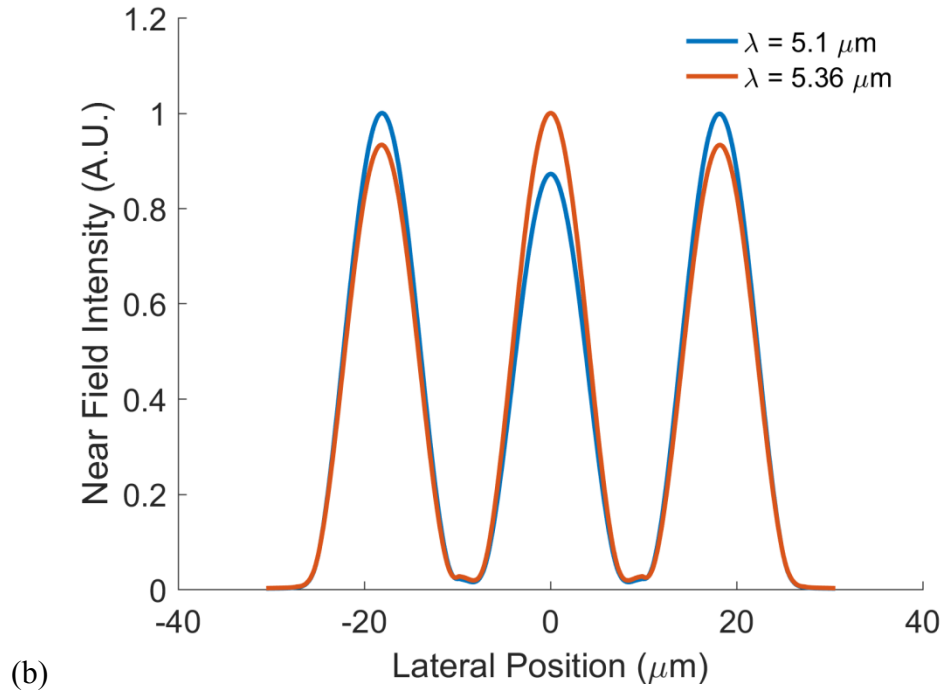
Fig. 6.31. (a) Linescan of the measured near field profile of the device in Fig. 6.29 at two drive currents in pulsed operation (200 ns-long pulse, 20 kHz repetition rate); (b) Modeled in-phase mode near-field intensity profile of the same device at wavelengths of 5.1 μm and 5.36 μm.
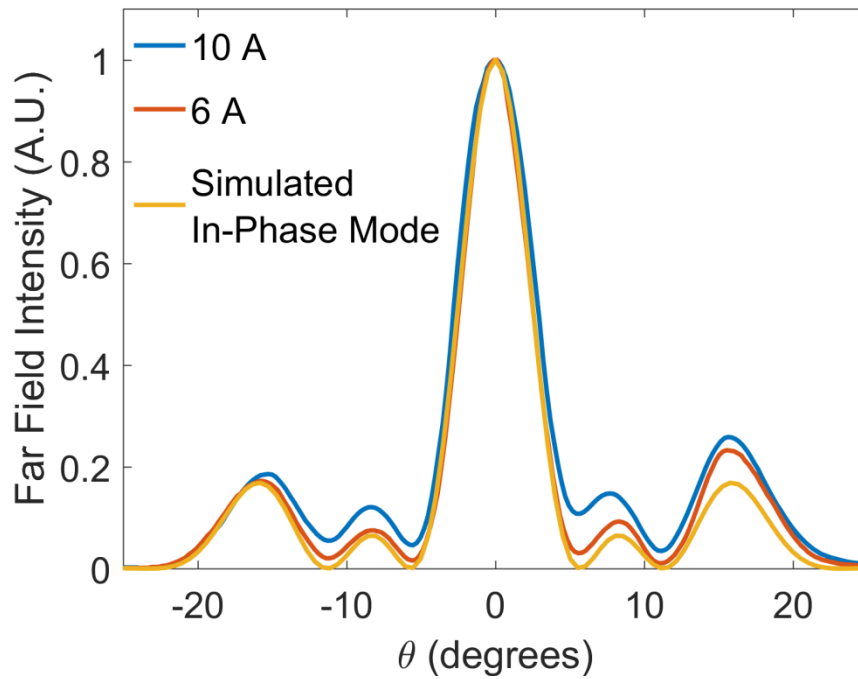


Fig. 6.32. (b) Simulated lateral far-field beam profile of the in-phase mode at the observed $S_t$ value of 4.8 μm for this device and with $\lambda = 5.36$ μm, along with the measured lateral far-field beam profile at two current drives.

## 6.8    Array CW Modeling

The model used to predict the CW performance of buried heterostructures (BHs) was modified to allow it to predict the CW or quasi-CW performance of HC-PCs. To model the quasi-CW performance of a device, we assume 1 μs-long pulses with a varying repetition rate depending on the duty cycle. A transient thermal model was used to calculate the relative temperature rise as a function of pulse duty cycle in COMSOL with a 1 μs-long pulse, and it was found that a linear fit from 100% temperature rise at 100% duty cycle to a 24% temperature rise at 0% duty cycle (effectively a one-shot pulse) would accurately model the effect of quasi-CW operation, for both a BH and an array. We assume that thermal lensing is eliminated by proper design, such as element chirping designed for the expected dissipated power levels. This model does not study mode competition above threshold, as in [150], and only considers the in-phase array mode, similar to how the BH model considered only the fundamental mode. Because we have found that devices with alternative packaging (from an external service) could be fit by the CW model without additional bond line resistance added, we do not add that additional thermal resistance to this model. We also assume that the stage can be improved to remove the thermal resistance added to the model for the stage/cooling system. Three-element HC-PC designs that have been found to have significant intermodal discrimination have a loss for the in-phase mode of at least 2.5 cm$^{-1}$, compared to a loss of ~1 cm$^{-1}$ found by COMSOL for BHs. Thus, we assume that the HC-PC in this model has an internal loss 1.5 cm$^{-1}$ higher than a BH, to ensure the HC-PC operates in a single mode (the loss reported by COMSOL was ignored, as we're just assuming the interelement layers could be adjusted to obtain the desired in-phase mode loss). The additional loss beyond the typical values for BHs is regarded as absorption by the metals and is not temperature-dependent. Here we initially use a three-element HC-PC to minimize heating,

though more elements were studied as well, and assume it is mounted epi-side down on a diamond submount with indium solder. The 0.5 μm-thick InP spacer in the core was found to not provide enough benefit in thermal resistance to justify the loss in the confinement factor, according to this model, so it was removed in this modeling. Additionally, as we will see, the model suggests using fewer stages is beneficial, at which point a spacer is not necessary. As no spacer was included, we assume the entire core is etched through and filled with semi-insulating InP:Fe, so that current spreading does not need to be considered.

To optimize the HC-PC, we sweep a 7-D parameter space of current, element width, number of stages, length, front facet reflectivity, injector doping, and pulse duty cycle. We assume that the injector doping affects the following: the current density due to backfilling, core region loss, and rollover current density are proportional to it; and the electrical series resistance (within the core) is inversely proportional to it. As non-uniform longitudinal gain saturation has a greater impact for long devices with high loss [80], such as an array, we limit the maximum length to 6 mm to ensure the accuracy of the model (we estimate that at this effect should not decrease the output power by more than 5% under these assumptions). For longer devices (e.g., 1 cm), the drop in power from this effect could be as much as 20%, in which case it should certainly be included.

The resulting design to maximize the average power operates in quasi-CW operation with a pulse duty cycle of 86%. If the optimization is restricted to CW operation, the maximum output power drops by only 40 mW. Quasi-CW operation results in temperature variations throughout the pulse which could affect the field profile of the in-phase mode, as techniques to mitigate thermal lensing, like element chirping, can require designing around a specific operating point. Additionally, some applications may be better served by CW operation, and a CW power source

is simpler than a source that can operate at these currents and voltages with such short pulses and high duty cycle. Thus, we will consider the CW design as the optimal design. It has 22 stages, 14 μm-wide elements, a length of 6 mm, a front facet reflectivity of 4.3%, and an injector sheet doping of $1.7 \times 10^{11}$ cm$^{-2}$ (for a rollover current density $J_{max}$ of 7.2 kA/cm$^2$). The predicted maximum CW output power for this device is 6.96 W at a current of 15.5 A and voltage of 11.2 V, for a wallplug efficiency of 4.0%, while the maximum power in pulsed operation (with short pulses and low duty) is 16.0 W at a current of 20 A. Due to the width and few number of stages, its thermal resistance is only 0.76 K/W. The resulting simulated CW L-I of this device is shown in Fig. 6.33, under the cooling conditions we have been using for measuring the CW power of BHs.

Optimization of five-element arrays for CW operation was also performed with the same assumptions. The resulting device has 22 stages, 12 μm-wide elements, a length of 6 mm, a front facet reflectivity of 6.5%, an injector sheet doping of $1.6 \times 10^{11}$ cm$^{-2}$. The predicted maximum CW output power for this device is 7.98 W at a current of 20.5 A and voltage of 11.0 V, for a wallplug efficiency of 3.5%, while the maximum power in pulsed operation (with short pulses and low duty) is 20.3 W at a current of 26.7 A. Its calculated thermal resistance is only 0.61 K/W. The simulated CW L-I curve for this device is shown in Fig. 6.33 as well. An in-phase modal loss of 2.5 cm$^{-1}$, the same as the three-element array, was assumed, which would result in worse intermodal discrimination for the larger array.

As a comparison, the same optimization was run for a single-mode BH (the maximum width was limited to 5 μm to ensure single-mode operation) mounted epi-side down on an indium-coated diamond submount, with the same assumptions on improvements in packaging. The maximum number of stages was limited to 40 as fewer stages is preferable for growth time

and to prevent strain relaxation. The resulting BH has 40 stages, is 5 µm-wide, has a length of 6 mm (again, the maximum allowed in the optimization to ensure a fair comparison), a front facet reflectivity of 2% (the minimum bound of the optimization as lower reflectivities are difficult to achieve in practice), an injector sheet doping of $1.8\times10^{11}$ cm$^{-2}$, and is run in CW operation. The model suggests that quasi-CW operation is never preferable for such narrow BHs, as they have quite good thermal conductance. The predicted maximum CW output power for this BH is 3.3 W at a current of 1.8 A and voltage of 18.7 V, for a wallplug efficiency of 9.7%, while the maximum power in pulsed operation is 4.8 W at a current of 2.3 A. Its thermal resistance is calculated to be 3.4 K/W. The simulated CW L-I curve is shown along with the arrays optimized for CW operation in Fig. 6.33. If the maximum number of stages is relaxed to 80, the resulting optimized BH has 80 stages, is 5 µm-wide, and the improvement in maximum CW power is 0.4 W, to 3.9 W. In addition to the reasons to not want a thicker core above, the minimum width for single-mode operation with such a thick core region is unknown, as the thicker core improves the confinement and could allow the 1$^{st}$-order lateral mode to lase at 5 µm-wide.
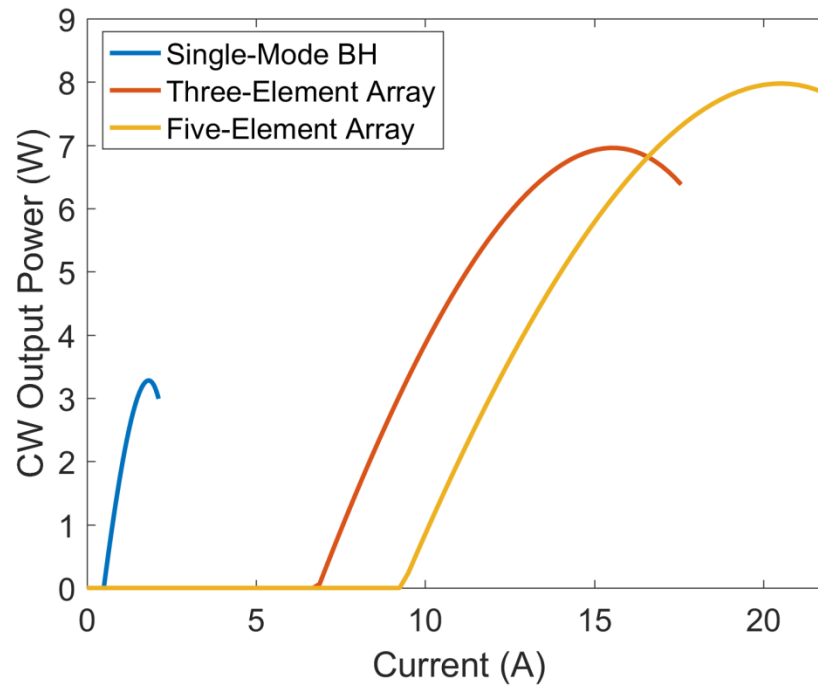
Fig. 6.33. Simulated CW L-I of a three-element HC-PC, five-element HC-PC, and a BH, all optimized to maximize the CW output power while maintaining single mode operation.

This modeling suggests that an optimized single-mode HC-PC running in CW operation should be able to emit about 2.1-2.4× higher power than an optimized single-mode BH from the same material (~3.3 W vs. ~ 7.0 W or 7.9 W). If more efficient or less temperature-sensitive core material is used, the array will improve more than the BH as thermal effects are the primary limiting factor for these larger-volume devices. Arrays with more elements are also likely to be more favored if the effects of heating can be reduced. The validity of the assumption on modal losses for the in-phase mode to maintain single-mode operation is not well known. An above-threshold mode competition model or further experimentation could help determine the necessary intermodal discrimination to maintain single-mode operation.

## 6.9    Conclusions

In conclusion, we have demonstrated five-element HC-PC QCL devices which operate predominately in an in-phase array mode up to at least 5.1 W peak pulsed output power. Analysis indicates that the devices are operating near the resonance condition for the in-phase leaky-wave coupled array mode. Spectrally-resolved near- and far-field measurements were taken of these devices. Near threshold the devices operate predominately in an in-phase mode, and with increasing drive above threshold significantly more power originates from lasing of competing array modes. The near- and far-field beam patterns vary across the spectra of the devices. The simulated competing array modes composed of coupled fundamental modes can be used to fit the measured near- and far-field beam patterns, indicating that no array modes composed of higher-order element modes are lasing. An optimized design is shown to provide large intermodal discrimination for sole in-phase mode operation across the full spectrum of the QCL core-region material, supporting the fact that a phase-locked laser array can operate with full spatial coherence in the absence of full temporal coherence. A resonant three-element HC-PC QCL device was demonstrated based on the optimized design, which emits a nearly diffraction-limited beam at high powers despite its broad spectrum. Modeling suggests these phase-locked arrays should be capable of emitting over two times higher single-mode powers than buried heterostructures. Further coherent-power scaling is expected by increasing the number of array elements, improving the device packaging, and producing a geometry optimized for resonant in-phase mode operation.

# Chapter 7 – Introduction to Distributed Feedback Quantum Cascade Lasers

## 7.1    Introduction

For the generation of high power, continuous-wave (CW), and coherent light, surface-emitting lasers, or surface-emitters (SEs), have many advantages over edge-emitters. They have a larger emitting aperture resulting in a narrower beam and lower optical power density, which improves reliability; scalability at the wafer level is possible; packaging can be simplified due to not requiring cleaved facets [151]; and they can be designed so that the emitting facet (and any coatings on it) does not heat as much as in an edge-emitter, which is a source of degradation for quantum cascade lasers (QCLs) [81], [152]. Additionally, surface-emitters can be combined with solutions for lateral coherent power scaling, such as high-index-contrast photonic crystals, for multi-watt CW diffraction-limited power [35]. The most common type of surface-emitter is a vertical-cavity surface-emitting laser (VCSEL), in which light propagates in the transverse direction. However, as discussed in Ch. 2, QCLs require a transverse component to the electric field, which is generally not possible in a typical VCSEL configuration. One vertical-cavity QCL has been proposed using a subwavelength monolithic high-refractive-index contrast grating to enable the required electric field component [48], though this has not been experimentally demonstrated. Thus, a different type of device is typically used which can emit light through the surface while the light propagates horizontally (in-plane). Incorporating a diffraction grating into the waveguide structure of a QCL (so-called grating-coupled surface-emitting laser, or GCSEL) can allow surface emission while still allowing for in-plane propagation, and is the most common solution for QCLs.

This chapter introduces the basic physics behind a GCSEL, briefly reviews the literature on GCSELs, and discusses methods for modeling such devices. The simplest method, known as coupled-mode theory, will be discussed in detail. A fundamental problem with these devices, their double-lobed beam pattern, will be explained and several methods for correcting this that have been reported in the literature will be presented.

## 7.2 Diffraction Gratings and Distributed Feedback

Fig. 7.1 below shows a schematic of a plane wave incident on a diffraction grating. When the angle of the incoming and outgoing waves satisfy the condition that the path length difference between regions of the waves incident at the same point of the grating in two different periods is an integer multiple of the wavelength in the medium, the reflected waves from the multiple interfaces will constructively interfere and the wave will 'diffract' at this angle. This condition is known as the Bragg condition. By examining Fig. 7.1, one can see that the Bragg condition is:

$$\Lambda \sin \theta_i - \Lambda \sin \theta_d = m\lambda \tag{7.1}$$

Each of these angles at which the Bragg condition is satisfied is known as a diffraction order. That is, each $m = 0, \pm1, \pm2, \dots$ corresponds to a different diffraction order. Thus, for a single incident wave, many diffracted waves could be emitted from the grating at different angles.
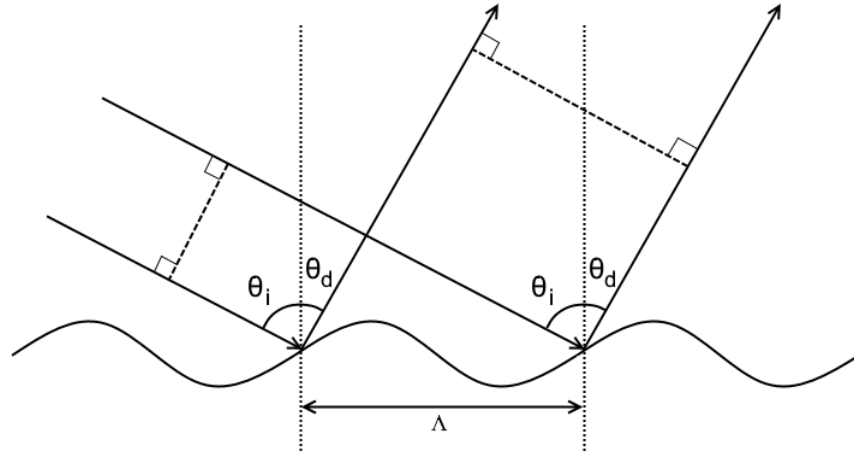
Fig. 7.1. Schematic of a reflective diffraction grating.

When a diffraction grating is placed near a waveguide, if a diffraction order exists in which the incoming and outgoing waves from the waveguide mode are traveling in nearly opposite directions, a forward propagating wave will slowly be reflected back into a backward propagating wave as it moves forward. This is known as 'distributed feedback,' or DFB. Semiconductor lasers can employ this technique in place of conventional mirrors to form an optical cavity. In some cases in this type of configuration, the electromagnetic wave is not propagating when it impinges upon the grating. Rather, it is evanescent, and thus the description above based on the angle of the incident plane wave does not apparently apply. The Bragg condition can instead be written using the propagation constant (longitudinal component of the wavevector) of the waves:

$$\beta_i - \beta_d = mK_0 \tag{7.2}$$

where $K_0 = 2\pi/\Lambda$ is the grating wavenumber and $\beta_i$ and $\beta_d$ are the propagation constants of the incident and diffracted waves. This formulation can apply whether the waves are propagating or evanescent in this region. The propagation constant for a mode is equivalent to $\beta_i = kn_{eff}$, where $n_{eff}$ is the effective index of the mode.

The grating is frequently referred to by the order of the diffraction which results in the incoming and outgoing waves travelling in opposite directions (ie. $\beta_i = -\beta_d$). For example, a 1st-order grating has a period $\Lambda = \lambda/(2n_{eff})$, where $\lambda$ is the vacuum wavelength. Then, for the 1st diffraction order ($m = 1$), the Bragg condition is satisfied for $\beta_i = -\beta_d$:

$$mK_0 = 1 \times \frac{2\pi}{\Lambda} = \frac{2\pi \times 2n_{eff}}{\lambda} = 2kn_{eff} = 2\beta_i = \beta_i - \beta_d \qquad (7.3)$$

An $m^{th}$-order grating then has period $\Lambda = m\lambda/(2n_{eff})$. For a 2nd-order grating, the 1st diffraction order has no longitudinal component to its propagation, or $\beta_d = 0$:

$$\beta_i - \beta_d = 1K_0 = \frac{2\pi \times 2n_{eff}}{2\lambda} = kn_{eff} = \beta_i \qquad (7.4)$$

Thus, this diffraction order travels directly away from the grating in the transverse and/or lateral directions, with no longitudinal component to the emission. This produces surface or substrate emission in a GCSEL when the grating is placed above the waveguide in a semiconductor laser.

## 7.3 Prior Work on GCSELs

DFB lasers and GCSELs have been studied since the 1970s [153]–[157], with the focus originally on transverse electric (TE)-polarized near-infrared-emitting interband lasers. Due to the feedback occurring only for this narrow Bragg condition, they produce very narrow linewidths [153], and are sometimes called 'single-frequency' lasers. They particularly have applications in telecommunications and spectroscopy, where narrow linewidths are important due to chromatic dispersion and narrow absorption peaks, respectively. For QCLs, a narrow spectrum is needed in such applications as trace gas sensing, industrial process monitoring, breath analysis, free-space communications, and pollution monitoring.

It has been found both theoretically and experimentally that GCSELs favor lasing in a longitudinally antisymmetric mode, which produces a double-lobed far field [158]. The reason

for this is that the infinite antisymmetric mode typically has lower loss than the symmetric mode, since it does not radiate light and thus only has absorption loss. The finite antisymmetric mode, then, has the lowest loss and is thus favored to lase, but a lower radiation loss results in it emitting less light, resulting in poor efficiency in addition to the double-lobed beam profile.

Another problem that DFBs in general have is that reflections from the facets can have a tremendous impact on the performance of the device [63], [159], [160]. Depending on where in the grating the device is cleaved, the phase of the reflection will cause the coupling between the modes to drastically change. Edge-emitting DFBs require the mode interact with the facet, so can use an anti-reflective coating, but they must be extremely low reflectance to avoid affecting the device. GCSELs can avoid having the mode interact with the facet at all if the mode is absorbed or reflected back by unpumped sections with a grating, which we call 'distributed Bragg reflectors' or DBRs, before reaching the facet.

Prior to this work, there have been several solutions implemented to attempt to correct this issue. A $\pi$-phaseshift in the grating at the center of the device flips the phases so that each half emits light in phase with the other, which allows constructive interference normal to the surface and thus produces a single-lobed beam [161]–[164]. However, the emitted near field still has a null in the center, which produces shoulders in the far field beam pattern and thus has a less than 100% fill factor (fraction of emitted intensity in the main lobe of the far field). Additionally, this method does not affect the outcoupling efficiency at all, which is low for the antisymmetric mode as mentioned above. Another possibility is to use a chirped grating corresponding to a distributed $\pi$-phaseshift [151], [165], which can produce a single-lobed far field but in a relatively broad beam for the size of the emitting aperture.

With the advent of QCLs in the mid '90s, GCSEL analysis and design turned to devices generating transverse magnetic (TM)-polarized light [166]. Surface-emitting DFB mid-IR-emitting QCLs that have been reported include: two-dimensional (2-D) photonic-crystal structures [167], air-metal/semiconductor gratings [168], metal/semiconductor gratings for emission only through the substrate [169], [170], metal/semiconductor biperiodic gratings [171], and all-semiconductor gratings [172], [173]. By and large the antisymmetric mode was found to be favored to lase, just like for TE-polarized GCSELs, with two exceptions: (a) excitation of a $2^{nd}$-order DFB region for outcoupling from a $1^{st}$-order DFB laser [170] which gave a single, diffraction-limited beam for only relatively short ($\leq 200$ μm) apertures; and (b) an edge- and surface-emitting device [173] that provided 100 mW CW surface-emitted power in a near-diffraction-limited beam, with significant power being emitted out of the edges, and occasional two-lobed beam patterns due to uncontrolled facet reflections. 500 mW of CW surface-emitted power was reported from ring-cavity devices [172], but with a complex far-field beam pattern indicative of operation in a high-order mode. More recently, ring-cavity GCSE QCLs have provided a symmetric-like, multi-lobe beam pattern, as a result of employing two $\pi$ phase shifts and a linear-polarization scheme [174], or by using an off-center grating [175]. THz-emitting SE-DFB QCLs have been found to operate in the antisymmetric mode as well with the solution for single-lobe operation being either a central $\pi$ phase shift [176], [177] or symmetric-mode selection via dual-slit unit-cell gratings [178] or gratings chirped from their centers to their edges [179]. Furthermore, by using resonant leaky-wave coupling [26], [27], 2-D GCSE THz-emitting QCLs emitting in diffraction-limited beams have been demonstrated [180], [181].

## 7.4 Coupled-Mode Theory

The distributed feedback mechanism has been frequently studied using a technique called 'coupled-mode theory' (CMT) [153]. In CMT, differential equations relate the amplitudes of a forwards and backwards propagating wave which are constantly feeding into each other throughout the structure. The amplitudes of these waves are a function of longitudinal position, $z$, and are typically referred to as $R(z)$ and $S(z)$ for the right- and left-propagating waves, respectively. Equations (8.5)-(8.6) show a typical incarnation of these equations [158]:

$$\frac{\partial R(z)}{\partial z} - [\alpha(z) + i\delta + i\zeta]R(z) = i\kappa S(z) \tag{7.5}$$

$$-\frac{\partial S(z)}{\partial z} - [\alpha(z) + i\delta + i\zeta]S(z) = i\kappa R(z) \tag{7.6}$$

$\kappa$ is known as the coupling coefficient, and is the rate at which the power in a wave traveling in one direction is transferred to the wave traveling in the opposite direction. $\zeta$ is known as the correction factor, and is related to the detuning and gain/loss of the wave when it does not diffract. $\alpha$ and $\delta$ are the loss and 'detuning' of the mode of the finite length structure. 'Detuning' is the difference in propagation constant from that required to meet the Bragg condition. Typically, for optimal performance $|\kappa|L$, that is, the magnitude of the coupling coefficient multiplied by the length of the DFB region, is unity [153]. When $|\kappa|L \ll 1$, the device is undercoupled, which means there is not enough feedback and the threshold will be high and/or Fabry-Perot modes may be able to lase. When $|\kappa|L \gg 1$, it is overcoupled, which results in the longitudinal mode being highly peaked in the center of the device. This leads to longitudinal gain spatial hole burning (GSHB), where the gain in the center is completely saturated and some of the gain near the ends of the device is unused, allowing other modes to lase above threshold if they have higher intensity in these regions (like Fabry-Perot modes). However, if the device has antireflective coatings at the facets, Fabry-Perot modes can still have high enough thresholds that

this is not an issue. Additionally, if the device is meant to be an edge-emitter, the intensity at the edge may be very low, resulting in a low power device. When $|\kappa|L \approx 1$, the mode profile is fairly uniform, in general, so that gain spatial hole burning is avoided.

These differential equations can be solved using a transfer matrix method [161]. We use the transfer matrix method to solve for the grating-related (intensity) loss coefficient, $2\alpha$, which is part of the *longitudinally-local* (i.e., only in current-pumped regions, which we will refer to as the 'DFB regions') threshold gain $g_{th}$, that, for interband-transition devices, is given by:

$$g_{th} = 2\alpha + \frac{\alpha_i}{\Gamma_{lg}} \tag{7.7}$$

where $\alpha_i$ is the internal cavity loss, assuming this is not included in calculating the infinite mode losses, and $\Gamma_{lg}$ is the percentage of field intensity residing in the DFB regions longitudinally. Then, the threshold current density is:

$$J_{th} = \frac{g_{th}}{\Gamma g} \tag{7.8}$$

where $\Gamma$ is the 2-D (transverse and lateral) optical confinement factor and $g$ is the differential gain coefficient. The corresponding calculations for a QCL will be discussed in the following chapter.

## 7.5 Methods for Calculating the Coupling Coefficient

Several methods for calculating the coupling coefficient have been developed. Some are only accurate under specific conditions, such as for low-index-contrast gratings, or only for shallow gratings. Such assumptions will be described for each method as necessary.

### 7.5.1 Bandstop Method

As initially presented by Kogelnik and Shank [153], the coupling coefficient can be calculated by solving for allowed eigenmodes using periodic boundary conditions for the chosen

grating order. Then two fundamental transverse modes are found across a stopband in the optical bandstructure. The coupling coefficient is:

$$\kappa = \frac{n\Delta\omega}{2c} \tag{7.9}$$

where $n$ is the effective index of the unperturbed mode (e.g., when the grating depth is zero), $\Delta\omega$ is the difference in angular frequency between the two modes, and $c$ is the speed of light. According to [158], the coupling coefficient can be found by:

$$Re(\kappa) = \frac{-(\Delta k^+ - \Delta k^-)K_0}{2k_0} \tag{7.10}$$

$$Im(\kappa) = \frac{\alpha^+ - \alpha^-}{2} \tag{7.11}$$

where $\Delta k$ is the change in wavenumber from the design wavenumber $k_0$, $K_0$ is the grating wavenumber, equal to $2\pi/\Lambda$. These are actually equivalent to (7.9) when the angular frequencies are considered to be complex eigenfrequencies of the modes. The modes can be solved for using a variety of methods. A Floquet-Bloch formulation using only a single wave in each direction can be used, as in [182], or a more accurate version using additional higher order waves as in [158], or the finite element method could be used, as described using COMSOL Multiphysics below. Using the finite element method inherently incorporates higher order waves, but the accuracy is limited by the mesh resolution. For high-index-contrast or metal-semiconductor gratings, a method including higher-order waves is necessary to obtain an accurate solution.

To utilize COMSOL Multiphysics for determining $\Delta\omega$ for waveguide modes, a 2-D model of the waveguide with a single period of the grating is used. Anti-periodic (periodic) boundary conditions are used at the sides of the model, using the same orientation as Fig. 7.2 below, to force the 1st-order (2nd-order) Bragg condition to be satisfied. For a 1st-order grating, the top and bottom boundary conditions can be set to be perfect electric conductors (PECs) provided they are sufficiently far away from the waveguide, as all diffraction orders in the outer

layers of the positive-index-step waveguide are evanescent for this grating condition. For $2^{nd}$-order gratings, the scattering boundary condition can be used, which is reflectionless for a normally-incident plane wave, such as the diffracted surface emission. The mesh is created such that it is identical along both borders of the anti-periodic or periodic boundary condition to ensure that condition can be maintained. For TM (TE) polarization, the model is set up to solve for only the in-plane components (out-of-plane component) of the electric field. An eigenfrequency analysis is used to solve for the two desired modes which define $\Delta\omega$. The real and imaginary parts of the two eigenfrequencies are converted into detuning and loss parameters, both in units of $cm^{-1}$, and then inserted into the equations for calculating the coupling coefficient, (7.10)-(7.11), and correction factor, (39)-(40) in [158].

The longitudinally finite mode calculated by CMT can be considered to be a linear combination of the two infinite modes throughout the length of the device. For a $2^{nd}$-order grating, the infinite modes can be considered 'symmetric' and 'antisymmetric' modes [158], as shown in Fig. 7.2.
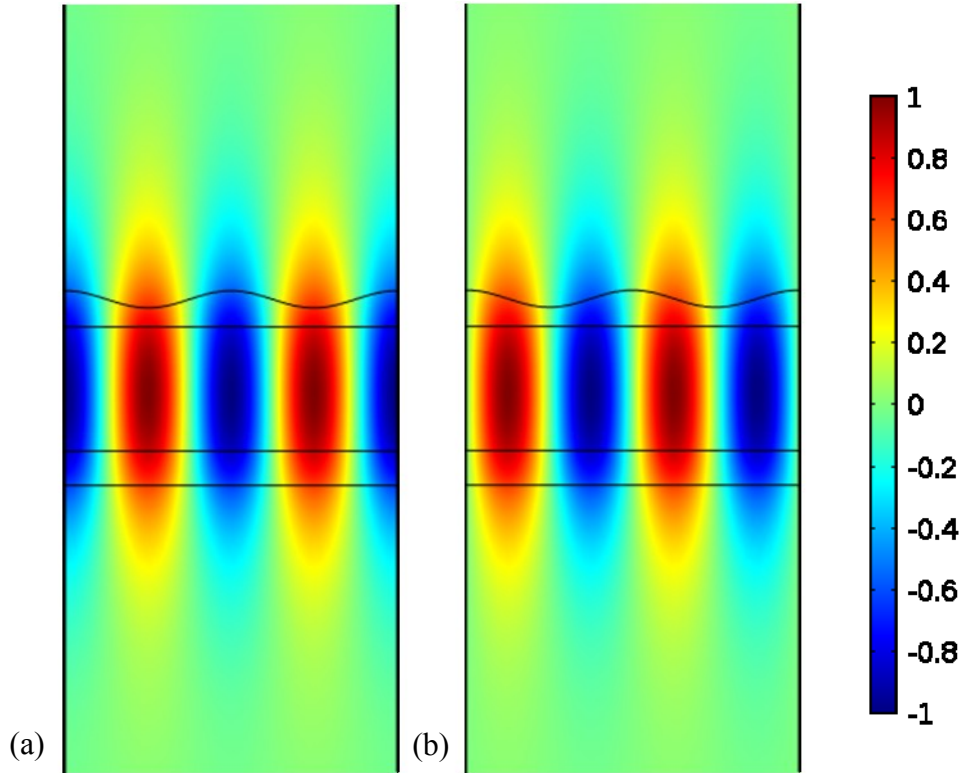
Fig. 7.2. Schematic of the amplitudes of the (a) symmetric and (b) antisymmetric modes in an infinitely-long 2$^{nd}$-order DFB laser.

Only the symmetric mode of an infinite device can produce surface emission, due to destructive interference in the antisymmetric mode. The symmetric mode amplitude of a finite-length device is equal to $R(z) + S(z)$, and the antisymmetric mode amplitude is equal to $R(z) - S(z)$. These can be used to break down the sources of loss for the finite mode, such as how the surface loss is calculated, as will be discussed later.

## 7.5.2 Overlap Method

Another common method for obtaining the coupling coefficient is to consider the grating to be a perturbation from the planar waveguide. The resulting coupling coefficient is found using a 1$^{st}$-order perturbation technique which requires calculating an overlap integral between the mode profile and index perturbation [159]. For a TE mode, the resulting formula is:

$$\kappa = \frac{k_0^2}{2\beta} \int_{corrugation} \Delta n^2(x,z)E^2(x)dx \qquad (7.12)$$

where $E(x)$ is the electric field profile of the unperturbed mode normalized such that

$$\int_{-\infty}^{\infty} E^2(x)dx = 1. \qquad (7.13)$$

In order to solve for the unperturbed mode, one assumes that the grating boundary is planar and positioned so that an equal area of each material is replaced when introducing the grating.

As is typical for perturbation analyses, it is accurate for a small perturbation (small index step and shallow grating), but is inaccurate for large perturbations, such as a metal-semiconductor gratings. An additional drawback is that this technique ignores other diffraction orders aside from whichever feeds back into the back-propagating mode. For example, [159] analyzed arbitrary-order gratings, with the conclusion that for a rectangular grating with a 50% duty cycle of even-numbered order, the coupling coefficient would be zero. However, from the analysis by [158], the surface loss of the symmetric mode is peaked around this duty cycle, so the coupling coefficient is never truly zero as the duty cycle varies. However, this surface loss is much larger for the metal-semiconductor grating analyzed in [158] than for a buried grating as in [159], so the coupling coefficient is still small for a 2nd-order buried grating of duty cycle near 50%.

### 7.5.3 Ray Optics Method

Another method for obtaining the coupling coefficient is based on using ray optics [183], [184]. This method is somewhat more intuitive than finding the stopband and is much simpler to calculate. It does not, however, incorporate higher-order waves, and so it is not appropriate for high-index-contrast (like metal-semiconductor) or even deep gratings. The basis of the ray optics method is to consider the mode as a ray bouncing down the waveguide at a particular mode bounce angle $\theta_m$. Every time the ray bounces off the grating, which it does at some spatial

bounce rate $R_m$ (the inverse of the longitudinal spacing between consecutive grating bounces), a small fraction ($\eta$) of its power is diffracted into the backwards travelling wave. The coupling coefficient is then related to this diffraction efficiency, $\eta$, and bounce rate $R_m$ by:

$$\kappa = R_m\sqrt{\eta} \tag{7.14}$$

The bounce rate is found by considering the mode 'width,' $w_m$, which is wider than the core due to penetration into the cladding, and angle the ray bounces at, $\theta_m$, as shown in Fig. 7.3 for a three-layer waveguide of indices $n_1$, $n_2$, and $n_3$ and core width $d$:
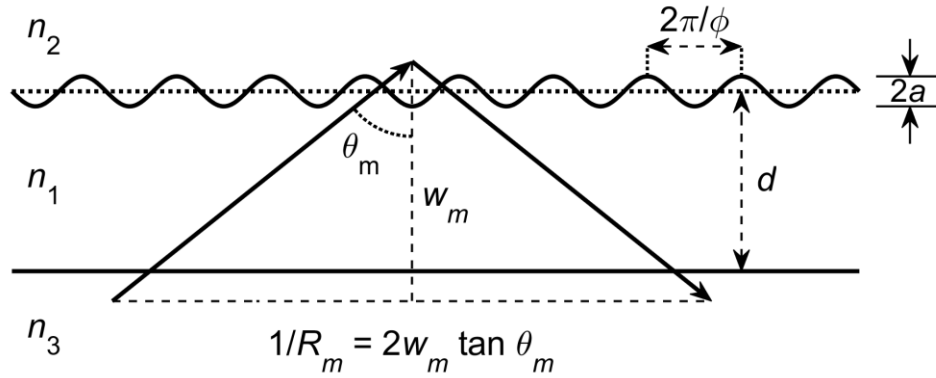


Fig. 7.3. Schematic showing the calculation of the bounce rate for a three layer waveguide.

The bounce rate is then:

$$R_m = (2w_m \tan\theta_m)^{-1} = \frac{\sqrt{n_1^2 - n_m^2}}{2n_m w_m} \tag{7.15}$$

Where $n_1$ is the core region refractive index and $n_m$ is the mode effective index. For a TE mode, the mode width is [185]:

$$w_m = d + 1/k\sqrt{n_m^2 - n_2^2} + 1/k\sqrt{n_m^2 - n_3^2} \tag{7.16}$$

and the diffraction efficiency is:

$$\eta = k^2 a^2 (n_1^2 - n_m^2) \tag{7.17}$$

where $2a$ is the grating depth. For TM polarization, the mode width and diffraction efficiency are slightly adjusted:

$$w_m = d + 1/\gamma_2 k\sqrt{n_m^2 - n_2^2} + 1/\gamma_3 k\sqrt{n_m^2 - n_3^2} \tag{7.18}$$

where

$$\gamma_x = \frac{n_m^2}{n_1^2} + \frac{n_m^2}{n_x^2} - 1 \tag{7.19}$$

and [186]

$$\eta = k^2 a^2 (n_1^2 - n_m^2)\left[1 - \frac{2n_m^2\left(\frac{n_1^2}{n_2^2}-1\right)}{(n_1^2-n_m^2)+\frac{n_1^4}{n_2^4}(n_m^2-n_2^2)}\right]^2 \tag{7.20}$$

This ray optics method for calculating the coupling coefficient can be extended to a more general and practical multi-layer waveguide, in which the grating is separated from the core by a buffer layer. The equation for diffraction efficiency at the grating, (7.20), still applies for such a structure, but the reflection and transmission between the grating and core needs to be taken into account. This can be accomplished using a transfer matrix approach [187]. In this section, we derive an analytic expression for the 1st-order TM coupling coefficient in a five-layer dielectric waveguide, schematically shown in Fig. 7.4. This work has been published in [186].
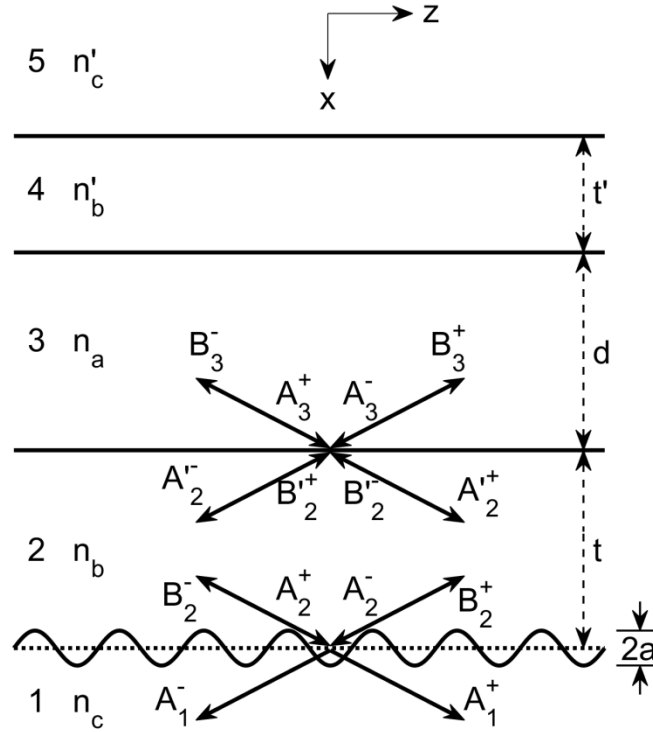
Fig. 7.4. Schematic of a 5-layer waveguide with a buffer layer between the active region and grating. For QCLs, layer 3 is actually a superlatticy called the 'core' and $n_a$ is the average refractive index of that region [86]. © 2018 IEEE

As shown in Fig. 7.4, we assume there are eight rays associated with the 3-2 interface and six rays associated with the 2-1 interface. The two rays shown in layer 1 are assumed to be evanescent. '$A$' represents the complex amplitude of rays traveling in the +x direction and '$B$' represents the amplitude of rays traveling in the −x direction. The '+' superscripts refer to rays traveling in the +z direction, and '-' refers to rays traveling in the −z direction. The subscript refers to the layer index; $A_l^+$ refers to the amplitude at the bottom of layer $l$, and $A_l'^+$ refers to the amplitude at the top of layer $l$ (similarly for $B$ and left-traveling rays). For TE polarization, the ray amplitude is the E-field amplitude, and for TM it is the H-field amplitude.

For calculating the overall diffraction efficiency, the top two layers are not considered. We model a ray incident at the lower boundary of the active region (layer 3) traveling to the

right, some $A_3^+$, and want to find the resulting $B_3^-$ at that boundary after the ray has traveled to the grating, been diffracted, and traveled back to the active region. That is, we want to find

$$\eta = |B_3^- / A_3^+|^2 \qquad (7.21)$$

Across an interface, the tangential components of the electric and magnetic fields must be constant. For a TE-polarized ray, these components can be found as follows:

$$E_{y,l} = A_l + B_l \qquad (7.22)$$

$$H_{z,l} = \varepsilon_0 c k_{x,l} / k (A_l - B_l) \qquad (7.23)$$

where $l$ is the layer index, $k_{x,l} = k\sqrt{n_l^2 - n_m^2}$, and $n_m$ is the effective refractive index of mode $m$. This can be written using the following 2×2 matrix, $D_l$:

$$\begin{bmatrix} E_{y,l} \\ H_{z,l}/\varepsilon_0 c \end{bmatrix} = \begin{bmatrix} 1 & 1 \\ k_{x,l}/k & -k_{x,l}/k \end{bmatrix} \begin{bmatrix} A_l \\ B_l \end{bmatrix} = D_l \begin{bmatrix} A_l \\ B_l \end{bmatrix} \qquad (7.24)$$

For TM polarization, the corresponding $D_l$ matrix is:

$$D_l = \begin{bmatrix} 1 & 1 \\ k_{x,l}/(kn_l^2) & -k_{x,l}/(kn_l^2) \end{bmatrix} \qquad (7.25)$$

The wave amplitudes on either side of an interface are then related as follows:

$$\begin{bmatrix} A_i^+ \\ B_i^+ \end{bmatrix} = D_i^{-1} D_j \begin{bmatrix} A_j^+ \\ B_j^+ \end{bmatrix} \qquad (7.26)$$

where $i$ and $j$ are layer indices, with $i = j + 1$. The resulting matrix relating them is:

$$T_{ij} = D_i^{-1} D_j = \frac{1}{2} \begin{bmatrix} 1 + \varepsilon_{ij}\frac{k_{x,j}}{k_{x,i}} & 1 - \varepsilon_{ij}\frac{k_{x,j}}{k_{x,i}} \\ 1 - \varepsilon_{ij}\frac{k_{x,j}}{k_{x,i}} & 1 + \varepsilon_{ij}\frac{k_{x,j}}{k_{x,i}} \end{bmatrix} \qquad (7.27)$$

where for TM polarization $\varepsilon_{ij} = n_i^2/n_j^2$ and for TE polarization $\varepsilon_{ij} = 1$. Propagation within a given layer $l$ is accounted for using the following matrix, $P_l$:

$$\begin{bmatrix} A_l^+ \\ B_l^+ \end{bmatrix} = \begin{bmatrix} e^{-ik_{x,l}t_l} & 0 \\ 0 & e^{ik_{x,l}t_l} \end{bmatrix} \begin{bmatrix} A'^+_l \\ B'^+_l \end{bmatrix} = P_l \begin{bmatrix} A'^+_l \\ B'^+_l \end{bmatrix} \qquad (7.28)$$

We define:

$$\beta_m = kn_a \sin \theta_m = kn_m \tag{7.29}$$

$$\sigma_0 = \sqrt{n_a^2 k^2 - \beta_m^2} = k_{x,3} \tag{7.30}$$

$$\rho_0 = \sqrt{n_b^2 k^2 - \beta_m^2} = k_{x,2} \tag{7.31}$$

$$\rho_0' = \sqrt{n_b^2 k^2 - \beta_m^2} = k_{x,4} \tag{7.32}$$

$$q_0 = \sqrt{\beta_m^2 - n_c^2 k^2} = -ik_{x,1} \tag{7.33}$$

$$q_0' = \sqrt{\beta_m^2 - n_c^2 k^2} = -ik_{x,5} \tag{7.34}$$

where $\beta_m$ is the z-axis spatial frequency and $\theta_m$ is the mode bounce angle. Here we assume that the rays are propagating in layers 2, 3, and 4, and are evanescent in layers 1 and 5, so that the resulting parameters defined in (7.29)-(7.34) are real numbers. Note that the general matrix formalism functions regardless of which layers contain propagating or evanescent waves, i.e., whether the active region has a higher or lower refractive index than the adjacent layers.

We can then compute the relationship between the forward rays at the grating interface and the boundary of the active region like so:

$$\begin{bmatrix} A_3^+ \\ B_3^+ \end{bmatrix} = T_{32} \begin{bmatrix} A_2^+ \\ B_2^+ \end{bmatrix} \tag{7.35}$$

The same equation applies for the backward-propagating rays by replacing the '+' superscripts with '-'.

The reflection and diffraction at the grating interface can be formulated using a transfer matrix as well. To find this matrix, we first write the behavior of the grating using a scattering matrix, $G_{scat}$ [39, p. 94]:

$$\begin{bmatrix} B_2^+ \\ B_2^- \end{bmatrix} = G_{scat} \begin{bmatrix} A_2^+ \\ A_2^- \end{bmatrix} = \begin{bmatrix} r & 0 \\ g & r \end{bmatrix} \begin{bmatrix} A_2^+ \\ A_2^- \end{bmatrix} \tag{7.36}$$

where the incoming rays to the grating are on the right-hand side and the outgoing rays are on the left-hand side of the equation. The diagonal elements, $r$, are the typical reflection coefficients for

a planar interface, $g$ is the amplitude ratio between the diffracted and incident rays at this interface. For TE polarization and a 1$^{st}$-order grating, these are:

$$r = \frac{\rho_0 - iq_0}{\rho_0 + iq_0} \tag{7.37}$$

$$g = \frac{\rho_0(\rho_0 - iq_0)}{\rho_0 + iq_0} a. \tag{7.38}$$

which are equivalent to (54) and (55) in [188] when the grating period is such that the 1$^{st}$-order ray is backwards diffracted. Note that the additional '$i$' terms in (7.37) and (7.38) are only due to the definition of $q_0$, which was made so that it is a real number if the ray is evanescent in layer 1. For TM polarization, these are:

$$r = \frac{\rho_0 - \varepsilon_{bc}iq_0}{\rho_0 + \varepsilon_{bc}iq_0} \tag{7.39}$$

$$g = \frac{\rho_0[\rho_0^2 + \varepsilon_{bc}q_0^2 - (\varepsilon_{bc}-1)(\beta_m^2 - \varepsilon_{bc}q_0^2)]}{(\rho_0 + \varepsilon_{bc}iq_0)^2} a \tag{7.40}$$

These also assume the 1$^{st}$-order diffracted beam is backwards diffracted (i.e. a 1$^{st}$-order grating). Note that (7.36) explicitly excludes backwards-to-forwards diffraction, from $A_2^-$ to $B_2^+$ (the 0 in the top right of $G_{scat}$). If we rearrange (7.36) to find the corresponding transfer matrix, we obtain:

$$\begin{bmatrix} A_2^+ \\ B_2^+ \end{bmatrix} = G \begin{bmatrix} A_2^- \\ B_2^- \end{bmatrix} = 1/g \begin{bmatrix} -r & 1 \\ -r^2 & r \end{bmatrix} \begin{bmatrix} A_2^- \\ B_2^- \end{bmatrix} \tag{7.41}$$

Then we can combine all the matrices required to calculate $B_3^-$ from $A_3^+$, which we call '$M$':

$$\begin{bmatrix} A_3^+ \\ B_3^+ \end{bmatrix} = T_{32}P_2 \begin{bmatrix} A_2^+ \\ B_2^+ \end{bmatrix} = T_{32}P_2 G \begin{bmatrix} A_2^- \\ B_2^- \end{bmatrix} = T_{32}P_2 G P_2^{-1} T_{32}^{-1} \begin{bmatrix} A_3^- \\ B_3^- \end{bmatrix} = M \begin{bmatrix} A_3^- \\ B_3^- \end{bmatrix} \tag{7.42}$$

where $M$ has the following structure:

$$M = \begin{bmatrix} M_{11} & M_{12} \\ M_{21} & M_{22} \end{bmatrix} \tag{7.43}$$

We are assuming the only input is $A_3^+$ with no layers above the active region for this analysis, so there are no reflections from $B_3^-$ to $A_3^-$. Thus, $A_3^- = 0$ and the top row of (51) is:

$$A_3^+ = M_{11}A_3^- + M_{12}B_3^- = 0 + M_{12}B_3^- \tag{7.44}$$

so that

$$\eta_m = |B_3^-/A_3^+|^2 = |1/M_{12}|^2 \tag{7.45}$$

is the final expression for the overall diffraction efficiency. The resulting expression for the diffraction efficiency for TM polarization is:

$$\sqrt{\eta_m} = a\sigma_0\rho_0^2 \frac{\rho_0^2+\varepsilon_{bc}^2 q_0^2-2k^2 n_m^2(\varepsilon_{bc}-1)}{\varepsilon_{ba}\sigma_0^2[\rho_0\cos(\rho_0 t)+\varepsilon_{bc}q_0\sin(\rho_0 t)]^2+\varepsilon_{ab}\rho_0^2[\rho_0\sin(\rho_0 t)-\varepsilon_{bc}q_0\cos(\rho_0 t)]^2}. \tag{7.46}$$

For TE polarization, $\varepsilon_{ab}$, $\varepsilon_{ba}$ and $\varepsilon_{bc}$ are replaced with unity, and the resulting expression is identical to (8) in [183].

The mode width, $w_m$, can be calculated from this approach as well. The general formula for the coupling coefficient, (7.14), still applies, where the diffraction efficiency used is (7.46) for TM polarization. The bounce rate, $R_m$, is given by (7.15) with $n_1$ replaced by $n_a$. Thus, the coupling coefficient $\kappa$ is given by:

$$\kappa = R_m\sqrt{\eta_m} = \frac{a\sigma_0^2\rho_0^2}{2\beta_m w_m} \frac{\rho_0^2+\varepsilon_{bc}^2 q_0^2-2k^2 n_m^2(\varepsilon_{bc}-1)}{\varepsilon_{ba}\sigma_0^2[\rho_0\cos(\rho_0 t)+\varepsilon_{bc}q_0\sin(\rho_0 t)]^2+\varepsilon_{ab}\rho_0^2[\rho_0\sin(\rho_0 t)-\varepsilon_{bc}q_0\cos(\rho_0 t)]^2}. \tag{7.47}$$

We use the 7.8μm-emitting QCL with a 1st-order buried grating shown in Fig. 7.5 [16] to verify this expression for the coupling coefficient for a 5-layer structure. The resulting coupling coefficient as a function of the grating amplitude is shown in Fig. 7.6 for the QCL structure in Fig. 7.5, and is compared against the coupling coefficient as calculated using COMSOL Multiphysics and the bandstop method described in Section 7.5.1. This assumes that the grating is sinusoidal, with the center of the grating placed at the boundary of the planar interface. The mode width is calculated numerically using this transfer matrix method, and is found to be 5.384 μm.
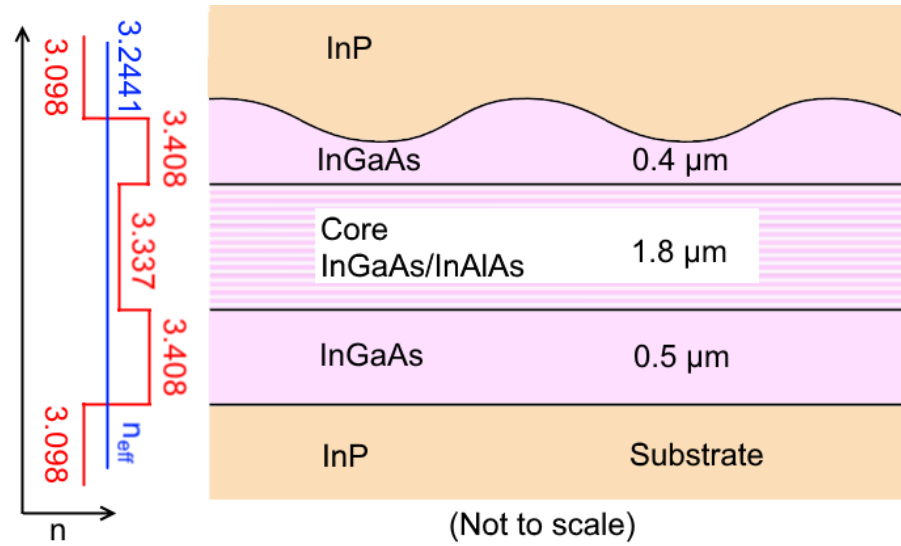
Fig. 7.5. Schematic of a 7.8µm-emitting QCL structure used for verifying the ray optics method for determining the coupling coefficient of a 5-layer TM-polarized DFB laser. © 2018 IEEE
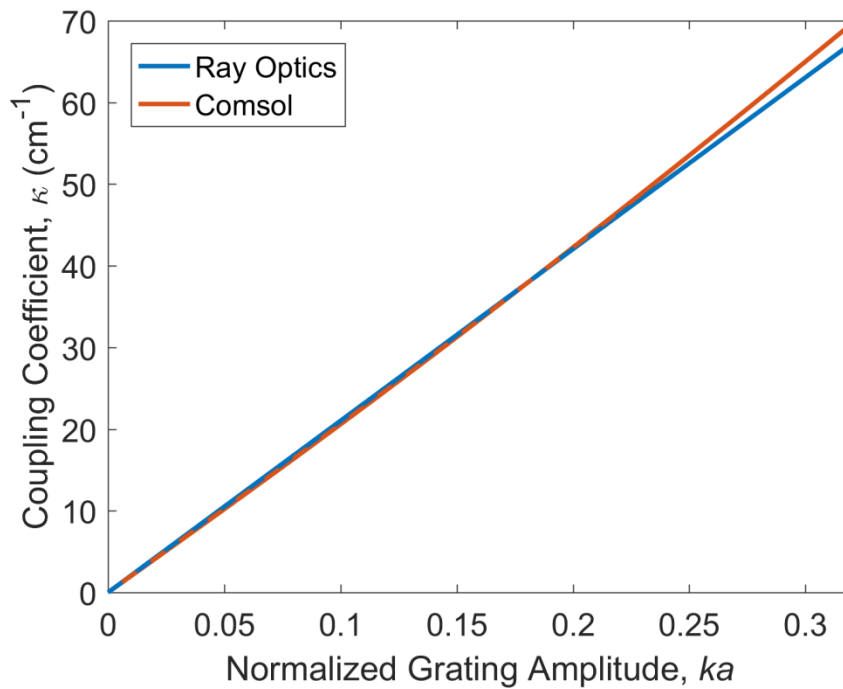


Fig. 7.6. Calculated coupling coefficient vs. normalized grating amplitude for the 5-layer waveguide structure with a 1st-order grating (as shown in Fig. 7.5) for a TM-polarized mode. The orange line is calculated from COMSOL using the stopband method described in 7.5.1 with (29), and the blue line is from the ray optics method using (56). © 2018 IEEE

It should be noted that in order to derive (7.46), diffraction from the backward ray back to the forward ray is ignored. Using a numerical analysis which includes this term (by making the top-right term of $G_{scat}$ in (7.36) be $g$), the calculated diffraction efficiency is 0.14% lower at $ka = 0.3$ compared with the approximation of (7.46), suggesting this is a reasonable approximation. In Fig. 7.6, the error in $\kappa$ for the ray optics method is -3.4% at the maximum value of $ka$ of 0.32. At this grating depth, the upper InGaAs confinement layer for this structure is entirely etched through. Thus, the grating thicknesses that can be modeled by the ray optics method are within the range of interests for most device applications using an entirely semiconductor grating.

When analyzing a $2^{nd}$-order grating, the $1^{st}$-order diffraction is first calculated, which is the surface loss, and then the $2^{nd}$-order diffraction is calculated using the $1^{st}$-order diffraction. Thus, while this method produces a real number for the coupling coefficient, the surface emission that affects the imaginary part of the coupling coefficient is still included. The matrix method for calculating the coupling coefficient structure is mostly unchanged, with the exception being that the $g$ term defined in (7.40) would be replaced with the appropriate expression for the square root of the $2^{nd}$-order diffraction efficiency.

## 7.6 Surface Outcoupling

As discussed previously, for a DFB laser with a $2^{nd}$-order grating, the $1^{st}$-diffraction order forms the surface emission for the infinite symmetric mode. The surface-emitted power causes an intensity decay as the guided modes propagate longitudinally, and can be considered as a loss mechanism per unit length of propagation, $\alpha_{surf}$. It can be calculated by Poynting's theorem as follows, which is left in generic terms due to the variety of methods and polarizations for calculating the mode [158]:

$$\alpha_{surf} = \frac{\int_{-\Lambda/2}^{\Lambda/2} -\hat{x} \cdot \mathbf{S}\, dz}{\int_{-\infty}^{\infty} \int_{-\Lambda/2}^{\Lambda/2} \frac{\epsilon |E|^2}{2} dz dx} \tag{7.48}$$

where $\mathbf{S}$ is the Poynting vector in the substrate (for substrate-side emission, otherwise air above the device for top-surface emission). In words, the surface loss is the fraction of the energy contained in the mode which is emitted through the surface per unit length.

The surface emission of the finite longitudinal mode calculated by coupled mode theory can be considered as a loss per unit length as well. Since only the symmetric mode surface-emits, only the $R(z) + S(z)$ component of the mode contributes to the surface radiation loss, which can be calculated as follows [35]:

$$\alpha_{surf,fin} = \alpha_{surf,inf} \frac{\int_{-L/2}^{L/2} |R(z)+S(z)|^2 dz}{\int_{-L/2}^{L/2} |R(z)|^2 + |S(z)|^2 dz} \tag{7.49}$$

where $\alpha_{surf,inf}$ is the surface loss of the infinite symmetric mode and $L$ is the length of the device (assuming the entire length contains the same waveguide and grating structure). This surface loss takes the place of mirror loss, $\alpha_m$, for a surface-emitter in calculating the output power or slope efficiency of the laser.

## 7.7    Conclusions

Distributed feedback and grating-coupled surface-emitting QCLs have a variety of useful applications that require narrow linewidths, particularly related to spectroscopy. They are most frequently analyzed with coupled mode theory, which can be used in a matrix form to study longitudinally complicated structures. The most important parameter in coupled mode theory, the coupling coefficient, can be found using a variety of methods. A simple ray optics based method for calculating the coupling coefficient of TM-polarized devices with a generalized waveguide and a low-index-step 1$^{st}$-order grating was developed in this work. GCSELs typically lase with a double-lobed beam pattern if special care is not taken to correct the beam. The following chapter

will detail a novel method to produce a single-lobed beam pattern while allowing for a high outcoupling efficiency and 100% fill factor in the far field.

# Chapter 8 – Single-Lobed Grating-Coupled Surface-Emitting Lasers by Surface-Plasmon Enhanced Absorption of Antisymmetric Modes

## 8.1 Introduction

This chapter presents a design for a mid-infared (mid-IR)-emitting grating-coupled surface-emitting (GCSE) quantum cascade laser (QCL) structure with inherent suppression of the antisymmetric modes, which allows symmetric-mode lasing at low (< 0.5 A) threshold currents and high (> 3 W/A) slope efficiencies [33]. The device relies on the antisymmetric modes being strongly absorbed due to resonant coupling of the (guided) optical mode to the antisymmetric surface plasmon mode of a metal/semiconductor grating. Efficient symmetric-mode operation can be obtained over controllable ranges in grating tooth height and duty cycle. In addition, the distributed feedback (DFB) grating is bounded by $2^{nd}$-order distributed Bragg reflector (DBR) gratings [151], [161]–[163]; thus, preventing uncontrolled reflections from cleaved facets which can affect the DFB operation [63], [160], [173], [189] as well as catastrophic facet degradation at high powers due the thermally-induced sheer stress [81]. By considering a 4.6 μm-emitting QCL structure which was previously reported to edge-emit watt-range continuous-wave (CW) power [138], we find that 7.03 mm-long DFB/DBR GCSE devices can have threshold currents as low as 0.45 A and slope efficiencies as high as 3.4 W/A, making it possible to obtain watts of CW diffraction-limited, single-lobe power from mid-IR surface-emitting QCLs. First, we analyze devices of infinite-length metal/semiconductor $2^{nd}$-order DFB gratings, in order to elucidate the mechanism via which the antisymmetric mode is suppressed. Then, we present the design and analysis of $2^{nd}$-order DFB/DBR devices of finite-length gratings, and provide examples of high-performance devices. Experimental demonstration of this

mechanism is presented, and finally projections of the single-mode CW power possible from devices using this are presented.

## 8.2    Surface Plasmons with Metal-Semiconductor Gratings

The antisymmetric surface plasmon mode at the interface(s) of a $2^{nd}$-order metal/semiconductor grating has its magnetic field ($H$-field) intensity nulls occur in the middle of the grating troughs and peaks (see an example in Fig. 8.1(b)). For an infinite-length grating with Ag as the metal and InP as the semiconductor and designed to be the $2^{nd}$-order DFB grating for a published [138] 4.6 μm-emitting QCL structure, we plot in Fig. 8.1(a) the wavevector of the antisymmetric surface plasmon mode as a function of grating duty cycle, defined as the percentage of metal in a grating period, and grating tooth height. A thin white line indicates the plasmon-wavevector curve corresponding to a wavelength, λ, of 4.6 μm; that is, where the DFB-QCL structure's optical-mode propagation constant matches the plasmon-mode propagation constant, and thus resonant coupling occurs between the two modes. We show in Fig. 8.1(b) the plasmon $H$-field intensity for a grating of 39% duty cycle and 0.217 μm tooth height (at λ = 4.6 μm).
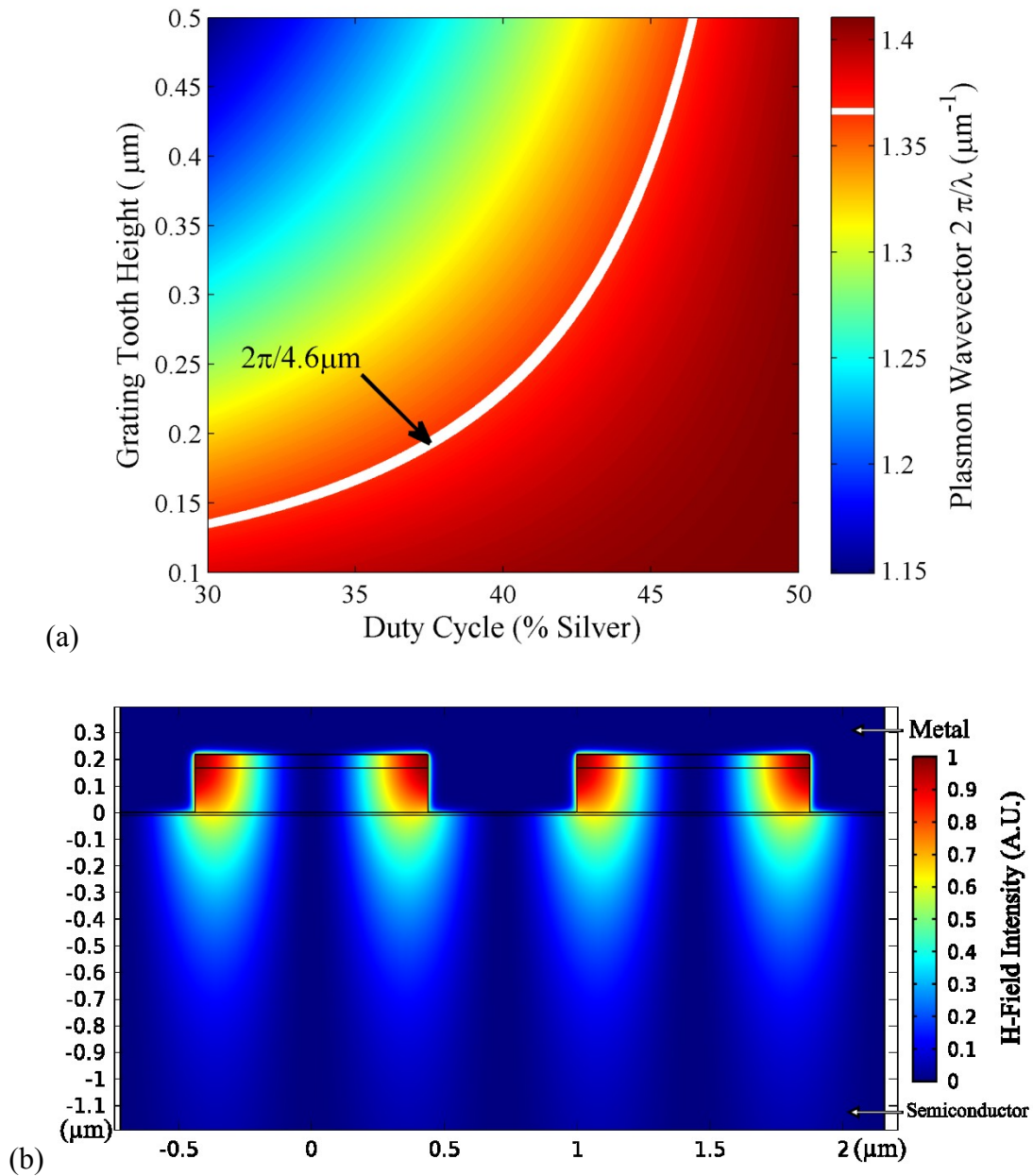
Fig. 8.1. Infinite-length grating: (a) Plasmon wavevector as function of grating duty cycle and tooth height for an Ag/InP grating designed to be a 2$^{nd}$-order DFB grating for a published 4.6 μm-emitting QCL structure [138]. The white line corresponds to resonant coupling between the (guided) optical mode and the plasmon mode; (b) *H*-field intensity pattern at a resonance point: 39% duty cycle and 0.217 μm grating tooth height, at λ= 4.6 μm.

## 8.3    DFB-QCL Structure

Next, we consider the DFB-QCL structure for which the (transverse) optical mode couples to the grating surface-plasmon modes. Coupling to the antisymmetric and symmetric plasmon modes results in antisymmetric and symmetric (longitudinally) modes of the structure. We use a 40-period, 4.6 μm-emitting QCL structure of 75% transverse optical-confinement factor Γ; essentially the same as the one published by Lyakh et al. [138]. The grating period Λ is fixed to be that ratio of the vacuum wavelength (4.6 μm) to the effective refractive index of the transverse mode, such that the $2^{nd}$-order Bragg-diffraction condition is met. For this $2^{nd}$-order DFB-QCL structure, we show in Fig. 8.2 the dispersion curves, at 39% grating duty cycle, for the antisymmetric and symmetric modes as a function of tooth height, $h$.
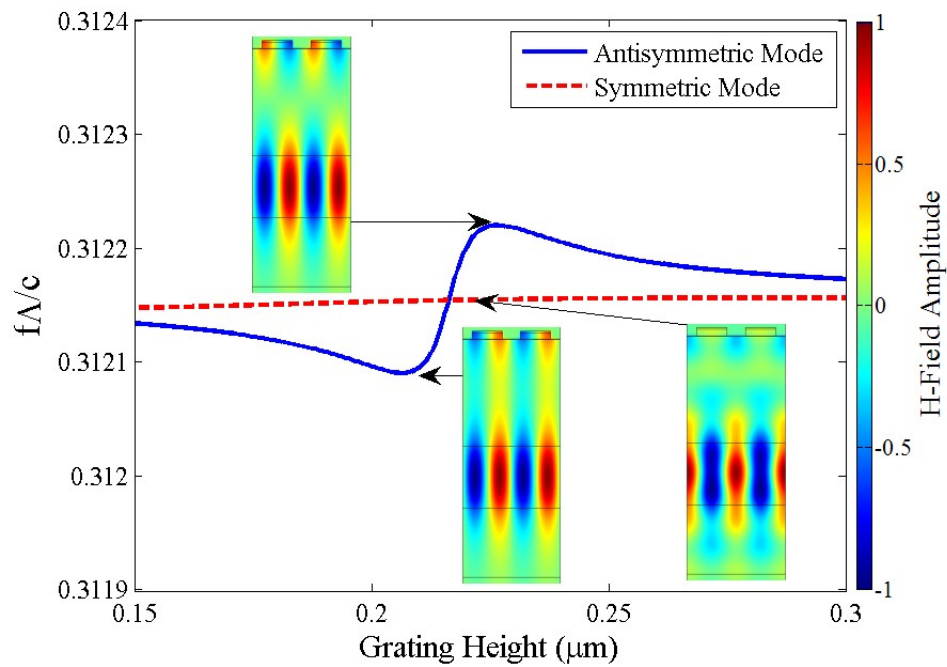


Fig. 8.2. Normalized frequencies for the symmetric and antisymmetric modes of 4.6 μm-emitting $2^{nd}$-order DFB-QCL structure, at 39% grating duty cycle, as a function of grating tooth height, $h$. Insets: H-field amplitude patterns. The antisymmetric mode is shown below and above resonance at h = 0.217 μm

As seen from the inserted pictures in Fig. 8.2, in the case of the antisymmetric mode for $h$ < 0.217 μm the guided mode couples in-phase with the antisymmetric plasmon mode, while for $h$ > 0.217 μm the guided mode couples out-of-phase with the antisymmetric plasmon mode. The symmetric mode couples weakly to the symmetric plasmon mode, as evidenced by negligible field at the grating interfaces. (However, the symmetric-mode couples strongly to the grating and is effectively outcoupled over a large range in $h$ [Fig. 8.4(b)]). Such modal behavior is somewhat similar to that for the modes of 1st-order metal/semiconductor DFB structures [190], in that the antisymmetric and symmetric modes qualitatively behave like the 1st-order DFB modes whose $H$-field maxima occur on the grating troughs and peaks, respectively (Fig. 3 in [190]).

Fig. 8.3 shows the antisymmetric-mode loss as a function of grating tooth height and duty cycle. We superimpose the white line from Fig. 8.1(b) on the locus of maximum-loss points, to highlight that the latter corresponds to resonant coupling between guided and plasmon modes.
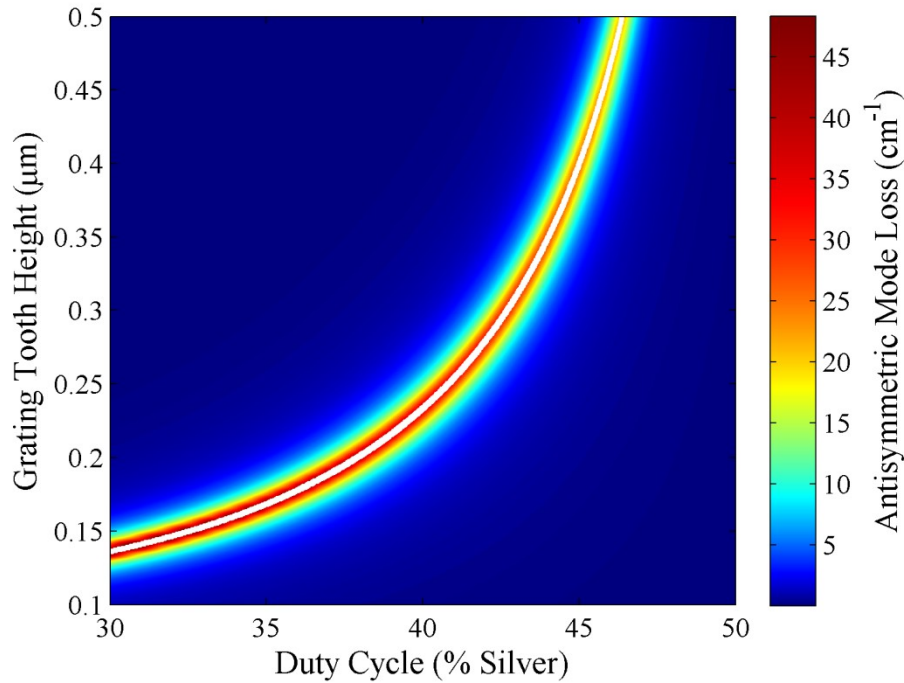


Fig. 8.3. The antisymmetric (A)-mode loss as a function of grating duty cycle and tooth height. The white line atop the locus of maximum-loss points is the same white line as in Fig. 8.1(a).

The losses for the antisymmetric and symmetric modes are shown in Fig. 8.4, as the grating height varies when the duty cycle is 39%. The antisymmetric -mode loss is only absorption loss which is peaked at resonance (*i.e.*, at $h = 0.217$ μm). (The antisymmetric mode has no surface-emission loss in infinite-length devices) [158]. The symmetric mode has both surface-emission and absorption losses; the latter being negligible ($\sim 0.1$ cm$^{-1}$) due to weak symmetric-mode coupling to the symmetric plasmon mode. The coupling coefficient at $h = 0.217$ and a duty cycle of 39% is $\kappa = 0.1929 - i9.231$ cm$^{-1}$, as calculated by (7.10) and (7.11). We note that significantly enhanced absorption of incident TM-polarized light, due to strong coupling to a surface-plasmon mode of a 2$^{nd}$-order DFB metal grating, has been previously obtained [191] for proposed high-performance mid-IR photodetectors.
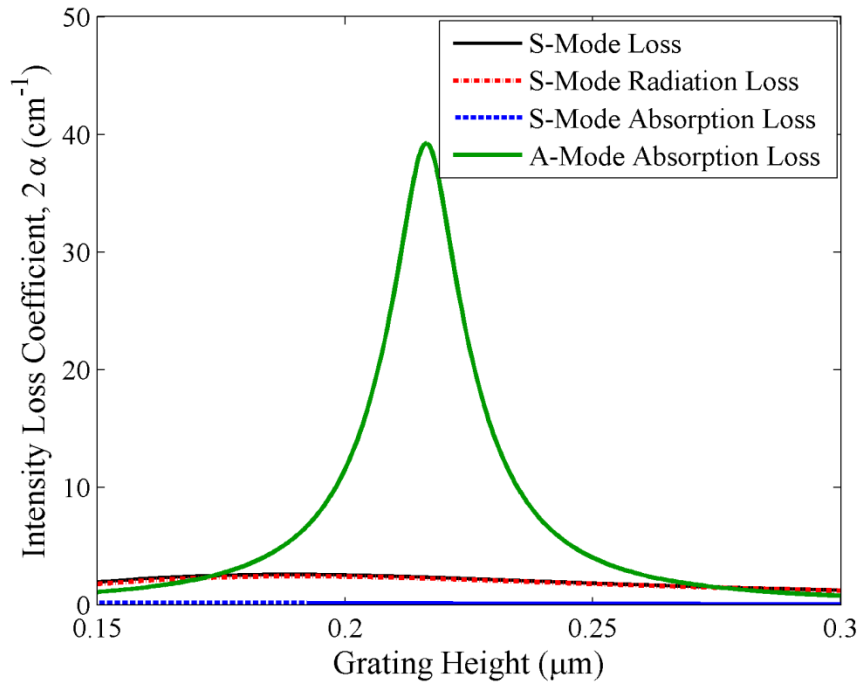


Fig. 8.4. Intensity loss coefficient [161] for the symmetric and antisymmetric modes as a function of grating height when the grating duty cycle is 39%. The symmetric-mode absorption loss is negligible.

## 8.4    Finite Length DFB-QCL

Next, we study a finite-length buried heterostructure (BH) device with DBR regions placed at the ends of the DFB region, shown in Fig. 8.5, just as done for high-power, near-IR-emitting GCSELs [151], [161]–[163]. The only difference between the DFB and DBR regions is that the DFB region is pumped with current, while the DBR regions are not. A longitudinal cross-section is shown in the insert of Fig. 8.5. A 40-period InGaAs/InAlAs core region of a high-CW-power, 4.6 μm-emitting QCL [138] is considered. Atop an InP cladding layer the metal/semiconductor grating is placed. To control the tooth height, a 10 nm-thick InGaAs etch-stop layer (visible in Fig. 8.1(b)) is introduced between the InP cladding layer and the grating. In addition, at the top of the semiconductor portions of the grating, a 50 nm-thick $n^+$-InP layer is added (also visible in Fig. 8.1(b)) to ensure good electrical contact. Ag is used as the primary grating metal since it is found, at $\lambda = 4.6$ μm, to provide less absorption than Au while still providing strong grating light-outcoupling efficiency. A 2 nm-thick Ti layer is used below the Ag, at the grating troughs and peaks, to promote good metal-contact adhesion.
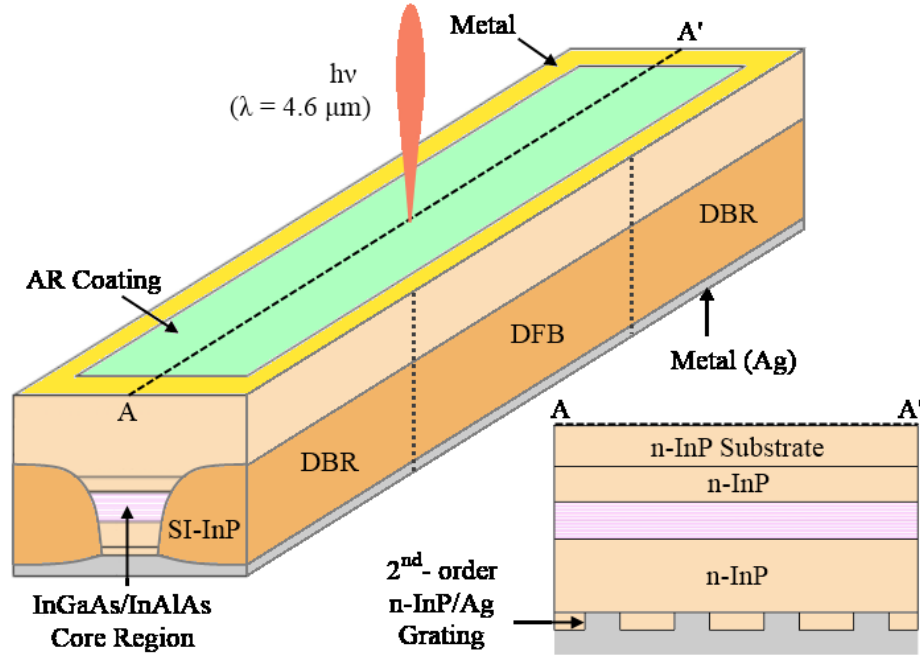
Fig. 8.5. Schematic representation of surface-emitting, buried-heterostructure DFB/DBR QCL for operation at 4.6 μm wavelength.

For finite-length devices, coupled-mode theory for 2$^{nd}$-order metal/semiconductor gratings is employed [158], as discussed in Sections 7.4 and 7.5, together with the matrix method for DFB/DBR structures [161]. We use the transfer matrix method to solve for the grating-related (intensity) loss coefficient, $2\alpha_q$, where $q$ is a mode index. This is part of the *longitudinally-local* (i.e., only in current-pumped regions) threshold gain $g_{th}$. For QCLs one has to take into account the backfilling-current density [53] and the leakage-current density [53] which are routinely subsumed with $\alpha_i$ (the internal cavity loss) as being parts of a 'waveguide' loss coefficient $\alpha_w$ in the threshold current density formula for Fabry-Perot-cavity devices: $J_{th} = (\alpha_m + \alpha_w)/\Gamma g$, where $\alpha_m$ is the mirror loss and $g$ is the differential gain coefficient. Since backfilling and carrier leakage occur only in the DFB region, the $g_{th}$ equation for mode $q$ for SE DFB/DBR QCLs is:

$$g_{th,q} = 2\alpha_q + \alpha_w + \left(\frac{1}{\Gamma_{lg,q}} - 1\right)\alpha_i \qquad (8.1)$$

where $\Gamma_{lg}$ is the percentage of field intensity residing in the DFB region. For $\alpha_w$ we take the experimental value obtained by Lyakh et al. [138]: 3.3 cm$^{-1}$, and for $\alpha_i$ we take a value of 0.5 cm$^{-1}$, typical of state-of-the-art, high-power 4.5-5.0 µm-emitting QCLs [22], [80]. The modal threshold gain [35] $G_{th,q} = \Gamma_{lg,q}g_{th,q}$. Then, the threshold current density is:

$$J_{th,q} = \frac{G_{th,q}}{\Gamma_{lg,q}\Gamma g} = \frac{g_{th,q}}{\Gamma g} \tag{8.2}$$

The finite-length structure chosen for analysis is one that maximizes the outcoupling loss for the symmetric mode, while maintaining a low value (*i.e.*, 2) for the symmetric-mode guided-field-intensity peak-to-valley ratio in the DFB region [161] $R_0$; chosen to prevent multimoding at high-drive levels due to longitudinal gain spatial hole burning. Then, for a 7.03 mm-long device of 3.07 mm-long DFB region and 1.98 mm-long DBR regions, we find for the symmetric mode that $2\alpha$ = 5.98 cm$^{-1}$ and $\Gamma_{lg}$ = 0.81. In turn, $g_{th,q}$ has a value of 9.4 cm$^{-1}$ and the $G_{th,q}$ value is 7.6 cm$^{-1}$. We estimate that only ~ 26% of the $G_{th,q}$ value (i.e., 2 cm$^{-1}$) is due to absorption to the metal. We show in Fig. 8.6 the $g_{th,q}$ values for antisymmetric and symmetric modes, as a function of detuning from the reference 4.6 µm wavelength, for a grating of 39% duty cycle and 0.217 µm tooth height. A symmetric mode is clearly favored to lase over two adjacent antisymmetric modes, which have $g_{th,q}$ values 23.1 cm$^{-1}$ and 23.9 cm$^{-1}$ higher than the symmetric mode. These large intermodal-discrimination values are dominated by the strong absorption of the antisymmetric modes.
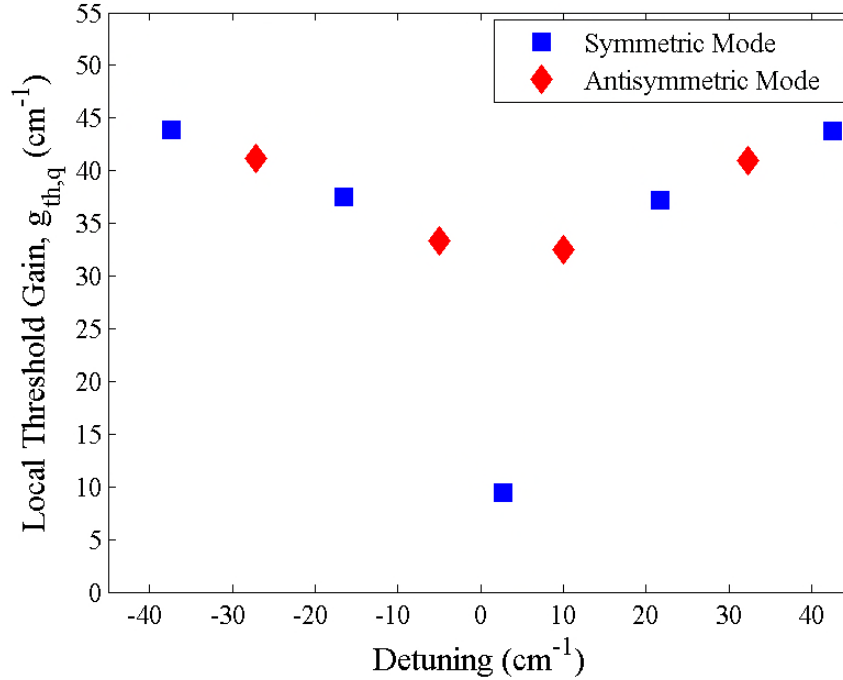
Fig. 8.6. Local threshold gain for symmetric and antisymmetric modes, at 39% duty cycle and 0.217 μm grating height, as a function of detuning from the 4.6 μm reference wavelength.

For the symmetric mode, by using (3.6) and the differential gain, $g$, value experimentally obtained by Lyakh et al. [138], we obtain a $J_{th}$ value of 1.84 kA/cm$^2$. Then, for a 3.07 mm-long DFB region and a 8.0 μm-wide ridge guide, the threshold current is 0.45 A, a value comparable to those of state-of-the-art, high-power edge-emitting QCLs operating in the 4.5-5.0 μm range [22], [80]. A COMSOL analysis of 8 μm-ridge device showed negligible changes: a 0.3% change in grating period and, for 39% duty cycle, changes in tooth height from 0.217 μm to 0.215 μm; thus, well within the 0.03 μm tolerance in grating tooth height.

Fig. 8.7 shows the $g_{th,q}$ values for the symmetric and the two adjacent antisymmetric modes as a function of grating height, at 39% duty cycle. The antisymmetric modes reach $g_{th,q}$ maxima at values corresponding to resonant coupling of the guided mode to the antisymmetric plasmon mode, at their respective oscillation wavelength. The intermodal discrimination is $\geq 10$

cm$^{-1}$ over a 0.030 μm-wide variation in tooth height, which is quite achievable when using a stop-etch layer.
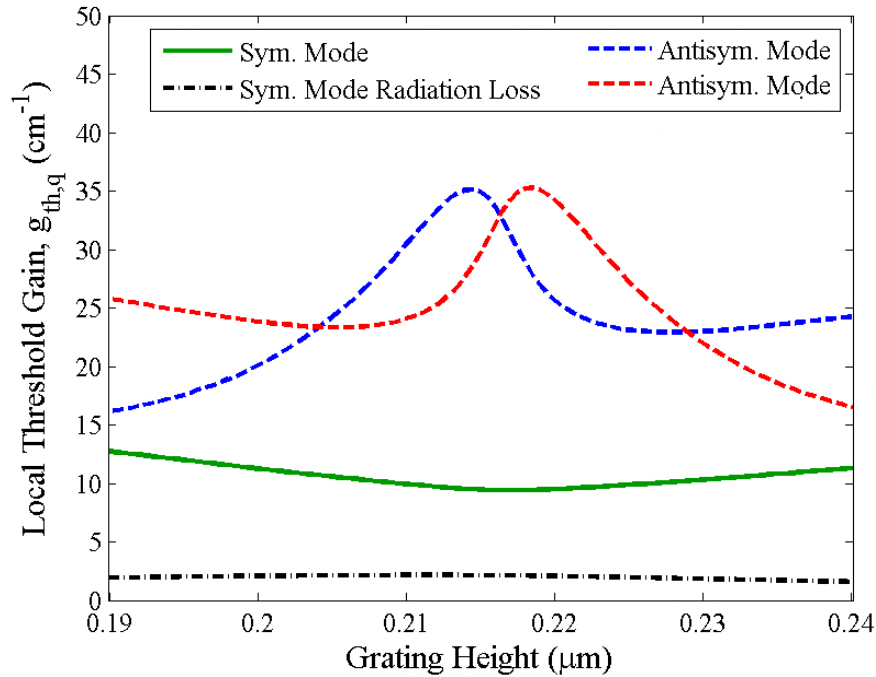


Fig. 8.7. Local threshold gain for symmetric and antisymmetric modes vs. grating height, at 39% duty cycle.

Fig. 8.8 shows the intermodal discrimination as a function of duty cycle and tooth height. Thin black lines indicate where the intermodal discrimination is 10 cm$^{-1}$; thus defining a curved-stripe-shaped domain over which the intermodal discrimination is ≥ 10 cm$^{-1}$. For a fixed duty cycle, intermodal discrimination is ≥ 10 cm$^{-1}$ over a 30 nm-wide variation in tooth height (e.g., over the 0.202-0.232 μm range in tooth height at 39% duty cycle). This can easily be achieved by using the InGaAs stop-etch layer. For a fixed tooth height, intermodal discrimination is ≥ 10 cm$^{-1}$ over a 2%-wide variation in duty cycle (e.g., over the 38-40% range in duty cycle at a 0.217 μm tooth height).  For a grating period of 1.44 μm, this corresponds to controlling the tooth width within 30 nm, which can be achieved with electron-beam lithography. Of course, if there is undercutting when etching the grating, adjusting the written pattern can compensate for it.
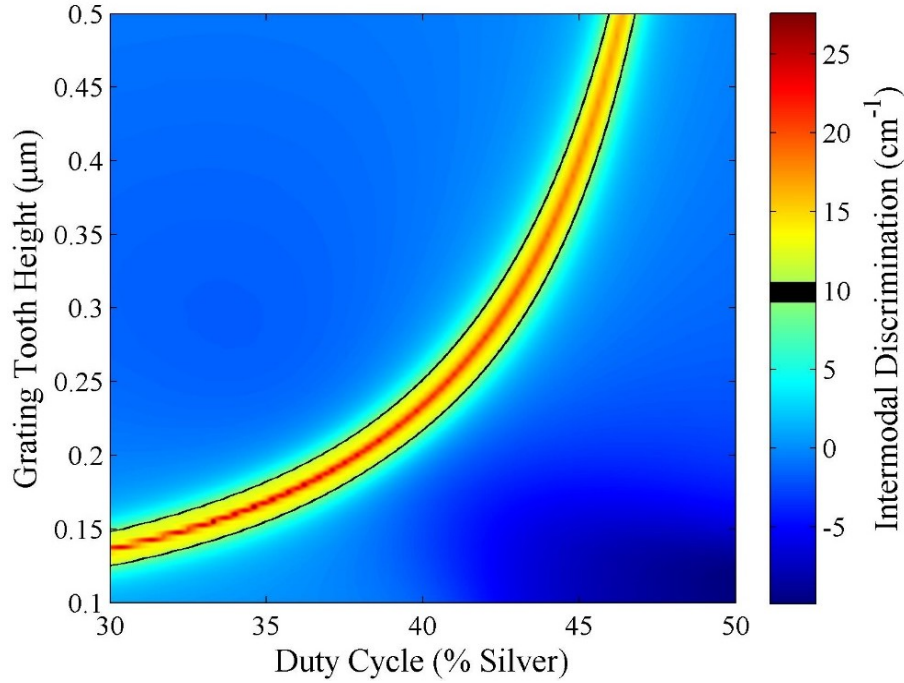
Fig. 8.8. Intermodal discriminations as a function of grating height and duty cycle.

We performed a study over the ranges 37-41% in duty cycle, and 0.202-0.232 μm in grating height, within the ≥ 10 cm$^{-1}$ domain in Fig. 8.8. We find that the grating outcoupling efficiency decreases by at most 15% (i.e., from 40% to 34%), The same outcoupling efficiency (i.e., 40%) is obtained for 38% duty cycle and 0.202 μm grating height, and for 40% duty cycle and 0.232 μm grating height. Thus, the chance of getting outcoupling efficiencies close to 40% is high. Finally, if the grating height is controlled, via the etch-stop layer to be within the 0.03 μm range, the range of acceptable duty-cycle values is 4% (i.e., from 37 to 41%); thus, the actual tolerance in grating-tooth width is 60 nm, which can be controlled via e-beam lithography.

Fig. 8.9 shows the *radiated* near-field intensity [161], [162] and the envelope of the guided-field intensity profiles for both symmetric and antisymmetric modes, when the grating duty cycle and tooth height are 39% and 0.217 μm. The near-field intensity is proportional to $|R(z) + S(z)|^2/2$, as only the symmetric component radiates (see Section 7.5.1), while the guided-field intensity envelope is proportional to $|R(z)|^2 + |S(z)|^2$. The difference between these two is

then $|R(z) - S(z)|^2/2$, proportional to the intensity of the antisymmetric component of the field. The symmetric mode's near field is almost equal to the guided field intensity envelope, indicating that this mode operates almost entirely like the infinite symmetric mode. The antisymmetric modes, meanwhile have significant symmetric and antisymmetric components, the former of which produces some surface emission and the latter of which produces high loss. The $R_0$ value is only 2 for the symmetric mode, to ensure single-longitudinal-mode operation to high drive levels [151], [161]. For the antisymmetric modes the guided-field intensity in the DFB region are fairly uniform, yet peaked in the center of the DFB region. Considering this, the fact that the intermodal discrimination is > 20 cm$^{-1}$ and that $R_0 = 2$, it is quite reasonable to assume that longitudinal spatial hole burning is unlikely to cause multi-moding at high drives above threshold.
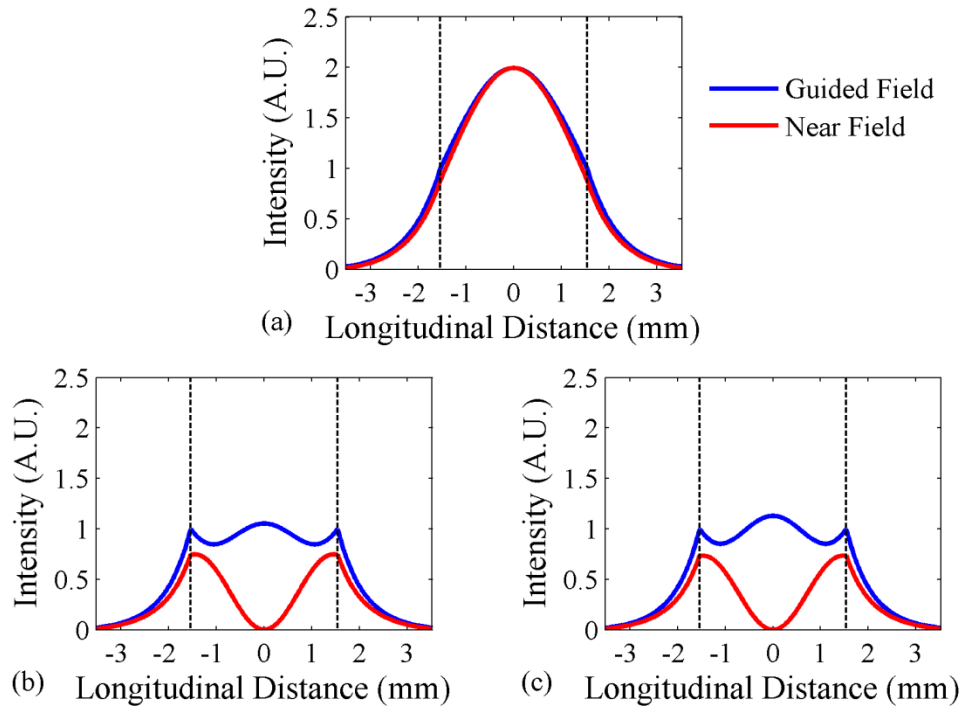


Fig. 8.9. Near-field intensity and envelope of guided-field intensity profiles for both (a) symmetric and (b,c) antisymmetric modes at 39% duty cycle and 0.217 μm grating height.

Fig. 8.10 shows the far-field beam pattern for the lowest-loss symmetric mode. This mode has a single-lobe beam pattern of 0.047° lobewidth (full-width half maximum). It is worth noting that in the case of TE-polarized GCSELs for which a central $\pi$ phase shift is needed to obtain single-lobe operation, the two-peaked near-field amplitude pattern caused 'shoulders' in the beam pattern [161]–[163] such that only 75-79% of the light is emitted in the central lobe. In turn, a factor of 0.75-0.79 multiplies the differential quantum efficiency [161]–[163]. Here, since the near-field amplitude profile is smooth and has a single peak, all light emitted in the single lobe can be used.
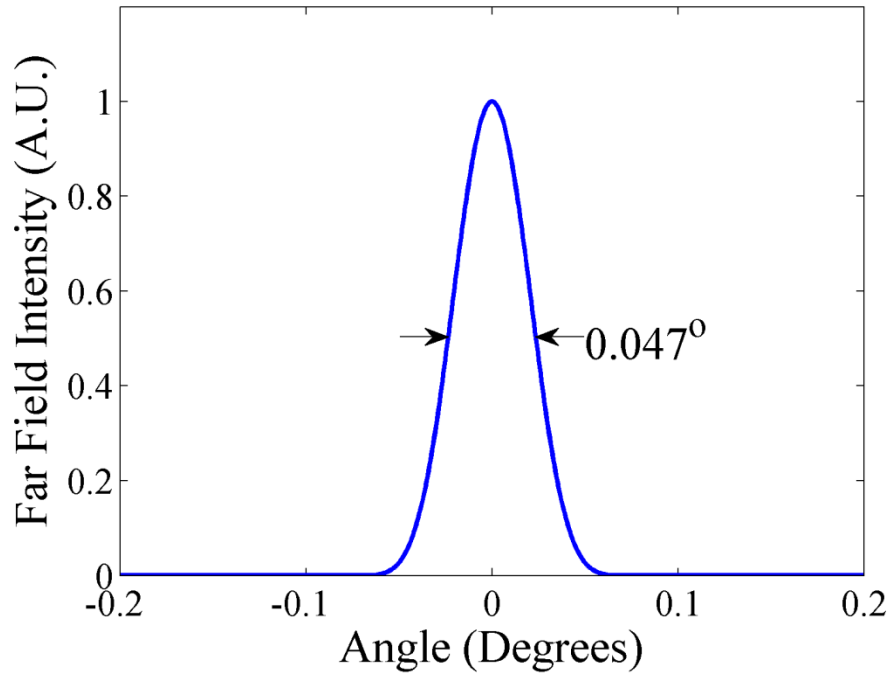


Fig. 8.10. Far-field beam pattern for the lowest-loss symmetric mode.

As for the differential quantum efficiency, the equation for GCSELs [35], [161] modified for QCLs is:

$$\eta_d = \eta_i^d \frac{\alpha_{surf}}{G_{th}} N_p = \eta_p \eta_{tr} \frac{\alpha_{surf}}{2\alpha\Gamma_{lg} + \alpha_i} N_p \tag{8.3}$$

where $\alpha_{surf}$ is the surface radiation loss defined in (7.49) and [35]; $\eta_i^d$ is the internal differential efficiency per period [53], [66], the product of $\eta_p$, the differential pumping efficiency, and $\eta_{tr}$, the laser-transition differential efficiency; and $N_p$ is the number of stages in the core. The $\frac{\alpha_{surf}}{G_{th}}$ term, known as outcoupling efficiency, is 40% in this case. While for devices with suppressed carrier leakage (*i.e.*, $\eta_p$ close to unity) the $\eta_i^d$ value is theoretically $\sim 0.85$, the best reported experimental values are in the 0.70-0.79 range [22], [192]. Then, taking $N_p = 40$ at $\lambda = 4.6$ μm, and assuming an AR-coated substrate-side window and negligible substrate absorption, the estimated slope efficiencies are 3.0-3.4 W/A, values comparable to best reported pulsed, single-facet values from 4.6 μm-emitting devices [193]. Furthermore, for devices with $R_0 = 2.5$ the outcoupling efficiency increases to 48%, in which case the estimated slope efficiencies are in the 3.6-4.1 W/A range. Since gain spatial hole burning is not well understood in QCLs, we chose to analyze the more conservative case of $R_0 = 2$, but that does not mean that devices with higher $R_0$ are not possible candidates for single-longitudinal-mode operation to watt-range output-power levels.

Using the estimated threshold and slope-efficiency values (i.e., 0.45 A and 3.4 W/A) the projected peak pulsed power at 3× threshold is 3.06 W.

## 8.5 Experimental Results

Devices fabricated by C. Boyle *et al*. [34] using a design similar to that presented above produced ~0.4 W in a single-lobed beam pattern from a 4.75 μm-emitting GCSE QCL. This device used Au instead of Ag, which provides less efficient coupling, and a different core region and structure from that modeled above. The measured far field agreed well with theory and confirmed longitudinally symmetric mode operation, as shown in Fig. 8.11. Simulations suggested that reflections from a rough substrate could cause some of the features seen in the far

field away from the main lobe. This method for obtaining symmetric mode operation has also been used in a ring configuration to obtain up to 200 mW of output power in CW operation in a beam pattern consisting of concentric rings (due to the ring geometry of the device) [194].
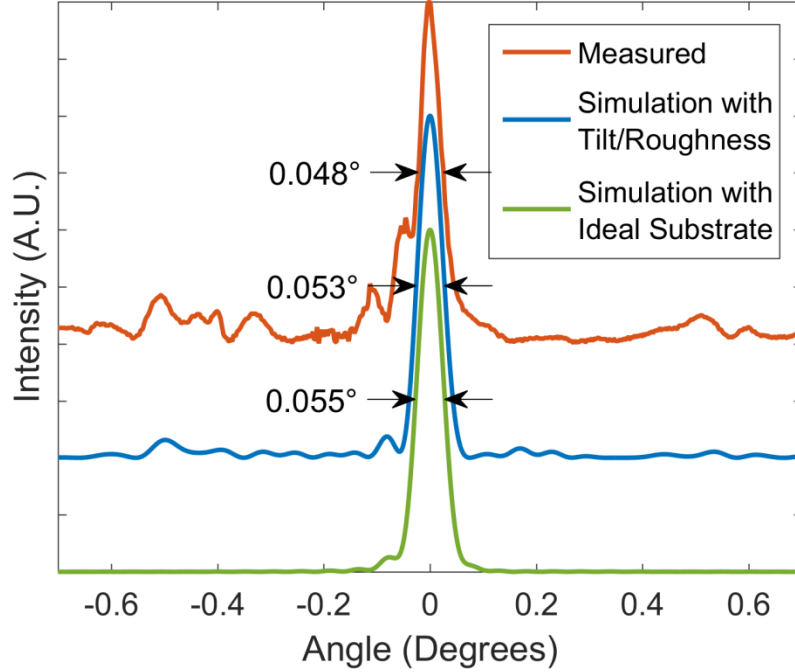


Fig. 8.11. (Upper) Measured longitudinal far-field beam pattern at a distance of 2 m for a device operating at 350 mW surface-emitted output power; (middle) simulated far-field pattern at 2 m distance, including the effects of substrate/air reflections, substrate/air interface tilt, and substrate surface roughness (the zero position has been shifted by 0.18° to align with the measured curve); (lower) simulated far-field pattern 2 m distance for a device with an ideal planar AR-coated substrate. [34]

## 8.6  Surface Emitter CW Modeling

The semi-empirical CW model from Ch. 3 was modified to function for a surface-emitter, in order to extend the threshold current and slope efficiency calculations into a calculation of the maximum CW power possible from a given design. The slope efficiency in (3.11) is replaced by:

$$\eta_s = F_{sub} \frac{\hbar\omega}{q} \eta_d = F_{sub} \eta_i^d \frac{\hbar\omega}{q} \frac{\alpha_{surf}}{G_{th}} N_p \tag{8.4}$$

where $\eta_d$ is taken from (8.3), and $F_{sub}$ is the fraction of power emitted from the waveguide which is transmitted through the substrate and into the air (the remaining portion is assumed to be absorbed in the substrate or reflected at the bottom interface). We estimate that 15% of the light would be absorbed in the substrate, though this could be lowered using a lower-doped substrate, and assume the bottom interface is AR-coated. Similarly, the threshold current density equation (3.6) is replaced by (8.2). Here, we use the core region parameters extracted for our 5.1 μm-emitting BH QCLs discussed in Ch. 3 [23], rather than the values used previously in this chapter. We also relax the condition limiting the guided-field peak-to-valley ratio, $R_0$, of the symmetric mode to a maximum value of 2.0, as the fabricated structure is unlikely to actually be at resonance, and $R_0$ drops significantly if the duty cycle of the grating misses its target value. Then, our target design for a 40-stage, 5 μm-wide BH (to ensure a single lateral mode), has a 2.5 mm-long DFB region, 1.875 mm-long DBR regions on either side, a 2.4 μm-thick upper cladding below the InGaAs etch-stop layer for the grating, a grating height of 160 nm, and a grating duty cycle of 27.1%. This grating design is shifted significantly to the lower-duty-cycle and shorter-grating side of the resonance curve in Fig. 8.3. This has the following major effects: the surface loss of the infinite-length symmetric mode is lower in this portion of the curve, which lowest both the threshold of the device and its slope efficiency, and it widens the tolerance on the grating duty cycle. The thinner upper cladding increases coupling to the grating, which increases $R_0$ of the symmetric mode, which is ~ 4.5 at resonance, as seen in Fig. 8.12(a). If the target duty cycle is missed by more than 2% though, $R_0$ drops below 2.5. The stronger coupling of this structure actually also has the effect of *decreasing* discrimination against the antisymmetric modes in the finite-length device. With such high loss for the infinite antisymmetric mode, the finite antisymmetric modes actually have a large component that appears symmetric within the

grating, though the overall envelope of the mode is still antisymmetric, as seen in Fig. 8.12(b) by the small difference between the near-field and guided-field intensity envelope (which represents the antisymmetric component of the mode). This little discrimination can be seen in the mode spectrum for this design in Fig. 8.13, where the relevant competing modes are shown. The modes on the opposite side of the bandstop have high threshold gains and are not shown. The intermodal discrimination is actually higher when the grating duty cycle is several percent off of resonance than directly at resonance.



(a)

(b)
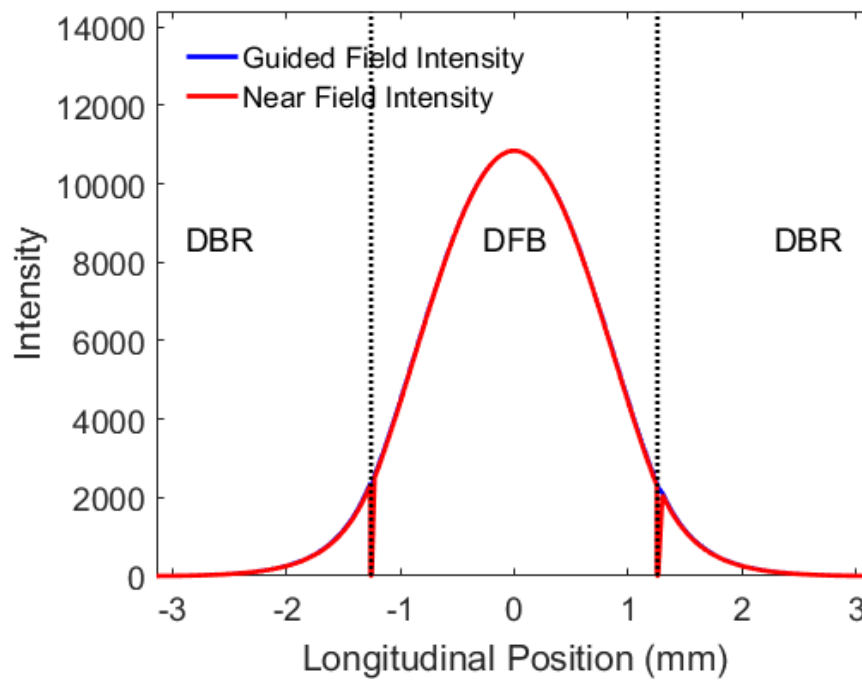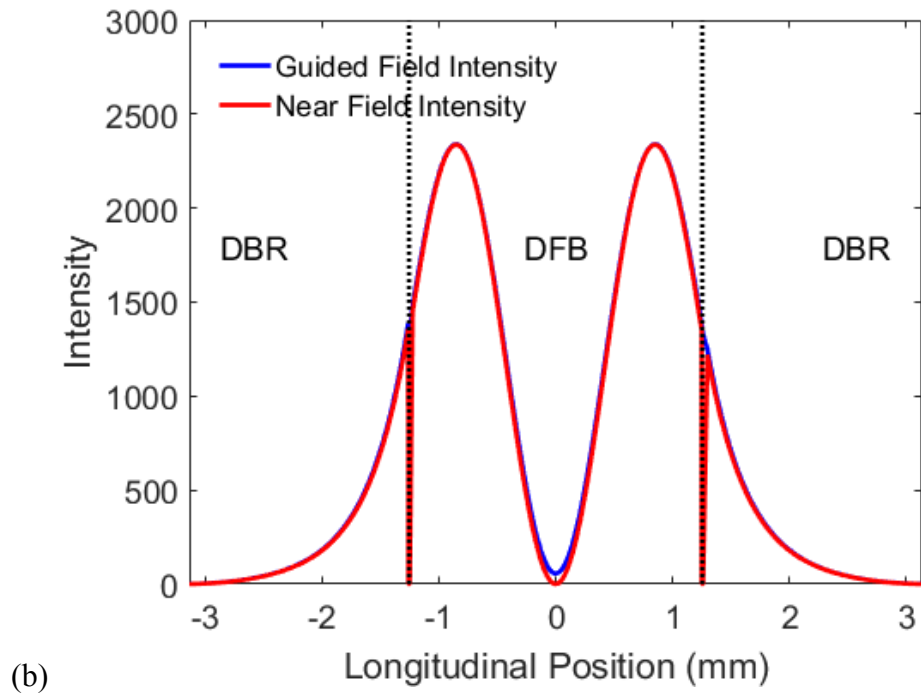
Fig. 8.12. Near-field intensity and envelope of guided-field intensity profiles for both (a) symmetric and (b) an antisymmetric mode at 27.1% duty cycle and 160 nm grating height.
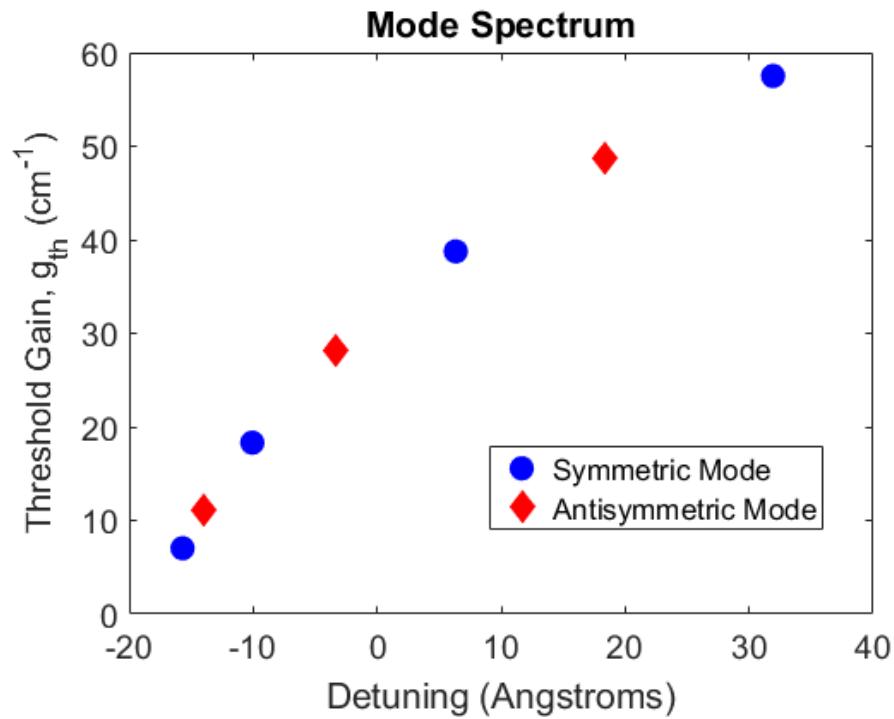


Fig. 8.13. Local threshold gain for symmetric and antisymmetric modes, at 27.1% duty cycle and 0.160 μm grating height, as a function of detuning from the 5.1 μm reference wavelength.

The resulting simulated CW light-current (L-I) curve for this device is shown in Fig. 8.14 below. The maximum CW power is 0.56 W at a current of 0.56 A, and the threshold is 0.23 A in CW operation. In pulsed operation, the maximum peak power is projected to be 0.96 W and the slope efficiency is 2.9 W/A. This maximum power is lower than that projected above in Section 8.4 for several reasons: this is a narrower device (5 μm here compared to 8 μm above), this is a shorter device (2.5 mm DFB-region length here vs. 3.0 mm above), and the grating is designed to lower the threshold for CW operation, which as mentioned above lowers the slope efficiency as well. If the DFB region is lengthened to 4 mm, the projected maximum CW power for this design increases to 1.0 W, though the intermodal discrimination is worse near resonance.
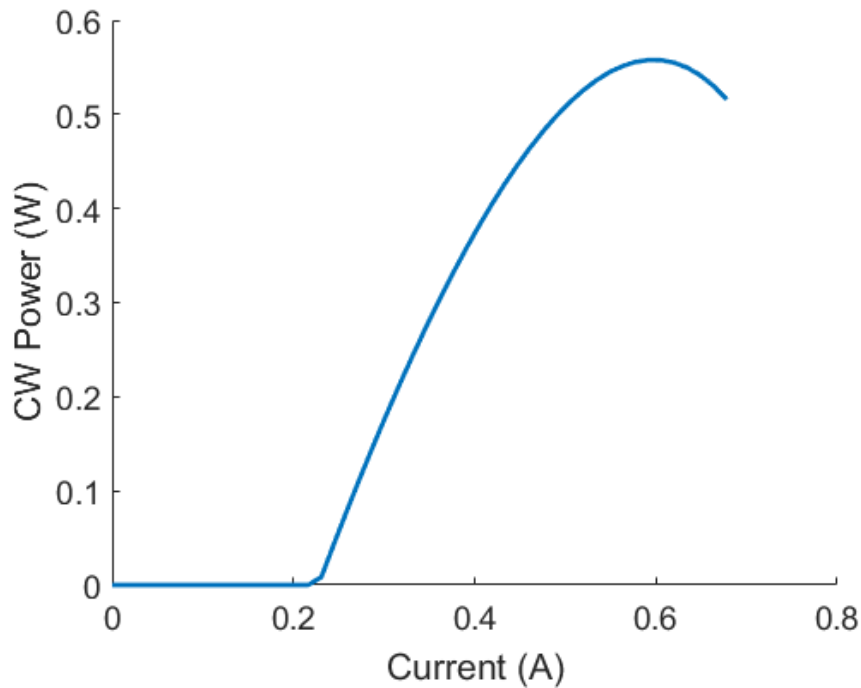


Fig. 8.14. Simulated CW L-I curve for the optimized GCSEL device.

This method for producing a single-lobed surface-emitting QCL was compared against the π-phaseshift method. The grating for each type of device was optimized for maximum CW output power, assuming a 5 μm-wide core and a 4 mm-long DFB region. The resulting CW L-I

curves are shown in Fig. 8.15(a) below, and their longitudinal far-field beam patterns are compared in Fig. 8.15 (b). The device operating in an internally-antisymmetric mode with a $\pi$-phaseshift has a narrower central lobe but small sidelobes on either side of it.



(a)



(b)
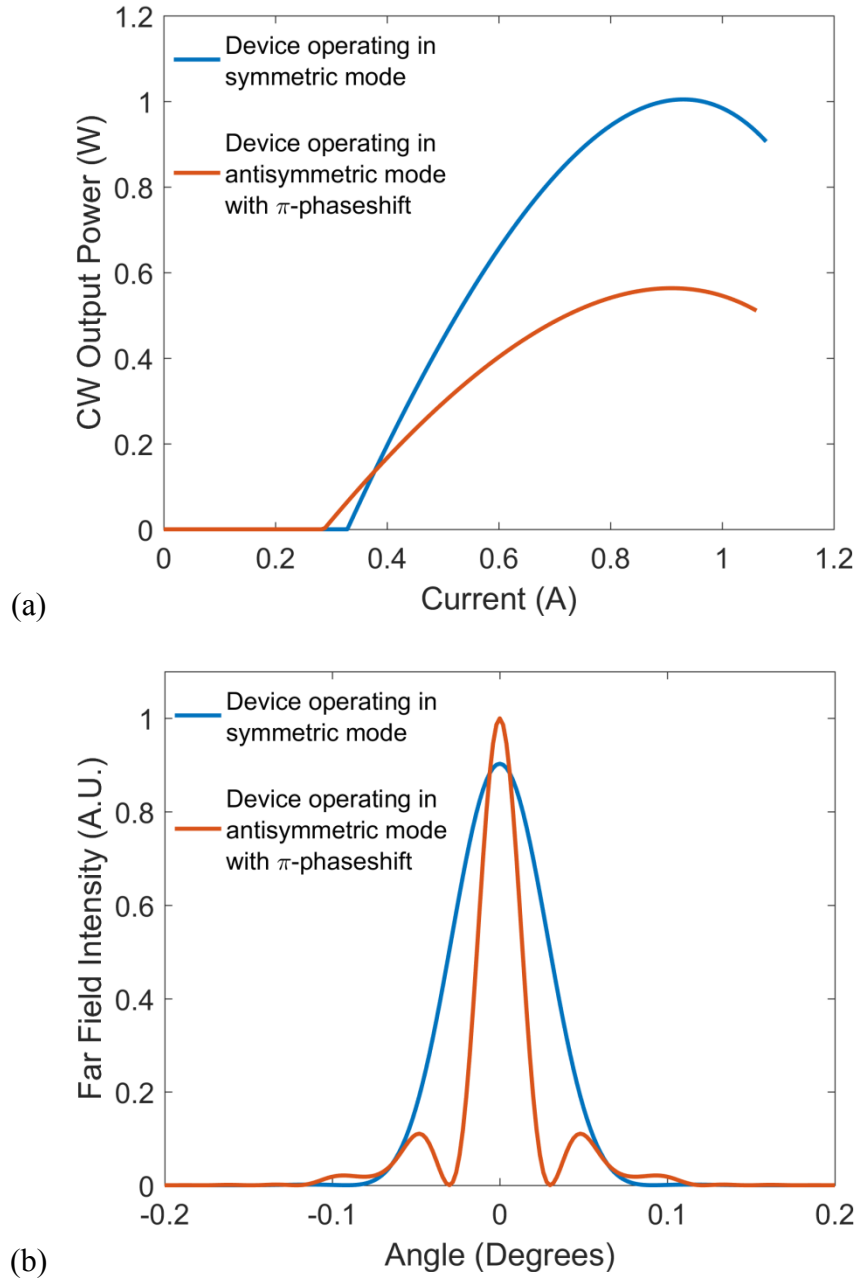
Fig. 8.15. (a) Simulated CW L-I curves for optimized GCSEL devices using either absorption to the antisymmetric plasmon mode (thus operating in a symmetric mode) or a $\pi$-phaseshift to produce a single-lobed beam pattern; (b) Simulated longitudinal far-field beam patterns for the same two devices.

As the length of a device increases, its behavior approaches that of the corresponding mode in an infinite-length device. Since this new method for producing a single-lobed beam pattern allows the device to operate in a truly symmetric mode, and the infinite symmetric mode is extremely efficient at outcoupling light, the device becomes more efficient as its length increases. In comparison, devices using a $\pi$-phaseshift still operate internally in an antisymmetric mode. As the infinite antisymmetric mode does not radiate at all, these devices become less efficient as the device is lengthened. This effect is demonstrated in Fig. 8.16 below, where there is far better power scaling for the device in (a), which operates in the symmetric mode, than for the device in (b), which uses a $\pi$-phaseshift (these are the same two designs as in Fig. 8.15).
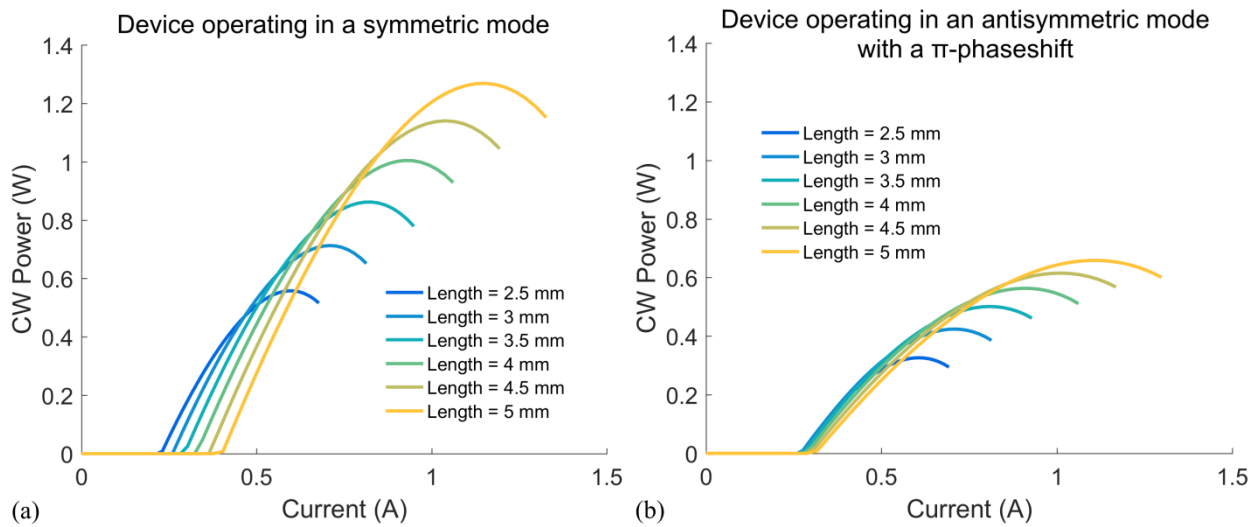


Fig. 8.16. Simulated CW L-I curves for GCSEL devices of varying lengths using either (a) absorption to the antisymmetric plasmon mode, thus operating in a symmetric mode; or (b) a $\pi$-phaseshift to produce a single-lobed beam pattern and operating in an antisymmetric mode.

## 8.7    Conclusions

A novel type of TM-polarized grating-coupled surface-emitting laser is presented that offers efficient single-lobe lasing due to antisymmetric modes being strongly absorbed via resonant coupling to surface plasmon modes. This method is not restricted to QCLs alone, but could also be used for TM-polarized devices in the near-IR. By employing a published QCL-core

structure, we simulate that DFB/ DBR devices can lase in a single-lobe pattern with threshold currents as low as 0.45 A and slope efficiencies as high as 3.4 W/A. Initial devices showed symmetric mode operation, emitting ~0.4 W of peak pulsed power in a single lobe. Projections of CW operation suggest that over 1 W of single-mode (both longitudinally and laterally), single-lobed output power from ~5.1 µm-emitting QCLs is possible with this method. Thus, these devices hold potential for watt-range CW coherent-power emission delivered reliably, since emitting-facet heating and subsequent degradation are avoided. This method allows for efficient longitudinal power scaling as these GCSELs become more efficient the longer they are. The coherent power can also be increased via resonant leaky-wave coupling of GCSE devices in the lateral direction [35], [180], [181]. Then, considering that typically ~67% of the coherent power is emitted in the array main far-field lobe, for a five-element phase-locked array of DFB/DBR QCLs peak coherent powers in excess of 10 W become possible.

# Chapter 9 – Concluding Remarks

## 9.1    Summary

Quantum cascade lasers (QCLs) have progressed rapidly since their inception in 1994. Today, watt-range powers can be obtained for continuous-wave (CW) operation at room temperatures in the mid-infrared [22]–[25]. Many challenges still remain, including scaling to higher powers while maintaining diffraction-limited beam quality. This dissertation explored methods for accomplishing this via scaling the core volume laterally using leaky-wave-coupled phased-locked arrays and longitudinally using grating-coupled surface-emitting quantum cascade lasers.

In Chapter 2, we were introduced to the operating principles of a quantum cascade laser. Several models for QCLs were presented in Chapter 3, including optical and thermal models, and a method for optimizing QCLs for high CW power. We find that this model predicts that wider devices with relatively fewer stages should be capable of emitting higher CW powers than conventional thicker and narrower devices. In Chapter 4, we explored methods for coherently scaling the output power of QCLs along with the advantages and disadvantages of them. Here, we introduced the leaky-wave-coupled phase-locked array, described how it operates and how it offers mode selectivity for a desirable beam pattern, a large core volume for high power, and good thermal conductance compared to broad area devices. In Chapter 5, we investigated the optical and thermal properties of planarized leaky-wave-coupled phase-locked QCL arrays and developed techniques to mitigate thermal lensing [28]. Anti-resonant reflective-optical waveguide terminations were found to lower the in-phase mode loss, improve discrimination against modes composed of 1st-order element modes, and reduce the effects of thermal lensing. Improving the transverse overlap between the element and interelement modes reduces the effect

of thermal lensing as well. Chirping of the element width was shown to eliminate variation in the in-phase field profile as a function of interelement width for a given CW operating condition, by compensating for the apparent widening (optically) of the central elements due to their more elevated refractive index. As QCL wallplug efficiencies improve, the dissipated power will drop substantially for a given output power, reducing the temperature gradient across these arrays and thus lessening thermal lensing. A demonstration of five-element leaky-wave-coupled phase-locked QCL arrays operating predominately in an in-phase array mode up to at least 5.1 W of peak pulsed output power was presented in Chapter 6 [29], along with an investigation into their spectrally-resolved modal properties [30] which found variations in the spatial coherence at different wavelengths due to the unoptimized structure and non-resonant nature of the devices. Projections for further power scaling from the CW model presented in Chapter 3 were also given, in which these arrays are expected to more than double the spatially-coherent CW power obtainable from buried heterostructures fabricated from the same material. In Chapter 7, we were introduced to distributed feedback and grating-coupled surface-emitting lasers (GCSELs), as well as a ray optics method for calculating the coupling coefficient of multi-layer transverse magnetic (TM)-polarized lasers with a low-index-step $1^{st}$-order grating [186]. Lastly, in Chapter 8 we proposed a novel method of obtaining longitudinally-symmetric mode operation from a TM-polarized GCSEL by resonant absorption of the antisymmetric mode [33]. By operating in a truly symmetric mode, this method scales to higher powers by lengthening the device more efficiently than the prior method utilizing a $\pi$-phaseshift. 400 mW of peak pulsed power has been obtained in a longitudinally diffraction-limited beam pattern with a 0.05° full-width at half-maximum using this method [34]. Projections show that these are capable of emitting over 1 W

of single-mode, single-lobe CW power when fabricated as a single-lateral-mode buried heterostructure.

## 9.2 Future Work

There are many paths forward from the work presented in this dissertation. Firstly, a major limiting factor in this work was poor electrical insulation by the in-house regrown InP:Fe, which affected buried heterostructures (and prevented the development of a BH surface-emitter), planarized arrays, and the curved layer arrays. Some devices had better current blocking than others, such as the curved layer arrays seeming to work well most of the time while the planarized arrays were resistor-like, and an external service was required for regrowth of the buried heterostructures to obtain good current-blocking. While a great deal of effort was put into finding the cause of the usually-leaky devices, the issue was not fixed during the period of time in which this work was performed. Correcting this problem would allow for further development of these devices.

Secondly, the effect of the non-uniform longitudinal gain saturation could be incorporated into the CW model using the method presented in [83]. This would allow for more accurate projections of longer and higher loss devices, such as the leaky-wave-coupled phase-locked arrays.

For the arrays, finishing development of the above-threshold model presented in [150] would help determine the amount of intermodal discrimination necessary to maintain single-lateral-mode operation. Too much discrimination results in high in-phase mode loss, which has a significantly deleterious effect on CW performance. Leaky-wave-coupling from the planarized arrays could be demonstrated using planar hydride vapor phase epitaxy (HVPE) regrowth for the InP:Fe, which would simplify the fabrication process [135] by removing a chemical polishing

step. The curved layer arrays can also be fabricated with thick electroplated gold (which could be polished down and planarized to remove voids) and mounted epi-side down for quasi-CW or CW operation, where we would like to demonstrate their stability in maintaining single-mode operation. The arrays could also be scaled up to higher pulsed power while maintaining beam quality by increasing the number of elements. Lastly, confining current flow to the elements in the lower core (such as by proton implantantion [148], etch and InP:Fe regrowth within the lower core, or removal of the lower core entirely while using fewer stages) is expected to reduce threshold currents by ~15% and improve output power by ensuring that the entire core is operating at the same current density and electric field.

In the future, surface-emitter devices employing absorption regions with thick Ti (and no grating) at the ends of the distributed Bragg reflectors and anti-reflection coatings at the facets to further suppress Fabry-Perot modes could be demonstrated. As mentioned above, BH surface-emitters operating in a single lateral mode for a spatially and temporally coherent single-lobed beam in CW operation can be fabricated once the leaky InP:Fe is fixed.

Lastly, combining the leaky-wave-coupled phase-locked array and single-lobed surface-emitter into a single device, as in [35], is an attractive path for scaling the spatially and temporally coherent output power of a monolithic QCL beyond 10 W.

# References

[1]     F. Capasso, C. Gmachl, R. Paiella, A. Tredicucci, A. L. Hutchinson, D. L. Sivco, J. N. Baillargeon, A. Y. Cho, and H. C. Liu, "New Frontiers in Quantum Cascade Lasers and Applications," *IEEE J. Sel. Top. Quantum Electron.*, vol. 6, no. 6, pp. 931–947, 2000.

[2]     J. Hodgkinson and R. P. Tatam, "Optical gas sensing: a review," *Meas. Sci. Technol.*, vol. 24, no. 1, p. 012004, 2013.

[3]     J. Jágerská, P. Jouy, A. Hugi, B. Tuzson, H. Looser, M. Mangold, M. Beck, L. Emmenegger, and J. Faist, "Dual-wavelength quantum cascade laser for trace gas spectroscopy," *Appl. Phys. Lett.*, vol. 105, no. 16, p. 161109, 2014.

[4]     J. Li, U. Parchatka, and H. Fischer, "Development of field-deployable QCL sensor for simultaneous detection of ambient $N_2O$ and CO," *Sensors Actuators, B Chem.*, vol. 182, pp. 659–667, 2013.

[5]     N. Liu, S. Zhou, L. Zhang, B. Yu, H. Fischer, W. Ren, and J. Li, "Standoff detection of VOCs using external cavity quantum cascade laser spectroscopy," *Laser Phys. Lett.*, vol. 15, no. 8, p. 085701, 2018.

[6]     M. F. Witinski, R. Blanchard, C. Pfluegl, L. Diehl, B. Li, K. Krishnamurthy, B. C. Pein, M. Azimi, P. Chen, G. Ulu, G. Vander Rhodes, C. R. Howle, L. Lee, R. J. Clewes, B. Williams, and D. Vakhshoori, "Portable standoff spectrometer for hazard identification using integrated quantum cascade laser arrays from 6.5 to 11 μm.," *Opt. Express*, vol. 26, no. 9, p. 12159, 2018.

[7]     M. C. Phillips and B. E. Brumfield, "Standoff detection of turbulent chemical mixture plumes using a swept external cavity quantum cascade laser," *Opt. Eng.*, vol. 57, no. 01, p. 011003, 2017.

[8]     S. Welzel, F. Hempel, M. Hübner, N. Lang, P. B. Davies, and J. Röpcke, "Quantum Cascade Laser Absorption Spectroscopy as a Plasma Diagnostic Tool: An Overview," *Sensors*, vol. 10, no. 7, pp. 6861–6900, 2010.

[9]     M. Jahjah, W. Ren, P. Stefański, R. Lewicki, J. Zhang, W. Jiang, J. Tarka, and F. K. Tittel, "A compact QCL based methane and nitrous oxide sensor for environmental and medical applications," *Analyst*, vol. 139, no. 9, pp. 2065–2069, 2014.

[10]    A. Reyes-Reyes, R. C. Horsten, H. P. Urbach, and N. Bhattacharya, "Study of the Exhaled Acetone in Type 1 Diabetes Using Quantum Cascade Laser Spectroscopy," *Anal. Chem.*, vol. 87, no. 1, pp. 507–512, 2015.

[11]    K. Hashimura, K. Ishii, N. Akikusa, T. Edamura, H. Yoshida, and K. Awazu, "Coagulation and ablation of biological soft tissue by quantum cascade laser with peak wavelength of 5.7 μm," *J. Innov. Opt. Health Sci.*, vol. 07, no. 03, p. 1450029, 2014.

[12]    R. Martini and E. A. Whittaker, "Quantum cascade laser-based free space optical

communications," *J. Opt. Fiber Commun. Reports*, vol. 2, no. 4, pp. 279–292, 2005.

[13]   A. Sijan, "Development of Military Lasers for Optical Countermeasures in the Mid-IR," in *Proceedings of SPIE*, 2009, vol. 7483, p. 748304.

[14]   W. Duley, *CO₂ Lasers Effects and Applications*, 1st ed. New York, NY: Academic Press, 1976.

[15]   Z. Shi, M. Tacke, A. Lambrecht, and H. Böttner, "Midinfrared lead salt multi-quantum-well diode lasers with 282 K operation," *Appl. Phys. Lett.*, vol. 66, no. 19, pp. 2537–2539, 1995.

[16]   U. P. Schießl and J. Rohr, "60°C lead salt laser emission near 5-μm wavelength," *Infrared Phys. Technol.*, vol. 40, pp. 325–328, 1999.

[17]   L. Shterengas, G. Belenky, T. Hosoda, G. Kipshidze, and S. Suchalkin, "Continuous wave operation of diode lasers at 3.36 μm at 12°C," *Appl. Phys. Lett.*, vol. 93, no. 1, p. 011103, 2008.

[18]   L. Shterengas, G. Kipshidze, T. Hosoda, J. Chen, and G. Belenky, "Diode lasers emitting at 3 μm with 300 mW of continuous-wave output power," *Electron. Lett.*, vol. 45, no. 18, pp. 942–943, 2009.

[19]   T. Hosoda, G. Kipshidze, L. Shterengas, and G. Belenky, "Diode lasers emitting near 3.44 μm in continuous-wave regime at 300K," *Electron. Lett.*, vol. 46, no. 21, pp. 1455–1457, 2010.

[20]   I. Vurgaftman, R. Weih, M. Kamp, J. R. Meyer, C. L. Canedy, C. S. Kim, M. Kim, W. W. Bewley, C. D. Merritt, J. Abell, and S. Höfling, "Interband cascade lasers," *J. Phys. D. Appl. Phys.*, vol. 48, no. 12, p. 123001, 2015.

[21]   J. Faist, F. Capasso, D. L. Sivco, C. Sirtori, A. L. Hutchinson, and A. Y. Cho, "Quantum Cascade Laser," *Science*, vol. 264, no. 5158, pp. 553–556, 1994.

[22]   Y. Bai, N. Bandyopadhyay, S. Tsao, S. Slivken, and M. Razeghi, "Room temperature quantum cascade lasers with 27% wall plug efficiency," *Appl. Phys. Lett.*, vol. 98, p. 181102, 2011.

[23]   D. Botez, J. D. Kirch, C. Boyle, K. M. Oresick, C. Sigler, H. Kim, B. B. Knipfer, J. H. Ryu, D. Lindberg III, T. Earles, L. J. Mawst, and Y. V. Flores, "High-efficiency, high-power mid-infrared quantum cascade lasers," *Opt. Mater. Express*, vol. 8, no. 5, pp. 1378–1398, 2018.

[24]   A. Lyakh, R. Maulini, A. Tsekoun, R. Go, and C. K. N. Patel, "Tapered 4.7 μm quantum cascade lasers with highly strained active region composition delivering over 4.5 watts of continuous wave optical power," *Opt. Express*, vol. 20, no. 4, p. 4382, 2012.

[25]   P. Figueiredo, M. Suttinger, R. Go, E. Tsvid, C. K. N. Patel, and A. Lyakh, "Progress in

high-power continuous-wave quantum cascade lasers," *Appl. Opt.*, vol. 56, no. 31, pp. H15–H23, 2017.

[26]  D. Botez, L. J. Mawst, and G. Peterson, "Resonant leaky-wave coupling in linear arrays of antiguides," *Electron. Lett.*, vol. 24, no. 21, pp. 1328–1330, 1988.

[27]  D. Botez, L. J. Mawst, G. Peterson, and T. J. Roth, "Resonant optical transmission and coupling in phase-locked diode laser arrays of antiguides: The resonant optical waveguide array," *Appl. Phys. Lett.*, vol. 54, no. 22, pp. 2183–2185, 1989.

[28]  C. Sigler, C.-C. Chang, J. D. Kirch, L. J. Mawst, D. Botez, and T. Earles, "Design of Resonant Leaky-Wave Coupled Phase-Locked Arrays of Mid-IR Quantum Cascade Lasers," *IEEE J. Sel. Top. Quantum Electron.*, vol. 21, no. 6, p. 1200810, 2015.

[29]  C. Sigler, C. A. Boyle, J. D. Kirch, D. Lindberg III, T. Earles, D. Botez, and L. J. Mawst, "4.7 μm-Emitting Near-Resonant Leaky-Wave-Coupled Quantum Cascade Laser Phase-Locked Arrays," *IEEE J. Sel. Top. Quantum Electron.*, vol. 23, no. 6, p. 1200706, 2017.

[30]  C. Sigler, R. Gibson, C. Boyle, J. D. Kirch, D. Lindberg III, T. Earles, D. Botez, L. J. Mawst, and R. Bedford, "Spectrally resolved modal characteristics of leaky-wave-coupled quantum cascade phase-locked laser arrays," *Opt. Eng.*, vol. 57, no. 1, p. 011013, 2018.

[31]  C. A. Zmudzinski, D. Botez, and L. J. Mawst, "Simple description of laterally resonant, distributed-feedback-like modes of arrays of antiguides," *Appl. Phys. Lett.*, vol. 60, no. 9, pp. 1049–1051, 1992.

[32]  H. Yang, L. J. Mawst, and D. Botez, "1.6 W continuous-wave coherent power from large-index-step ($\Delta n \approx 0.1$) near-resonant, antiguided diode laser arrays," *Appl. Phys. Lett.*, vol. 76, no. 10, pp. 1219–1221, 2000.

[33]  C. Sigler, J. D. Kirch, T. Earles, L. J. Mawst, Z. Yu, and D. Botez, "Design for high-power, single-lobe, grating-surface-emitting quantum cascade lasers enabled by plasmon-enhanced absorption of antisymmetric modes," *Appl. Phys. Lett.*, vol. 104, no. 13, p. 131108, 2014.

[34]  C. Boyle, C. Sigler, J. D. Kirch, D. F. Lindberg III, T. Earles, D. Botez, and L. J. Mawst, "High-power, surface-emitting quantum cascade laser operating in a symmetric grating mode," *Appl. Phys. Lett.*, vol. 108, no. 12, p. 121107, 2016.

[35]  S. Li and D. Botez, "Analysis of 2-D Surface-Emitting ROW-DFB Semiconductor Lasers for High-Power Single-Mode Operation," *IEEE J. Quantum Electron.*, vol. 43, no. 8, pp. 655–668, 2007.

[36]  A. Yariv and P. Yeh, *Photonics: Optical Electronics in Modern Communications*, 6th ed. New York, NY: Oxford University Press, Inc, 2007.

[37]  B. E. A. Saleh and M. C. Teich, *Fundamentals of Photonics*, 2nd ed. Hoboken, New Jersey: John Wiley & Sons, Inc., 2007.

[38] G. B. Stringfellow, *Organometallic Vapor-Phase Epitaxy - Theory and Practice*, 2nd ed. San Diego, CA: Academic Press, 1999.

[39] L. A. Coldren, S. W. Corzine, and M. L. Mašanović, *Diode Lasers and Photonic Integrated Circuits*, 2nd ed. Hoboken, NJ: Wiley, 2012.

[40] J. Faist, F. Capasso, C. Sirtori, D. Sivco, and A. Cho, "Quantum Cascade Lasers," in *Intersubband Transitions in Quantum Wells*, New York, NY: Academic Press, 1999, pp. 1–83.

[41] J. Kim, M. Lerttamrab, S. L. Chuang, C. Gmachl, D. L. Sivco, F. Capasso, and A. Y. Cho, "Theoretical and experimental study of optical gain and linewidth enhancement factor of type-I quantum-cascade lasers," *IEEE J. Quantum Electron.*, vol. 40, no. 12, pp. 1663–1674, 2004.

[42] G. Dehlinger, L. Diehl, U. Gennser, H. Sigg, J. Faist, K. Ensslin, D. Grutzmacher, and E. Muller, "Intersubband electroluminescence from silicon-based quantum cascade structures.," *Science*, vol. 290, no. 5500, pp. 2277–80, 2000.

[43] A. Rajeev, C. Sigler, T. Earles, Y. V. Flores, L. J. Mawst, and D. Botez, "Design considerations for λ ~ 3.0- to 3.5-μm-emitting quantum cascade lasers on metamorphic buffer layers," *Opt. Eng.*, vol. 57, no. 1, p. 011017, 2018.

[44] A. Rajeev, L. J. Mawst, J. D. Kirch, D. Botez, J. Miao, P. Buelow, T. F. Kuech, X. Li, C. Sigler, S. E. Babcock, and T. Earles, "Regrowth of quantum cascade laser active regions on metamorphic buffer layers," *J. Cryst. Growth*, vol. 452, pp. 268–271, 2016.

[45] R. Go, H. Krysiak, M. Fetters, P. Figueiredo, M. Suttinger, J. Leshin, X. M. Fang, J. M. Fastenau, D. Lubyshev, A. W. K. Liu, A. Eisenbach, M. J. Furlong, and A. Lyakh, "Room temperature operation of quantum cascade lasers monolithically integrated onto a lattice-mismatched substrate," *Appl. Phys. Lett.*, vol. 112, no. 3, p. 031103, 2018.

[46] C. Sirtori and R. Teissier, "Quantum Cascade Lasers: Overview of Basic Principles and State of the Art," in *Intersubband Transitions in Quantum Structures*, 1st ed., R. Paiella, Ed. McGraw-Hill, 2006, pp. 1–44.

[47] G. Bastard, *Wave Mechanics Applied to Semiconductor Heterostructures*. New York, NY: Halsted Press, 1990.

[48] T. Czyszanowski, "Quantum-Cascade Vertical-Cavity Surface-Emitting Laser," *IEEE Photonics Technol. Lett.*, vol. 30, no. 4, pp. 351–354, 2018.

[49] R. Köhler, A. Tredicucci, F. Beltram, H. E. Beere, E. H. Linfield, A. G. Davies, D. A. Ritchie, R. C. Iotti, and F. Rossi, "Terahertz semiconductor-heterostructure laser," *Nature*, vol. 417, pp. 156–159, 2002.

[50] J. Faist, F. Capasso, C. Sirtori, D. L. Sivco, A. L. Hutchinson, and A. Y. Cho, "Vertical transition quantum cascade laser with Bragg confined excited state," *Appl. Phys. Lett.*, vol.

66, no. 5, pp. 538–540, 1995.

[51] J. Faist, D. Hofstetter, M. Beck, T. Aellen, M. Rochat, and S. Blaser, "Bound-to-Continuum and Two-Phonon Resonance Quantum-Cascade Lasers for High Duty Cycle, High-Temperature Operation," *IEEE J. Quantum Electron.*, vol. 38, no. 6, pp. 533–546, 2002.

[52] J. Faist, "Wallplug efficiency of quantum cascade lasers: Critical parameters and fundamental limits," *Appl. Phys. Lett.*, vol. 90, no. 25, p. 253512, 2007.

[53] D. Botez, S. Kumar, J. C. Shin, L. J. Mawst, I. Vurgaftman, and J. R. Meyer, "Temperature dependence of the key electro-optical characteristics for midinfrared emitting quantum cascade lasers," *Appl. Phys. Lett.*, vol. 97, no. 7, p. 071101, 2010.

[54] D. Botez, J. C. Shin, S. Kumar, L. J. Mawst, I. Vurgaftman, and J. R. Meyer, "Electron leakage and its suppression via deep-well structures in 4.5- to 5.0-μm-emitting quantum cascade lasers," *Opt. Eng.*, vol. 49, no. 11, p. 111108, 2010.

[55] R. Maulini, A. Lyakh, A. Tsekoun, and C. K. N. Patel, "λ~7.1 μm quantum cascade lasers with 19% wall-plug efficiency at room temperature," *Opt. Express*, vol. 19, no. 18, pp. 17203–17211, 2011.

[56] D. Botez, C. Chang, and L. J. Mawst, "Temperature sensitivity of the electro-optical characteristics for mid-infrared (λ = 3–16 μm)-emitting quantum cascade lasers," *J. Phys. D. Appl. Phys.*, vol. 49, no. 4, p. 043001, 2016.

[57] T. S. Mansuripur, C. Vernet, P. Chevalier, G. Aoust, B. Schwarz, F. Xie, C. Caneau, K. Lascola, C.-E. Zah, D. P. Caffey, T. Day, L. J. Missaggia, M. K. Connors, C. A. Wang, A. Belyanin, and F. Capasso, "Single-mode instability in standing-wave lasers: The quantum cascade laser as a self-pumped parametric oscillator," *Phys. Rev. A*, vol. 94, no. 6, p. 063807, 2016.

[58] D. F. Nelson, R. C. Miller, and D. A. Kleinman, "Band nonparabolicity effects in semiconductor quantum wells.," *Phys. Rev. B*, vol. 35, no. 14, pp. 7770–7773, 1987.

[59] B. Gelmont, V. Gorfinkel, and S. Luryi, "Theory of the spectral line shape and gain in quantum wells with intersubband transitions," *Appl. Phys. Lett.*, vol. 68, no. 16, pp. 2171–2173, 1996.

[60] A. Wittmann, Y. Bonetti, J. Faist, E. Gini, and M. Giovannini, "Intersubband linewidths in quantum cascade laser designs," *Appl. Phys. Lett.*, vol. 93, no. 14, p. 141103, 2008.

[61] T. Aellen, R. Maulini, R. Terazzi, N. Hoyler, M. Giovannini, J. Faist, S. Blaser, and L. Hvozdara, "Direct measurement of the linewidth enhancement factor by optical heterodyning of an amplitude-modulated quantum cascade laser," *Appl. Phys. Lett.*, vol. 89, no. 9, p. 091121, 2006.

[62] M. Lerttamrab, S. L. Chuang, C. Gmachl, D. L. Sivco, F. Capasso, and A. Y. Cho,

"Linewidth enhancement factor of a type-I quantum-cascade laser," *J. Appl. Phys.*, vol. 94, no. 8, p. 5426, 2003.

[63]  S. H. Macomber, "Design of high-power, surface-emitting DFB lasers for suppression of filamentation," in *Proceedings of SPIE*, 2003, vol. 4993, pp. 37–49.

[64]  Y. Bai, S. Slivken, S. R. Darvish, A. Haddadi, B. Gokden, and M. Razeghi, "High power broad area quantum cascade lasers," *Appl. Phys. Lett.*, vol. 95, no. 22, p. 221104, 2009.

[65]  S. S. Howard, Z. Liu, and C. F. Gmachl, "Thermal and Stark-Effect Roll-Over of Quantum-Cascade Lasers," *IEEE J. Quantum Electron.*, vol. 44, no. 4, pp. 319–323, 2008.

[66]  D. Botez, J. C. Shin, J. D. Kirch, C.-C. Chang, L. J. Mawst, and T. Earles, "Multidimensional Conduction-Band Engineering for Maximizing the Continuous-Wave (CW) Wallplug Efficiencies of Mid-Infrared Quantum Cascade Lasers," *IEEE J. Sel. Top. Quantum Electron.*, vol. 19, no. 4, p. 1200312, 2013.

[67]  J. C. Shin, M. D'Souza, Z. Liu, J. Kirch, L. J. Mawst, D. Botez, I. Vurgaftman, and J. R. Meyer, "Highly temperature insensitive, deep-well 4.8 μm emitting quantum cascade semiconductor lasers," *Appl. Phys. Lett.*, vol. 94, no. 20, p. 201103, 2009.

[68]  J. C. Shin, "Very Low Temperature Sensitive , Deep-Well Quantum Cascade Lasers (λ = 4.8 μm) grown by MOCVD," Ph.D. dissertation, Dept. Elect. and Comput. Eng., Univ. of Wisconsin-Madison, 2010.

[69]  Y. Bai, N. Bandyopadhyay, S. Tsao, E. Selcuk, S. Slivken, and M. Razeghi, "Highly temperature insensitive quantum cascade lasers," *Appl. Phys. Lett.*, vol. 97, no. 25, p. 251104, 2010.

[70]  J. D. Kirch, J. C. Shin, C.-C. Chang, L. J. Mawst, D. Botez, and T. Earles, "Tapered active-region quantum cascade lasers (lambda=4.8 um) for virtual suppression of carrier-leakage currents," *Electron. Lett.*, vol. 48, no. 4, p. 234, 2012.

[71]  J. Faist, F. Capasso, D. L. Sivco, A. L. Hutchinson, C. Sirtori, S. N. G. Chu, and A. Y. Cho, "Quantum cascade laser: Temperature dependence of the performance characteristics and high $T_0$ operation," *Appl. Phys. Lett.*, vol. 65, no. 23, pp. 2901–2903, 1994.

[72]  V. Spagnolo, A. Lops, G. Scamarcio, M. S. Vitiello, and C. Di Franco, "Improved thermal management of mid-IR quantum cascade lasers," *J. Appl. Phys.*, vol. 103, no. 4, p. 043103, 2008.

[73]  H. K. Lee and J. S. Yu, "Thermal effects in quantum cascade lasers at λ ~ 4.6 μm under pulsed and continuous-wave modes," *Appl. Phys. B*, vol. 106, no. 3, pp. 619–627, 2012.

[74]  A. Bismuto, T. Gresch, A. Bächle, and J. Faist, "Large cavity quantum cascade lasers with InP interstacks," *Appl. Phys. Lett.*, vol. 93, no. 23, p. 231104, 2008.

[75]  M. A. Ordal, R. J. Bell, R. W. Alexander Jr., L. A. Newquist, and M. R. Querry, "Optical

properties of Al, Fe, Ti, Ta, W, and Mo at submillimeter wavelengths," *Appl. Opt.*, vol. 27, no. 6, pp. 1203–1209, 1988.

[76]  M. A. Ordal, L. L. Long, R. J. Bell, S. E. Bell, R. R. Bell, R. W. Alexander Jr., and C. A. Ward, "Optical properties of the metals Al, Co, Cu, Au, Fe, Pb, Ni, Pd, Pt, Ag, Ti, and W in the infrared and far infrared," *Appl. Opt.*, vol. 22, no. 7, pp. 1099–1120, 1983.

[77]  M. A. Ordal, R. J. Bell, R. W. Alexander, L. L. Long, and M. R. Querry, "Optical properties of Au, Ni, and Pb at submillimeter wavelengths," *Appl. Opt.*, vol. 26, no. 4, pp. 744–752, 1987.

[78]  N. Yu, L. Diehl, E. Cubukcu, C. Pflügl, D. Bour, S. Corzine, J. Zhu, G. Höfler, K. B. Crozier, and F. Capasso, "Near-field imaging of quantum cascade laser transverse modes," *Opt. Express*, vol. 15, no. 20, pp. 13227–13235, 2007.

[79]  M. Razeghi, "High-performance InP-based mid-IR quantum cascade lasers," *IEEE J. Sel. Top. Quantum Electron.*, vol. 15, no. 3, pp. 941–951, 2009.

[80]  R. Maulini, A. Lyakh, A. Tsekoun, R. Go, C. Pflügl, L. Diehl, F. Capasso, and C. K. N. Patel, "High power thermoelectrically cooled and uncooled quantum cascade lasers with optimized reflectivity facet coatings," *Appl. Phys. Lett.*, vol. 95, no. 15, p. 151112, 2009.

[81]  Q. Zhang, F.-Q. Liu, W. Zhang, Q. Lu, L. Wang, L. Li, and Z. Wang, "Thermal induced facet destructive feature of quantum cascade lasers," *Appl. Phys. Lett.*, vol. 96, no. 14, p. 141117, 2010.

[82]  M. Suttinger, R. Go, P. Figueiredo, A. Todi, H. Shu, J. Leshin, and A. Lyakh, "Power scaling and experimentally fitted model for broad area quantum cascade lasers in continuous wave operation," *Opt. Eng.*, vol. 57, no. 1, p. 011011, 2018.

[83]  G. M. Schindler, "Optimum Output Efficiency of Homogeneously Broadened Lasers with Constant Loss," *IEEE J. Quantum Electron.*, vol. 16, no. 5, pp. 546–549, 1980.

[84]  M. Kanskar, T. Earles, T. Goodnough, E. Stiers, D. Botez, and L. J. Mawst, "High-power conversion efficiency Al-free diode lasers for pumping high-power solid-state laser systems," in *Proceedings of SPIE*, 2005, vol. 5738, pp. 47–56.

[85]  M. E. Aryaee Panah, L. Han, K. Norrman, N. Pryds, A. Nadtochiy, A. E. Zhukov, A. V. Lavrinenko, and E. S. Semenova, "Mid-IR optical properties of silicon doped InP," *Opt. Mater. Express*, vol. 7, no. 7, pp. 2260–2271, 2017.

[86]  J. Faist, *Quantum cascade lasers*, 1st ed. Oxford, United Kingdom: Oxford University Press, 2013.

[87]  A. Lyakh, R. Maulini, A. Tsekoun, R. Go, S. Von der Porten, C. Pflugl, L. Diehl, F. Capasso, and C. K. N. Patel, "High-performance continuous-wave room temperature 4.0-μm quantum cascade lasers with single-facet optical emission exceeding 2 W," *Proc. Natl. Acad. Sci.*, vol. 107, no. 44, pp. 18799–18802, 2010.

[88] P. Figueiredo, M. Suttinger, R. Go, A. Todi, H. Shu, E. Tsvid, C. K. N. Patel, and A. Lyakh, "Continuous Wave Quantum Cascade Lasers With Reduced Number of Stages," *IEEE Photonics Technol. Lett.*, vol. 29, no. 16, pp. 1328–1331, 2017.

[89] A. Aleksandrova, Y. V. Flores, S. S. Kurlov, M. P. Semtsiv, and W. T. Masselink, "Impact of Cascade Number on the Thermal Properties of Broad-Area Quantum Cascade Lasers," *Phys. Status Solidi*, vol. 215, no. 8, p. 1700441, 2017.

[90] W. T. Masselink, M. P. Semtsiv, A. Aleksandrova, and S. Kurlov, "Power scaling in quantum cascade lasers using broad-area stripes with reduced cascade number," *Opt. Eng.*, vol. 57, no. 1, p. 011015, 2018.

[91] J. N. Walpole, "Semiconductor amplifiers and lasers with tapered gain regions," *Opt. Quantum Electron.*, vol. 28, no. 6, pp. 623–645, 1996.

[92] P. Rauter and F. Capasso, "Multi-wavelength quantum cascade laser arrays," *Laser Photonics Rev.*, vol. 9, no. 5, pp. 452–477, 2015.

[93] R. Kaspi, S. Luong, C. Yang, C. Lu, T. C. Newell, and T. Bate, "Extracting fundamental transverse mode operation in broad area quantum cascade lasers," *Appl. Phys. Lett.*, vol. 109, no. 21, p. 211102, 2016.

[94] R. Kaspi, S. Luong, T. Bate, C. Lu, T. C. Newell, and C. Yang, "Distributed loss method to suppress high order modes in broad area quantum cascade lasers," *Appl. Phys. Lett.*, vol. 111, no. 20, p. 201109, 2017.

[95] P. Rauter, S. Menzel, A. K. Goyal, B. Gökden, C. A. Wang, A. Sanchez, G. W. Turner, F. Capasso, B. Gökden, C. A. Wang, A. Sanchez, G. W. Turner, and F. Capasso, "Master-oscillator power-amplifier quantum cascade laser array," *Appl. Phys. Lett.*, vol. 101, no. 26, p. 261117, 2012.

[96] S. Menzel, L. Diehl, C. Pflügl, A. Goyal, C. Wang, A. Sanchez, G. Turner, and F. Capasso, "Quantum cascade laser master-oscillator power-amplifier with 1.5 W output power at 300 K," *Opt. Express*, vol. 19, no. 17, pp. 16229–16235, 2011.

[97] D. Botez, "Monolithic phase-locked semiconductor laser arrays," in *Diode Laser Arrays*, D. Botez and D. R. Scifres, Eds. Cambridge University Press, 1994, pp. 1–72.

[98] B. G. Saar, K. J. Creedon, L. J. Missaggia, C. A. Wang, M. K. Connors, J. P. Donnelly, G. W. Turner, A. Sanchez-Rubio, and W. D. Herzog, "Coherent Beam-Combining of Quantum Cascade Amplifier Arrays," in *CLEO: Science and Innovations*, 2015, p. STu4G.3.

[99] L. Missaggia, C. Wang, M. Connors, B. Saar, A. Sanchez-Rubio, K. Creedon, G. Turner, and W. Herzog, "Thermal management of quantum cascade lasers in an individually addressable monolithic array architecture," in *Proceedings of SPIE*, 2016, vol. 9730, p. 973008.

[100] P. Rauter, S. Menzel, B. Gokden, A. K. Goyal, C. A. Wang, A. Sanchez, G. Turner, and F. Capasso, "Single-mode tapered quantum cascade lasers," *Appl. Phys. Lett.*, vol. 102, no. 18, p. 181102, 2013.

[101] B. Gökden, T. S. Mansuripur, R. Blanchard, C. Wang, A. Goyal, A. Sanchez-Rubio, G. Turner, and F. Capasso, "High-brightness tapered quantum cascade lasers," *Appl. Phys. Lett.*, vol. 102, no. 5, p. 053503, 2013.

[102] R. Blanchard, T. S. Mansuripur, B. Gökden, N. Yu, M. Kats, P. Genevet, K. Fujita, T. Edamura, M. Yamanishi, and F. Capasso, "High-power low-divergence tapered quantum cascade lasers with plasmonic collimators," *Appl. Phys. Lett.*, vol. 102, no. 19, p. 191114, 2013.

[103] C.-H. Tsai, Y.-S. Su, C.-W. Tsai, D. P. Tsai, and C.-F. Lin, "High-Power Angled Broad-Area 1.3-µm Laser Diodes With Good Beam Quality," *IEEE Photonics Technol. Lett.*, vol. 16, no. 11, pp. 2412–2414, 2004.

[104] S. Ahn, C. Schwarzer, T. Zederbauer, D. C. MacFarland, H. Detz, A. M. Andrews, W. Schrenk, and G. Strasser, "High-power, low-lateral divergence broad area quantum cascade lasers with a tilted front facet," *Appl. Phys. Lett.*, vol. 104, no. 5, p. 051101, 2014.

[105] D. Heydari, Y. Bai, N. Bandyopadhyay, S. Slivken, and M. Razeghi, "High brightness angled cavity quantum cascade lasers," *Appl. Phys. Lett.*, vol. 106, no. 9, p. 091105, 2015.

[106] A. Sanchez-Rubio, T. Y. Fan, S. J. Augst, A. K. Goyal, K. J. Creedon, J. T. Gopinath, V. Daneu, B. Chann, and R. Huang, "Wavelength Beam Combining for Power and Brightness Scaling of Laser Systems," *Lincoln Lab. J.*, vol. 20, no. 2, pp. 52–66, 2014.

[107] R. K. Huang, B. Chann, J. Burgess, B. Lochman, W. Zhou, M. Cruz, R. Cook, D. Dugmore, J. Shattuck, and P. Tayebati, "Teradiode's high brightness semiconductor lasers," in *Proceedings of SPIE*, 2016, vol. 9730, p. 97300C.

[108] B. G. Lee, J. Kansky, A. K. Goyal, C. Pflügl, L. Diehl, M. A. Belkin, A. Sanchez, and F. Capasso, "Beam combining of quantum cascade laser arrays," *Opt. Express*, vol. 17, no. 18, pp. 16216–16224, 2009.

[109] S. Hugger, F. Fuchs, R. Aidam, W. Bronner, R. Loesch, Q. Yang, N. Schulz, J. Wagner, E. Romasew, M. Raab, and H. D. Tholl, "Spectral beam combining of quantum cascade lasers in an external cavity," *Proc. SPIE*, vol. 7325, p. 73250H, 2009.

[110] W. J. Fader and G. E. Palma, "Normal modes of N coupled lasers," *Opt. Lett.*, vol. 10, no. 8, pp. 381–383, 1985.

[111] R. Li and T. Erneux, "Stability conditions for coupled lasers: series coupling versus parallel coupling," *Opt. Commun.*, vol. 99, no. 3–4, pp. 196–200, 1993.

[112] D. Ackley, D. Botez, and B. Bogner, "Phase-locked injection laser arrays with integrated phase shifters," *RCA Rev.*, vol. 44, no. 4, pp. 625–633, 1983.

[113] G. M. de Naurois, M. Carras, B. Simozrag, O. Patard, F. Alexandre, and X. Marcadet, "Coherent quantum cascade laser micro-stripe arrays," *AIP Adv.*, vol. 1, no. 3, p. 032165, 2011.

[114] F.-L. Yan, J.-C. Zhang, Z.-W. Jia, N. Zhuo, S.-Q. Zhai, S.-M. Liu, F.-Q. Liu, and Z.-G. Wang, "High-power phase-locked quantum cascade laser array emitting at $\lambda \sim 4.6$ μm," *AIP Adv.*, vol. 6, no. 3, p. 035022, 2016.

[115] L. K. Hoffmann, M. Klinkmüller, E. Mujagić, M. P. Semtsiv, W. Schrenk, W. T. Masselink, and G. Strasser, "Tree array quantum cascade laser," *Opt. Express*, vol. 17, no. 2, pp. 649–657, 2009.

[116] A. Lyakh, R. Maulini, A. Tsekoun, R. Go, and C. K. N. K. N. Patel, "Continuous wave operation of buried heterostructure 4.6μm quantum cascade laser Y-junctions and tree arrays," *Opt. Express*, vol. 22, no. 1, pp. 1203–1208, 2014.

[117] L. K. Hoffmann, C. A. Hurni, S. Schartner, M. Austerer, E. Mujagić, M. Nobile, A. Benz, W. Schrenk, A. M. Andrews, P. Klang, and G. Strasser, "Coherence in Y-coupled quantum cascade lasers," *Appl. Phys. Lett.*, vol. 91, no. 16, p. 161106, 2007.

[118] W. Zhou, S. Slivken, and M. Razeghi, "Phase-locked, high power, mid-infrared quantum cascade laser arrays," *Appl. Phys. Lett.*, vol. 112, no. 18, p. 181106, 2018.

[119] L. Wang, J. Zhang, Z. Jia, Y. Zhao, C. Liu, Y. Liu, S. Zhai, Z. Ning, X. Xu, and F. Liu, "Phase-locked array of quantum cascade lasers with an integrated Talbot cavity," *Opt. Express*, vol. 24, no. 26, pp. 30275–30281, 2016.

[120] B. Meng, B. Qiang, E. Rodriguez, X. N. Hu, G. Liang, and Q. J. Wang, "Coherent emission from integrated Talbot-cavity quantum cascade lasers," *Opt. Express*, vol. 25, no. 4, pp. 3077–3082, 2017.

[121] A. A. Golubentsev, V. V Likhanskii, and A. P. Napartovich, "Theory of phase locking of an array of lasers," *Sov. Phys. JETP*, vol. 66, no. 4, pp. 676–682, 1987.

[122] D. Mehuys, W. Streifer, R. G. Waarts, and D. F. Welch, "Modal analysis of linear Talbot-cavity semiconductor lasers," *Opt. Lett.*, vol. 16, no. 11, pp. 823–825, 1991.

[123] Y. Bai, S. R. Darvish, S. Slivken, P. Sung, J. Nguyen, A. Evans, W. Zhang, and M. Razeghi, "Electrically pumped photonic crystal distributed feedback quantum cascade lasers," *Appl. Phys. Lett.*, vol. 91, no. 14, p. 141123, 2007.

[124] Y. Bai, B. Gokden, S. R. Darvish, S. Slivken, and M. Razeghi, "Photonic crystal distributed feedback quantum cascade lasers with 12 W output power," *Appl. Phys. Lett.*, vol. 95, no. 3, p. 031105, 2009.

[125] B. Gökden, Y. Bai, N. Bandyopadhyay, S. Slivken, and M. Razeghi, "Broad area photonic crystal distributed feedback quantum cascade lasers emitting 34 W at $\lambda \sim 4.36$ μm," *Appl. Phys. Lett.*, vol. 97, no. 13, p. 131112, 2010.

[126] R. Peretti, V. Liverini, M. J. Süess, Y. Liang, P.-B. Vigneron, J. M. Wolf, C. Bonzon, A. Bismuto, W. Metaferia, M. Balaji, S. Lourdudoss, E. Gini, M. Beck, and J. Faist, "Room temperature operation of a deep etched buried heterostructure photonic crystal quantum cascade laser," *Laser Photon. Rev.*, vol. 10, no. 5, pp. 843–848, 2016.

[127] D. Botez, L. J. Mawst, G. L. Peterson, and T. J. Roth, "Phase-Locked Arrays of Antiguides: Modal Content and Discrimination," *IEEE J. Quantum Electron.*, vol. 26, no. 3, pp. 482–495, 1990.

[128] L. J. Mawst, D. Botez, T. J. Roth, and G. Peterson, "High-power, in-phase-mode operation from resonant phase-locked arrays of antiguided diode lasers," *Appl. Phys. Lett.*, vol. 55, no. 1, pp. 10–12, 1989.

[129] A. P. Napartovich and D. Botez, "Analytical theory of phase-locked arrays of antiguided diode lasers," in *Proceedings of SPIE*, 1997, vol. 2994, pp. 600–610.

[130] D. Botez, "High-power monolithic phase-locked arrays of antiguided semiconductor diode lasers," *IEE Proc. J - Optoelectron.*, vol. 139, no. 1, pp. 14–23, 1992.

[131] H. Yang, L. J. Mawst, M. Nesnidal, J. Lopez, A. Bhattacharya, and D. Botez, "10 W near-diffraction-limited peak pulsed power from Al-free, 0.98 μm-emitting phase-locked antiguided arrays," *Electron. Lett.*, vol. 33, no. 2, pp. 136–137, 1997.

[132] J. D. Kirch, C.-C. Chang, C. Boyle, L. J. Mawst, D. Lindberg, T. Earles, and D. Botez, "5.5 W near-diffraction-limited power from resonant leaky-wave coupled phase-locked arrays of quantum cascade lasers," *Appl. Phys. Lett.*, vol. 106, no. 6, p. 061113, 2015.

[133] H. C. Casey and M. B. Panish, "Optical Fields and Wave Propagation," in *Heterostructure lasers, Part A*, New York, NY: Academic Press, 1978, pp. 20–109.

[134] C. Zmudzinski, D. Botez, L. J. Mawst, A. Bhattacharya, M. Nesnidal, and R. F. Nabiev, "Three-Core ARROW-Type Diode Laser: Novel High-Power, Single-Mode Device, and Effective Master Oscillator for Flared Antiguided MOPA's," *IEEE J. Sel. Top. Quantum Electron.*, vol. 1, no. 2, pp. 129–137, 1995.

[135] C.-C. Chang, J. D. Kirch, C. Boyle, C. Sigler, L. J. Mawst, D. Botez, B. Zutter, P. Buelow, K. Schulte, T. Kuech, and T. Earles, "Planarized process for resonant leaky-wave coupled phase-locked arrays of mid-IR quantum cascade lasers," in *Proceedings of SPIE*, 2015, vol. 9382, p. 938213.

[136] A. Evans, J. S. Yu, S. Slivken, and M. Razeghi, "Continuous-wave operation of λ~4.8 μm quantum-cascade lasers at room temperature," *Appl. Phys. Lett.*, vol. 85, no. 12, pp. 2166–2168, 2004.

[137] W. Metaferia, B. Simozrag, C. Junesand, Y.-T. Sun, M. Carras, R. Blanchard, F. Capasso, and S. Lourdudoss, "Demonstration of a quick process to achieve buried heterostructure quantum cascade laser leading to high power and wall plug efficiency," *Opt. Eng.*, vol. 53, no. 8, p. 087104, 2014.

[138] A. Lyakh, C. Pflügl, L. Diehl, Q. J. Wang, F. Capasso, X. J. Wang, J. Y. Fan, T. Tanbun-Ek, R. Maulini, A. Tsekoun, R. Go, and C. Kumar N. Patel, "1.6 W high wall plug efficiency, continuous-wave room temperature quantum cascade laser emitting at 4.6 μm," *Appl. Phys. Lett.*, vol. 92, no. 11, p. 111110, 2008.

[139] C. Gmachl, A. Straub, R. Colombelli, F. Capasso, D. L. Sivco, A. M. Sergent, and A. Y. Cho, "Single-Mode, Tunable Distributed-Feedback and Multiple-Wavelength Quantum Cascade Lasers," *IEEE J. Quantum Electron.*, vol. 38, no. 6, pp. 569–581, 2002.

[140] D.-Y. Yao, J.-C. Zhang, F.-Q. Liu, Z.-W. Jia, F. Yan, L.-J. Wang, J.-Q. Liu, and Z.-G. Wang, "1.8-W Room Temperature Pulsed Operation of Substrate-Emitting Quantum Cascade Lasers," *IEEE Photonics Technol. Lett.*, vol. 26, no. 4, pp. 323–325, 2014.

[141] Q. Y. Lu, Y. Bai, N. Bandyopadhyay, S. Slivken, and M. Razeghi, "Room-temperature continuous wave operation of distributed feedback quantum cascade lasers with watt-level power output," *Appl. Phys. Lett.*, vol. 97, no. 23, p. 231119, 2010.

[142] P. Yeh, C. Gu, and D. Botez, "Optical properties of dual-state Fabry–Perot étalons," *Opt. Lett.*, vol. 17, no. 24, pp. 1818–1820, 1992.

[143] D. Botez, A. P. Napartovich, and C. A. Zmudzinski, "Phase-Locked Arrays of Antiguides: Analytical Theory II," *IEEE J. Quantum Electron.*, vol. 31, no. 2, pp. 244–253, 1995.

[144] A. P. Napartovich, N. N. Elkin, D. V Vysotsky, S. Mao, J. Kirch, and L. J. Mawst, "Two-Dimensional Antiguided Vertical Cavity Surface Emitting Laser Arrays With Reflecting Boundary," *IEEE J. Sel. Top. Quantum Electron.*, vol. 19, no. 4, p. 1700208, 2013.

[145] R. F. Nabiev and D. Botez, "Comprehensive Above-Threshold Analysis of Antiguided Diode Laser Arrays," *IEEE J. Sel. Top. Quantum Electron.*, vol. I, no. 2, pp. 138–149, 1995.

[146] A. Evans, S. R. Darvish, S. Slivken, J. Nguyen, Y. Bai, and M. Razeghi, "Buried heterostructure quantum cascade lasers with high continuous-wave wall plug efficiency," *Appl. Phys. Lett.*, vol. 91, no. 7, p. 071101, 2007.

[147] D. Pierścińska, K. Pierściński, M. Płuska, G. Sobczak, A. Kuźmicz, P. Gutowski, and M. Bugajski, "Temperature induced degradation mechanisms of AlInAs/InGaAs/InP quantum cascade lasers," *Mater. Res. Express*, vol. 5, no. 1, p. 016204, 2018.

[148] J. D. Kirch, H. Kim, C. Boyle, C.-C. Chang, L. J. Mawst, D. Lindberg III, T. Earles, D. Botez, M. Helm, J. von Borany, S. Akhmadaliev, R. Böttger, and C. Reyner, "Proton implantation for electrical insulation of the InGaAs/InAlAs superlattice material used in 8–15 μm-emitting quantum cascade lasers," *Appl. Phys. Lett.*, vol. 110, no. 8, p. 082102, 2017.

[149] M. Brandstetter, S. Schönhuber, M. Krall, M. A. A. Kainz, H. Detz, T. Zederbauer, A. M. Andrews, G. Strasser, and K. Unterrainer, "Spectrally resolved far-fields of terahertz quantum cascade lasers," *Opt. Express*, vol. 24, no. 22, pp. 25462–25470, 2016.

[150] A. P. Napartovich, N. N. Elkin, D. V. Vysotsky, J. Kirch, C. Sigler, D. Botez, L. J. Mawst, and A. Belyanin, "Above-threshold numerical modeling of high-index-contrast photonic-crystal quantum cascade lasers," in *Proceedings of SPIE*, 2015, vol. 9382, p. 93821L.

[151] S. H. Macomber, J. S. Mott, B. D. Schwartz, R. S. Setzko, J. J. Powers, P. A. Lee, D. P. Kwo, R. M. Dixon, and J. E. Logue, "Curved-Grating, Surface-Emitting DFB Lasers and Arrays," in *Proceedings of SPIE*, 1997, vol. 3001, pp. 42–54.

[152] Y. Sin, Z. Lingley, M. Brodie, N. Presser, S. C. Moss, J. Kirch, C. C. Chang, C. Boyle, L. J. Mawst, D. Botez, D. Lindberg III, and T. Earles, "Destructive physical analysis of degraded quantum cascade lasers," in *Proceedings of SPIE*, 2015, vol. 9382, p. 93821P.

[153] H. Kogelnik and C. V Shank, "Coupled-wave theory of distributed feedback lasers," *J. Appl. Phys.*, vol. 43, no. 5, pp. 2327–2335, 1972.

[154] R. F. Kazarinov and R. A. Suris, "Injection Heterojunction Laser with a Diffraction Grating on its Contact Surface," *Sov Phys Semicond*, vol. 6, no. 7, pp. 1184–1189, 1973.

[155] P. Zory, "Laser oscillation in leaky corrugated optical waveguides," *Appl. Phys. Lett.*, vol. 22, no. 4, pp. 125–128, 1973.

[156] G. A. Evans, J. M. Hammer, N. W. Carlson, F. R. Elia, E. A. James, and J. B. Kirk, "Surface-emitting second order distributed Bragg reflector laser with dynamic wavelength stabilization and far-field angle of 0.25°," *Appl. Phys. Lett.*, vol. 49, no. 6, pp. 314–315, 1986.

[157] K. Mitsunaga, M. Kameya, K. Kojima, S. Noda, K. Kyuma, K. Hamanaka, and T. Nakayama, "cw surface-emitting grating-coupled GaAs/AlGaAs distributed feedback laser with very narrow beam divergence," *Appl. Phys. Lett.*, vol. 50, no. 25, pp. 1788–1790, 1987.

[158] R. J. Noll and S. H. Macomber, "Analysis of Grating Surface Emitting Lasers," *IEEE J. Quantum Electron.*, vol. 26, no. 3, pp. 456–466, 1990.

[159] W. Streifer, D. R. Scifres, and R. D. Burnham, "Coupling coefficients for distributed feedback single- and double-heterostructure diode lasers," *IEEE J. Quantum Electron.*, vol. 11, no. 11, pp. 867–873, 1975.

[160] B. G. Lee, M. A. Belkin, C. Pflugl, L. Diehl, H. A. Zhang, R. M. Audet, J. MacArthur, D. P. Bour, S. W. Corzine, G. E. Höfler, and F. Capasso, "DFB Quantum Cascade Laser Arrays," *IEEE J. Quantum Electron.*, vol. 45, no. 5, pp. 554–565, 2009.

[161] S. Li, G. Witjaksono, S. Macomber, and D. Botez, "Analysis of surface-emitting second-order distributed feedback lasers with central grating phaseshift," *IEEE J. Sel. Top. Quantum Electron.*, vol. 9, no. 5, pp. 1153–1165, 2003.

[162] G. Witjaksono and D. Botez, "Surface-emitting, single-lobe operation from second-order distributed-reflector lasers with central grating phaseshift," *Appl. Phys. Lett.*, vol. 78, no.

26, pp. 4088–4090, 2001.

[163] G. Witjaksono, S. Li, J. J. Lee, D. Botez, and W. K. Chan, "Single-lobe, surface-normal beam surface emission from second-order distributed feedback lasers with half-wave grating phase shift," *Appl. Phys. Lett.*, vol. 83, no. 26, pp. 5365–5367, 2003.

[164] E. Miyai and S. Noda, "Phase-shift effect on a two-dimensional surface-emitting photonic-crystal laser," *Appl. Phys. Lett.*, vol. 86, no. 11, p. 111113, 2005.

[165] S. H. Macomber, "Nonlinear Analysis of Surface-Emitting Distributed Feedback Lasers," *IEEE J. Quantum Electron.*, vol. 26, no. 12, pp. 2065–2074, 1990.

[166] N. Finger, W. Schrenk, and E. Gornik, "Analysis of TM-Polarized DFB Laser Structures with Metal Surface Gratings," *IEEE J. Quantum Electron.*, vol. 36, no. 7, pp. 780–786, 2000.

[167] R. Colombelli, K. Srinivasan, M. Troccoli, O. Painter, C. F. Gmachl, D. M. Tennant, A. M. Sergent, D. L. Sivco, A. Y. Cho, and F. Capasso, "Quantum Cascade Surface-Emitting Photonic Crystal Laser," *Science*, vol. 302, no. 5649, pp. 1374–1377, 2003.

[168] C. Pflügl, M. Austerer, W. Schrenk, S. Golka, G. Strasser, R. P. Green, L. R. Wilson, J. W. Cockburn, A. B. Krysa, and J. S. Roberts, "Single-mode surface-emitting quantum-cascade lasers," *Appl. Phys. Lett.*, vol. 86, no. 21, p. 211102, 2005.

[169] A. Lyakh, P. Zory, M. D'Souza, D. Botez, D. Bour, M. D. Souza, D. Botez, and D. Bour, "Substrate-emitting, distributed feedback quantum cascade lasers," *Appl. Phys. Lett.*, vol. 91, no. 18, p. 181116, 2007.

[170] G. Maisons, M. Carras, M. Garcia, B. Simozrag, and X. Marcadet, "Directional single mode quantum cascade laser emission using second-order metal grating coupler," *Appl. Phys. Lett.*, vol. 98, no. 2, p. 021101, 2011.

[171] G. Maisons, M. Carras, M. Garcia, O. Parillaud, B. Simozrag, X. Marcadet, and a. De Rossi, "Substrate emitting index coupled quantum cascade lasers using biperiodic top metal grating," *Appl. Phys. Lett.*, vol. 94, no. 15, p. 151104, 2009.

[172] Y. Bai, S. Tsao, N. Bandyopadhyay, S. Slivken, Q. Y. Lu, D. Caffey, M. Pushkarsky, T. Day, and M. Razeghi, "High power, continuous wave, quantum cascade ring laser," *Appl. Phys. Lett.*, vol. 99, no. 26, p. 261104, 2011.

[173] D.-Y. Yao, J. Zhang, F.-Q. Liu, N. Zhuo, F.-L. Yan, L.-J. Wang, J.-Q. Liu, and Z.-G. Wang, "Surface emitting quantum cascade lasers operating in continuous-wave mode above 70 °C at $\lambda \sim 4.6$ μm," *Appl. Phys. Lett.*, vol. 103, no. 4, p. 041121, 2013.

[174] C. Schwarzer, R. Szedlak, S. Il Ahn, T. Zederbauer, H. Detz, A. M. Andrews, W. Schrenk, and G. Strasser, "Linearly polarized light from substrate emitting ring cavity quantum cascade lasers," *Appl. Phys. Lett.*, vol. 103, no. 8, p. 081101, 2013.

[175] R. Szedlak, C. Schwarzer, T. Zederbauer, H. Detz, A. M. Andrews, W. Schrenk, and G. Strasser, "Grating-based far field modifications of ring quantum cascade lasers," *Opt. Express*, vol. 22, no. 13, pp. 15829–15836, 2014.

[176] S. Kumar, B. S. Williams, Q. Qin, A. W. M. Lee, Q. Hu, and J. L. Reno, "Surface-emitting distributed feedback terahertz quantum-cascade lasers in metal-metal waveguides.," *Opt. Express*, vol. 15, no. 1, pp. 113–128, 2007.

[177] G. Sevin, D. Fowler, G. Xu, F. H. Julien, R. Colombelli, S. P. Khanna, E. H. Linfield, and A. G. Davies, "Optimized surface-emitting photonic-crystal terahertz quantum cascade lasers with reduced resonator dimensions," *Appl. Phys. Lett.*, vol. 97, no. 13, p. 131101, 2010.

[178] L. Mahler, A. Tredicucci, F. Beltram, C. Walther, J. Faist, H. E. Beere, and D. A. Ritchie, "High-power surface emission from terahertz distributed feedback lasers with a dual-slit unit cell," *Appl. Phys. Lett.*, vol. 96, no. 19, p. 191109, 2010.

[179] G. Xu, R. Colombelli, S. P. Khanna, A. Belarouci, X. Letartre, L. Li, E. H. Linfield, A. G. Davies, H. E. Beere, and D. A. Ritchie, "Efficient power extraction in surface-emitting semiconductor lasers using graded photonic heterostructures," *Nat. Commun.*, vol. 3, p. 952, 2012.

[180] T.-Y. Kao, Q. Hu, and J. L. Reno, "Phase-locked arrays of surface-emitting terahertz quantum-cascade lasers," *Appl. Phys. Lett.*, vol. 96, no. 10, p. 101106, 2010.

[181] Y. Halioua, G. Xu, S. Moumdji, L. Li, J. Zhu, E. H. Linfield, A. G. Davies, H. E. Beere, D. A. Ritchie, and R. Colombelli, "Phase-locked arrays of surface-emitting graded-photonic-heterostructure terahertz semiconductor lasers," *Opt. Express*, vol. 23, no. 5, pp. 6915–6923, 2015.

[182] A. Yariv and A. Gover, "Equivalence of the coupled-mode and Floquet-Bloch formalisms in periodic optical waveguides," *Appl. Phys. Lett.*, vol. 26, no. 9, pp. 537–539, 1975.

[183] H. J. Luo and P. S. Zory, "Ray Optics Determination of the DFB Coupling Coefficient in Separate Confinement and Multiquantum-Well Laser Structures," *IEEE J. Quantum Electron.*, vol. 30, no. 1, pp. 10–14, 1994.

[184] H. J. Luo and P. S. Zory, "Distributed Feedback Coupling Coefficient in Diode Lasers with Metallized Gratings," *IEEE Photonics Technol. Lett.*, vol. 2, no. 9, pp. 614–616, 1990.

[185] H. Kogelnik, "Theory of Dielectric Waveguides," in *Integrated Optics*, 1975, pp. 13–81.

[186] C. Sigler, X. Wang, L. J. Mawst, and P. S. Zory, "First-Order Grating TM Coupling Coefficients for Distributed Feedback Quantum Cascade Lasers," *IEEE J. Quantum Electron.*, vol. 54, no. 4, pp. 1–7, 2018.

[187] P. Yeh, "Matrix Formulation for Isotropic Layered Media," in *Optical Waves in Layered*

*Media*, Wiley, 2005.

[188] D. Marcuse, "Higher-Order Scattering Losses in Dielectric Waveguides," *Bell Syst. Tech. J.*, vol. 51, no. 8, pp. 1801–1817, 1972.

[189] W. Streifer, R. D. Burnham, and D. R. Scifres, "Effect of External Reflectors on Longitudinal Modes of Distributed Feedback Lasers," *IEEE J. Quantum Electron.*, vol. 11, no. 4, pp. 154–161, 1975.

[190] M. Carras and A. De Rossi, "Photonic modes of metallodielectric periodic waveguides in the midinfrared spectral range," *Phys. Rev. B*, vol. 74, no. 23, p. 235120, 2006.

[191] Z. Yu, G. Veronis, S. Fan, and M. L. Brongersma, "Design of midinfrared photodetectors enhanced by surface plasmons on grating structures," *Appl. Phys. Lett.*, vol. 89, no. 15, p. 151116, 2006.

[192] A. Wittmann, A. Hugi, E. Gini, N. Hoyler, and J. Faist, "Heterogeneous High-Performance Quantum-Cascade Laser Sources for Broad-Band Tuning," *IEEE J. Quantum Electron.*, vol. 44, no. 11, pp. 1083–1088, 2008.

[193] A. Lyakh, R. Maulini, A. Tsekoun, R. Go, C. Pflügl, L. Diehl, Q. J. Wang, F. Capasso, and C. K. N. Patel, "3 W continuous-wave room temperature single-facet emission from quantum cascade lasers based on nonresonant extraction design approach," *Appl. Phys. Lett.*, vol. 95, no. 14, p. 141113, 2009.

[194] D. H. Wu and M. Razeghi, "High power, low divergent, substrate emitting quantum cascade ring laser in continuous wave operation," *APL Mater.*, vol. 5, no. 3, p. 035505, 2017.